Spectral Properties of Single Raman-Scattered Photons

Dissertation

zur Erlangung des Grades
des Doktors der Naturwissenschaften
der Naturwissenschaftlich-Technischen Fakultät
der Universität des Saarlandes

von

Matthias Hermann Kreis

Saarbrücken
2022

Abstract

Single photons with well controlled spectral and temporal properties are an essential resource for quantum communication protocols, such as the quantum repeater. Such photons can be generated from a single ion by Raman scattering. A fundamental understanding of the underlying scattering process allows to tailor properties of these Raman photons for the respective application. This work contains a comprehensive experimental study on spectral properties of single Raman-scattered photons, generated by laser excitation. The necessary experimental tools to measure spectra of single photons are presented. In addition, I expand an existing quantum optical model description to corroborate the experimental results. With study of $393\,\mathrm{nm}$ and $854\,\mathrm{nm}$ photons emitted from a single $^{40}\mathrm{Ca}^+$ ion, I am able to characterize the dependence of their spectra on properties of the excitation laser. With that, I confirm that the linewidth of a photon generated with weak laser excitation is narrower than the corresponding transition in the $^{40}\mathrm{Ca}^+$ ion. Furthermore, I study the influence of quantum interference effects on the spectrum of the scattered photon. In all cases, the measured spectra are in good agreement with spectra calculated using the model. As an application of tailored spectral properties, atom-photon entanglement is generated. Thereby spectral filtering erases the correlation between frequency and polarization.

Zusammenfassung

Einzelne Photonen mit kontrollierten spektralen und zeitlichen Eigenschaften sind eine wichtige Ressource für Quantenkommunikationsprotokolle wie den Quantenrepeater. Solche Photonen können mit einem einzelnen Ion durch Raman-Streuung erzeugt werden. Ein grundlegendes Verständnis des Streuprozesses erlaubt es Raman-Photonen an die jeweilige Anwendung anzupassen. Diese Arbeit enthält eine umfassende experimentelle Analyse der spektralen Eigenschaften von einzelnen durch Laseranregung gestreuten Raman-Photonen. Ich stelle die benötigten experimentellen Werkzeuge zum Messen der Spektren einzelner Photonen vor. Zusätzlich erweitere ich ein bestehendes quantenoptisches Modell, um die experimentellen Ergebnisse zu untermauern. Ich untersuche $393\,\mathrm{nm}$ und $854\,\mathrm{nm}$ Photonen, welche mit einem $^{40}\mathrm{Ca}^+$ Ion erzeugt werden um die Abhängigkeit des Spektrums von den Parametern des anregenden Lasers zu charakterisieren. Damit zeige ich, dass die Photonen für eine schwache Laseranregung eine schmalere Linienbreite haben als der entsprechende Übergang im $^{40}\mathrm{Ca}^+$ Ion. Zusätzlich untersuche ich den Einfluss von Quanteninterferenzeffekten auf das Spektrum des gestreuten Photons. In allen Fällen zeigen die gemessenen Spektren eine gute Übereinstimmung mit den modellierten Spektren. Als Anwendung von maßgeschneiderten Spektren wird Atom-Photon Verschränkung erzeugt. Dabei löst spektrales filtern die Korrelation zwischen Frequenz und Polarisation auf.

Contents

1. Introduction

A quantum network connects several quantum systems and enables to distribute quantum information between individual nodes. Thereby, many individual small quantum computers can be linked to form a large quantum computer. Additionally, a quantum network offers applications such as secure communication or metrology [1]. The implementation of a quantum network thereby requires well controlled stationary qubits located at the network nodes and flying qubits to distribute entanglement between network nodes. Furthermore, it is necessary to convert stationary qubits into flying qubits and vice versa and to reliably transmit these flying qubits between network nodes [2].

In recent years, the prerequisites to build a large scale quantum network have been successfully implemented. A quantum state encoded in a photon was transmitted successfully through the air over $100\,\text{km}$ across a lake [3], $143\,\text{km}$ between two Canary Islands [4] or over $1000\,\text{km}$ between a satellite and the ground station [5]. The drawback of this free space transmission is that it cannot be done if an obstacle blocks the path or if the weather is bad. These problems do not exist in the case of transmission through optical fibers. This approach would also allow to leverage the existing fiber infrastructure. However, optical fibers have their own disadvantages as the maximum transmission distance is limited by absorption losses. These absorption losses scale exponentially with the length of the transmission channel. Doubling the length of a transmission line with $1\,\%$ transmission results in a transmission of $0.01\,\%$.

To reduce absorption losses, the photon carrying the quantum information can be converted to telecommunication wavelengths. Bock et al. demonstrated a successful conversion of $854\,\text{nm}$ photons to $1310\,\text{nm}$ without losing quantum information or entanglement [6]. Using quantum frequency conversion, atom-photon entanglement was transmitted through $50\,\text{km}$ of optical fiber [7]. Additionally, quantum frequency conversion allows to connect several atom and ion species with different wavelengths. While quantum frequency conversion reduces absorption losses, they are still present. Consequently, the maximal transmission distance is limited. Therefore, an additional approach has to be taken to spread quantum information through a fiber based network with distant network nodes. Amplification as used in the case of classical signals can not be used for quantum information, as the no-cloning theorem [8] prevents copying and consequently amplification of the signal. Instead, the problem of exponential scaling absorption losses can be solved with a quantum repeated protocol [9].

This quantum repeater protocol divides the transmission channel into shorter transmission segments between individual repeater nodes. First, the repeater nodes at the end of each segment are entangled. Thereafter, this entanglement is distributed with entanglement swapping until finally the network nodes at the end of the transmission channel are entangled [10]. The estab-

lished entanglement between nodes at the end of the full transmission channel is then used to transmit quantum information via teleportation. The teleportation itself requires the exchange of classical information, which can be transmitted over the full distance without any problems. With this approach, the quantum repeater trades the exponentially scaling absorption loss for an effort in material and time that scales polynomial with the length of the full transmission channel [9]. Therefore, the quantum repeater protocol allows to transmit quantum information over distances which can not be bridged by direct transmission.

A quantum repeater can be realized in the sender configuration with single ions as repeater nodes and photons to distribute entanglement between repeater nodes. In this configuration, the ion as a network node stores stationary qubits. Each network node emits single photons that are entangled with the ion. These photons act as flying qubits to distribute entanglement. An important role in this repeater scheme is thereby played by the quantum-interface connecting the stationary network nodes with the flying photons. Such an atom-photon quantum interface can be build on the basis of Raman scattering of single photons. Various experiments showed possible applications of this atom-photon quantum-interface [11–15]. It was used for atom-photon entanglement generation, to store the polarization qubit from an incoming photon or to send out the atomic qubit encoded in the polarization of an emitted photon. The scattered Raman photon thereby either carries quantum information or is used as herald for a successful storage process.

To improve the atom-photon quantum-interface, various experiments have studied the wave packets of Raman photons emitted into free space or from an emitter located inside a cavity. These studies showed that the shape and duration of the wave packet can be controlled by the pulse shape and Rabi frequency of the exciting laser [16–18]. Further experiments studied quantum interference effects in photons scattered from an initial superposition state, where the interference in the absorption or emission process leads to quantum beats in the wave packet of the scattered photon [19]. In contrast to these studies on the temporal shape of the scattered Raman photon, studies on spectral properties are mainly theoretical [20] or focus on resonance fluorescence [21, 22], that means Rayleigh scattering. Experimental studies with photons scattered from a quantum dot emitting into free space [23] or into a cavity [24] show only rudimentary results.

The overarching goal of this work is to characterize the spectral properties of single Raman-scattered photons. Therefore, I measure spectra of single Raman photons generated from a single ^{40}Ca$^+$ ion with a custom-built high-resolution optical spectrum analyzer. I study mainly 393 nm photons scattered on the $P_{3/2}$ to $S_{1/2}$ transition of the calcium ion but also 854 nm photons scattered on the $P_{3/2}$ to $D_{5/2}$ transition. On the way to the main goal three individual objectives are addressed:

1. Extend existing models [20, 25] to describe the spectrum of a scattered Raman photon in a multi level system and for modulated laser excitation.

2. Characterize the influence of the Rabi frequency, detuning and pulse shape of the laser excitation as well as the influence of interference in absorption, in emission or due to coupling to other levels on the spectral properties of the scattered Raman photon.

3. Tailor spectral properties with the parameters of the laser excitation to improve atom-photon entanglement.

The first objective is targeted in Chapter 5. Throughout the work, the developed model is used to simulate the performed experiments. Chapter 6 deals with the second objective. I explore the spectral shape and width of a single Raman scattered photon. For this purpose, I analyze how the spectrum depends on the parameters of the exciting laser and study the effect of various quantum interference mechanisms on the emitted spectrum. Chapter 7 seeks to leverage results from the previous two chapters to generate atom-photon entanglement with spectral tailored photons. I discuss how the spectrum of the scattered photon and a spectral filter influence the generated atom-photon state. The findings of this work are summarized in Chapter 8.

The results presented in the later chapters of this work require some preparation which is done in the first chapters of this work. In Chapter 2 I introduce the formalism, the $^{40}\text{Ca}^+$ ion as physical platform, ion trapping and other required basics. In the following chapters 3 and 4 the experimental setup and methods are presented. This contains two custom-built single photon spectrometer setups based on Fabry-Pérot resonators, one for 393 nm photons the other one for 854 nm photons.

2. Fundamental concepts

2.1. The ^{40}Ca$^+$ ion

Calcium is the element with the atomic number 20. As an element from the alkaline earth metal group it has two electrons in the outer shell. One of these electrons is removed in an ionization process to create a single charged hydrogen-like calcium ion. For this reason calcium has two main benefits for quantum optical experiments. The calcium ion can be trapped in a Paul trap and it features a simple hydrogen-like level scheme. From the available stable isotopes, ^{40}Ca$^+$ has no nuclear spin and thus shows no hyperfine splitting in contrast to, for example, ^{43}Ca$^+$. In addition, there are commercially available laser systems for all relevant optical transitions. For these reasons, the ^{40}Ca$^+$ ion is a good candidate for quantum optics experiments and was chosen for the experimental setup.

From the full term scheme of the ^{40}Ca$^+$ ion, five states are of interest for this work. Together with their respective Zeeman levels they form an eighteen-level system with seven optical transitions (see Figure 2.1 and properties in Table 2.1). Two excited states $P_{3/2}$ and $P_{1/2}$ with a lifetime of 6.9 ns respectively 7.1 ns decay on electric dipole transitions into the stable ground state $S_{1/2}$ or the meta stable states $D_{5/2}$ respectively $D_{3/2}$. Both D states have a lifetime of about 1.2 s and decay on electric quadrupole transitions into the $S_{1/2}$ ground state. Due to the long lifetimes of the D states compared to the life time of the P states, the D states are treated as stable in most cases.
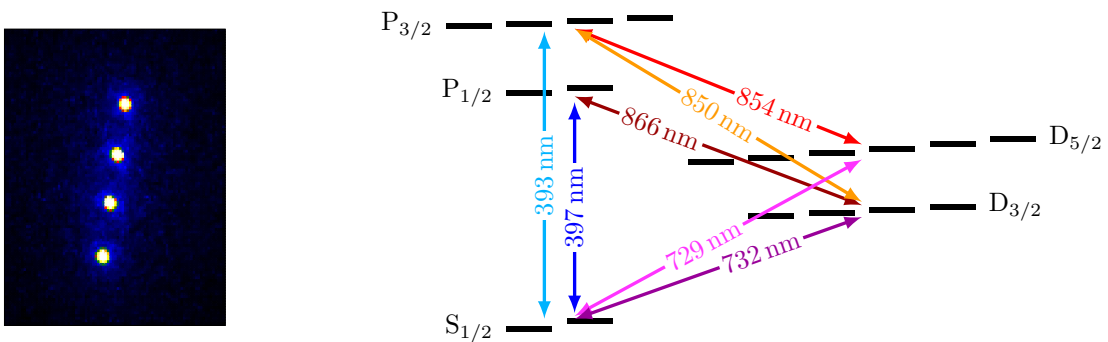
Figure 2.1.: String of four ^{40}Ca$^+$ ions trapped during this work and the relevant level scheme of a single ^{40}Ca$^+$ ion with all optical transitions and their wavelengths. Each state is split up in several Zeeman levels which are separated in energy due to the applied magnetic field.

Table 2.1.: Properties of the relevant states and transitions of the $^{40}\text{Ca}^+$ ion. Life times and branching ratios are taken from [26–29]. Decay rates are calculated from these values. Vacuum wavelengths are taken from [25].

State	life time	decay to	wavelength	decay rate	ratio
$P_{1/2}$	7.098(20) ns	$\to S_{1/2}$	396.95915(3) nm	20.98(6) MHz	0.93565(7)
$P_{1/2}$	7.098(20) ns	$\to D_{3/2}$	866.45211(15) nm	1.442(4) MHz	0.06435(7)
$P_{3/2}$	6.924(19) ns	$\to S_{1/2}$	393.48075(3) nm	21.49(6) MHz	0.9347(3)
$P_{3/2}$	6.924(19) ns	$\to D_{5/2}$	854.44337(15) nm	1.349(6) MHz	0.0587(2)
$P_{3/2}$	6.924(19) ns	$\to D_{3/2}$	850.03561(14) nm	0.152(1) MHz	0.00661(4)
$D_{5/2}$	1.168(9) s	$\to S_{1/2}$	729.34765(11) nm	1363(8) mHz	1
$D_{3/2}$	1.176(11) s	$\to S_{1/2}$	732.5905(2) nm	1353(9) mHz	1
$S_{1/2}$	∞	stable			

The eighteen level system can be split in two smaller systems, which are almost independent from each other. The first system contains the stats $S_{1/2}$, $P_{1/2}$ and $D_{3/2}$ with a total number of eight Zeeman levels. This system is utilized for Doppler cooling and fluorescence detection with the 397 nm and 866 nm laser. The second system contains the $S_{1/2}$, $P_{3/2}$ and $D_{5/2}$ states. It has a total number of 12 Zeeman levels. In this work single Raman-scattered photons are generated with this system. I study the spectra from these photons and generate atom-photon entanglement with them. Both smaller systems are connected by the 850 nm transition. The decay rate on this transitions is small compared to the 854 nm and 393 nm decay rates and therefore I neglect this decay in most discussions. In photon generation schemes the 850 nm decay acts as a loss channel that reduces the efficiency of the protocols. However, in the experimental realization, a possible 850 nm decay has to be taken into account in state detection schemes.

To drive transitions between these states, laser systems for all transitions except for the 732 nm transition are available in the laboratory setup. From these lasers, the 850 nm laser was not operated. Additionally, two coils are available to drive the transitions between adjacent Zeeman sublevels with microwave field. A coil to drive the transition in the $S_{1/2}$ state has been operated for a long time [12]. A second coil to drive transitions in the $D_{5/2}$ state has been installed and studied recently [30].

2.2. Ion trapping with a linear Paul trap

The Paul trap developed with the ideas of W. Paul [31] and E. Fischer [32] utilizes oscillating and static electric fields to trap charged particles. In a Paul trap, single ions can be well isolated from the environment and as consequence stored in principle indefinitely long [33]. A feature of the Paul trap is that only electric fields generate the trapping potential. Consequently, the trap itself has no influence on the electronic level structure of the stored ion. This is an important advantage for quantum information and other applications, where the magnetic field defines the quantization axis and sets the energy splitting of the electronic levels.

Quantum optical experiments operate Paul traps with many different designs. The simplest design consists of a ring electrode and two end caps. A different common design is the linear Paul trap. This trap consists of four electrodes mounted in quadrupole configuration and two end caps. The oscillating field is applied to the quadrupole electrodes for the radial confinement, wile a static field is applied to the end caps for the axial confinement. In different experiments, linear Paul traps are further developed into surface or segmented traps [34–37] suited for specific applications. One example would be moving ions around and swap their position [38]. However, for many applications a linear Paul trap without any modifications is most suitable. Here, I summarize the working principle of such a linear Paul trap as mounted in the experimental setup (details see Section 3.1). A more detailed description is given for example in [39–41].

The linear Paul trap consists of four electrodes in quadrupole configuration with an oscillating voltage U_{rf} applied to them for the radial confinement of the ion string (gray, see Figure 2.2). Opposite electrodes are put on the same electric potential. For the axial confinement a voltage U_{et} is applied to the two end tip electrodes (brown, see Figure 2.2). Additional electrodes placed around the trap (purple) shift the ion position to compensate the micromotion (see below).

For the description, the center of the trap is placed in the origin. The symmetry axis of the quadrupole electrodes becomes the z-axis. These quadrupole electrodes are placed on the x- and y-axis in a distance a from the z-axis. The end tip electrodes have a distance b from the
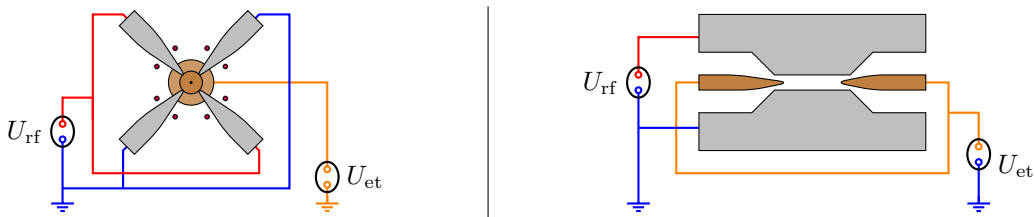
Figure 2.2.: Electrode arrangement in a linear Paul trap as seen in the cut through the xy-plane (left) or in a cut through the yz-plan (right). Opposite quadrupole electrodes (gray) are put on the same electric potential, with two electrodes connected to ground. The end tips (brown) on both sides keep the ion trapped in the third dimension. Around the trap there are additional electrodes (purple) to shift the ion around by applying additional voltages.

trap center. In this case, the electric potential around the center of the trap, caused by the applied voltages is

$$\Phi(x,y,z,t) = \Phi_{\mathrm{rf}}(x,y,t) + \Phi_{\mathrm{et}}(x,y,z) = \frac{U_{\mathrm{rf}}}{2a^2}(x^2 - y^2 + a^2)\cos(\Omega_{\mathrm{rf}}t)) + \frac{\alpha U_{\mathrm{et}}}{2b}(2z^2 - x^2 - y^2). \quad (2.1)$$

The parameter α is given by the geometry of the trap and takes the effect of the quadrupole potential into account.

The trap potential accelerates a positive charged ion located near the center of the trap towards one of the electrodes connected to the negative voltage. As this voltage is inverted, the ion becomes accelerated towards one of the other electrodes. This process is repeated periodically, which leads to an effective trapping potential, if the trap parameters, for example the frequency of the oscillating quadrupole field, are chosen right. In this case equations of motion for the ion in the trap can be derived from the trap potential. These equations of motion for the three dimensions $r_k = x, y, z$ can be express in form of the Mathieu differential equation

$$\ddot{r}_k + (p_k - 2q_k\cos(\Omega_{\mathrm{rf}}t))\frac{\Omega_{\mathrm{rf}}^2}{2}r_k = 0. \quad (2.2)$$

In these equations, the coefficients

$$p_x = p_y = -\frac{4e\alpha U_{\mathrm{et}}}{mb^2\Omega_{\mathrm{rf}}^2}, \qquad p_z = -\frac{p_x}{2}, \qquad q_x = -\frac{2eU_{\mathrm{rf}}}{ma^2\Omega_{\mathrm{rf}}^2} = -q_y \quad \text{and} \quad q_z = 0 \quad (2.3)$$

are the stability parameters of the trap. They depend on the geometry of the trap (α, a, b), the applied voltages $(U_{\mathrm{et}}, U_{\mathrm{rf}}, \Omega_{\mathrm{rf}})$ and the trapped ion (m, e). If the trap parameters are chosen such that a stable solution for the Mathieu differential equation exists, it is possible to trap the ion with this trap.

Usually the parameters are chosen such that $p_k \ll 1$ and $q_k^2 \ll 1$ holds. In this case the solutions of equation 2.2 are approximated by

$$r_k(t) = r_{0,k}\cos(\omega_k t)\left(1 + \frac{q_k}{2}\cos(\Omega_{\mathrm{rf}}t)\right). \quad (2.4)$$

These solutions describe oscillations along the trap axis with frequencies

$$\omega_k = \frac{\Omega_{\mathrm{rf}}}{2}\sqrt{p_k + \frac{q_k}{2}} \quad (2.5)$$

which are called the secular motion. The oscillation frequencies of this secular motion are called axial (ω_z) and radial (ω_x, ω_y) trap frequencies[1]. The radial trap frequencies depend on the applied power and frequency of the driving radio frequency. The axial trap frequency is set mainly by the end tip voltage.

---

[1]Not to mix up with the frequency Ω_{rf} that drives the quadrupole electrodes of the trap.

The secular motion is superimposed by a second oscillation with frequency Ω_{rf} which is called micromotion. This micromotion increases, if the ion is shifted outside of the trap center. Causes of this shift are additional electrical potentials and manufacturing tolerances of the trap itself. Constant voltages applied to additional compensation electrodes mounted around the trap electrodes shift the ion position back into the trap center.

2.3. Qubits, entangled states and the dynamic of a driven system

This section gives a short introductions on qubits and the dynamic of a driven two level system based on the textbook from M. Nielsen & I. Chuang [42] and lecture notes from D. Steck [43].

2.3.1. Qubits and entangled states

Qubits are the central building blocks of quantum information. In contrast to a bit in a classical computer which has only the states 0 and 1, a qubit is described by a state vector in a two dimensional Hilbert space spanned by the basis states $|0\rangle = (1,0)^T$ and $|1\rangle = (0,1)^T$. All possible qubit states are of the form

$$|\Psi\rangle = \alpha |0\rangle + \beta |1\rangle, \tag{2.6}$$

with the complex amplitudes α and β, which fulfill the normalization condition $|\alpha|^2 + |\beta|^2 = 1$. The complex amplitudes contain the probabilities $|\alpha|^2$ respective $|\beta|^2$ to measure the qubit in the individual basis states $|0\rangle$ and $|1\rangle$, which will be referred to as the population in these states, as well as the relative phase $\phi = \arg(\alpha) - \arg(\beta)$ between both components.

In an experimental situation, the state vector $|\Psi\rangle$ is often not sufficient to describe the qubit state. Instead, the density matrix ρ describes the qubit state, where

$$\rho = \sum_k p_k |\Psi_k\rangle \langle\Psi_k|. \tag{2.7}$$

This density matrix is built as the incoherent sum of several quantum states $|\Psi_k\rangle$, which are defined as in Equation 2.6, weighted by the probabilities p_k to be in the respective state. A physical density matrix has to be normalized ($\text{Tr}\,\rho = 1$), Hermitian ($\rho^\dagger = \rho$) and positive semi-definite (all eigenvalues non negative). If the density matrix can be written as $\rho = |\Psi\rangle \langle\Psi|$ with a single state $|\Psi\rangle$, the state of the system is called a pure quantum state. If this state is a superposition state the off-diagonal elements of the density matrix called coherences are maximal, with the modulus $|\alpha\beta^*|$. In this case the relative phase of the superposition can be extracted from the coherences. A system whose density matrix is not described by a single pure quantum state is called a mixed state.

To describe systems containing multiple qubits, the same formalism is extended to a more dimensional Hilbert space. This Hilbert space is created by the tensor product of the individual Hilbert spaces of each qubit. In the same way the state vector, the density matrix or any

operator acting on the qubits is given by the tensor product of the respective elements in their individual subsystems. In this work only two qubit systems are relevant. One qubit is encoded in the polarization of a single photon. The second qubit is encoded in the electronic state of a calcium ion. In this case the resulting states and density matrices are given by

$$|\Psi\rangle = |\Psi\rangle^{(at)} \otimes |\Psi\rangle^{(ph)} \qquad \text{and} \qquad \rho = \rho^{(at)} \otimes \rho^{(ph)}, \qquad (2.8)$$

where $|\Psi\rangle^{(at)}$ respective $\rho^{(at)}$ describe the atomic qubit and $|\Psi\rangle^{(ph)}$ respective $\rho^{(ph)}$ describe the polarization qubit. The symbol $\otimes$ that indicates the tensor product between both individual subsystems is often omitted. The same holds for the superscripts (at) and (ph) indicating the atomic qubit and polarization qubit.

Such a two qubit system can be in an entangled state. An entangled state is a pure quantum state, which cannot be separated into a product state that describes each subsystem independently, even though the underlying Hilbert space is a tensor product of both individual Hilbert spaces. These entangled states are of special interest in many applications. Example for such entangled states are

$$|\Psi\rangle = \frac{1}{\sqrt{2}} \left[|0\rangle^{(at)} |1\rangle^{(ph)} + |1\rangle^{(at)} |0\rangle^{(ph)} \right] \text{ or } |\Phi\rangle = \frac{1}{\sqrt{2}} \left[|0\rangle^{(at)} |0\rangle^{(ph)} + |1\rangle^{(at)} |1\rangle^{(ph)} \right]. \quad (2.9)$$

In contrast to these entangled states, the state

$$\begin{aligned}
|\Psi\rangle &= \frac{1}{2} \left[|0\rangle^{(at)} |0\rangle^{(ph)} + |0\rangle^{(at)} |1\rangle^{(ph)} + |1\rangle^{(at)} |0\rangle^{(ph)} + |1\rangle^{(at)} |1\rangle^{(ph)} \right] \\
&= \frac{1}{2} \left(|0\rangle^{(at)} + |1\rangle^{(at)} \right) \left(|0\rangle^{(ph)} + |1\rangle^{(ph)} \right)
\end{aligned} \qquad (2.10)$$

can be separated into a product as shown and is therefore not an entangled state.

To quantify the quality of a quantum state and to compare it with other states, I calculate different measures from the density matrix ρ. These refer to the introduced properties of a quantum state. For every quantum state the purity $\mathcal{P}$ quantifies how much of the given quantum state ρ can be written as a pure quantum state. The purity $\mathcal{P}$ of a density matrix ρ is calculated by

$$\mathcal{P}(\rho) = \operatorname{Tr} \rho^2. \qquad (2.11)$$

For a pure quantum state the purity becomes 1. In case of a maximally mixed quantum state the purity becomes 2^{-N}, where N is the number of qubits.

The overlap with a second target state ρ_t is quantified with the overlap fidelity $\mathcal{F}$. If the target state is a pure quantum state the overlap fidelity can be calculated with

$$\mathcal{F}(\rho) = \operatorname{Tr} \rho_t \rho. \qquad (2.12)$$

The overlap fidelity reaches the maximum of 1, if the state ρ is equal to the target state ρ_t and a minimum of 0, if the state ρ is perpendicular to the target state.

The entanglement of a two qubit state is quantified with two measures. The concurrence $\mathcal{C}$ is calculated by

$$\mathcal{C}(\rho) = \max\{0, \sqrt{\lambda_1} - \sqrt{\lambda_2} - \sqrt{\lambda_3} - \sqrt{\lambda_4}\}, \tag{2.13}$$

where λ_k are the eigenvalues of the matrix $\rho \cdot (\sigma_y \otimes \sigma_y) \cdot \rho^* \cdot (\sigma_y \otimes \sigma_y)$ in decreasing order $(\lambda_1 > \lambda_2 > \lambda_3 > \lambda_4)$ [44, 45]. Therein σ_y is the Pauli Y matrix and ρ^* is the element wise complex conjugate of ρ. The concurrence takes values between 0 for a mixed state and 1 for a maximally entangled state as in Equation 2.9. The second measure is the Bell parameter $\mathcal{S}$, which describes correlations between different measurement outcomes for a set of measurement bases. If a value $\mathcal{S} > 2$ is found for the chosen measurement bases, the state is at least partially entangled. In the CHSH formulation [46], the Bell parameter is given by

$$\mathcal{S} = \langle \sigma_\alpha \otimes \sigma_1 \rangle + \langle \sigma_\beta \otimes \sigma_1 \rangle + |\langle \sigma_\alpha \otimes \sigma_2 \rangle - \langle \sigma_\beta \otimes \sigma_2 \rangle|, \tag{2.14}$$

where σ_α and σ_β describe the measurement bases of the first qubit, while σ_1 and σ_2 describe the measurement bases of the second qubit. In this formulation, the Bell parameter can be calculated from a given density matrix ρ or the four correlations in Equation 2.14 are measured directly. For the best choice of measurement bases the Bell parameter becomes $2\sqrt{2}$ for a maximal entangled state. Note that the value of the Bell parameter strongly depends on the chosen set of measurement bases and a value $\mathcal{S} < 2$ is possible for an entangled state. Thus the Bell parameter is unpractical to argue that a state is mixed but can easy verify that a state is entangled.

2.3.2. The driven two level system

A two level system consisting of a ground state $|g\rangle$ and an excited state $|e\rangle$ separated by the energy $E = \hbar\omega_g$ describes the basic interaction on any transition [2]. These states are for example the two basis states of a qubit or a subsystem from an atomic level scheme. I will assume that the energy of the excited state is the reference point and set to zero. With this, the internal Hamilton of the system becomes

$$\hat{H}_0 = -\hbar\omega_g |g\rangle \langle g| \tag{2.15}$$

This system is excited by an external field with frequency ω_L. Depending on the system and the transition, this external field corresponds to a laser or microwave field. After performing the rotating wave approximation, the interaction is described by the operator

$$\hat{V} = \hbar\frac{\Omega}{2} |e\rangle \langle g| e^{-i\omega_L t} + \hbar\frac{\Omega^*}{2} |g\rangle \langle e| e^{i\omega_L t}. \tag{2.16}$$

Therein the Rabi frequency $\Omega = \frac{\mathbf{d} \cdot \mathbf{E}}{\hbar}$, with the dipole moment $\mathbf{d}$ of the transition and the field amplitude $\mathbf{E}$, describes the coupling strength to the transition. To be able to describe

---

[2]Instead of the energy of a transition, I often talk about the frequency of the transition instead. The same applies to energy shifts, for example by applied magnetic fields, which are discussed as frequency shifts.

the time evolution driven by the external field more easily, the system is transformed into a system rotating with the frequency ω_L of the applied field. In this new, rotating system the time dependence of the interaction Hamilton vanishes and the energy of the ground state is given by the detuning $\Delta = \omega_L - \omega_g$ of the applied external field. Thus the Hamilton describing the whole system becomes

$$\hat{H} = \hbar\Delta \, |g\rangle \, \langle g| + \hbar\frac{\Omega}{2} \, |e\rangle \, \langle g| + \hbar\frac{\Omega^*}{2} \, |g\rangle \, \langle e| \, . \tag{2.17}$$

Solving Schrödinger's equation for the state $|\Psi\rangle = c_g \, |g\rangle + c_e \, |e\rangle$ of the system with the initial condition $c_g(0) = \alpha$ and $c_e(0) = \beta$ leads to the equations

$$
\begin{aligned}
c_e &= e^{\mathrm{i}(-\frac{\Delta}{2})t} \left[\beta \cos(\frac{\tilde{\Omega}}{2}t) + \mathrm{i}\frac{\Delta}{\tilde{\Omega}} \beta \sin(\frac{\tilde{\Omega}}{2}t) - \mathrm{i}\frac{\Omega}{\tilde{\Omega}} \alpha \sin(\frac{\tilde{\Omega}}{2}t) \right] \\
c_g &= e^{\mathrm{i}(-\frac{\Delta}{2})t} \left[\alpha \cos(\frac{\tilde{\Omega}}{2}t) - \mathrm{i}\frac{\Delta}{\tilde{\Omega}} \alpha \sin(\frac{\tilde{\Omega}}{2}t) - \mathrm{i}\frac{\Omega^*}{\tilde{\Omega}} \beta \sin(\frac{\tilde{\Omega}}{2}t) \right]
\end{aligned}
\tag{2.18}
$$

describing the time evolution of the state. The resulting oscillation of the population between the ground state and the excited state with the generalized Rabi frequency $\tilde{\Omega} = \sqrt{|\Omega|^2 + \Delta^2}$ is called a Rabi oscillation. The amplitude of this oscillation depends on the detuning Δ of the excitation. For an excitation on resonance the amplitude of this oscillation is maximal. If the laser is detuned $|\Delta| > 0$, the amplitude is reduced.

The population transfer between both states defines names for pulses with a certain interaction duration. These names are deduced from the effect of a pulse with pulse area $\Omega\tau$ on the initial state, for an interaction on resonance. A π-pulse with $\Omega\tau = \pi$ swaps the population stored in both states. A $\frac{\pi}{2}$-pulse (with pulse area $\Omega\tau = \frac{\pi}{2}$) creates a balanced superposition between the initial state and the state perpendicular to the initial state. In all cases, the relative phase of the created state depends on the phase of the pulse. This phase, given by the phase of the applied field **E**, is encoded in the phase of the complex Rabi frequency.

Arbitrarily modulated driving field

In the previous treatment of the interaction a monochromatic external field was assumed. To describe a modulated laser field, the description has to be adapted. In the most general case the external field contains multiple components with carrier frequencies ω_k, time dependent amplitudes $A_k(t)$, phase modulations $\phi_k(t)$ and frequency modulations $\alpha_k(t)$. In contrast to a monochromatic case, in this case it is impossible to find a rotating frame, where the whole time dependence is eliminated, even for the simple case of two monochromatic fields. Nevertheless the system can be transformed into a frame rotating with the average frequency

$$\bar{\omega} = \frac{1}{N} \sum_k^N \omega_k. \tag{2.19}$$

Using this average frequency each carrier frequency can be expressed as

$$\omega_k = \bar{\omega} + \delta_k = \omega_g + \Delta + \delta_k, \tag{2.20}$$

with the atomic transition frequency given by ω_g and the detuning Δ of the average frequency $\bar{\omega}$ with respect to the transition frequency. In the rotating frame, the interaction operator becomes

$$\hat{V} = \sum_k \frac{\Omega_k(t)}{2} e^{-i(\delta_k t + \alpha_k t + \phi_k)} |e\rangle \langle g| + \text{h.c} = \frac{\Omega_{\text{eff}}(t)}{2} |e\rangle \langle g| + \text{h.c}, \tag{2.21}$$

where each of the individual Rabi frequencies Ω_k are proportional to the amplitude $A_k(t)$ of the respective field component. All these Rabi frequencies are summarized in the effective Rabi frequency Ω_{eff}. With this, the whole system is described analog to the monochromatic case by

$$\hat{H} = \hbar\Delta |g\rangle \langle g| + \hbar\frac{\Omega_{\text{eff}}}{2} |e\rangle \langle g| + \hbar\frac{\Omega_{\text{eff}}^*}{2} |g\rangle \langle e| , \tag{2.22}$$

where the only difference is given by the Rabi frequency acting on the transition. In the monochromatic case this Rabi frequency is time independent, while for an arbitrary combination of field components this Rabi frequency is time dependent. As an example for two monochromatic fields with the same amplitude one gets

$$\Omega_{\text{eff}} = \Omega e^{-i\delta_1 t + \phi_1} + \Omega e^{-i\delta_2 t + \phi_2} = \Omega e^{-i\delta t + \phi_1} + \Omega e^{i\delta t + \phi_2} = 2\Omega\cos(\delta t + \phi_0). \tag{2.23}$$

This corresponds to an amplitude modulation of a monochromatic field.

2.4. Names for qubit states

In this work, a qubit as discussed in Section 2.3.1 is realized with two different platforms. A stationary qubit is encoded in the state of a single $^{40}\text{Ca}^+$ ion, for example two Zeeman levels of the $\text{S}_{1/2}$ ground state. In such a case the energy eigenstates are the basis states. For the chosen example one gets

$$|0\rangle \,\hat{=}\, |\uparrow\rangle \,\hat{=}\, |\text{S}_{1/2}, +\tfrac{1}{2}\rangle \,\hat{=}\, |+\tfrac{1}{2}\rangle \qquad \text{and} \qquad |1\rangle \,\hat{=}\, |\downarrow\rangle \,\hat{=}\, |\text{S}_{1/2}, -\tfrac{1}{2}\rangle \,\hat{=}\, |-\tfrac{1}{2}\rangle . \tag{2.24}$$

A second example of states that encode a qubit are two Zeeman levels of the $\text{D}_{5/2}$ manifold. In this case the basis states are

$$|0\rangle \,\hat{=}\, |\uparrow\rangle \,\hat{=}\, |\text{D}_{5/2}, +\tfrac{1}{2}\rangle \,\hat{=}\, |+\tfrac{1}{2}\rangle \qquad \text{and} \qquad |1\rangle \,\hat{=}\, |\downarrow\rangle \,\hat{=}\, |\text{D}_{5/2}, -\tfrac{3}{2}\rangle \,\hat{=}\, |-\tfrac{3}{2}\rangle . \tag{2.25}$$

If the magnetic quantum number is sufficient to distinguish both qubits states, I utilize this abbreviation. In a more general context, for example to define the names of special superposition states, I use the assignments $|\uparrow\rangle$ and $|\downarrow\rangle$, where $|\uparrow\rangle$ denotes the atomic state with the larger magnetic quantum number.

With these basis states, which are eigenstates of the Pauli Z operator, the eigenstates of the Pauli X and Pauli Y operator are assigned the special names

$$|-\rangle = \frac{-1}{\sqrt{2}}(|\!\uparrow\rangle - |\!\downarrow\rangle), \qquad\qquad |+\rangle = \frac{i}{\sqrt{2}}(|\!\uparrow\rangle + |\!\downarrow\rangle),$$

$$|-i\rangle = \frac{i-1}{2}\left(|\!\uparrow\rangle - i\,|\!\downarrow\rangle\right) \quad \text{and} \quad |+i\rangle = \frac{i+1}{2}\left(|\!\uparrow\rangle + i\,|\!\downarrow\rangle\right). \tag{2.26}$$

With a calibration measurement, I assign these states to specific atomic superpositions.
The second platform are single photons, where the qubit is encoded in the polarization state of the photon[3]. In this case the basis states are assigned to the circular polarization $|0\rangle \,\hat{=}\, |\mathrm{L}\rangle$ and $|1\rangle \,\hat{=}\, |\mathrm{R}\rangle$ which again are the eigenstates of the Pauli Z operator. The eigenstates of the Pauli X and Pauli Y operator are the linear polarization

$$|\mathrm{H}\rangle = \frac{-1}{\sqrt{2}}(|\mathrm{L}\rangle - |\mathrm{R}\rangle), \qquad\qquad |\mathrm{V}\rangle = \frac{i}{\sqrt{2}}(|\mathrm{L}\rangle + |\mathrm{R}\rangle)$$

$$|\mathrm{D}\rangle = \frac{i-1}{2}\left(|\mathrm{L}\rangle - i\,|\mathrm{R}\rangle\right) \quad \text{and} \quad |\mathrm{A}\rangle = \frac{i+1}{2}\left(|\mathrm{L}\rangle + i\,|\mathrm{R}\rangle\right). \tag{2.27}$$

given as superposition of both circular polarization states. Note that the definitions of the polarization and superposition states are analog. As an example the atomic superposition $|+\rangle$ is analogously defined as the linear polarization state $|\mathrm{V}\rangle$.

2.5. Electrical dipole transitions

I generate single Raman-scattered photons with the dipole transitions of the calcium ion. They are also utilized for laser cooling and fluorescence detection during the measurement sequences. Thereby the angular dependence of the dipole emission pattern plays a crucial part in whether a specific decay channel can be observed or if a transition can be excited. This also involves the polarization of the laser or the polarization of the emitted photon. This angular dependence including the polarization is shortly sketched here following the derivation by Hertel & Schulz [47].

2.5.1. Dipole emission pattern

I want to describe the dipole interaction between a ground state $|g\rangle = |\gamma_g j_g m_g\rangle$ and an excited state $|e\rangle = |\gamma_e j_e m_e\rangle$. The quantum numbers j and m describe to the total angular momentum while γ summarizes all other quantum numbers of the state. The dipole interaction between these states is described by the operators $\hat{D} = \mathbf{r}^{(at)} \cdot \mathbf{e}^{(ph)}$ for the absorption and $\hat{D}^\dagger = \mathbf{r}^{(at)} \cdot \mathbf{e}^{(ph)*}$ for the emission. In these operators $\mathbf{r}^{(at)}$ describes the electron in the atom, while the polarization of the electric field is described by $\mathbf{e}^{(ph)}$. The relevant matrix elements

---

[3]Polarization of light is a classical property and the quantum nature comes from the single photon. However, I use the polarization qubit notation also for laser polarization and polarization projections.
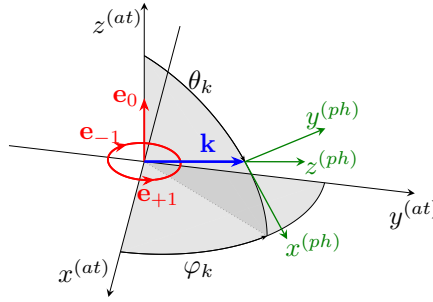
Figure 2.3.: Coordinate systems to describe the dipole emission pattern. The photon system $^{(ph)}$ (green) is rotated with respect to the atom system $^{(at)}$ (red) by the angles θ_k and φ_k such that the $z^{(ph)}$ axis points in direction of the wave vector $\mathbf{k}$ (blue) of the traveling light. The $z^{(ph)}$ axis of the atom system is given by the quantization axis defined with an external magnetic field.

of the operators $\hat{D}$ and $\hat{D}^\dagger$ are

$$
\begin{aligned}
\langle e|\, \hat{D}\, |g\rangle &= \langle e|\, \mathbf{r}^{(at)}\, |g\rangle \cdot \mathbf{e}^{(ph)} = \mathbf{r}^{(at)}_{eg} \cdot \mathbf{e}^{(ph)} \quad \text{and} \\
\langle g|\, \hat{D}^\dagger\, |e\rangle &= \langle g|\, \mathbf{r}^{(at)}\, |e\rangle \cdot \mathbf{e}^{(ph)*} = \mathbf{r}^{(at)}_{ge} \cdot \mathbf{e}^{(ph)*} = \left(\mathbf{r}^{(at)}_{eg} \cdot \mathbf{e}^{(ph)}\right)^*.
\end{aligned}
\tag{2.28}
$$

Only if these matrix elements are non-zero a transition can occur. This means that either a light field with the respective polarization excites this transition, or the emission on this transition goes into this polarization mode. To calculate the product in the matrix element, either $\mathbf{r}^{(at)}_{eg}$ is expressed in the basis of $\mathbf{e}^{(ph)}$ or vice versa. The respective coordinate systems are given by the systems itself. The $z^{(at)}$ direction is defined by the quantization axis while the $z^{(ph)}$ direction is given by the propagation direction of the light. Both coordinate systems are rotated with respect to each other by the angles θ_k and φ_k (see Figure 2.3).

A natural coordinate system is given by the complex helicity basis with the basis vectors

$$
\mathbf{e}_{+1} = -\frac{1}{\sqrt{2}}(\mathbf{e}_x + \mathrm{i}\mathbf{e}_y), \qquad \mathbf{e}_{-1} = \frac{1}{\sqrt{2}}(\mathbf{e}_x - \mathrm{i}\mathbf{e}_y) \quad \text{and} \quad \mathbf{e}_0 = \mathbf{e}_z.
\tag{2.29}
$$

These basis vectors fulfill the conditions

$$
\mathbf{e}_q \cdot \mathbf{e}^*_{q'} = \delta_{qq'} \qquad \text{and} \qquad \mathbf{e}^*_q = (-1)^q\, \mathbf{e}_{-q}.
\tag{2.30}
$$

In this coordinate system, the transition matrix element from the state $|\gamma_a j_a m_a\rangle$ to the state $|\gamma_b j_b m_b\rangle$ becomes

$$
\begin{aligned}
\langle \gamma_b j_b m_b|\, \mathbf{r}\, |\gamma_a j_a m_a\rangle &= \sum_{q=-1}^{1} \langle \gamma_b j_b m_b|\, r_q\, |\gamma_a j_a m_a\rangle\, \mathbf{e}^*_q \\
&= \sqrt{\frac{4\pi}{3}} \sum_{q=-1}^{1} \langle \gamma_b|\, r\, |\gamma_a\rangle\, \langle j_b m_b|\, Y_{1q}\, |j_a m_a\rangle\, \mathbf{e}^*_q := \sum_{q=-1}^{1} \langle m_b|\, r_q\, |m_a\rangle\, \mathbf{e}^*_q,
\end{aligned}
\tag{2.31}
$$

with the spherical harmonics $Y_{1q}(\theta, \phi)$. The evaluation of the radial part $\langle \gamma_b | r | \gamma_a \rangle$ of this matrix element can be of high numerical effort and is not of interest for this derivation. In the experiment, it is a constant specific to the atom (or molecule) and is found in tables. The evaluation of the angular part $\langle j_b m_b | Y_{1q} | j_a m_a \rangle$ leads to the Clebsch-Gordan coefficients, which cover the strength of individual transitions between Zeeman levels. The relative strength of individual transitions is not important for the angular dependence of a single transition. I discuss the Glebsch-Gordan coefficients in Section 2.5.2. The abbreviation

$$\langle m_b | r_q | m_a \rangle = \langle m_a | r_{-q} | m_b \rangle \propto \delta_{m_b, m_a + q} \tag{2.32}$$

contains the selection rule for dipole transitions found by evaluating $\langle j_b m_b | Y_{1q} | j_a m_a \rangle$. The atomic transitions are named $\sigma^{\pm}$ transition ($\Delta m = q = \pm 1$) or π transition ($\Delta m = 0$) depending on the value of q which is connected to the spin of the involved photon. Note that the name of a transition is independent of whether the photon is absorbed or emitted.

Emission

In case of emission, the polarization as well as the amount of radiation emitted into a certain solid angle is of interest. Therefore, the atomic coordinate system $\mathbf{e}_q^{(at)}$ is expressed in the photon basis. Since the polarization of the emitted photon cannot have a component in the emission direction, the terms with $\mathbf{e}_0^{(ph)}$ have no physical relevance and are dropped. Thus only the contribution with $\mathbf{e}_{\pm 1}^{(ph)}$ remains. The resulting atomic vectors are

$$\mathbf{u}_{-1}^{(at)} = e^{-\mathrm{i}\varphi_k} \left[\frac{1}{2} \left(1 + \cos(\theta_k) \right) \mathbf{e}_{-1}^{(ph)} + \frac{1}{2} (1 - \cos(\theta_k)) \mathbf{e}_{+1}^{(ph)} \right],$$

$$\mathbf{u}_0^{(at)} = -\frac{\sin(\theta_k)}{\sqrt{2}} \mathbf{e}_{-1}^{(ph)} + \frac{\sin(\theta_k)}{\sqrt{2}} \mathbf{e}_{+1}^{(ph)} = \sin(\theta_k) \mathbf{e}_x^{(ph)}, \tag{2.33}$$

$$\mathbf{u}_{+1}^{(at)} = e^{\mathrm{i}\varphi_k} \left[\frac{1}{2} (1 - \cos(\theta_k)) \mathbf{e}_{-1}^{(ph)} + \frac{1}{2} (1 + \cos(\theta_k)) \mathbf{e}_{+1}^{(ph)} \right].$$

Since the component in direction of the photon emission was dropped, these vectors are not normalized anymore. This is compensated by a factor $f_q(\theta_k, \varphi_k)$, so that one can express the atomic vectors as [4]

$$\mathbf{u}_q^{(at)} = f_q(\theta_k, \varphi_k) \mathbf{e}_{el,q}^{(ph)} = f_q(\theta_k, \varphi_k) \left(e^{-\mathrm{i}\delta_q} \cos(\beta_q) \mathbf{e}_{+1}^{(ph)} - e^{\mathrm{i}\delta_q} \sin(\beta_q) \mathbf{e}_{-1}^{(ph)} \right). \tag{2.34}$$

Therein the unity vector $\mathbf{e}_{el,q}^{(ph)}$ corresponds to the elliptic polarization emitted by the transition labeled with q. With the atomic vectors expressed in the coordinate system of the emitted

---

[4] $f_0(\theta_k, \varphi_k) = \sin(\theta_k)$, $f_{\pm 1}(\theta_k, \varphi_k) = -\mathrm{i} e^{\pm \mathrm{i}\varphi_k} \frac{(1 + \cos^2(\theta_k))^{1/2}}{\sqrt{2}}$
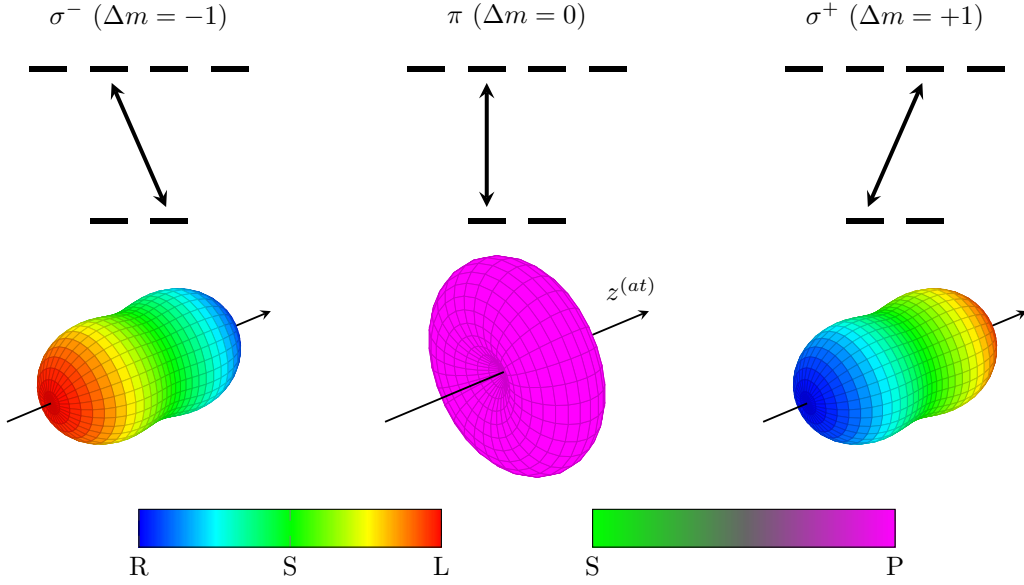
Figure 2.4.: Emission pattern for dipole transitions. The magnitude shows the rate of spontaneous emission in specific directions. The color codes the polarization as seen by an observer. The polarization S is perpendicular to the plane spanned by the quantization axis $z^{(at)}$ and the direction of propagation. The polarization P is parallel to the quantization axis $z^{(at)}$.

photon, the relevant dipole matrix from equation 2.28 can be written as

$$\langle g| \hat{D}^\dagger |e\rangle = \mathbf{r}_{ge}^{(at)} \cdot \mathbf{e}^{(ph)*} = \sum_{q=-1}^{1} (-1)^q \langle m_g| r_{-q} |m_e\rangle f_q(\theta_k, \varphi_k) \mathbf{e}_{el,q}^{(ph)} \cdot \mathbf{e}^{(ph)*}. \tag{2.35}$$

Because we are interested in the angular dependence of a specific transition, only the corresponding component of the sum is relevant for the calculation of the spontaneous emission rate. Also we consider only light of the corresponding polarization thus we can set $\mathbf{e}^{(ph)} := \mathbf{e}_{el,q}^{(ph)}$. For this setting, we calculate the angular dependence of the spontaneous emission with $\mathrm{d}R_q \propto \left| \langle g| \hat{D}^\dagger |e\rangle \right|^2$. For the three possible transitions this leads to the angular dependent emission rates

$$\mathrm{d}R_{\sigma^-} \propto \frac{1 + \cos^2(\theta_k)}{2} \qquad \mathrm{d}R_\pi \propto \sin^2(\theta_k) \qquad \mathrm{d}R_{\sigma^+} \frac{1 + \cos^2(\theta_k)}{2}. \tag{2.36}$$

To find the emitted polarization the prefactors in equation 2.33 and 2.34 are compared. As an example, a photon emitted on a σ^+ transition in direction of the quantization axis ($\theta_k = 0$) has a polarization corresponding to $\mathbf{e}_{+1}^{(ph)}$, which is left-circularly polarized [5]. Figure 2.4 contains plots of the angular dependence of the spontaneous emission rate and polarization for σ^+, σ^- and π transitions.

---

[5]For the polarization convention see Section 2.5.3

Absorption

Similar to the emission process the absorption is calculated. In this case, the photon system $\mathbf{e}_q^{(ph)}$ is transformed into the atomic system. After this transformation the light is expressed as it is seen by the atom. Since the photon polarization $\mathbf{e}_{\text{el}}^{(ph)}$ can only be perpendicular to the propagation direction, it is a linear combination of $\mathbf{e}_{-1}^{(ph)}$ and $\mathbf{e}_{+1}^{(ph)}$ and only these vectors have to be transformed into the atomic system. One gets

$$
\begin{aligned}
\mathbf{e}_{-1}^{(ph)} &= e^{\mathrm{i}\varphi_k} \cos^2(\frac{\theta_k}{2})\mathbf{e}_{-1}^{(at)} - \frac{\sin(\theta_k)}{\sqrt{2}}\mathbf{e}_0^{(at)} + e^{-\mathrm{i}\varphi_k} \sin^2(\frac{\theta_k}{2})\mathbf{e}_{+1}^{(at)}, \\
\mathbf{e}_{+1}^{(ph)} &= e^{\mathrm{i}\varphi_k} \sin^2(\frac{\theta_k}{2})\mathbf{e}_{-1}^{(at)} + \frac{\sin(\theta_k)}{\sqrt{2}}\mathbf{e}_0^{(at)} + e^{-\mathrm{i}\varphi_k} \cos^2(\frac{\theta_k}{2})\mathbf{e}_{+1}^{(at)}.
\end{aligned}
\tag{2.37}
$$

These equations are used to calculate the transition rate R_{eg} between to states, from the dipole transition matrix element for absorption in equation 2.28. To study a certain transition the value of q is set to $q = 0, \pm 1$. In this case the transition rate is proportional to

$$
\begin{aligned}
R_{eg} \propto \left|\mathbf{r}_{eg}^{(at)} \cdot \mathbf{e}^{(ph)}\right|^2 &= \left|\langle m_e | r_q | m_g \rangle \, \mathbf{e}_q^{(at)*} \cdot \mathbf{e}^{(ph)}\right|^2 \\
&= |\langle m_e | r_q | m_g \rangle|^2 \left|\mathbf{e}_q^{(at)*} \cdot \mathbf{e}_{\text{el}}^{(at)}\right|^2 .
\end{aligned}
\tag{2.38}
$$

The value of $|\langle m_e | r_q | m_g \rangle|^2$ is constant for a certain transition. Thus we can compare the transition rate by looking at $\left|\mathbf{e}_q^{(at)*} \cdot \mathbf{e}_{\text{el}}^{(at)}\right|^2$. Given for example a σ^+ transition ($q = +1$) and right or left circularly polarized light (this corresponds to $\mathbf{e}_{\text{el}}^{(ph)} = \mathbf{e}_{\pm 1}^{(ph)}$) the transition rate becomes

$$
R_{\sigma^+, \mathrm{R}} \propto \sin^4(\frac{\theta_k}{2}) \qquad\qquad R_{\sigma^+, \mathrm{L}} \propto \cos^4(\frac{\theta_k}{2}).
\tag{2.39}
$$

This shows, that a left circularly polarized laser beam excites the σ^+ optimally, when coupled in parallel to the quantization axis ($\theta_k = 0$) or not at all, if coupled in anti parallel to the quantization axis ($\theta_k = \pi$). For a right circularly polarized laser one finds the opposite. Note that the laser polarization, which excites a σ transition on quantization axis, is the polarization of a photon that is emitted in the propagation direction of the laser beam.

2.5.2. Clebsch-Gordan coefficients

One part of the transition matrix element is given by $\langle j_b m_b | Y_{1q} | j_a m_a \rangle$. With the Wigner-Eckart theorem the transition matrix element can be written as

$$
\langle j_b m_b | Y_{1q} | j_a m_a \rangle = \langle j_a m_a 1 q | j_b m_b \rangle \, \langle j_b || Y_1 || j_a \rangle .
\tag{2.40}
$$

In this product the factor $\langle j_b || Y_1 || j_a \rangle$ depends only on j_a and j_b and is therefor constant for the whole atomic transition. The factors $\langle j_a m_a 1 q | j_b m_b \rangle$ are the so called Clebsch-Gordan
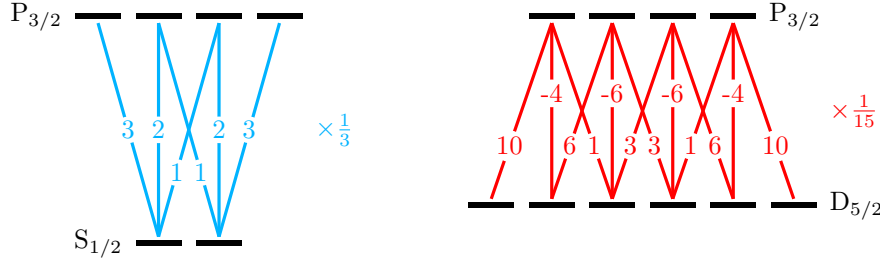
Figure 2.5.: Clebsch-Gordan coefficients of the $P_{3/2} \leftrightarrow S_{1/2}$ and $P_{3/2} \leftrightarrow D_{5/2}$ transition. The coefficients have to be read as the square root of the respective fraction together with the depicted sign. As example the Clebsch-Gordan coefficient between the $|P_{3/2}, -\frac{3}{2}\rangle$ and $|D_{5/2}, -\frac{3}{2}\rangle$ states is $-\sqrt{\frac{4}{15}}$.

coefficients. With these coefficients the coupled angular momentum $|j_b m_b\rangle$ can be expressed in the basis of the uncoupled states $|j_a m_a\rangle$ and $|j_{ph} = 1, m_{ph}\rangle$. The Clebsch-Gordan coefficients can be calculated with the formula

$$\langle j_a m_a 1 q | j_b m_b \rangle = (-1)^{j_b - m_b} \sqrt{2j_b + 1} \begin{pmatrix} j_b & 1 & j_a \\ -m_b & q & m_a \end{pmatrix} \tag{2.41}$$

that contains the Wigner 3j symbol. In the context of dipole transitions the Clebsch-Gordan coefficients give the relative strength of transitions between individual Zeeman levels. Figure 2.5 contains the Clebsch-Gordan coefficients of all dipole allowed transitions between the Zeeman levels of the $S_{1/2}$, $P_{3/2}$ and $D_{5/2}$ states. The Clebsch-Gordan coefficients have to be taken into account if multiple transitions between individual Zeeman levels are involved in the studied process. This is for example the case, when generating a Raman photon out of a superposition in the $D_{5/2}$ Zeeman levels.

2.5.3. Polarization convention

As seen in the previous Section 2.5.1, the polarization of light interacting with an atom is linked directly to the specific atomic transition and the angle of incidence with respect to the quantization axis. During experiments the polarization is measured (or specified) in the laboratory frame which is aligned with respect to the setup around the ion trap. The $\mathbf{e}_y^{(\text{lab})}$ direction is perpendicular to the plane of the optical table. The $\mathbf{e}_z^{(\text{lab})}$ vector is aligned in direction of the photon collection optics or the incident laser beam of the corresponding view port. It lies in a plane parallel to the optical table. The ion is located in the origin of this coordinate system that rotates around $\mathbf{e}_y^{(\text{lab})}$. With this definition the laboratory coordinate system is the same as the photonic system and the indices describing the coordinate system can be omitted.
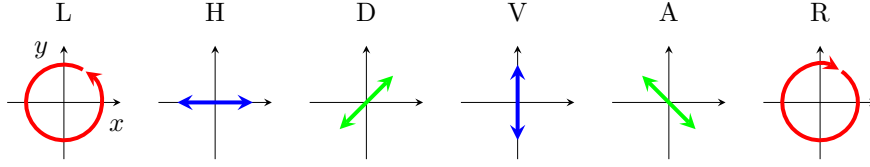
Figure 2.6.: Direction of the electric field oscillation for different polarization as seen by an observer. The light is traveling in z-direction.

In this system the polarization is given by a vector $\mathbf{e}$ in the $x-y$ plane and is therefore described in the Helicity basis from the previous Section 2.5.1. Following the same notation the electric field of the light is written as a real quantity

$$\mathbf{E}(\mathbf{r},\mathbf{t}) = \frac{E_0}{2}\left(\mathbf{e}e^{\mathrm{i}(k_z z - \omega t)} + \mathbf{e}^* e^{-\mathrm{i}(k_z z - \omega t)}\right). \tag{2.42}$$

Both parts of the sum are important for the light matter interaction as they lead to the contributions for the absorption and emission as discussed in the previous section. In the eye of an observer, with the light traveling in his direction, the following six vectors

$$
\begin{aligned}
\mathbf{e}_{\mathrm{H}} &:= \mathbf{e}_x & \mathbf{e}_{\mathrm{V}} &:= \mathbf{e}_y \\
\mathbf{e}_{\mathrm{L}} &:= \mathbf{e}_{+1} = \frac{-1}{\sqrt{2}}(\mathbf{e}_x + \mathrm{i}\mathbf{e}_y) & \mathbf{e}_{\mathrm{R}} &:= \mathbf{e}_{-1} = \frac{1}{\sqrt{2}}(\mathbf{e}_x - \mathrm{i}\mathbf{e}_y) \\
\mathbf{e}_{\mathrm{D}} &:= \frac{1}{\sqrt{2}}(\mathbf{e}_x + \mathbf{e}_y) & \mathbf{e}_{\mathrm{A}} &:= \frac{-1}{\sqrt{2}}(\mathbf{e}_x - \mathbf{e}_y)
\end{aligned}
\tag{2.43}
$$

describe the polarizations **H**orizontal, **V**ertical, **L**eft circular, **R**ight circular, **D**iagonal and **A**nti diagonal. Figure 2.6 shows the direction of the oscillating electric field in the plane of the observer for the six mentioned polarization. Additionally to these polarization, in the characterization of optical elements like mirrors or beam splitter, two other polarization are used. They are named with respect to the plane of incidence on the optical element. If the electric field oscillation is parallel to the plane of incidence, the light is called **P**-polarized. If the oscillation is perpendicular to this plane it is called **S**-polarized. These names can also describe the light emitted by an atom as shown in Figure 2.4. In this case, the electric field oscillation of **P**-polarized light lies in the plane spanned by the emission direction of the photon and the quantization axis of the emitter.

2.6. Signals behind a filter cavity

Central part of the single photon spectrometers (see Section 3.3) is a Fabry-Pèrot resonator that acts as spectral filter. To calculate the influence of this resonator on the incident photon the frequency dependent transmission and phase shift due to this resonator have to be taken into account. For a Fabry Pérot resonator with two mirrors with power transmission T and power reflection R, the electric field $\mathbf{E}_T$ transmitted through the cavity depends on the incident

field $\mathbf{E}_I$. It is calculated by [48]

$$\mathbf{E}_T(\nu) = \frac{T}{1 - Re^{i\phi(\nu)}}\mathbf{E}_I(\nu) = \hat{u}(\nu)\mathbf{E}_I(\nu), \tag{2.44}$$

where $\phi = 2\pi\nu\frac{2L}{c}$ is the phase shift accumulated during a round trip in the cavity. This phase shift is given by the frequency ν of the electric field, the cavity length L and the speed of light c. The effect of the cavity is summarized in the transfer function $\hat{u}(\nu)$. This transfer function can be approximated as a sum of Lorentzian lines separated by the free spectral range ν_{FSR} with unity transmission on resonance. With this approximation the transfer function becomes

$$\hat{u}(\nu) = \frac{T}{1 - Re^{i\phi(\nu)}} \approx \sum_q \hat{g}_{\delta_q}(\nu) = \sum_q \frac{\frac{\gamma}{2}}{\nu - \delta_q + i\frac{\gamma}{2}}. \tag{2.45}$$

Therein the line width γ of the cavity defines the line width of the Lorentzians, while the resonance frequencies $\delta_q = q \cdot \nu_{\text{FSR}}$ give the line position of the Lorentzians. In case of the transmitted intensity $I_T(\nu) = |\mathbf{E}_T(\nu)|^2$ the approximation is exact [49]. In another approximation only the component closest to the frequency δ is considered, because the frequencies of all measured signals are expected within the approximate range $\delta \pm \frac{1}{4}\nu_{\text{FSR}}$. In this range the contribution of the neighboring modes can be neglected and the transfer function of the cavity is approximated by a Lorentzian shaped curve

$$\hat{g}_\delta(\nu) = \frac{\frac{\gamma}{2}}{\nu - \delta + i\frac{\gamma}{2}} := \hat{g}_0(\nu - \delta) \tag{2.46}$$

with central frequency δ. In contrast to a photon spectrum, the transfer function $\hat{g}_\delta(\nu)$ is normalized to unity transmission on resonance[6].

This approximated transfer function $\hat{g}_\delta(\nu)$ is put into equation 2.44 to calculate the amplitude spectrum of a photon transmitted through the resonator. For a photon with spectrum $\hat{h}(\nu)$ the transmitted amplitude spectrum $\hat{s}_\delta(\nu)$ of the photon becomes

$$\hat{s}_\delta(\nu) = \hat{g}_\delta(\nu)\hat{h}(\nu). \tag{2.47}$$

Note that for a normalized incident spectrum $\hat{h}(\nu)$ this transmitted spectrum is not normalized. Instead it gives the transmitted fraction of the incident light.

To obtain the (amplitude) wave packet of the transmitted photon, the transmitted spectrum is Fourier transformed. By applying properties of the Fourier transformation one finds

$$s_\delta(t) = \mathfrak{F}(\hat{s}_\delta(\nu)) = \mathfrak{F}(\hat{h}(\nu)\hat{g}_\delta(\nu)) = \mathfrak{F}(\hat{h}(\nu)) * \mathfrak{F}(\hat{g}_\delta(\nu)) = h(t) * g_\delta(t). \tag{2.48}$$

As result, the transmitted wave packet $s_\delta(t)$ can be calculated directly as convolution of the

---

[6]Or a value smaller than 1 for a cavity with losses.

original wave packet $h(t)$ with the cavity decay function $g_\delta(t)$ given by

$$g_\delta(t) = \mathfrak{F}(\hat{g}(\nu)) = \int\limits_{-\infty}^{\infty} e^{-i2\pi\nu t}\hat{g}(\nu)\mathrm{d}\nu = -\mathrm{i}\pi\gamma\Theta(t)e^{-\pi\gamma t - 2\mathrm{i}\pi\delta t}. \tag{2.49}$$

If one measures the power spectrum of an incident photon with spectrum $\hat{h}(\nu)$, the transmitted intensity is measured for several shifted resonance frequencies δ of the cavity. For each resonance frequency, the expected transmission $P(\delta)$ is given by integrating the transmitted intensity spectrum. With properties of the Fourier transform one calculates

$$\begin{aligned}
\mathrm{P}(\delta) &= \int\limits_{-\infty}^{\infty} |\hat{s}_\delta(\nu)|^2\,\mathrm{d}\nu = \int\limits_{-\infty}^{\infty} \left|\hat{h}(\nu)\hat{g}_\delta(\nu)\right|^2\mathrm{d}\nu = \int\limits_{-\infty}^{\infty} \left|\hat{h}(\nu)\hat{g}_0(\nu-\delta)\right|^2\mathrm{d}\nu \\
&= \int\limits_{-\infty}^{\infty} \left|\hat{h}(\nu)\right|^2 |\hat{g}_0(\nu-\delta)|^2\,\mathrm{d}\nu = \int\limits_{-\infty}^{\infty} \left|\hat{h}(\nu)\right|^2 |\hat{g}_0(\delta-\nu)|^2\,\mathrm{d}\nu = \left|\hat{h}(\nu)\right|^2 * |\hat{g}_0(\nu)|^2.
\end{aligned} \tag{2.50}$$

The expected spectrum $P(\delta)$ can be calculated as convolution of the power spectrum of the incident spectrum and the power spectrum of the un shifted cavity transmission. Due to this convolution, the measured spectrum $P(\delta)$ is broader than the actual power spectrum $\left|\hat{h}(\nu)\right|^2$ of the incident photon. This has to be kept in mind when discussing the spectral width of the photon[7].

2.7. Measures for a spectral or temporal distribution

When discussing properties of a single photon the spectral width and the time duration, as well as the time-bandwidth product of the photon are of interest. Additionally the purity of the photon state may be important, if the photon is used for quantum information applications. In this context a pure photon, is a photon where the spectral and temporal amplitude are Fourier transforms of each other. Here I discuss the measure that I use to determine the time-bandwidth product of a single Raman photon. I also discuss, how the obtained value can be interpreted regarding the purity of the photon state.

To specify the width of a function $f(x)$ one usually calculates the standard deviation (STD). The standard deviation has the problem, that it is not defined for all distributions. This is for example the case for Lorentzian shaped distributions or also other distributions that are relevant in this work. This problems is solved by the Süßmann measure [50, 51] which determines the width as the average height of the distribution. It is calculated by

$$\delta_S[f] = \frac{1}{\int\limits_{-\infty}^{\infty} f^2(x)\,\mathrm{d}x} \tag{2.51}$$

---

[7]The same "problem" also occurs for the duration of the wave packet. As the resolution of the time detection is much higher than the time scales in the photon wave packet this can be neglected there.

for a normalized distribution function $f(x)$. With this measure, I calculate the spectral width $\Delta\nu$ and duration $\Delta\nu$ of a single photon as

$$\Delta\nu = \frac{\delta_S[S(\nu)]}{\pi} \qquad \text{and} \qquad \Delta\tau = \frac{\delta_S[A(t)]}{2}, \tag{2.52}$$

where $S(\nu)$ is the power spectral density and $A(t)$ is the power wave packet of the photon. With the additional factors π and 2 in the denominator I match the width of a Lorentzian spectrum and the duration of an exponential decay calculated with the Süßmann measure to the values obtained by the full width at half maximum and $1/e$-time. With the spectral width and duration of the photon, the time-bandwidth product

$$\text{TBP} = 2\pi\Delta\nu\Delta\tau, \tag{2.53}$$

is calculated. The factor 2π compensates the factors introduced in the spectral width and duration. Using this definition, the time-bandwidth product of a Fourier limited photon with Lorentzian or Gaussian shaped spectrum is 1.

This result can be inverted for a Gaussian or Lorentzian shaped wave packet in the sense, that if a time-bandwidth product of 1 was measured the photon is Fourier limited and therefore the photon was in a pure state. However, this cannot be generalized, as a simple example shows. I consider a superposition of two Lorentzian shaped components of the form

$$g(\nu) = \sqrt{\frac{\delta}{2\pi}} \frac{1}{\nu - \nu_0 + i\frac{\delta}{2}} \tag{2.54}$$

with the line widths $\delta_1 = 10$ and $\delta_2 = 1$ and the line positions $\nu_1 = 2$ and $\nu_2 = -15$. Both components are in a superposition with the relative strengths A_1 and A_2. Analog a superposition of two Gaussian shaped components of the form

$$g(\nu) = \sqrt[4]{\frac{2}{\pi\delta^2}} \exp\left(\left(\frac{\nu - \nu_0}{\delta}\right)^2\right) \exp\left(2\pi i(\nu - \nu_0)\tau\right) \tag{2.55}$$

with line widths $\delta_1 = 15$ and $\delta_2 = 3$, line positions $\nu_1 = -2$ and $\nu_2 = 1$ which are created at times $\tau_1 = 0$ and $\tau_2 = 0.1$ are considered. The calculated time-bandwidth product for different relative strengths A_1 and A_2 of both components are shown in Figure 2.7. Also values for the same relative strength but different phases between both components and an incoherent superposition are shown. In case of the superposition of Gaussian components I calculate the time-bandwidth product also with the standard deviation. In all cases each component of the superposition has a time-bandwidth product of 1.

The found time-bandwidth product strongly depends on the ratio of both components of the superposition and the measure for the photon width and duration. With the Süßmann measure values below 1 are possible. In case of the standard deviation all superpositions have a time-bandwidth product bigger than 1. Also the phase of the superposition influences the time-bandwidth product as it can be seen in (c) and (d). There are also cases, where the time-
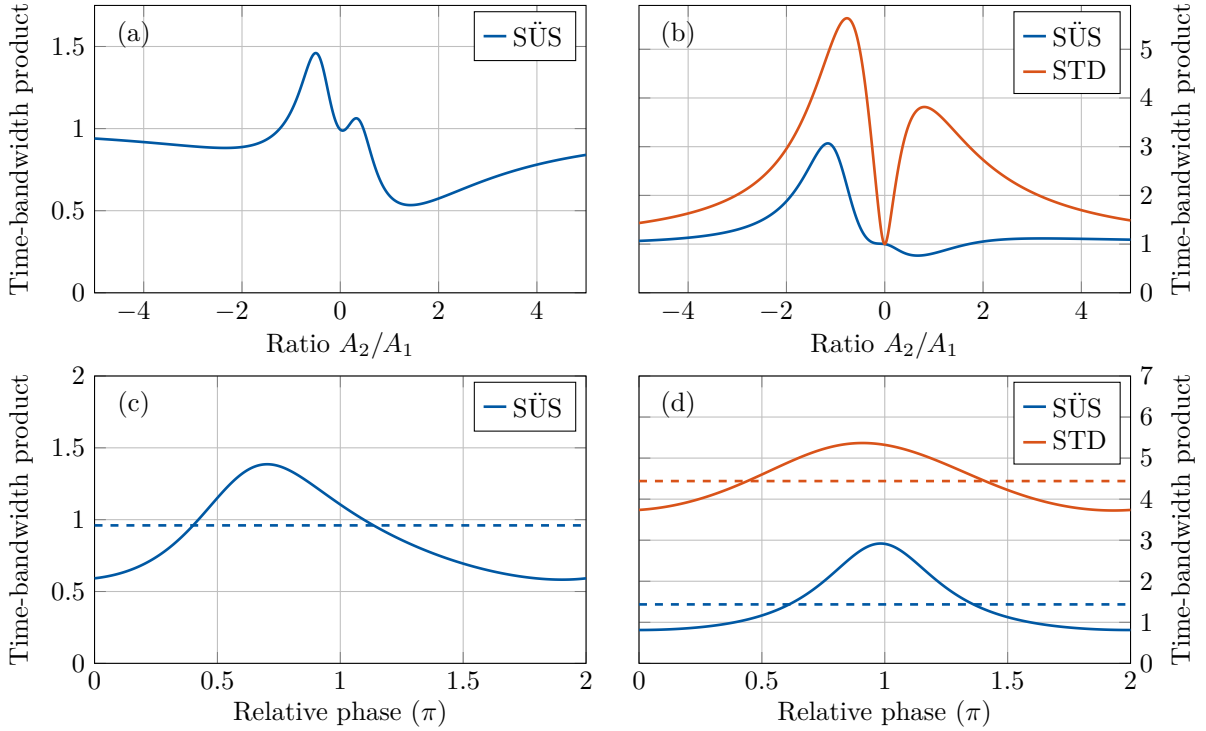
Figure 2.7.: Time-bandwidth product for a superposition of Lorentzian (a,c) or Gaussian (b,d) shaped photons. The relative strength (a,b) or relative phase (c,d) of both components is scanned. The dashed line corresponds to a mixed superposition of both components. The parameters are given in the text.

bandwidth product of the incoherent superposition is smaller than the time-bandwidth product of the coherent superposition. From this short example I draw the conclusion, that in general I cannot infer whether the photon is in a pure quantum state or not from the time-bandwidth product. However, with additional knowledge about the photon one can evaluate the purity of the photon state from the time-bandwidth product. In case of a Raman photon generated from a three level system it was shown [20] that the decay back into the initial state does not change the power spectrum but only affects the wave packet, which is elongated by a factor given by the branching ratio. In this case, the time-bandwidth product of a photon generated in a system without back decay is smaller than the time-bandwidth product of a photon generated in a system with back decay. In this case, the value without back decays gives a reference value for comparison.[8]

---

[8]In principle the duration of the photon is sufficient in this case. Despite this I still use the time-bandwidth product, as it is shows less dependence form the excitation laser parameters. A more reliable way to determine the photon purity utilizes the Wigner function together with a two dimensional Süßmann measure [50]. In this case the Wigner function has to be reconstructed from a series of measurement.

3. Experimental setup

The experimental setup to trap, control and manipulate the $^{40}\text{Ca}^+$ ion can be seen as a large machine that contains multiple smaller modules which fulfill different purposes. The first module contains the ion trap and the setup around the trap to focus laser and photon beams on the ion and to collect photons emitted by the ion. The second module contains the frequency stabilization of the laser systems and the setups that are required to switch individual laser beams. These two modules were setup and improved over the course of multiple generations of PHD students [25, 52–59] including myself. The third module of the setup are two analysis cavities I set up, which act as tunable spectral filter and that are used to measure spectra of single Raman scattered photons. Finally, the experimental control unit connects these modules. It controls pulse sequences and experimental parameters for individual measurements. In this Chapter, I will give an overview over these four modules of the experimental setup. Additionally, two further modules exist which are operated together with the presented setup in other experiments. A photon pair source generates polarization-entangled photon pairs matching the 854 nm transition of the calcium ion [58]. Furthermore, a quantum frequency converter in the group of C. Becher is available to convert single 854 nm photons to telecommunication wavelengths [60].

3.1. The ion trap setup

The ion trap module consists of two linear Paul traps with the same design, which are mounted in independent vacuum vessels, and the optics around the vacuum chambers to focus laser or photon beams on the ion and to collect emitted photons. The setup was developed and built by the first generation of PHD students in this group [52–54]. For more details regarding the construction, dimensions, materials, parts and mounting of the traps I refer to their work. Due to a different color after the back out, the traps are referred to as "bright" and "dark" trap.
In principle, the setup is designed to operate both traps together [61], but during my time only one of both traps was operated at a time. In the first years, we operated the bright trap almost exclusively, as this trap was optimized and running well. After a shortcut in the bright trap (details see Appendix A) the performance of the bright trap reduced drastically. The trap had to be driven with a smaller power what lead to a shallower trap potential and therefore smaller trap frequencies and higher vibration quanta of the ion. Additionally the average storage time of an ion, previously limited mostly by the failure of other routines in the laboratory (laser feedback loops e.g.), was reduced to below one day. Thus, we decided
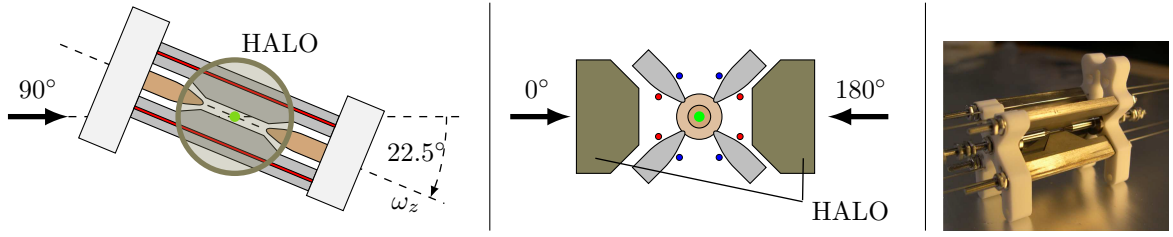
Figure 3.1.: The linear Paul trap as seen through the 0° view port (left) and on the trap axis ω_z defined by the end tip electrodes (middle). The red drawn compensation electrodes are not mounted in the bright trap. (right) Picture of the linear Paul trap taken from [53].

to switch to the dark trap, which we previously remodeled by adding additional electrodes for micromotion compensation to target the issue described in [52].

3.1.1. The linear Paul trap

Central part of the ion trap setup are two linear Paul traps of identical design (see Figure 3.1). Four electrodes (gray) are mounted in quadrupole configuration in a distance of $a = 0.8\,\text{mm}$ from the symmetry axis. A geometry factor $\alpha = 0.075$ was found for the trap. A radio frequency drive with $2\,\text{W}$ up to $12\,\text{W}$ power and frequencies between $\Omega_{\text{rf}} = (2\pi)24\,\text{MHz}$ and $\Omega_{\text{rf}} = (2\pi)26\,\text{MHz}$ is applied to the quadrupole electrodes to confine the $^{40}\text{Ca}^+$ ion string in radial direction [1]. The radio frequency is feed into a helical resonator, which is mounted on top of the vacuum vessel. This helical resonator generates the high voltage applied to the quadrupole electrodes. With the applied radio frequency power radial trap frequencies from $\omega_x \approx \omega_y = (2\pi)2.1\,\text{MHz}$ to $\omega_x \approx \omega_y = (2\pi)4.0\,\text{MHz}$ are reached. To confine the ion string in axial direction two end tip electrodes (light brown) are mounted in a distance of $b = 2.5\,\text{mm}$ from the trap center on the symmetry axis of the quadrupole electrodes. A voltage between $200\,\text{V}$ and $400\,\text{V}$ is applied to obtain axial trap frequencies $\omega_z \approx (2\pi)\,850\,\text{kHz}$ and $\omega_z \approx (2\pi)\,1.2\,\text{MHz}$. Voltages applied to compensation electrodes (red and blue) shift the position of the ion in the trap to compensate the micromotion.

Both traps are mounted in the center of their vacuum vessel. The axis through the end tips is tilted by 22.5° with respect to the plane of the optical table. On both radial sides of the trap two high aperture lens objectives (Linos Photonics HALO 25/0.4, referred to as HALOs) are mounted [53] to collect photons emitted by the ion and to tightly focus incoming light. The positions of these HALOs can be adjusted in all three axes to optimize the photon collection and coupling to the ion. The focal spot diameter of about $2\,\text{µm}$ enables single ion addressing. Due to a difference in the focal length of the HALO depending on the wavelength, for example $1.4\,\text{mm}$ between $866\,\text{nm}$ and $397\,\text{nm}$, the distance to the ion has to be adjusted to reach optimal collection of a specific wavelength. If the magnetic field is aligned in direction of the HALOs $6.0\,\%$ of the photons emitted on a σ-transition are collected. For a magnetic field aligned

---

[1] For the working principal of a linear Paul trap see Section 2.2.

perpendicular to the HALO axis 6.0 % of the photons emitted on a π-transition and 3.3 % of the photons emitted on a σ-transition are collected [56].

Eight view ports in the plane of the optical table, a big view port on the bottom of the vacuum chamber and two small view ports on top of the vacuum chamber enable optical access from many directions (see Figure 3.2 and 3.3). I name the view ports to access the ion through the HALOs 0° and 180° view port. The other view ports are labeled accordingly. Two coils that are mounted at the 0° and 180° view ports, a second pair that is mounted at the 90° and 270° view ports, and a third coil that is mounted on the top flange set the magnetic field that defines and aligns the quantization axis.

Following this rough overview regarding the traps itself, in the following two sections I will discuss the optic setup at both traps more detailed. This includes the lasers to drive transitions as well as the setup for fluorescence and single photon collection.

3.1.2. Bright trap optics and laser setup

The setup at the bright trap is shown in Figure 3.2. All laser beams focused on the ion are set up in the same way. A polarization maintaining single mode fiber brings the laser light from the laser table to the ion table. On the ion table a polarizing beam splitter mounted after the
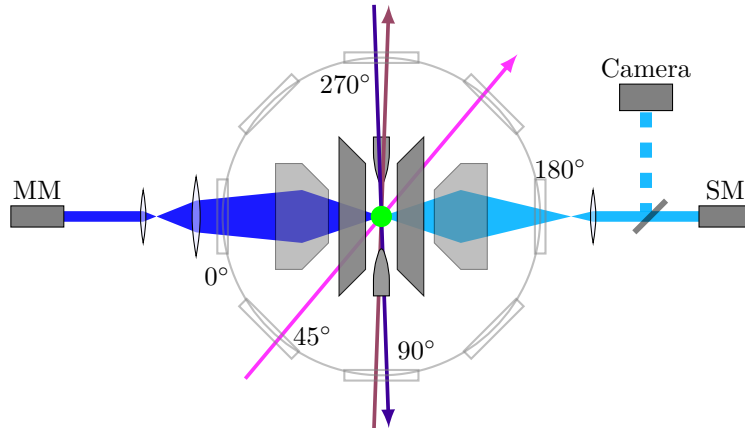
Figure 3.2.: Sketch of the setup at the bright trap. 397 nm and 866 nm beams are focused on the ion through the 270° view port for Doppler cooling and fluorescence detection. Counter-propagating, 393 nm and 854 nm beams are focused on the ion through the 90° view port. To drive the 729 nm transitions a laser beam is focused on the ion through the 45° view port. This enables to address all 729 nm transitions, depending on the polarization of this laser beam [55]. As the trap is tilted, the 729 nm beam is not exactly aligned with the center of the 45° and 225° view ports. Blue photons are coupled into a multi mode fiber (MM), a single mode fiber (SM, optimized for 393 nm photon) or imaged onto a camera (with a flip mirror). The coupling into the multi mode fiber or on the camera is optimized for 393 nm or 397 nm photons by adding or removing a single lens.

fiber output sets a fixed polarization. Behind this beam splitter a half wave plate followed by a quarter wave plate set the desired polarization state before the beam is focused on the ion. To control the laser power at the ion, the power is measured behind the polarizing beam with a photo diode. During a pulse sequence, the measured power is feedback controlled by adjusting the voltage applied to the acuosto-optic modulator that switches the laser beam.

For the displayed 393 nm single mode coupling, I measured a detection efficiency of 0.24 %. I generate single 393 nm photons (details see Section 4.5.2) and determine the detection efficiency from the number of detected single 393 nm photons divided by the number of generated single photons. The number of generated single photons is given by the sequence repetitions and the photon generation efficiency. Thus, the detection efficiency contains the collection efficiency, all coupling efficiencies, transmission losses and the quantum efficiency of the detector (80 % quantum efficiency, Laser Components COUNT-50B).

Not shown in Figure 3.2 is a coil mounted below the trap that drives the $S_{1/2}$ ground state transition and several other beams. A 729 nm beam is focused on the ion through the 0° view port for single ion addressing. There are two 854 nm single mode couplings set up at the 0° and 180° view port. As the HALOs were optimized for these 854 nm single mode couplings, the blue beams leave the respective HALO focused. For photon ionization, a frequency-doubled 845 nm laser and a blue LED were imaged onto the trap center through the bottom view port. This photon ionization setup was later replaced by a 375 nm and 422 nm laser (see Section 3.2). These new lasers were coupled into the same single mode fiber and focused onto the trap center through the 135° view port

After first successful steps with the new dark trap setup (see next section), we removed some parts of the bright trap optics to make space for the dark trap setup. At the moment it is planned to mount a new, segmented Paul trap that is currently under development [62] in the bright trap vacuum vessel.

3.1.3. Dark trap optics and laser setup

After the reconstruction of the trap mounted in the dark trap vacuum vessel, the setup around the trap (see Figure 3.3) was build up from scratch. A goal of the new setup is to tackle decoherence problems caused by the power grid and nearby electric devices. For this a µ-metal box similar to other setups [63, 64] and permanent magnets instead of the magnetic field coils [65] were planned. While this box was not finished for the measurements presented in this work, the later completion of this task by Hubert Lam showed promising results [66].

For the 854 nm single mode coupling (SM2), I determine a detection efficiency of 1.26 % for photon scattered on 854 nm σ transitions. I generate single 854 nm photons (details see Section 4.5.2) and determine the detection efficiency from the number of detected 854 nm photons divided by the number of generated single photons. The later contains a correction for possible 850 nm decay and not collected 854 nm π-decay. Thus, this detection efficiency contains the collection efficiency, all coupling efficiencies, transmission losses and the quantum efficiency of the detector (> 90 % quantum efficiency, ID Quantique-ID281). In the same way, I measure
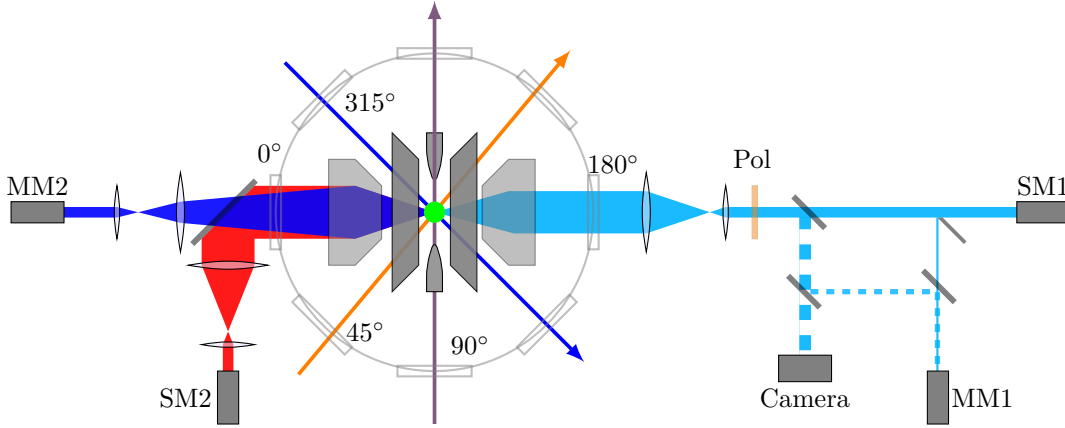
Figure 3.3.: Sketch of the setup at the dark trap. Vertical boards at the 45° and 90° view port feature space for four different laser beams. A 393 nm, 397 nm, 729 nm and 854 nm beam are focused on the ion through the 90° view port. The board at the 45° view port holds a 397 nm, 729 nm and 866 nm beam. The 0° HALO is optimized for 854 nm single mode coupling (SM2). Additionally, a multi mode coupling for 397 nm photons is set up at the 0° side (MM2) that also collects 393 nm photons sufficiently well without compensation for the wavelength difference. The 180° HALO is optimized for 393 nm single mode coupling (SM1). For some measurements a polarization projection setup (Pol) was inserted in the beam. A small part of the beam is cut off with a D-shaped mirror and coupled into a multi mode fiber (MM1) without reducing the single mode coupling efficiency. With flip mirrors the ion is imaged on a camera or the fluorescence is completely coupled into a multi mode fiber (MM1). By exchanging a single lens, the coupling into the multi mode fiber (MM1) and the imaging onto the camera is optimized for either 393 nm or 397 nm photons. An additional 397 nm cooling and trapping beam with a bigger focal spot is focused on the ion through the 315° view port.

the detection efficiency for the 393 nm single mode coupling (SM1). A detection efficiency of 0.63 % was found. At the same time I reach a detection efficiency of 0.0832 % into the multi mode coupling (MM1). Both values contain the collection efficiency, all couplings and the respective single photon detector efficiency (SM1: Laser Components COUNT-10B, 80 % quantum efficiency; MM1: Hamamatsu H7422P-40 SEL, 40 % quantum efficiency). With the 393 nm single mode and multi mode coupling, it is possible to simultaneously measure the wave packet and spectrum of the generated photon or a spectrally filtered and directly detected atom-photon state (see parts of Chapter 6 and Chapter 7).

Not shown in Figure 3.3 are a radio frequency coil mounted below the vacuum chamber that drives the $S_{1/2}$ ground state transition and two beams that are set up for photoionization, which are focused on the trap center through the 135° view port and a small view port on top of the vacuum chamber. Additionally to these beams, there is a 854 nm single mode coupling set up on the 180° side, an additional 393 nm beam path on the 180° side to a direct polarization projection setup, a 729 nm laser beam on the 0° side for single ion addressing and the ablation laser going in through the 90° view port.

3.2. Laser sytem

To manipulate the state of the calcium ion, well-controlled lasers are needed to drive the optical transitions. For this purpose laser systems for the 393 nm, 397 nm, 729 nm, 850 nm, 854 nm and 866 nm transition are used. Furthermore, there are a 375 nm and 422 nm laser for photo ionization and a 852 nm reference laser[2]. The 397 nm laser is generated from a frequency doubled 794 nm laser. The 854 nm laser can be frequency doubled to get a 427 nm laser. This 427 nm laser drives a photon pair source that matches the 854 nm transition in the calcium ion [58]. Most of the lasers are frequency stabilized with the transfer lock scheme described in [52–54, 67]: The laser is stabilized to a transfer cavity with the electronics supplied by TOPTICA and the Pound–Drever–Hall (PDH) technique. The transfer cavity itself is stabilized to a reference laser with the Pound–Drever–Hall (PDH) technique and a self-built cavity locker (see below). Most of the transfer cavities are stabilized to the 852 nm reference laser that is stabilized to a cesium vapor cell. The transfer cavity for the 393 nm laser is stabilized to the 397 nm laser. Because the 729 nm laser requires a much narrower linewidth, it is stabilized to a passively stable, high finesse reference cavity which is set up in a vacuum chamber [55]. The lasers for photo ionization are not frequency stabilized. Only the 422 nm laser has to emit at a specific wavelength that is adjusted by hand with a wavelength meter as monitor tool. Compared to the laser setup described in previous work by our group [25,52–54,56,59,67] some improvements were done in this work. These improvements involve a new cavity locker, the stabilization of the 393 nm laser, a new 729 nm laser and new lasers for photo ionization and trapping. In the following sections I describe these improvements.

393 nm laser

The 393 nm laser drives the $S_{1/2}$ to $P_{3/2}$ transition. Furthermore, it acts as reference for the stabilization of the 393 nm analysis cavity. Especially for the use as reference a good stability is crucial. To achieve the required stability the well established transfer lock scheme was set up for this laser with the 397 nm laser as reference. After implementing this scheme, it turned out that frequency shifts due to changing environmental conditions are to large to ignore. Due to changes in air pressure, a frequency shift of $-425\,\text{kHz/mbar}$ is expected. Cause of this shift is the dependence of the refractive index of air on environmental conditions and the wavelength of the light [68, 69]. This leads to a differential shift for each of the transfer locks that can be neglected in most cases, but not for the stability of the 393 nm laser. To get rid of this frequency shift, the 393 nm and 794 nm transfer lock cavities were mounted in self-built vacuum tubes. These tubes are evacuated at the beginning of every measurement session. For the evacuated cavity tubes a pressure change of 0.1 mbar per day was measured.

A second problem that occurred were frequency shifts, which I attributed to thermal drifts of the setup. It was not possible to set up the 393 nm transfer cavity in the confocal regime. This

---

[2]All lasers are from TOPTICA Photonics AG: DL 100, DL pro, TA pro, TA-SHG pro and iBeam smart. Additionally, there is a second 729 nm laser from M Squared (SolsTiS).

led to a change of the resonance frequency depending on the angle of the incident light. Also the appearance (form and offset) of the generated Pound–Drever–Hall error signal changed, depending on the incident angle. This problem was solved by increasing the cavity mirror distance. The cavity was set up in a single mode regime and both lasers for the transfer lock (393 nm and 397 nm) are coupled into the TEM_{00} mode of the cavity. A problem that remains unsolved is dust that is attracted by the blue light and disposed on the window that closes the cavity tube. As consequence, the coupling of both lasers into the TEM_{00} mode is slowly decreasing. To fix this, the window has to be cleaned every now and then.

792 nm laser

To get a 729 nm laser with a cleaner spectrum compared to the Diode laser, a new Ti:Sa laser system was bought during the time of this projected. With this laser 729 nm pulses that transfer more population into the $D_{5/2}$ state could be observed. Also a lower mean vibrational quantum number of the axial trap motion is measured after optimizing the Doppler cooling. With the new Ti:Sa laser a minimal value of $\langle \bar{n} \rangle \approx 10$ was measured in the bright trap. With the old Diode laser the minimal value measured was $\langle \bar{n} \rangle \approx 16$ in the bright trap and $\langle \bar{n} \rangle = 11.4(3)$ in the dark trap[3].

Unfortunately I could not operate the Ti:Sa laser system reliably over longer periods of time. The reason are recurring problems mainly with the pump laser. During times where the Ti:Sa laser could not be operated I switched back to the diode laser. Luckily all experiments which benefit from a "better" laser could be performed with the new laser. These are the atom-photon entanglement measurements presented in Chapter 7. Many of the spectrum measurements presented in Chapter 6 were performed with the diode laser. In this case a sub optimal preparation in the $|D_{5/2}\rangle$ state leads to a small reduction of the efficiency that is negligible compared to other losses.

Photo ionization laser

The ionization of neutral calcium to a calcium ion is done in a two-photon process. First the $4s^2$ $^1S_0 \rightarrow 4s4p$ $^1P_1$ transition is excited. In the second step the electron is removed from the atom by exciting the $4s4p {}^1P_1$ electron above the ionization threshold. The created calcium ion is trapped and laser cooled. This photo ionization was done a long time with a frequency doubled 845 nm laser and a blue high-power LED. This setup was replaced after my first years by two lasers, one running at 422.79148 nm (measured with the wavelength meter, Doppler shift of the calcium beam not compensated) to address the $4s^2$ $^1S_0 \rightarrow 4s4p$ $^1P_1$ transition in neutral calcium, the other one running at a fixed wavelength of 375 nm for the final ionization. Both lasers are coupled in the same single mode fiber and focused on the ion. With the setup it takes about five to ten minutes to trap a single $^{40}Ca^+$ ion.

---

[3]In both traps the same geometry and similar trap frequencies were used. The lower value measured with the diode laser at the dark trap is attributed to an improved feedback loop that results in a cleaner spectrum. Nevertheless, even after optimizing the Diode laser feedback by looking at the laser spectrum (this was mainly done by Omar Elshehy), the temperature measured with the Ti:Sa laser remained lower.

Cavity Locker

To stabilize a cavity to the reference laser we have our so-called cavity locker. For the stabilization of the analysis cavities and additional transfer lock schemes, more cavity locker modules were needed. This led to the development of a new version based on the old version described in [54]. The first steps of this development were done by Konstantin Klein [70] on the basis of modules that were designed by Stephan Kucera for the stabilization of a cavity for a photon pair source. I finished this development. The new version has the same features as the old version, including the "magic button" to jump to the next cavity mode. The cavity locker runs a feedback loop with $50\,\mathrm{kHz}$ with an output resolution of 20bit and an output range of $\pm 10\,V$. An additional feature is the possibility to hold and continue the stabilization. This is needed for the analysis cavity, where a mechanical chopper switches between the photon beam and the reference beam going to the cavity. The biggest change is the main user interface which is running on a Raspberry Pi. This Raspberry Pi is accessed over the group network, what enables to reinitialize a cavity feedback loop remotely. A more detailed description of the new cavity locker is given in Appendix F.

3.3. Analysis cavity setup

The single photon spectrometer I operate in this work is a setup with a Fabry-Pérot cavity as central part. The setup acts as tunable spectral filter. In the course of this work, two nearly identical setups were built, the first for $393\,\mathrm{nm}$ photons and the second for $854\,\mathrm{nm}$ photons.
In both setups, two different beams are coupled into the Fabry-Pérot cavity. The "photon beam" filters photons arriving from the ion. The "feedback beam" is required to stabilize the cavity to the reference laser. Both beams are overlapped at a non-polarizing beam splitter and coupled into the TEM_{00} mode of the resonator. A mechanical chopper switches between the photon and feedback beam. This chopper is built from a computer hard drive with a ratio of 2:3:13 between the transmission times of closed:feedback:photon beam. The chopper blocks the photon beam in front and after the cavity, if the feedback beam is coupled into the cavity. This avoids damage at the single photon detectors mounted at the ion table and in transmission of the cavity. The transmission of the cavity is coupled into a single mode fiber and sent to a single photon detector. The single mode coupling performs spatial filtering and suppresses unwanted transmission of higher order cavity modes. The reflection of the cavity is focused on a fast photo diode to stabilize the cavity with the Pound-Drever-Hall technique implemented in the above mentioned cavity locker. Controlled by the state of the chopper, the feedback is switched on, if the feedback beam is open or set to hold, if the feedback beam is closed. Consequently, the cavity is free running while the photon beam is open. During a measurement the chopper is set to 1000 turns per minute what results in a measurement window of $20\,\mathrm{ms}$ during a $30\,\mathrm{ms}$ cycle. To avoid unwanted background events, the photon generation at the ion is paused and continued by the state of the chopper so that the photon generation is only executed during the $20\,\mathrm{ms}$ time window when the chopper is open for photon transmission.

By tuning the frequency of the reference laser the cavity is set to any desired frequency as the cavity resonance is shifted by the same amount. From the detuning of the reference laser with respect to the calcium ion, the detuning of the cavity with respect to the corresponding transition is known.

3.3.1. 393 nm analysis cavity

The design of the 393 nm analysis cavity and first rudimentary characterizations were done by Konstantin Klein [70]. The final setup as operated in this work (see Figure 3.4) was done by myself together with Christian Haen [71], Jurek Frey [72] and Max Bergerhoff [73] over the course of their Bachelor projects.
The transmission spectrum of the full setup (see Figure 3.5, left), measured after the single mode fiber output (FC3), shows suppression larger than 50 of unwanted higher order modes. From the cavity decay (see Figure 3.5, right) a linewidth $\Delta\nu = 622(4)\,\mathrm{kHz}$ is determined. Together with the free spectral range $\nu_{\mathrm{FSR}} = 377\,\mathrm{MHz}$, calculated from the cavity length, a finesse of 606(4) is found. For the stability of the free-running cavity in between two stabilization periods a value
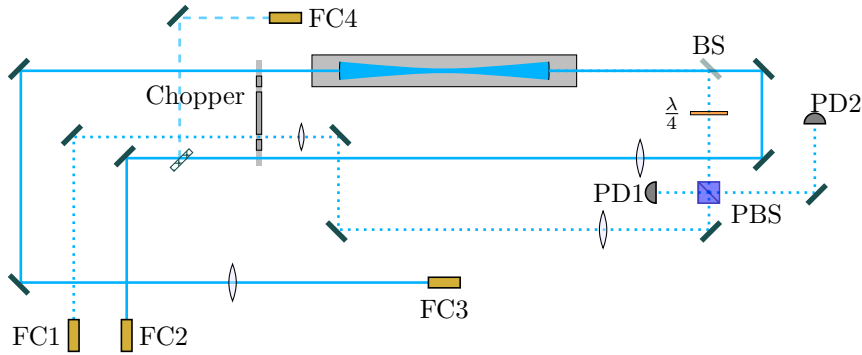
Figure 3.4.: Sketch of the 393 nm analysis cavity setup. The cavity is built with two mirrors with a curvature $\rho = 30\,\mathrm{cm}$ and a reflection of 99.6 % that are mounted in a tube with a distance of 398 mm from each other. The cavity is constructed to have a low thermal expansion [70]. The photon beam (FC2, solid) is overlapped with the feedback beam (FC1, dashed) at a non polarizing 90:10 beam splitter (BS) and coupled into the cavity. The transmission is coupled into a single mode fiber (FC3) and sent to a single photon detector. A mechanical chopper periodically blocks either beam to switch between stabilization and measurement mode. To check the single mode coupling at the ion table, the photon beam can be coupled into a multi mode fiber (FC4). This coupling has no relevance for the function as spectrometer, but is important to check the single mode coupling at the ion table without disconnecting and reconnecting the fiber of the photon beam at the analysis cavity setup. This avoids unwanted misalignment during the measurements. The chopper state is read out with an independent photo diode (PD1). The Poud-Drever-Hall error signal is generated with the cavity reflection that is measured by the photo diode PD2. Pictures of the setup are shown in Appendix G.
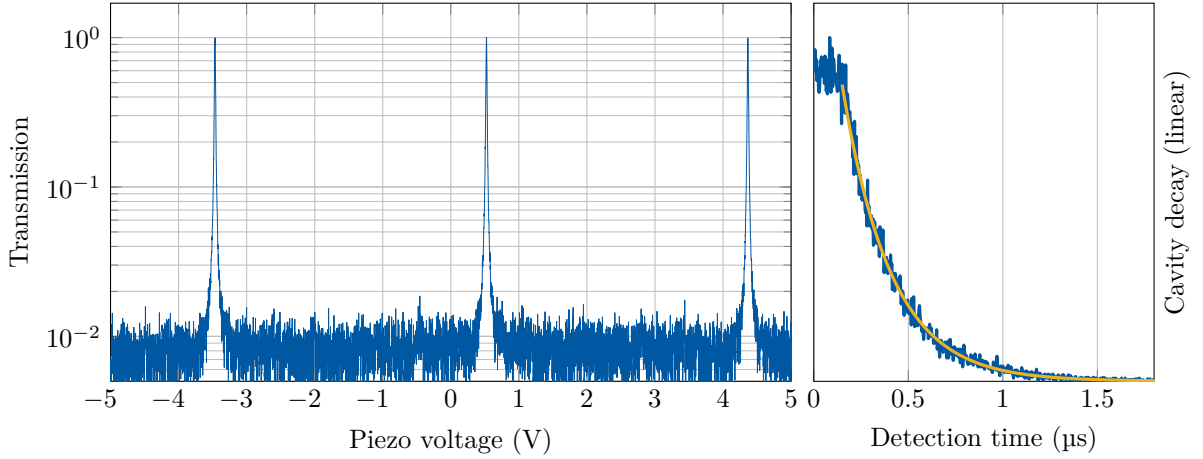
Figure 3.5.: Transmission spectrum of the photon beam of the 393 nm analysis cavity (left) and cavity decay (right). Two cavity modes are separated by $\nu_{\text{FSR}} = 377\,\text{MHz}$.

of $\Delta\nu_{\text{cav}} = 112\,\text{kHz}$, with respect to the stabilization laser, was measured. The value is obtained from the standard deviation of the Pound-Drever-Hall error signal. Together with the stability of the reference laser an absolute stability of $\Delta\nu_{\text{tot}} = \sqrt{\Delta\nu_{\text{cav}}^2 + \Delta\nu_{393}^2} = 460\,\text{kHz}$ is found for the cavity during the measurement period. Therein $\Delta\nu_{393}$ is the stability of the 393 nm laser obtained from the transfer-lock scheme [71]. No dependence of the cavity resonance on the polarization was found. The on-resonance transmission of the cavity setup is given by the ratio of the power behind the output fiber (connected to FC3) divided by the power at the input (FC2). The value is corrected for the time, where the photon beam is closed by the chopper and thus corresponds to the transmission as seen by single photons. Over the period of two and a half years during that I performed measurements with the setup, the transmission decreased from 12 % to 4.5 %. I suspect dust that is attracted by the reference laser and deposited on the mirrors as the cause. After cleaning the mirrors, as preparation for a later measurement, an on resonance transmission of 12 % was reached again.

3.3.2. 854 nm analysis cavity

The 854 nm analysis cavity was designed after many measurements with the 393 nm cavity. Compared to the 393 nm cavity that was designed to measure spectra, the 854 nm cavity was designed to act as spectral filter for the atom-photon entanglement generation scheme presented in Chapter 7. Simulations showed that a cavity with a linewidth between 1 MHz and 2 MHz offers a good trade-off between efficiency and quality of the generated atom-photon state. The setup was built and characterized during the Bachelor thesis of Jelena Ritter [74] supervised by myself. A scheme of the setup is depicted in Figure 3.6
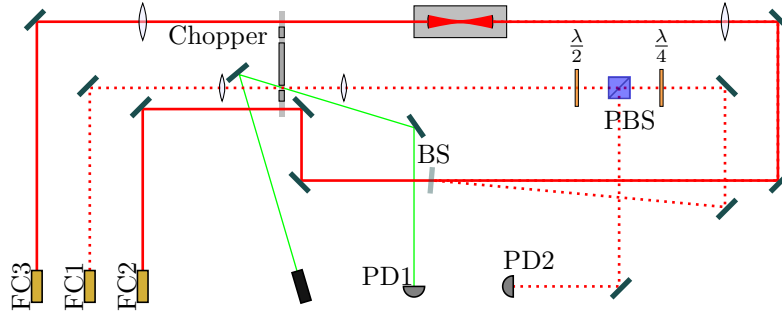
Figure 3.6.: Sketch of the 854 nm analysis cavity setup. The cavity is built with two mirrors with 99.5 % reflection mounted 127 mm from each other. The feedback beam (FC1, dashed) is overlapped with the photon beam (FC2, solid) at a glass plate (BS) with 4 % reflection that is mounted almost perpendicular to the photon beam to reduce polarizing effects on the photon beam. The transmission of the photon beam is coupled into a single mode fiber (FC3) and send to a single photon detector. The reflection of the cavity is focused on a photo diode (PD2) to generate the Pound-Drever-Hall error signal for the feedback loop. A green laser beam coupled through the chopper on a second photo diode (PD1) measures the chopper state. This controls the feedback loop and measurement sequence. No additional setup to check the 854 nm single mode coupling on the ion table is needed because the coupling can be checked without disconnecting the fiber at the photon beam input (FC2). Pictures of the setup are shown in Appendix G.

During first measurements it turned out that the reference laser induces a high number of background events. Additional shielding material glued on the chopper could only partially reduce the induced background. To completely remove the background events an additional laser beam, from a cheap green laser diode was set up to detect if the chopper is open for the feedback beam. This green laser beam switches the reference laser on, when the feedback beam is open and off otherwise. With this technique, the background induced by the reference laser could be removed so that no measurable background from the setup remained.

The transmission spectrum of the analysis cavity setup (see Figure 3.7, left), measured after the single mode fiber output (FC3), shows suppression larger than 250 of unwanted higher order cavity modes. From the cavity decay (see Figure 3.7, right) a line width of $\Delta\nu = 1.689(7)$ MHz was measured. Together with the free spectral range $\nu_{\mathrm{FSR}} = 1.18$ GHz, calculated from the cavity length, this results in a finesse of 669(3). For the free running cavity in between two feedback windows a stability of 0.49 MHz, with respect to the stabilization laser, was found. Together with the line width of the 854 nm reference laser [52, 67], the absolute stability is better than 0.51 MHz. Only a negligible polarizing effect of the cavity was found [74]. Thus a polarization projection can be done behind the cavity. The on-resonance transmission of the cavity, given by the laser power behind a fiber connected to the output fiber coupler (FC3) divided by the power behind the input fiber coupler (FC2) is 45 %. As for the 393 nm case this transmission is corrected by the closed time of the chopper and thus corresponds to the transmission of the setup as seen by single photons.
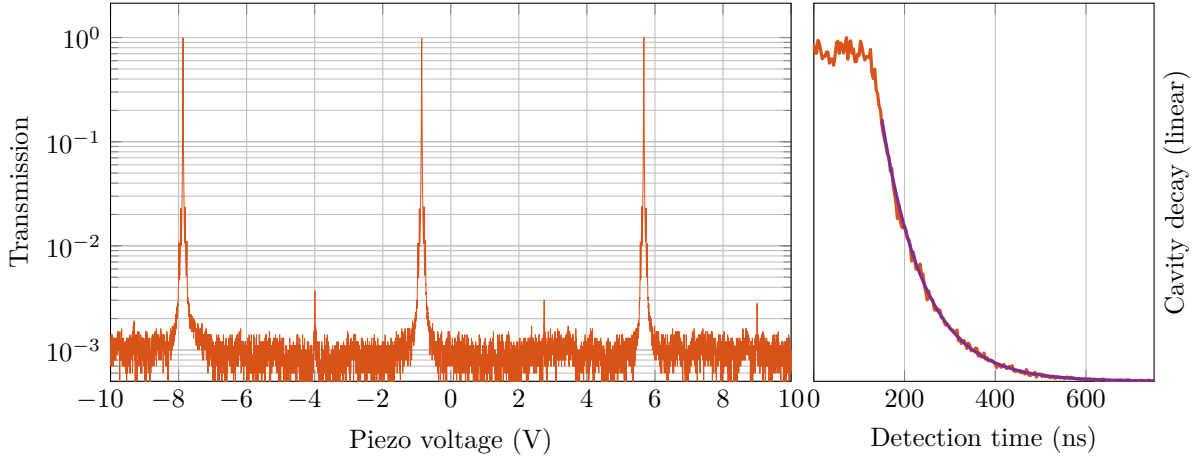
Figure 3.7.: Transmission spectrum of the photon beam of the 854 nm analysis cavity (left) and cavity decay (right). The sidebands are from the laser feedback loops. The different distances between the cavity modes are caused by a different slope of the piezo for positive and negative voltages.

3.4. Experimental control

To run desired pulse sequences, specific laser beams have to be switched on and off with well controlled frequencies and phases. This is done by a device called HYDRA-II, a commercial further development of the "old" HYDRA described in [54]. It is a multi-channel arbitrary waveform generator with digital in- and outputs and a time-to-digital module. Twenty independent, synchronized arbitrary-waveform generators with 1 GHz sampling rate are available to tune and switch acousto-optic modulators or to drive the radio-frequency coil below the trap. The time-to-digital module has eight independent channels, which record time stamps of photon and trigger events during a pulse sequence with a resolution of 625 ps. The digital input-output module has more than twenty channels available to generate or read trigger signals. Additionally, this module reads the laser powers, digitized by a device called KARKINOS. This is needed to control the laser power during a measurement sequence via feedback control. The HYDRA-II executes previously programmed pulse sequences, that are loaded by MATLAB together with the required sequence parameters (detunings, amplitudes, pulse duration, ...). The MATLAB scripts and functions and the the HYDRA-II pulse sequences were mainly written by myself, together with my colleague Stephan Kucera who did the first steps with this new system [75]. The new system enables larger schedules with consecutive sequences which run automatically with updated sequence parameters, as for example 729 nm transition frequencies, after each sequence. The measured 729 nm transition frequency can be set in the subsequent pulse duration scans without any further interaction by the experimenter (for an example see Section 4.5.1). Additionally, other devices or operations can be included in such a schedule, if they can be controlled by MATLAB. An important example is the magnetic field control

I built during my master thesis [76] or a wave plate controller turning quarter and half wave plates for a polarization projection. This automation allows to write measurement schedules that perform all necessary measurements without further interaction. In such a case, the only remaining interaction with the experiment is to monitor everything, check the alignment every now and then and similar tasks. If all involved alignments are stable and no other interaction is needed, the measurement schedule can run completely on its own until something goes wrong. Only this automation allowed me to collect the data presented in this work.

4. Experimental methods

4.1. Basic operations for an ion qubit

To perform experiments with the calcium ion, a toolbox with basic operations is needed. Each experimental sequence is built by combining these basic operations. The toolbox contains Doppler cooling, optical pumping, coherent manipulation of qubit states and fluorescence detection. In the following few sections I introduce these basis operations.

4.1.1. Doppler cooling

Typically, Doppler cooling is the first step in a pulse sequence. It extracts vibration quanta from the ion to counteract heating processes, induced for example by collisions with background gas or fluorescence detection. For Doppler cooling many photons are scattered on an atomic dipole transition. This scattering process is modeled semi-classical with rate equations for the quantum number n [40,77], which describes the vibration state of the ion, to describe different scattering paths where the ion ends in a vibration state with less, equal or more quanta. Solving the rate equations for the quantum number n leads to the steady state solution

$$\bar{n}_f = \frac{\cos^2(\theta)W(\Delta - \nu) + \alpha W(\Delta)}{\cos^2(\theta)\left[W(\Delta + \nu) - W(\Delta - \nu)\right]} \tag{4.1}$$

for a laser detuned by Δ from the excited transition. Therein, $W(\Delta)$ describes the scattering rate of a photon on the carrier transition, while $W(\Delta - \nu)$ and $W(\Delta - \nu)$ describe the scattering rates on the red $(-\nu)$ respective blue $(+\nu)$ side band. The parameter $\alpha = \frac{2}{5}$ [78] accounts for the angular dependence of the dipole emission (see Section 2.5), θ is the angle between the direction of the cooling laser and the oscillation of the trap mode. The steady state solution shows that cooling is most efficient for a cooling laser parallel to the ion vibration. Scattering photons with a laser perpendicular to the oscillation direction does not cool but heats the ion instead. With the cooling lasers one has to ensure that all three vibration directions (in our case one axial and two radial vibrations) are cooled.

The $^{40}\mathrm{Ca}^+$ ion is Doppler cooled with the 397 nm, 866 nm and 854 nm laser. The 397 nm laser and 866 nm laser are required to scatter photons on the $\mathrm{S}_{1/2}$ to $\mathrm{P}_{1/2}$ transition. The 854 nm laser brings population from the $\mathrm{D}_{5/2}$ state back to the $\mathrm{S}_{1/2}$ state. At the bright trap the 397 nm laser and 866 nm laser are coupled in through the 90° view port. At the dark trap the 397 nm laser is coupled in either through the 90° or 45° view port while the 866 nm laser is coupled in through the 45° view port.

To optimize the cooling process, the detunings Δ_{397} and Δ_{866}, the laser powers P_{397} and P_{866} and the cooling duration are scanned to minimize the mean vibration number $\langle n \rangle$. The mean vibration number is inferred from the ratio of the coupling strengths of a 729 nm transition on the red sideband divided by the coupling strength on the carrier for small pulse areas $\Omega\tau < \frac{\pi}{5}$ on the carrier transition [55].

The best cooling is achieved for the detunings $\Delta_{397} \approx -18.0\,\text{MHz}$ and $\Delta_{866} \approx +16\,\text{MHz}$[1] with respect to the line center. The optimal laser powers depend on the focus of the laser beams at the ion position. For the 397 nm laser coupled in from 90 °, the minimal mean vibration numbers $\langle \bar{n}_{\text{ax}} \rangle = 11.4(3)$ and $\langle \bar{n}_{\text{rad}} \rangle = 14(1)$ and cooling rates $R_{\text{ax}} = 28(2)\,\text{ms}^{-1}$ and $R_{\text{rad}} = 8(3)\,\text{ms}^{-1}$ were found[2]. The 397 nm laser from 45 ° has a worse projection on the axial trap frequency and a better projection on the radial trap frequency. Consequently the minimal mean vibration numbers change: $\langle \bar{n}_{\text{ax}} \rangle = 12.8(3)$ and $\langle \bar{n}_{\text{rad}} \rangle = 4.2(2)$ and cooling rates $R_{\text{ax}} = 18.5(8)\,\text{ms}^{-1}$ and $R_{\text{rad}} = 35(3)\,\text{ms}^{-1}$ were measured[3].

To cool the ion closer to the vibration ground state ($\langle \bar{n} \rangle = 0$) other techniques as resolved side band cooling [79] or cooling with electromagnetically induced transparency [80,81] are required. Because these techniques typically require longer cooling duration and the experiments presented here do not require an ion that is cooled to the vibration ground state, Doppler cooling is sufficient.

4.1.2. Optical pumping

Optical pumping initializes the ion from a mixed state to a pure quantum state. In this work, optical pumping transfers all population either into the $|\text{S}_{1/2}, +\frac{1}{2}\rangle$ state or into the $|\text{S}_{1/2}, -\frac{1}{2}\rangle$ state. For this purpose the respective other state is emptied by a laser that couples only to this state. Two options are possible: frequency selective or polarization selective optical pumping. Frequency selective optical pumping (see Figure 4.1, left) requires well separated transitions that are selectively addressed. In the setup this is only possible with the 729 nm transitions. The $|\text{S}_{1/2}, +\frac{1}{2}\rangle$ level is coupled to the $|\text{D}_{5/2}, -\frac{3}{2}\rangle$ level with the 729 nm laser. Other $\text{D}_{5/2}$ states are possible, but this choice is the most efficient. The 854 nm laser empties the $\text{D}_{5/2}$ manifold, while the 866 nm laser (not drawn) empties the $\text{D}_{3/2}$ manifold. All population that decays into the $|\text{S}_{1/2}, +\frac{1}{2}\rangle$ state is pumped through the cycle again until finally all population is stored in the $|\text{S}_{1/2}, -\frac{1}{2}\rangle$ state. By scanning the power of the 729 nm and 854 nm laser and the pumping duration, the pumping is optimized. As the excitation on the 729 nm transition is slow, the typical pumping time (100 µs) is rather long. However, the scheme does not require a specific polarization or direction and is therefore rather flexible and applied during most of the pulse sequences.

---

[1]A 866 nm detuning between $\Delta_{866} \approx +6 \ldots 16\,\text{MHz}$ leads to similar cooling results.

[2]With the new Ti:Sa laser a value $\langle \bar{n}_{\text{ax}} \rangle \approx 10$ could be reached. We attribute the better value to the cleaner spectrum of the Ti:Sa laser. However, the comparison between different 397 nm directions was done with the Diode laser. Thus these values are stated here.

[3]The second radial mode is cooled badly by the 45 ° beam. With the assumption, that all trap frequencies are perpendicular to each other, the direction and Lamb-Dicke parameter of the first radial mode is calculated.
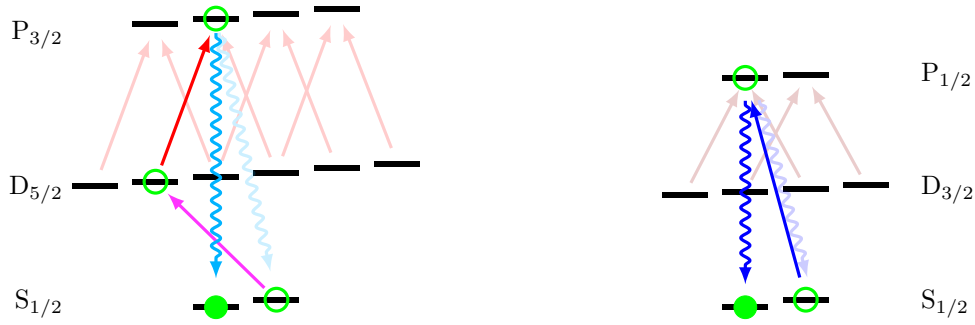
Figure 4.1.: Frequency selective (left) and polarization selective (right) optical pumping into the $|S_{1/2}, -\frac{1}{2}\rangle$ state. Pumping schemes into the $|S_{1/2}, +\frac{1}{2}\rangle$ state are mirror inverted.

Polarization selective optical pumping pumping (see Figure 4.1, right) addresses individual dipole transitions by polarization and direction of the laser beam. The $|S_{1/2}, +\frac{1}{2}\rangle \rightarrow |P_{1/2}, -\frac{1}{2}\rangle$ transition is excited with a circularly polarized 397 nm laser parallel to the magnetic field. From this state the ion decays back to either of the $S_{1/2}$ Zeeman levels or into the $D_{3/2}$ state. The population in the $|S_{1/2}, +\frac{1}{2}\rangle$ state is excited again while the population in the $|S_{1/2}, -\frac{1}{2}\rangle$ state is not excited. The $D_{3/2}$ state is emptied by the 866 nm laser. Due to the excited dipole transition it is much faster (3 μs) than the frequency selective optical pumping with the quadropule transition. However, as it has specific requirements on polarization and direction it can only be applied for specific setups. In this work polarization selective optical pumping was applied during the measurement of quantum interference spectra presented in the Sections 6.2.3 and 6.2.4.

4.1.3. State manipulation

To manipulate the state of the ion laser or radio frequency pulses are applied. The radio frequency pulse drives the transition between the $S_{1/2}$ Zeeman levels while laser pulses drive optical transitions. In all cases the frequency, phase, Rabi frequency and duration of the pulse are controlled by parameters that are set in HYDRA-II. The chosen sequence of pulses together with the initialization and following state analysis determines the performed measurement. The specific pulse sequences to generate Raman photons and to generate and detect atom-photon entanglement are discussed detailed in Sections 4.5 and 4.6.

4.1.4. State analysis

To determine the state of the ion state analysis is done (see Figure 4.2). It contains two steps state projection and fluorescence detection. In the first step the population from the state of interest is brought into the bright manifold with a series of pulses. Afterwards fluorescence detection is applied to determine whether the ion was in the bright or dark manifold. The process may be repeated, if the ion was not found in the bright state to probe the population in a further state until the ion is found in a bright state. More detail about the state projection
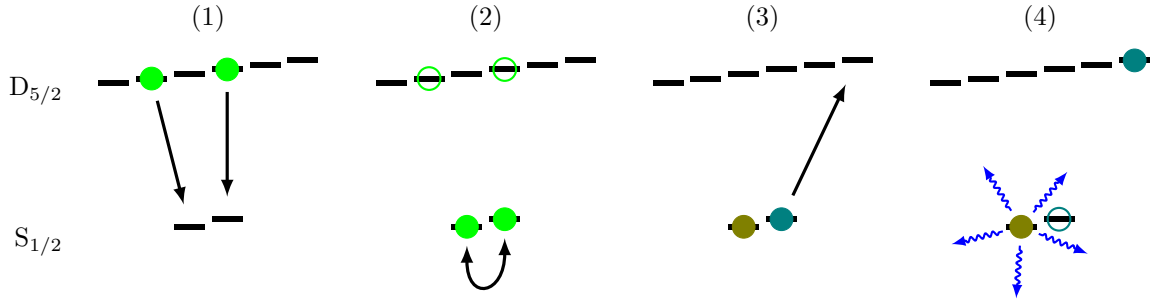
Figure 4.2.: State projection to a $D_{5/2}$ superposition. (1) Two π pulses transfer the superposition to the $S_{1/2}$ ground state. (2) A $\frac{\pi}{2}$ pulse with controlled phase is applied to set the projection basis. (3) The population from one of the mapped states is shelved to a not populated $D_{5/2}$ level. (4) Fluorescence detection: the ion scatters 397 nm photons, if it is not in one of the $D_{5/2}$ states. The process can be repeated with a different state, if the ion was not in the bright state. If multiple fluorescence detections are done, it must be remembered that a bright detection projects the ion into a mixture in the $S_{1/2}$ state, while a dark decision does not affect any state stored in the $D_{5/2}$ levels. To project onto energy eigenstates, the first two steps (1,2) are skipped.

onto different superposition states is discussed in Section 4.6. The explicitly pulses for the state projection are explained with the respective pulse sequences.

For fluorescence detection the 397 nm and 866 nm laser scatter photons on the $S_{1/2} \leftrightarrow P_{1/2}$ transition. The 866 nm laser is required to re pump population that decayed to the $D_{3/2}$ manifold. If the ion was in the $S_{1/2}$ or $D_{3/2}$ state prior to the fluorescence detection, photons are scattered and the ion appears bright. If the ion is in the $D_{5/2}$ manifold, no photons are scattered and the ion appears dark. Due to detector dark counts or stray light a few photons events may be detected, even though the ion was in a dark state. The power of the 397 nm and 866 nm laser are set to maximize the photon scattering rate. Typical values are $r_b \geq 173000\,\mathrm{s}^{-1}$ and $r_d \leq 220\,\mathrm{s}^{-1}$ if the ion is in the bright respective dark state.

To distinguish whether the ion is in a bright or dark state the number of photon detections n_c in the integration time window is counted and compared with a chosen threshold n_t. The dark state is assigned if $n_c \leq n_t$. The optimal threshold n_t is calculated from the rates r_b and r_d of detected photons for an ion in the bright or dark state together with the integration duration τ by minimizing the probability of a wrong decision [57]. A Poisson distribution is assumed for detector dark counts, laser stray light and the ion fluorescence. In case of the ion fluorescence this can be done because of the small detection efficiency of less than 1 %. For an integration time of 70 µs and the above mentioned scattering rates, the optimal threshold is $n_t = 1$. For this threshold a decision error of $\epsilon = 9.5 \cdot 10^{-5}$ is expected. In Figure 4.3 the measured number of photon events in a 70 µs time window for these rates are shown. From the measured distributions a decision error of $\epsilon = 3.0 \cdot 10^{-4}$ is inferred for this threshold.
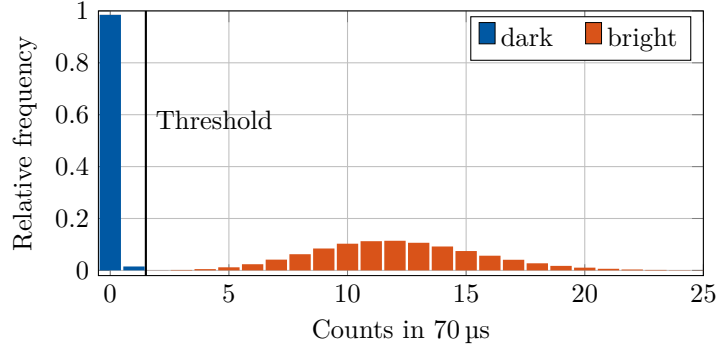
Figure 4.3.: Relative frequencies of detected photon numbers during a $70\,\mu s$ fluorescence detection window with $r_b = 173000\,\mathrm{s}^{-1}$ and $r_d = 220\,\mathrm{s}^{-1}$ measured with $1.4 \cdot 10^6$ repetitions for each case. With the threshold method the dark state is assigned if there are less counts than the marked threshold. Otherwise the bright state is assigned.

Increasing the integration time to further reduce the decision error is limited by the life time of the dark $D_{5/2}$ state[4]. Due to the limited life time of $1.17\,\mathrm{s}$ [27] a fraction of the population ($3.8 \cdot 10^{-4}$ in $70\,\mu s$) decays into the bright state and causes wrong decisions. This is neglected in the calculation done for the threshold, but can be taken into account to find the optimal threshold [57]. However, the difference compared to the calculated threshold is negligible for the chosen integration time. Additionally, the measured decision error is much smaller as for example the error due to limited pulse efficiencies (around $5 \cdot 10^{-3}$) and is therefore neglected. To estimate the probability to find the ion in the dark or bright state the whole experimental sequence is repeated several times. For every repetition the state of the ion is measured by fluorescence detection. The expectation value $\langle p \rangle$ and standard deviation Δp of the probability to find the ion in the dark state are calculated with Bayesian inference. For m repetitions with k measured dark events one gets

$$\langle p \rangle = \frac{k+1}{m+2}, \qquad \langle p^2 \rangle = \frac{(k+1)(k+2)}{(m+2)(m+3)}, \quad \text{and} \quad \Delta p = \sqrt{\langle p^2 \rangle - \langle p \rangle^2} \qquad (4.2)$$

as derived in [57].

4.2. Preparation and calibration measurements

Before complex experimental sequences several calibration measurements are necessary to determine all required parameters. These calibration measurements are done on a regular basis throughout the day to determine transition frequencies and pulse amplitudes or to check the coherence time. With continuously running version I check the alignment of laser beams on the ion or the polarization. Here, I will give a brief overview over these calibration sequences. For more details I refer to [55–57, 59] who developed many of these calibration measurements.

---

[4]Additionally a longer integration time slows down the sequence repetition rate. This is also not wanted.

866 nm and 854 nm dark resonance spectroscopies

The detunings of the 397 nm and 866 nm respectively 393 nm and 854 nm laser are measured with 866 nm respective 854 nm dark resonance spectroscopies. If the detuning of the red laser (866 nm respective 854 nm) matches the detuning of the blue laser (397 nm respective 393 nm), population is transferred to the $|D\rangle$ state and the fluorescence decreases. In both cases the blue laser driving the $|S\rangle \rightarrow |P\rangle$ transition is set to $\Delta \approx -20\,\mathrm{MHz}$ from the resonance. The frequency of the red laser driving the $|D\rangle \rightarrow |P\rangle$ transition is scanned. The measured fluorescence is fitted with optical Bloch equations to determine the transition line centers with respect to the laser frequencies. In principal also the Rabi frequencies, polarization and the magnetic field strength can be extracted. The Rabi frequency is fitted but not required for further measurements or evaluation. The magnetic field is measured more precisely with other spectroscopies. However, to get a first estimate the 866 nm dark resonance spectroscopy is a good tool. The polarization of the laser beams are fixed during the evaluation.

The 866 nm dark resonance spectroscopy involves the $S_{1/2}$, $P_{1/2}$ and $D_{3/2}$ states. The measured 397 nm fluorescence is fitted with eight level Bloch equations to determine the 397 nm and 866 nm detunings for Doppler cooling. Additionally, the first steps for the micromotion compensation and new cooling parameters are done with the 866 nm dark resonance spectroscopy. A better Doppler cooling results in deeper dark resonances [82]. Depending on the micromotion of the ion, side bands arise in the measured dark resonance spectrum [83]. Therefore, I
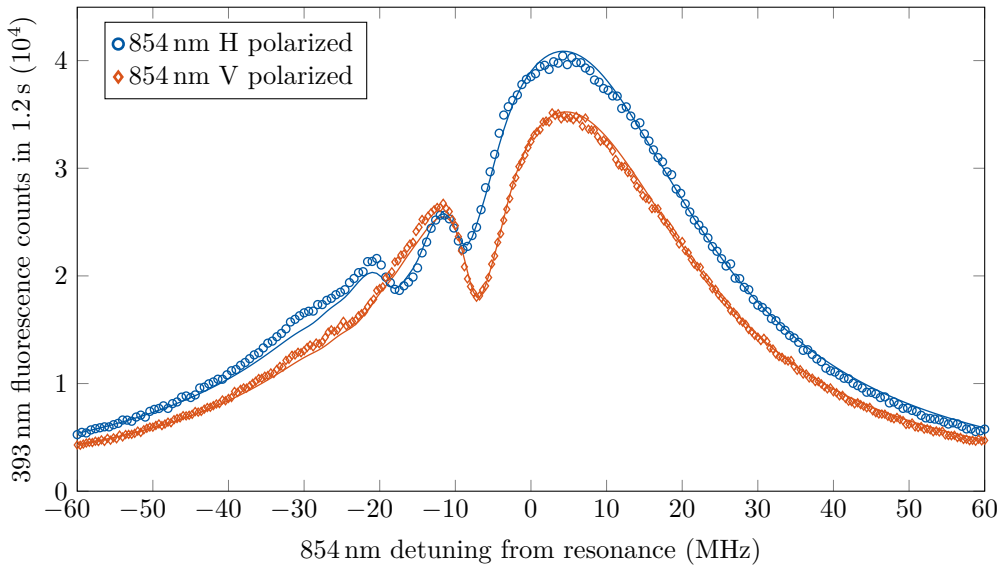
Figure 4.4.: 854 nm dark resonance spectroscopies for horizontally or vertically polarized 854 nm laser and horizontally polarized 393 nm laser coupled in on quantization axis. From the evaluation the laser parameter are extracted. Vertically polarized 854 nm laser: $\Omega_{393} = 16.9\,\mathrm{MHz}$, $\Omega_{854} = 6.7\,\mathrm{MHz}$ and $\Delta_{393} = -14.8\,\mathrm{MHz}$. Horizontally polarized 854 nm laser: $\Omega_{393} = 14.7\,\mathrm{MHz}$, $\Omega_{854} = 6.1\,\mathrm{MHz}$ and $\Delta_{393} = -16.4\,\mathrm{MHz}$.

utilize the 866 nm dark resonance spectroscopy to find good starting parameters for a further optimization.

The 854 nm dark resonance spectroscopy involves mainly the $S_{1/2}$, $P_{3/2}$ and $D_{5/2}$ states. Due to the decay on the 850 nm transition into the $D_{3/2}$ state the 866 nm laser is required to re pump the population. The 393 nm fluorescence from the $P_{3/2}$ decay is measured and fitted with twelve level Bloch equations to determine the detunings of the 393 nm and 854 nm laser (two examples see Figure 4.4). The 850 nm decay is neglected in the model to reduce the evaluation time. The effect of this simplification on the extracted laser detunings is smaller than the difference between consecutive measurements with the same 393 nm and 854 nm parameters.

Pulsed spectroscopies

Compared to the dark resonance spectroscopy that is done with a continuous laser excitation, in a pulsed spectroscopy the laser that probes the transition is applied for a short time. Afterwards one measures how often the probed transition was excited. With the 729 nm spectroscopy the frequencies of individual quadrupole transitions between the $S_{1/2}$ and $D_{5/2}$ Zeeman levels are measured. The magnetic dipole transition between both Zeeman levels in the $S_{1/2}$ ground state is measured with a radio frequency spectroscopy. With a 854 nm spectroscopy I measure the detuning of the 854 nm laser compared to the calcium transition. For the 729 nm or radio frequency spectroscopy, the ion is prepared in one of the $S_{1/2}$ Zeeman levels. In case of the 854 nm spectroscopy, the ion is prepared in one of the $D_{5/2}$ Zeeman levels. After the state preparation, the probe pulse is applied. Finally, the state of the ion is measured with fluorescence detection.

Pulse area scans

To calibrate the pulse area $\Omega\tau$ of a 729 nm or radio frequency pulse, either the pulse duration τ or the Rabi frequency Ω of the pulse is scanned. The latter is done by scanning the amplitude of the radio frequency that is applied to the acousto-optic modulator that switches the laser pulse. A Rabi oscillation is measured to infer parameters for a π-pulse, a $\frac{\pi}{2}$-pulse, or a pulse with arbitrary pulse area. Although pulse duration and pulse amplitude scans are in principal exchangeable, pulse amplitude scans are of more practical use due to the fixed pulse duration. This ensures constant timings in the measurement sequence, which is crucial in many experiments to have constant phase offsets due to the Larmor precession. Therefore, in the experiments presented in the later chapters, I calibrate pulse areas exclusively with pulse amplitude scans. A typical chosen pulse duration is 5 µs for a π-pulse.

Ramsey phase scan

In a Ramsey phase scan, a balanced superposition between the $S_{1/2}$ Zeeman levels, between two $D_{5/2}$ Zeeman levels or between a $S_{1/2}$ Zeeman level and a $D_{5/2}$ Zeeman level is created with a $\frac{\pi}{2}$-pulse. After a waiting time τ and if needed additional shelving pulses, a second

$\frac{\pi}{2}$-pulse with phase ϕ with respect to the first pulse is applied. After this pulse the population in one of both energy eigenstates is measured. The population in this state oscillates with the phase ϕ between both pulses. The visibility of the oscillation is reduced if the coherence of the system is reduced as for example by magnetic field fluctuations (see next section). From the waiting time dependent visibility $V(\tau)$ one can determine the coherence time of the prepared superposition state [84]. An exemplary Ramsey phase scan as well as a series of phase scans for different waiting times are depicted in Figure 4.6. During a longer series of measurements a phase scan with a fixed waiting time, typically around $100\,\mu s$, monitors the coherence time if the experiment is susceptible to fast magnetic field noise.

4.3. Magnetic field control

During all experiments the magnetic field defines the quantization axis and by this sets the orientation of the dipole emission pattern (see Section 2.5.1). Thus the magnetic field axis sets which transitions are exited from a given direction and which transitions are observed. In most experiments, the magnetic field is aligned in direction of the HALOs. In this configuration the HALOs collect photons emitted on σ transitions. Photons emitted on π transitions are not collected. For the measurements presented in Section 6.2.3 and Section 6.2.4 the magnetic field was aligned in direction of the $90\,^\circ$ and $270\,^\circ$ view ports. In this configuration photons emitted on all transitions are collected with the HALOs.

Additionally, the magnetic field splits the Zeeman levels. It sets the energy splitting and by this the frequency of individual transitions. During all measurements a magnetic field of $2.86\,G$ is applied, which splits the Zeeman levels in the $S_{1/2}$ ground state by $8\,MHz$, the Zeeman levels in the $P_{3/2}$ state by $5.3\,MHz$, and the Zeeman levels in the $D_{5/2}$ state by $4.8\,MHz$. Fluctuations of the magnetic field change these energy splittings and thereby the transitions frequencies. This results in phase fluctuations in superposition states that reduce the coherence time of the generated state. Therefore a good control of the magnetic field strength is crucial.

Direction of the magnetic field

The dipole emission pattern is utilized to align the direction of the magnetic field. A circularly polarized laser parallel to the quantization axis excites only σ^+ or σ^- transitions depending on the chosen polarization. With the correct set of lasers this results in optical pumping into a dark state where no photons are scattered. By minimizing the scattered photons, the magnetic field can be aligned parallel to the circularly polarized laser beam. To change the direction of the magnetic field, the current through the coils mounted around the vacuum chamber and the polarization of the reference beam are alternately adjusted until optimal pumping is reached. If the polarization of the laser beam is known only the magnetic field direction is adjusted.

Two different combinations of laser beams are used depending on the magnetic field direction. To set the magnetic field in direction of the $90\,^\circ$ and $270\,^\circ$ view port, the $397\,nm$ laser and $866\,nm$ laser are used. The $397\,nm$ beam is set to circular polarization, which then results in

optical pumping to one the $S_{1/2}$ ground states. In this case the detected 397 nm fluorescence is minimized. The setup corresponds to the one needed for polarization dependent optical pumping as described in Section 4.1.2.

To set the magnetic field in direction of the HALO axis, the 397 nm laser cannot be used, as there are single photons detectors for 397 nm photons mounted in this direction. In this case a circularly polarized 854 nm laser pumps the ion into a dark state. Together with the 393 nm and 866 nm laser the ion is pumped to either the two outer left or outer right $D_{5/2}$ Zeeman sublevels. In this case the 393 nm fluorescence is minimized.

Slow drifts of the magnetic field

With slow drifts, I refer to drifts happening over the day on the timescale of a few minutes. Cause are changing ambient conditions in the laboratory, changing activities in the building or current changes in the magnetic field coils. These slow drifts change the frequency of transitions and by this reduce the efficiency of laser pulses and affect the phase of generated states. These drifts are eliminated with a feedback loop that contains the ion as sensor for the magnetic field strength. The magnetic field strength is measured with the transition frequency between the $S_{1/2}$ ground states. A deviation from the set point changes the current through a small compensation coil mounted in direction of the quantization axis. To calculate the necessary current change, the effect of this small coil was calibrated in advance. With this technique I keep the magnetic field at the desired value. As an example, Figure 4.5 shows the magnetic field deviation from the set point $B = 2.85807\,\text{G}$ over the course of three days. The values result from the feedback spectroscopies performed during spectrum measurements. It shows, that the magnetic field value is controlled to $\pm 200\,\mu\text{G}$ around the set point. The systems that control the slow and fast magnetic field drifts (next paragraph) are described in more detail in my master thesis [76]. Both controls relay on the possible automation with the new experimental control through HYDRA-II.
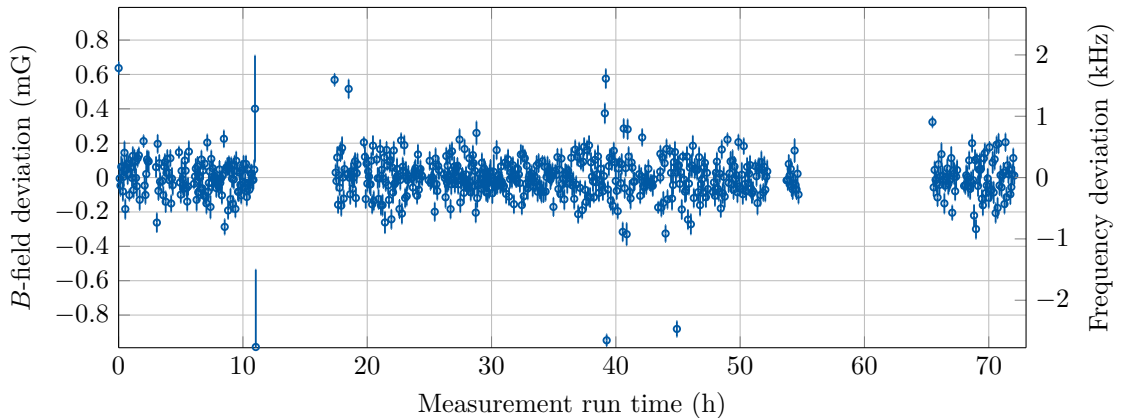
Figure 4.5.: Deviation of the magnetic field and corresponding transition frequency from the chosen set point. Periods without data points correspond to pauses during the measurement.

Fast drifts of the magnetic field

With fast magnetic field drifts, I refer to noise induced by the 50 Hz power grid. These drifts are addressed with a feed forward control. A phase looked loop generates a clock signal that is phase-stable to the power grid. A compensation signal is generated with this clock signal and applied to the compensation coil. Because the clock signal is generated from the power grid, it covers the small deviations from 50 Hz happening in the power grid frequency. The feed forward signal is optimized by changing phase and amplitude of the frequency components so that the coherence time of a superposition prepared in the $S_{1/2}$ or $D_{5/2}$ manifold is maximized. Typically, the compensation signal contains a 50 Hz and 150 Hz component. Other components show no positive effect on the measured coherence time. Due to different energy splittings between the Zeeman levels of the $S_{1/2}$ and $D_{5/2}$ state, some superpositions are more sensitive to magnetic field fluctuations and therefore the coherence time depends on the prepared superposition. This is utilized in the optimization process. To find new feed forward parameters, a first optimization is done with a $|S_{1/2}, \pm\frac{1}{2}\rangle$ superposition. In a second iteration, the three times more sensitive $|D_{5/2}, \pm\frac{5}{2}\rangle$ superposition is prepared, to further improve the feed forward control. The effect of this feed forward compensation is shown in Figure 4.6 with Ramsey fringe visibilities, measured for different waiting times and a $|S_{1/2}, \pm\frac{1}{2}\rangle$ superposition with and without feed forward control. The coherence time could be increased from about 15 µs to 250 µs. This corresponds to the typically reached improvements from about 10-50 µs coherence time without feed forward control to 200-500 µs coherence time with feed forward control.

During a longer measurement the coherence time is measured repeatedly and if the coherence time drops, a feed forward optimization is done. Usually the longest coherence times are reached during nighttime and over the weekend. Daily at around 6 o'clock in the morning and evening
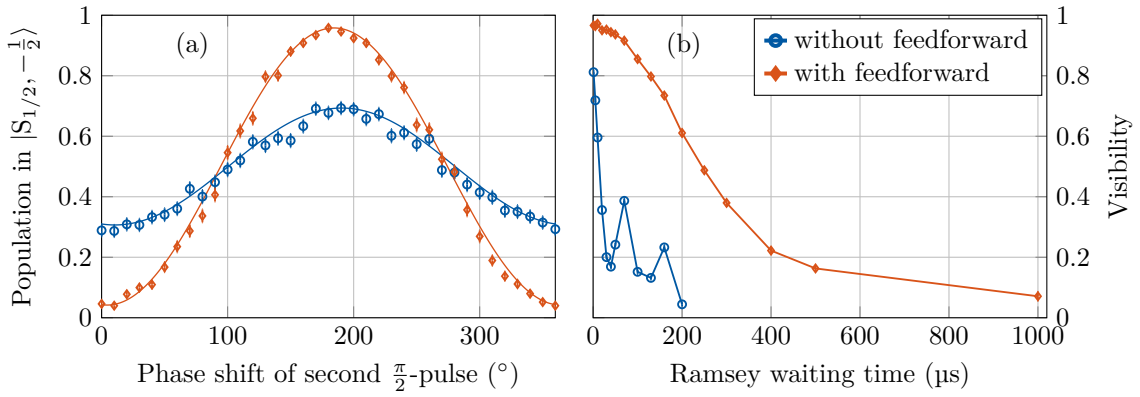
Figure 4.6.: Phase scan for a waiting time of 70 µs (left) and visibilities determined from equivalent phase scans for different waiting times (right). With the feed forward compensation the coherence time can be improved by a factor larger than 10. The dips in the Ramsey measurement that are caused by oscillating fields [57] are reduced significantly by the feed forward compensation.

the absolut magnetic field and the fast fluctuations changed the most. These observations were accounted for in the measurement time schedule if possible. Measurements that are more sensitive to magnetic field fluctuations were done on the weekend or during nighttime.

Note that both described methods to address slow and fast magnetic field drifts cover a specific frequency range. Fast fluctuations unrelated to the 50 Hz power grid are not compensated with the described method. Despite this, both methods implemented by myself helped to increase the absolute stability and the coherence time significantly. Nevertheless a passive stability is always preferable. Although the achieved values are sufficient for the experiments performed in this work, a longer coherence time is needed for future experiments. To achieve this, a passive shielding around the trap is build by my colleagues [66]. Also the coils to generate the magnetic field are replaced by permanent magnets [65].

4.4. Background correction

During measurements with single photons not only photon events but also background events are detected. By shielding the relevant optical paths and performing measurements in a dark laboratory the back ground events are drastically reduced. The remaining background events are detector dark counts, which are eliminated with ideal detectors. To predict the performance of the system with ideal detectors without any dark counts, a background correction is done. The idea of the background correction is to subtract the expected background events B from the measured events C in the signal window to obtain the signal events S. In case of a small number of events, this may lead to a negative number of signal events what is obviously not possible. Therefore a slightly different approach than simple subtraction is chosen. This approach takes the underlying distribution of the background and signal events into account [58]. For a number of C detected events, one calculates the probability for all possible combinations of S signal events and $B = C - S$ background events. To calculate the probabilities for both the signal and background events Poisson distributions are assumed. From the resulting probability distribution, the background corrected signal events S_{corr} are calculated as the expectation value of the distribution.

To infer the expected dark count events the detection time window is divided into smaller regions (see Figure 4.7). The expected background is calculated from time windows where no signal events occur before the emission process started and long after the emission process terminated (red). From the number of background events B_{bgr} and the duration τ_{bgr} of the time windows, the dark count rate r_{bgr} is calculated. With the dark count rate one calculates the expected dark count events B_{sig} in the time window where signal events are expected (yellow). From the dark count events B and the detected events C one calculates the background corrected signal events S_{corr}. A background correction to time bins, frequency bins or phase bins is done analogously.

Such a dark count correction is done for all measurements involving 393 nm photons. No background correction was performed for the 854 nm measurements because superconducting single photon detectors with negligible dark counts were available for these measurements.
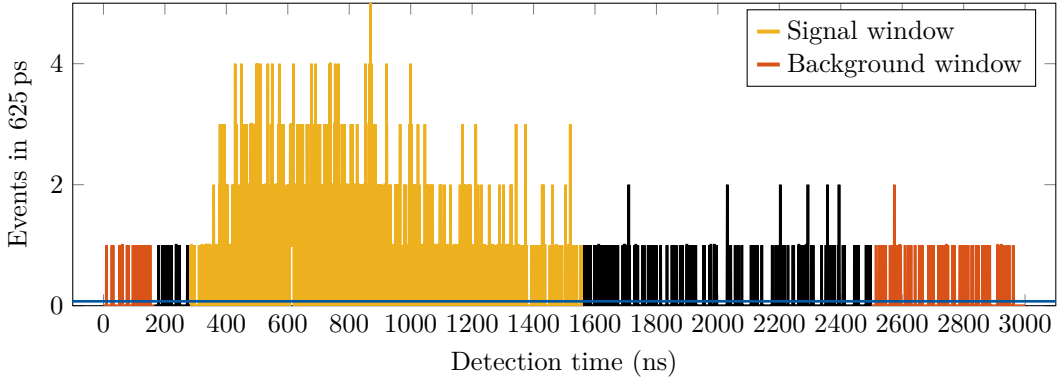
Figure 4.7.: Wave packet from the 393 nm atom-photon entanglement in Section 7.2.2 with windows for the dark count correction. The horizontal blue line indicates the expected dark count level per 625 ps time bin (0.072). One obtains: $B_{\text{bgr}} = 72$, $\tau_{\text{bgr}} = 665$ ns, $r_{\text{bgr}} = 1.93$ Hz, $B_{\text{sig}} = 148$, $C = 1291$, $\tau_{\text{sig}} = 1280$ ns, $S_{\text{corr}} = 1143$.

4.5. Spectrum measurements

4.5.1. Measurement protocol

To measure the spectrum of a generated Raman photon, I scan the analysis cavity and count the number of transmitted photons for each frequency point. I run a measurement schedule with all necessary calibration measurements, monitor measurements and the photon generation sequence that can be divided into four blocks (see Figure 4.8).

(1) Recall transition frequencies: I reset all transition frequencies to previously measured values. This ensures a clean restart, if a spectroscopy failed during a previous iteration of the measurement schedule.

(2) Preparation measurements: I measure the frequency of all excited 729 nm transitions. Afterwards I calibrate π- and $\frac{\pi}{2}$-pulses with the obtained frequencies. A 854 nm spectroscopy completes the preparation measurements.

(3) Spectrum measurement: A loop scans the analysis cavity. For each frequency point the photon generation sequence is executed (line 24). The loop contains a feedback to the magnetic field (lines 19-23) that is performed about once every five minutes. The radio frequency spectroscopy of the $S_{1/2}$ ground state transition therein acts as further monitor tool.

(4) Monitor measurement: The last block contains a 854 nm dark resonance spectroscopy to calibrate the 854 nm and 393 nm line centers and monitor the 393 nm laser.

I repeat the described schedule several times, with an alternating scan direction of the analysis cavity to acquire integration time almost parallel for all frequency points. I set the run time of a

```
1  %% (1) Recall transition frequencies
2  ion.trans729(6).freq = -12.4341; % |S_{1/2}, m=+1/2⟩ → |D_{5/2}, m=-3/2⟩
3  ion.trans729(1).freq = -9.2290;  % |S_{1/2}, m=-1/2⟩ → |D_{5/2}, m=-5/2⟩
4  ion.RFC.freq = 8.003;
5
6  %% (2) Preparation measurements
7  [...] = radio_frequency_spectroscopy (...);
8  compensate_magnetic_field_drift (...);
9  [...] = radio_frequency_spectroscopy (...);
10 compensate_magnetic_field_drift (...);
11 [...] = 729nm_spectroscopy(trans=6 ,...);
12 [...] = 729nm_spectroscopy(trans=1 ,...);
13 [...] = 729nm_pulse_amplitude_scan(trans=1 ,...);
14 [...] = 854nm_spectroscopy (...);
15
16 %% (3) Spectrum measurement
17 for k = 1:length(cavity_detuning)
18     set_cavity_to_detuning(cavity_detuning(k));
19     if rem(k,5) == 0
20         ion.RFC.freq = 8.003; % ≙ B ≈ 2.86 G
21         [...] = radio_frequency_spectroscopy (...);
22         compensate_magnetic_field_drift (...);
23     end
24     [...] = photon_generation_sequence (Δ, Ω, τ ,...)
25 end
26
27 %% (4) Monitor measurement
28 [...] = 854nm_dark_resonance_spectroscopy (...)
```

Figure 4.8.: Schedule to measure a Raman photon spectrum. The cavity detuning is set to the next frequency in line 18. Afterwards the photon generation sequence is executed (line 24).

single iteration of the full schedule to about one hour by adjusting the repetitions in the photon generation sequence. This run time provides a good balance between unwanted overhead and robustness against disruptions.

This schedule is executed to measure the spectra of 393 nm Raman photons generated from an energy eigenstate in the $D_{5/2}$ manifold. If a superposition is prepared or the spectrum of a 854 nm photon is measured the schedule contains more calibration measurements for additional 729 nm pulses. I execute a similar schedule to measure atom-photon entanglement (see Section 4.6.1). Therein, I set different projection bases instead of frequencies of the analysis cavity.

4.5.2. Pulse sequences for photon generation

I execute three different pulse sequences to generate Raman photons: two for 393 nm photons and one for 854 nm photons. To generate a 393 nm photon, the ion is prepared in the $D_{5/2}$ manifold and excited into the $P_{3/2}$ state with an 854 nm pulse. A 393 nm photon is emittted and the ion returns in the into the $S_{1/2}$ ground state. To generate 854 nm photons, the roles of
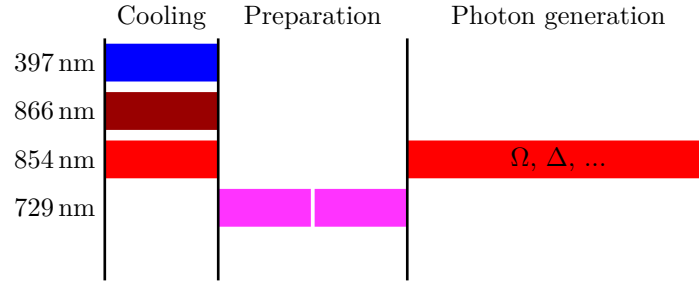
Figure 4.9.: Pulse sequence to generate 393 nm photons without optical pumping. Depending on the prepared initial state, the sequence contains one or two 729 nm pulses.

the initial $D_{5/2}$ and final $S_{1/2}$ state of the 393 nm photon generation are exchanged. A 393 nm pulse excites the ion from the $S_{1/2}$ ground state into the $P_{3/2}$ state. The ion emits a 854 nm photon on the decay into the $D_{5/2}$ manifold.

393 nm photon generation without optical pumping

The first pulse sequence (see Figure 4.9) to generate 393 nm photons is executed if the magnetic field is aligned in direction of the HALO axis.

Cooling: The pulse sequence starts with a Doppler cooling period with the 397 nm, 866 nm and 854 nm laser. The 854 nm laser brings population from the $D_{5/2}$ manifold back into the $S_{1/2}$ manifold. Because there is no fluorescence detection in the pulse sequence that heats the ion a short Doppler cooling period of 1 µs to 2 µs is sufficient to hold the ion at the temperature reached by longer Doppler cooling periods during idle times.

Preparation: After Doppler cooling, the initial state of the ion is prepared with one or two 729 nm pulses. The detuning, Rabi frequency and phase of both pulses are set to address individual 729 nm transitions and to control the phase of a created superposition. If both pulses transfer population from the same $S_{1/2}$ Zeeman level to the $D_{5/2}$ manifold a superposition is prepared. If population from both $S_{1/2}$ Zeeman levels is brought into the $D_{5/2}$ manifold, a mixed state is prepared. A single 729 nm pulses is applied to initialize the ion in a single Zeeman level of the $D_{5/2}$ manifold.

Photon generation: After the ion is prepared in the $D_{5/2}$ levels, a vertically polarized 854 nm pulse is applied perpendicular to the magnetic field. The frequency, power, pulse shape and phase of the pulse are adjusted to generate Raman photons with different properties. Arbitrary modulations as for example a bichromatic laser pulse are possible. Except for the measurements in Section 6.1.3, I set the duration of the pulse to generate the full photon wave packet.

The pulse sequence contains no optical pumping, as optical pumping can only be performed with the 729 nm laser, if the magnetic field is aligned in direction of the HALO axis. The optical pumping would slow down the sequence repetition rate by a factor of five to twenty, depending

on the parameters of the individual pulses, with the only advantage that the full population is initialized in either of the $S_{1/2}$ Zeeman levels. Without optical pumping the ion is initialized in a mixed state with about 65 % of the population in the $|S_{1/2}, -\frac{1}{2}\rangle$ state. The reduced efficiency, if only this population is transferred into the $D_{5/2}$ manifold, is compensated by the larger repetition rate without optical pumping, so that in total a higher photon generation rate is achieved. The population that remains in the $S_{1/2}$ ground state has no effect on the photon generation. If population from both $S_{1/2}$ Zeeman levels is transferred into different $D_{5/2}$ Zeeman levels, an imbalanced mixed state is created. With this, I measure the spectrum of photons created from a mixture between the $|D_{5/2}, -\frac{5}{2}\rangle$ and $|D_{5/2}, +\frac{5}{2}\rangle$ Zeeman levels. The spectrum of these photons is the same as the spectrum of photons created with the similar atom-photon entanglement sequence. However, the atom-photon entanglement sequence requires optical pumping, as a balances superposition between the $|D_{5/2}, -\frac{5}{2}\rangle$ and $|D_{5/2}, +\frac{5}{2}\rangle$ Zeeman level is required as initial state.

The described pulse sequence runs with a maximal repetition rate up to 200 kHz, depending on the duration of the involved pulses. This repetition rate reduces due to the power stabilization of laser pulses, the saving of the measured data and waiting times where the chopper is closed (closed 30 % of all times). External overhead in the measurement schedule further reduces the repetitions rate. All together, I generate photons with an average repetition rate of 40 kHz to 100 kHz over the course of a single iteration from the measurement schedule described above.

393 nm photon generation with optical pumping

If the magnetic field is aligned in direction of the 90 ° and 270 ° view port, I execute a sequence that contains polarization selective optical pumping with the 397 nm and 866 nm laser (see Figure 4.10). The rest of the pulse sequence is the same as for the previous sequence. The optical pumping with a circularly polarized 397 nm laser initializes the ion in the $|S_{1/2}, -\frac{1}{2}\rangle$ state. Thus, a different 397 nm laser beam is required for Doppler cooling. Due to the optical pumping all population is initialized in the $|S_{1/2}, -\frac{1}{2}\rangle$ state and the photon generation efficiency is increased compared to the previous sequence. The additional pumping time of 3 μs has no significant influence on the sequence repetition rate. With this sequence, I measured the spectra presented in Section 6.2.3 and Section 6.2.4.
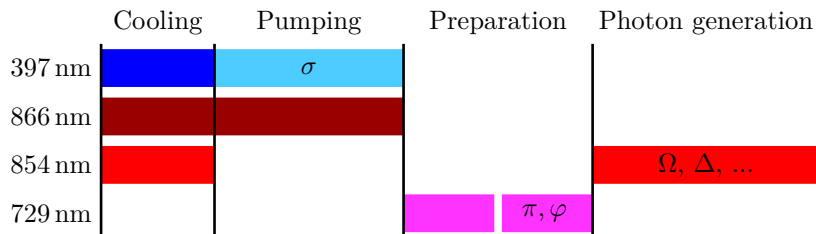
Figure 4.10.: Pulse sequence to generate 393 nm photons with optical pumping. I execute this pulse sequence always with two 729 nm pulses.
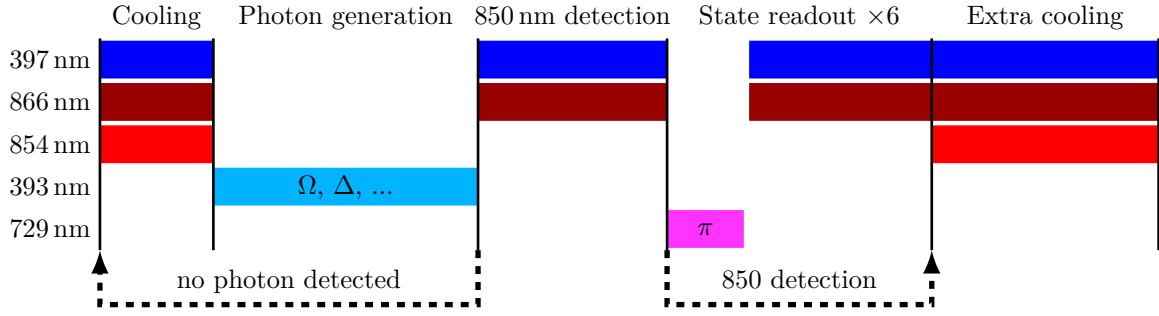
Figure 4.11.: Pulse sequence to generate 854 nm photons. The state detection measures the population in each $D_{5/2}$ Zeeman level.

854 nm photon generation

The pulse sequence to generate 854 nm photons is affected by the small branching ratio $\frac{\Gamma_{854}}{\Gamma} = 0.059$ of the 854 nm decay compared to $\frac{\Gamma_{393}}{\Gamma} = 0.935$ for the 393 nm decay. Thus a decay back into the initial state happens much more frequently, than the scattering of a 854 nm photon. As a consequence, any pure state initialized in the $S_{1/2}$ ground state becomes a mixed state before the Raman photon is scattered. Thus the photon generation is done from a mixed state without optical pumping. The second difference to the 393 nm sequences is a state detection to distinguish different 854 nm decay channels. The pulse sequence is as follows (see Figure 4.11):

Cooling: The pulse sequence starts with a short Doppler cooling period with the 397 nm, 866 nm and 854 nm laser. The 854 nm laser pumps all population from the $D_{5/2}$ manifold back into the $S_{1/2}$ ground state.

Photon generation: Afterwards a 393 nm pulse is applied to scatter the 854 nm photon. The parameters of the pulse (Rabi frequency, detuning, pulse shape) are set to generate photons with different properties. If a 854 nm photon was detected, atomic state detection is done. Otherwise, the next sequence repetition is started with Doppler cooling.

850 nm detection: In the state analysis, I first exclude a possible 850 nm decay by probing the population in the $D_{3/2}$ state with fluorescence detection.

State readout: Then, I measure the population in the $D_{5/2}$ Zeeman levels. I transfer the population in the probed $D_{5/2}$ level to the $S_{1/2}$ state with a 729 nm π-pulse and perform fluorescence detection. In all cases, the state detection is stopped after the first bright decision as a bright decision projects the ion to a mixed $S_{1/2}$ state. Up to six fluorescence detection are done to probe the population in all $D_{5/2}$ Zeeman levels.

Extra cooling: After the state detection an additional longer Doppler cooling period removes the vibration quanta induced by the fluorescence detection from the ion.

With this pulse sequence 854 nm photons are generated with a maximal repetition rate of 81 kHz, given mainly by the duration of the 393 nm pulse. Due to additional overhead, the average repetition rate during the spectrum measurement drops to 35 kHz to 60 kHz.

4.5.3. Evaluation

Goal of the evaluation is to calculate the expected spectrum from the model presented in Chapter 5. I determine the required model parameters from calibration measurements, settings during the measurement, and the measured wave packet. In detail, the following parameters are required:

- the parameters of the excitation laser pulse (Rabi frequency Ω, detuning Δ, polarization, pulse shape, ...),

- the frequency axis of the scattered photon,

- the position and strength of visible side bands,

- the observed atomic transitions

- and the transfer function of the analysis cavity.

In the following paragraphs I guide through the evaluation of a 393 nm Raman photon spectrum. The evaluation of a 854 nm Raman photon spectrum is analog with exchanged roles of the 854 nm and 393 nm transition.

Frequency calibration

The first step in the evaluation is to determine the line centers of the 854 nm and 393 nm laser during the spectrum measurement. I determine both values as average from all measured 854 nm dark resonance spectroscopies. From the 393 nm line center, I calculate the detunings $\Delta_{393,\mathrm{m}}$ of the analysis cavity with respect to the 393 nm transition with

$$\Delta_{393,\mathrm{m}} = \Delta_{\mathrm{cav}} - \Delta_{\mathrm{LC},393}, \tag{4.3}$$

where Δ_{cav} are the detunings of the reference laser of the analysis cavity and Δ_{LC} is the measured 393 nm line center. In some measurements, the 393 nm detuning is displayed with respect to an individual transition of the ion ($\Delta_{393,\mathrm{t}}$). In this case, the shift of this transitions has to be taken into account. As example, for a magnetic field of $B = 2.86\,\mathrm{G}$ the $|\mathrm{P}_{3/2}, -\frac{3}{2}\rangle$ to $|\mathrm{S}_{1/2}, -\frac{1}{2}\rangle$ transition shifts by $-4\,\mathrm{MHz}$ with respect to the line center. Thus one gets $\Delta_{393,\mathrm{t}} = \Delta_{393,\mathrm{m}} + 4\,\mathrm{MHz}$ for the 393 nm frequency axis.

With the 854 nm line center $\Delta_{\mathrm{LC},854}$, I calculate the detuning $\Delta_{854,\mathrm{m}}$ of the applied 854 nm laser pulse with respect to the transition line center. As for the 393 nm detunings in some cases, the detuning with respect to a single atomic transition is of interest. In this case, the shift of the transition has to be taken into account. As example, for the magnetic field of $B = 2.86\,\mathrm{G}$ the $|\mathrm{D}_{5/2}, -\frac{5}{2}\rangle$ to $|\mathrm{P}_{3/2}, -\frac{3}{2}\rangle$ transition is shifted by $+4\,\mathrm{MHz}$. Consequently, the laser detuning with respect to this transition becomes $\Delta_{854,\mathrm{t}} = \Delta_{854,\mathrm{m}} - 4\,\mathrm{MHz}$. However, in all cases the model is calculated with the detunings $\Delta_{393,\mathrm{m}}$ and $\Delta_{854,\mathrm{m}}$ with respect to the line centers, because the model takes all atomic levels into account.

Rabi frequency Ω and pulse shape

The second important model parameter is the Rabi frequency of the applied laser pulse. I determine the Rabi frequency $\Omega_{854,\mathrm{m}}$ from the photon wave packet measured together with the spectrum. I fit the wave packet with twelve level optical Bloch equations that take possible modulations as for example a bichromatic laser pulse into account. The 854 nm detuning $\Delta_{854,\mathrm{m}}$ is fixed at the value obtained from the frequency calibration. As additional parameters I determine the rise and fall time of the laser pulse. Especially for larger Rabi frequencies, what corresponds to shorter wave packets, the rise time has a significant influence on the spectrum of the scattered photon. As for the detuning, in some cases, the Rabi frequency on individual transition is of interest. I calculate the Rabi frequency $\Omega_{854,\mathrm{t}}$ from the fitted value $\Omega_{854,\mathrm{m}}$ considering the corresponding Clebsch-Gordan coefficient as well as the polarization and direction of the laser beam. For the above taken example of the $|\mathrm{D}_{5/2}, -\frac{5}{2}\rangle$ to $|\mathrm{P}_{3/2}, -\frac{3}{2}\rangle$ transition, the Clebsch-Gordan coefficient is $\sqrt{\frac{10}{15}}$. For a vertically polarized laser beam perpendicular to the magnetic field axis, the polarization results in an additional factor $\frac{1}{\sqrt{2}}$. Thus one gets $\Omega_{854,\mathrm{t}} = \sqrt{\frac{1}{3}}\Omega_{854,\mathrm{m}}$.

Other parameters

The other model parameters are given by the experimental setup. The collected transitions depend on the direction of the quantization axis and a possible polarization and state projection. The radial trap frequencies that determine the position of the sidebands (see Section 6.1.2) are measured with 729 nm spectroscopies. The transfer function of the analysis cavity setup is given by a convolution of the the line width and stability of cavity.

Model curve of the photon spectrum

I calculate the model curve in three steps. As first step, I calculate the spectrum of the scattered photon without sidebands with the parameters of the excitation laser ($\Delta_{854,\mathrm{m}}$, $\Omega_{854,\mathrm{m}}$, rise time, ...) and the collected transitions. I call this spectrum, the **ideal** spectrum. In the second step, I calculate the sidebands with the ideal spectrum as carrier. I shift the carrier by the sideband frequency to obtain the red and blue sideband. I introduce the parameter c_{sb} to describe the relative population in each side band compared to the carrier population. The three spectra, carrier and sidebands, are summed incoherently to obtain the spectrum that is emitted by the ion. I call this spectrum the **emitted** spectrum. The third step takes the transfer function of the analysis cavity into account. I calculate the **expected** spectrum as convolution of the emitted spectrum and the transfer function of the analysis cavity setup. This expected spectrum is the model curve shown in all measurements. I fit the model curve to the measured data with a scaling factor that corresponds to the one-shot detection efficiency ε of the setup for monochromatic photons emitted on-resonance of the cavity. For narrow spectra generated with a weak laser excitation, where the sidebands are separated from the carrier, I additionally fit the relative strength c_{sb} of the sidebands. The obtained value is taken for the other evaluations.

	$\Delta_{854,m}$	$\Delta_{854,t}$	$\Omega_{854,m}$	$\Omega_{854,t}$	c_{sb}	δ_b
(a)	$+3.5\,\text{MHz}$	$-0.5\,\text{MHz}$	$4.67(1)\,\text{MHz}$	$2.695(8)\,\text{MHz}$	$0.43(2)$	$-0.07(2)\,\text{MHz}$
(b)	$-7.4\,\text{MHz}$	$-11.4\,\text{MHz}$	$21.4(1)\,\text{MHz}$	$12.37(5)\,\text{MHz}$	0.44	$-0.2(2)\,\text{MHz}$
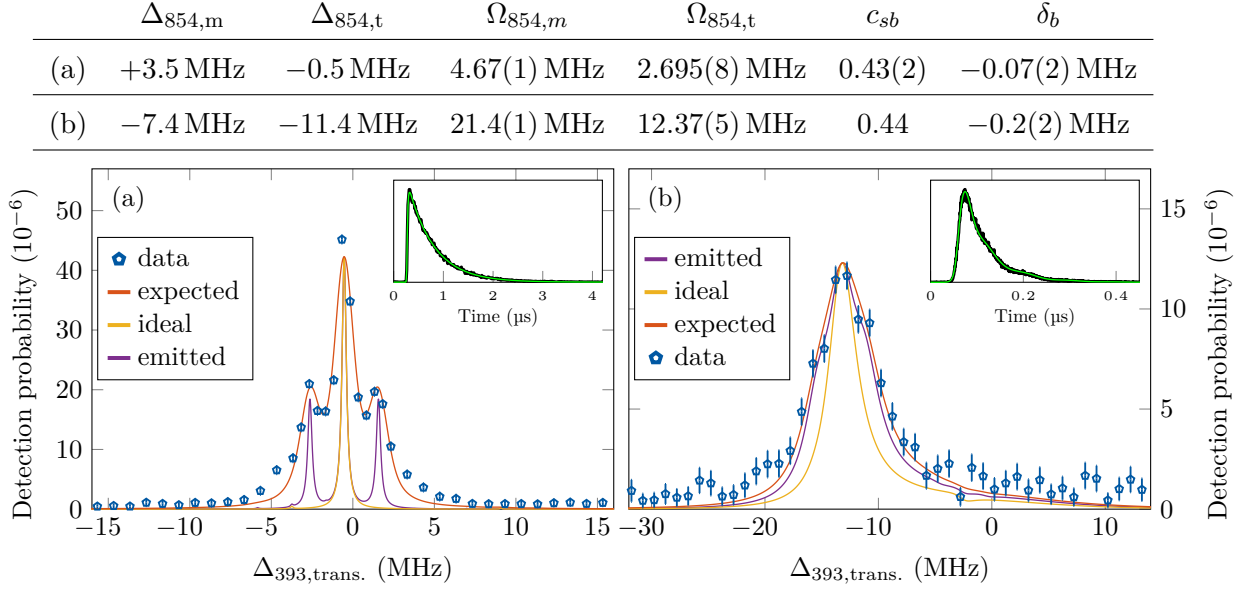
Figure 4.12.: Measured spectra and wave packets with model curves from $393\,\text{nm}$ Raman photons. The definitions of the **ideal**, **emitted** and **expected** spectrum are given in the text. The emitted and ideal spectrum are scaled to have the same maximum as the expected spectrum. The table contains the numeric values that were used to calculate the model curves. The relative strength c_{sb} of the side bands is fitted fitted for the spectrum in (a).

For the $393\,\text{nm}$ spectra I introduce an additional shift δ_b that is added to the $393\,\text{nm}$ detuning Δ_{393}. This shift accounts for the uncertainties in the line centers of the $854\,\text{nm}$ and $393\,\text{nm}$ transitions. I shift the $393\,\text{nm}$ detuning as I expect a bigger uncertainty in the $393\,\text{nm}$ line center compared to the uncertainty in the $854\,\text{nm}$ line center[5]. I fit the detuning δ_b to match the model to the measured data. I get shifts $|\delta_b| \leq 0.5\,\text{MHz}$ for many measured spectra (see Appendix C.1). This matches the expected uncertainty of the line centers obtained from the dark resonance spectroscopies. Larger shifts are attributed to uncompensated drifts during the measurement.

In Figure 4.12 I show two measured spectra (from Section 6.1.1) with model curves for the **expected**, **ideal** and **emitted** spectrum obtained by the evaluation. Additionally, I list the model parameters obtained during the evaluation.

---

[5]A shift δ_r added to the $854\,\text{nm}$ detuning shifts the spectrum approximately by the same amount. Additionally, the shape is slightly changed in this case. A shift δ_b of the $393\,\text{nm}$ laser and a shift δ_r of the $854\,\text{nm}$ laser compensate each other.
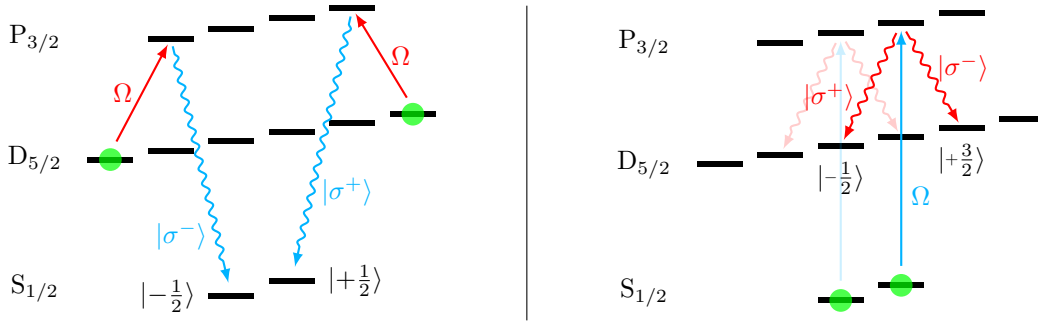
Figure 4.13.: Simplified schemes to create 393 nm (left) or 854 nm (right) atom-photon entanglement. One side of the mirror inverted 854 nm schemes is selected.

4.6. Generation and detection of atom-photon entanglement

In this work I implement the schemes in Figure 4.13 to create entangled atom-photon states of the form

$$|\Psi\rangle = \alpha(t)\,|\uparrow\rangle\,|\sigma^\uparrow\rangle + \beta(t)\,|\downarrow\rangle\,|\sigma^\downarrow\rangle\,, \tag{4.4}$$

where $|\uparrow\rangle$ and $|\downarrow\rangle$ denote two Zeeman levels of the $^{40}\text{Ca}^+$ ion. The photons scattered on the σ-transitions going into these Zeeman levels carry the polarization state $|\sigma^\uparrow\rangle$ and $|\sigma^\downarrow\rangle$ that translate into a $|\text{L}\rangle$ or $|\text{R}\rangle$ circularly polarized photon. The dependence of the coefficients $\alpha(t)$ and $\beta(t)$ on the scheme and the experimental realization is studied in Chapter 7.

In the next sections I guide through the experimental process to generate, detect and reconstruct the generated atom-photon states. I first present the executed pulse sequences that generates the atom-photon state and measures the required state projections. Afterwards, I discuss the atom and photon state projections that are required to reconstruct the density matrix of the atom-photon state. Finally, I present the algorithm for the quantum-state tomography that reconstructs the density matrix of the created atom-photon state from the measured state projections.

4.6.1. Measurement protocol and pulse sequences

The measurement protocol to generate and detect atom-photon entanglement is similar to the measurement protocol for spectrum measurements presented in Section 4.5.1. It contains preparation measurements to calibrate laser pulses and measurements to control experimental parameters as for example the magnetic field. The spectrum measurement block is replaced by a block where the atom-photon entanglement pulse sequence is executed with different projections of the polarization and atomic state. The central pulse sequence in this block is discussed below. As for the spectrum measurement, the schedule is iterated until the wanted integration time is reached.
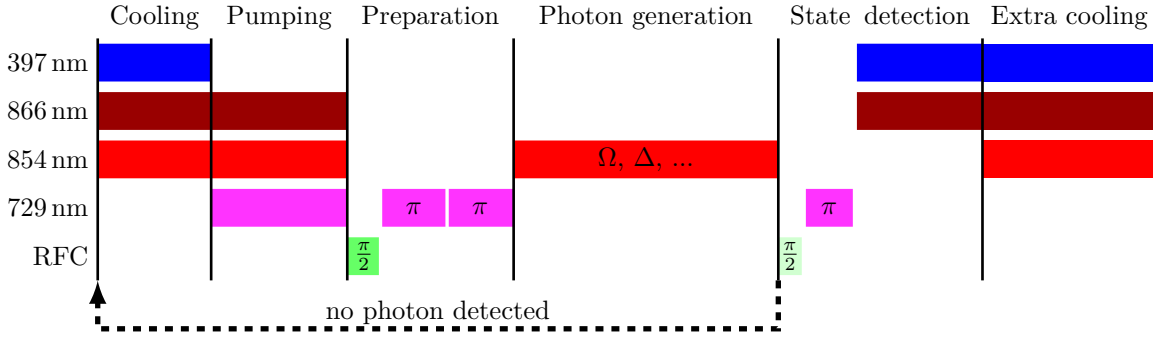
Figure 4.14.: Pulse sequence to generate and detect 393 nm atom-photon entanglement.

393 nm atom-photon entanglement generation

To generate and detect 393 nm atom-photon entanglement, I execute a pulse sequence with the following steps (see Figure 4.14):

Cooling and Pumping: The pulse sequence starts with 2 µs Doppler cooling followed by 30 µs frequency selective optical pumping with the 729 nm, 854 nm and 866 nm laser to initialize the ion in the $|S_{1/2}, -\frac{1}{2}\rangle$ state.

Preparation: Afterwards a 4 µs radio frequency pulse $\frac{\pi}{2}$-pulse creates a superposition in the $S_{1/2}$ ground state. This superposition is transferred to the $|D_{5/2}, -\frac{5}{2}\rangle$ and $|D_{5/2}, +\frac{5}{2}\rangle$ Zeeman levels with two 729 nm π-pulses of 2 µs and 3 µs duration.

Photon generation: To generate the 393 nm photon, I apply a monochromatic (2 µs) or bichromatic (3 µs) 854 nm pulse (details see Section 7.2.1 and 7.2.2).

State detection: If a 393 nm photon is detected, I project the atomic state. To project on the atomic superposition base I apply a 4 µs radio frequency $\frac{\pi}{2}$-pulse with phase θ. This pulse is skipped, if the atom is projected on the energy eigenstates. Afterwards, a 2 µs 729 nm π pulse maps the population from the projected states into the bright and dark manifold. The following fluorescence detection (70 µs) completes the state readout.

Extra cooling: To remove additional vibration quanta introduced by the fluorescence detection, I extend the Doppler cooling period by 70 µs if fluorescence detection was done. If no photon is detected the atomic state detection and the second Doppler cooling period are skipped.

The pulse sequence generates 393 nm photons at a maximal rate of 21 kHz. Due to additional overhead (mainly the chopper) the repetition rate slows down to an average repetition rate of 14 kHz during the measurement. This average rate does not includes any other slowdowns as for example measurements to control experimental parameters or coupling efficiencies.

I collect the generated 393 nm photons in direction of the magnetic field and send them through a polarization projection setup. The polarization projection setup consist of two parts. The first part contains three wave plates ($\frac{\lambda}{4} \rightarrow \frac{\lambda}{2} \rightarrow \frac{\lambda}{4}$) to compensate polarization changes induced

by components in the beam line in front of the projections setup. The second part contains two wave plates and a polarizing beamsplitter ($\frac{\lambda}{2} \rightarrow \frac{\lambda}{4} \rightarrow$ PBS) to project the photons on arbitrary polarization. I couple the photons transmitted through the polarizing beamsplitter into a single mode fiber and send them to the analysis cavity for spectral filtering (the reflection is discarded). With a D-shaped mirror a small fraction of the beam is cut out and coupled into a multi mode fiber for direct detection (see Figure 3.3). To calibrate the polarization compensation I generate 393 nm Raman photons from the $|D_{5/2}, -\frac{5}{2}\rangle$ state on the σ^- transition from the $|P_{3/2}, -\frac{3}{2}\rangle$ state into the $|S_{1/2}, -\frac{1}{2}\rangle$ state (see Section 4.5.2). The photons collected in direction of the magnetic field are therefore $|R\rangle$ polarized. I set the polarization projection to $|L\rangle$ and minimize the number of detected photons by turning the three compensation wave plates. A suppression off the wrong polarization detection to 1.4 % is reached.

854 nm atom-photon entanglement generation

To generate and detect 854 nm atom-photon entanglement, I execute a pulse sequence with the following steps (see Figure 4.15):

Cooling: The pulse sequence starts with Doppler cooling with the 397 nm, 866 nm and 854 nm laser. In contrast to the generation of 393 nm atom-photon entanglement, the initialization in a pure quantum state is not required.

Photon generation: To generate the 854 nm photon, I apply a horizontally polarized monochromatic (1.8 µs) or bichromatic (10 µs) 393 nm laser pulse perpendicular to the magnetic field (details see Section 7.3.1 and 7.3.2). This laser exclusively drives the π transitions. State analysis is done if a photon is detected. Otherwise, the next repetition of the pulse sequence is started with Doppler cooling.

Trash pumping: To ensure an empty $S_{1/2}$ state for the following operations, the population remaining in the $S_{1/2}$ ground state is pumped into the $D_{3/2}$ state with a 397 nm laser pulse. Afterwards a 729 nm pulse can be applied to bring population from one of the $D_{5/2}$ Zeeman levels to the ground state. A second 397 nm laser pulse pumps this population into the $D_{3/2}$ state. These two pulses to manipulate the population in the $D_{5/2}$ manifold are applied in the monochromatic scheme to compensate the Clebsch-Gordan coefficients of the 854 nm decay channels.

Projection: The atomic state analysis is started by defining the projection basis. If the atomic state is projected onto the energy eigenstates no projection pulses are applied. If the atomic state is projected on superposition states, two 729 nm π-pulses transfer the atomic superposition from the $D_{5/2}$ state into the $S_{1/2}$ ground state. A 5 µs long radio frequency $\frac{\pi}{2}$-pulse with phase θ sets the projection basis before a second pair of 729 nm π-pulses brings the projected superposition back into the $D_{5/2}$ state. To reduce the influence of magnetic field noise, the projection is done before the following "Trash detection".

Trash detection: To sort out all cases were a 850 nm photon or dark count was detected or population was removed from the $D_{5/2}$ manifold a first fluorescence detection (70 µs) is
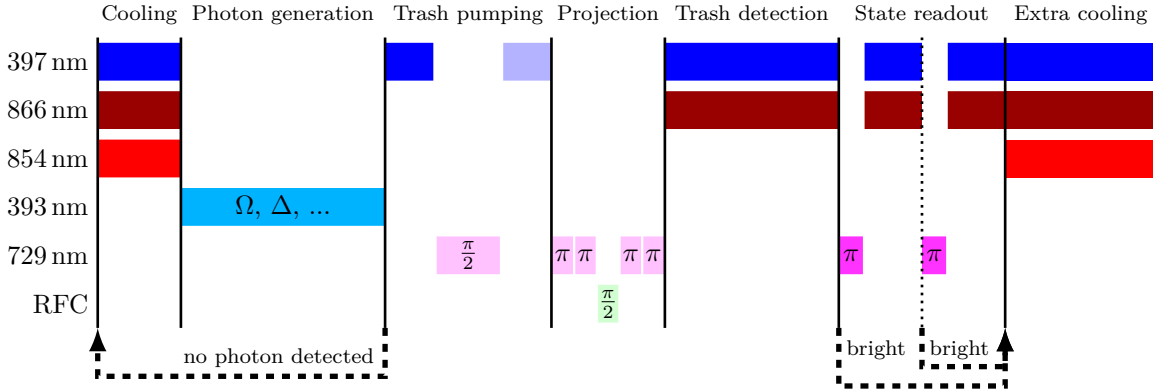
Figure 4.15.: Pulse sequence to generate and detect 854 nm atom-photon entanglement. The 729 nm pulse that balances the state population (Trash pumping) is only applied in the monochromatic scheme.

done. If the ion is found in the bright $D_{3/2}$ state, what means that one of the three mentioned cases happened, the remaining state analysis is skipped.

State readout: If the ion is not found in the $D_{3/2}$ state, the population in both projected atomic states is measured. The population in the respective state is transferred into the $S_{1/2}$ ground state with a 729 nm π-pulse before fluorescence detection (70 µs) is applied. The population in both states has to be measured to sort out photon events where an 854 nm photon was created in the "unwanted" scheme. If the ion is found in the first state, the read out of the second state is skipped. If none of the three fluorescence detection result in a bright ion, a 854 nm photon was created in the "unwanted" left scheme (see Figure 4.13). These unwanted 854 nm photon events are discarded.

Extra cooling: If fluorescence detection was done, an additional Doppler cooling period removes the induced vibration quanta from the ion.

All 729 nm pulses in the sequence have a duration of 10 µs. The duration of the Doppler cooling period and the 397 nm pump pulse duration is different in the monochromatic and bichromatic scheme. In the monochromatic scheme, the first Doppler cooling period and the duration of the 397 nm pulses to pump population into the $D_{3/2}$ state is set to 1 µs. The same pulses have a duration of 3 µs in the bichromatic scheme. The additional Doppler cooling after the fluorescence detection has a duration of 50 µs (monochromatic) respective 100 µs (bichromatic). In the monochromatic scheme, the pulse sequence generates 854 nm photons with a maximal sequence repetition rate of 236 kHz. Due to the state detection and other overhead this repetition rate slows down to an average repetition rate of 175 kHz over the whole measurement. In case of the bichromatic scheme, the longer pulses lead to a smaller maximal repetition rate of 62 kHz. Due to state detection and other overhead the repetition rate drops to an average repetition rate of 57 kHz in case of direct detected photons and 41 kHz in case of photons filtered by the cavity. In contrast to the 393 nm scheme the generated atom-photon state for directly

61

detected or cavity filtered photons are measured after each other.

The created 854 nm photons are collected anti parallel to the magnetic field and coupled into a single mode fiber. With the single mode fiber the photons are sent to the analysis cavity or to a polarization projection setup. If the photons are sent to the analysis cavity, the transmission of the cavity is sent to the polarization projection setup. The polarization projection is done with two wave plates and a Wollaston prism ($\frac{\lambda}{2} \to \frac{\lambda}{4} \to$ prism). In the monochromatic case, the polarization is projected with three different settings of the wave plates onto the three polarization bases $\{|R\rangle, |L\rangle\}$, $\{|H\rangle, |V\rangle\}$ and $\{|D\rangle, |A\rangle\}$, where the orthogonal polarization of the same basis are measured simultaneously at both outputs of the Wollaston prism. In this case, the detection efficiencies at both outputs of the Wollaston prism are balanced by inducing a loss in the more efficient arm. In the bichromatic case, the polarization is projected with six different settings of the wave plates onto the polarization $|R\rangle$, $|L\rangle$, $|H\rangle$, $|V\rangle$, $|D\rangle$ and $|A\rangle$. Both outputs of the Wollaston prism are detected and summed up in the evaluation. With this method, it is not necessary to adjust the efficiency of the two detector paths. During the measurement polarization drifts are monitored and controlled with a reference beam that is coupled into the same single mode fiber on the ion table. Polarization drifts are compensated with a manual paddle-fiber-polarization-controller at the fiber going to the polarization projection setup.

4.6.2. Atom and photon state projection

To project the generated atom-photon state, the polarization of the generated photon is projected onto the six polarization states $|R\rangle$, $|L\rangle$, $|H\rangle$, $|V\rangle$, $|D\rangle$ and $|A\rangle$. If a photon is detected the atomic state is projected onto the energy eigenbasis (Z) or two superposition bases (X and Y). The projection onto the energy eigenstates $|\uparrow\rangle$ and $|\downarrow\rangle$ does not require additional projection pulses, but only pulses to bring the population into the bright $S_{1/2}$ and dark $D_{5/2}$ manifold. To project the atom onto the superposition basis, the atomic superposition states $|+\rangle$ and $|-\rangle$ (X-basis) respectively $|+i\rangle$ and $|-i\rangle$ (Y-basis) are mapped into the bright and dark state before fluorescence detection is done. A radio frequency $\frac{\pi}{2}$-pulse with phase θ maps the superposition state, where θ defines the phase of the superposition state that is mapped into the bright and dark state (see below). Additional 729 nm π-pulses for shelving complete the state projection.

Projection with two phases in separate iterations

To derive the atomic superposition state that is mapped into the bright or dark manifold I consider the superposition state

$$|\Psi\rangle = \frac{1}{\sqrt{2}} \left(|\uparrow\rangle + e^{i\phi} |\downarrow\rangle \right), \tag{4.5}$$

where the phase ϕ defines the superposition state (see Section 2.4). A $\frac{\pi}{2}$-pulse with phase θ is applied for projection. After this projection pulse, the population P in the energy eigenstates depends on the phase ϕ of the superposition state and the phase θ of the applied projection

pulse. With Equation 2.18 one finds for the population in the energy eigenstates

$$P_{|\uparrow\rangle} = \frac{1}{2}\left(1 + \sin(\phi - \theta)\right) \qquad \text{and} \qquad P_{|\downarrow\rangle} = \frac{1}{2}\left(1 - \sin(\phi - \theta)\right). \qquad (4.6)$$

The maximum of this function gives the superposition state that is mapped into the energy eigenstates for a projection pulse with phase θ. A projection pulse with phase θ maps the atomic superposition with phase $\phi = \theta + \frac{\pi}{2}$ into the state $|\uparrow\rangle$. The perpendicular state is mapped into the state $|\downarrow\rangle$. For an increasing projection phase θ this corresponds to the order

$$\cdots \rightarrow \ |+\rangle \ \rightarrow \ |+\mathrm{i}\rangle \rightarrow \ |-\rangle \rightarrow \ |-\mathrm{i}\rangle \rightarrow \ |+\rangle \ \rightarrow \cdots \qquad (4.7)$$

of the superposition states, that are mapped into the state $|\uparrow\rangle$ and $|\downarrow\rangle$ (shifted by 180°). If a projection pulse with phase θ_x projects the atomic state on the X-basis, then a projection pulse with phase $\theta_y = \theta_x + 90\,^\circ$ projects the atomic state on the Y-basis.

In the bichromatic atom-photon entanglement schemes, I search the phase θ_1 of the projection pulse that transfers a maximum of population into one of the energy eigenstates for a chosen polarization projection. I assign a name to the projected atomic superposition state. To find the phase, I project the generated photons to a linear polarization and measure the population in the energy eigenstates $|\uparrow\rangle$ and $|\downarrow\rangle$ for a scanned phase θ of the projection pulse. For the 393 nm atom-photon entanglement, I project the photon polarization to $|A\rangle$ and assign the name $|+\mathrm{i}\rangle$ to the superposition state, that is mapped into $|S_{1/2}, +\frac{1}{2}\rangle$ (see Figure 4.16 (a)). In case of the 854 nm atom-photon entanglement I project the photon polarization to $|V\rangle$ and assign the name $|+\rangle$ to the superposition state, that is mapped into the $|D_{5/2}, -\frac{1}{2}\rangle$ state (see Figure 4.16 (b)). The chosen linear polarization and the name of the assigned atomic superposition states are arbitrary but affect the phase of the reconstructed density matrix[6].
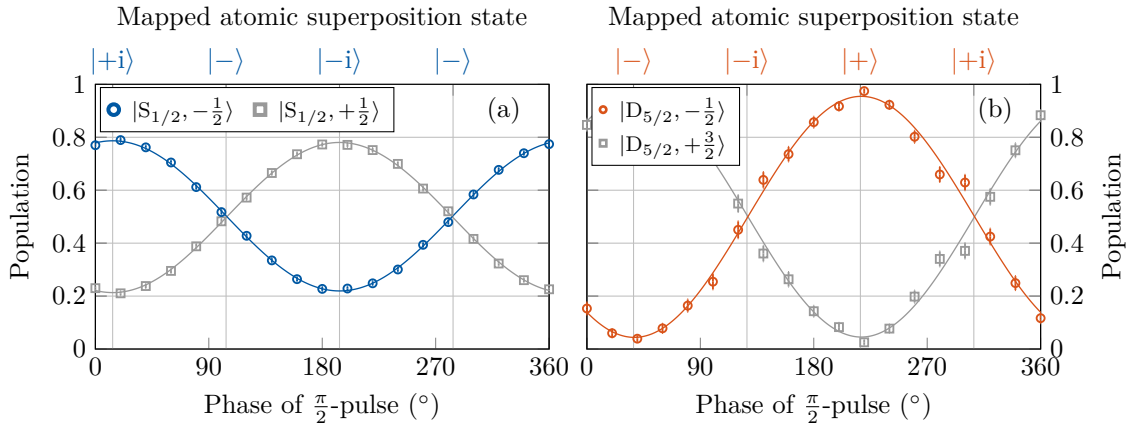
Figure 4.16.: Atomic superposition state that is mapped by the projection pulse (colored). The perpendicular state is mapped in the respective other energy eigenstate (gray). (a) 393 nm and (b) 854 nm atom-photon entanglement.

---

[6]I assign the superposition state that has the same "form" as the polarization used in the callibration measurement (see Section 2.4).

In case of the 393 nm atom-photon entanglement, the visibility of the fringe is reduced because the calibration was done with unfiltered photons what corresponds to a partially entangled atom-photon state (see Section 7.2.2). From a fit the phases $\theta_1 = 13.7\,^\circ$ is found to map the the state $|+i\rangle$ into the state $|S_{1/2}, +\frac{1}{2}\rangle$. From this follows the second phase $\theta_2 = 103.7\,^\circ$ that maps the state $|-\rangle$ into the state $|S_{1/2}, +\frac{1}{2}\rangle$. The population of the perpendicular superposition states are found in the dark state. For the 854 nm atom-photon entanglement the fringe has a higher visibility as the calibration measurement was done with cavity filtered photons what corresponds to a maximally entangled state (see Section 7.3.2). The projection phases $\theta_1 = 217\,^\circ$ and $\theta_2 = 307\,^\circ$ are found to map the population from the superposition states $|+\rangle$ respective $|+i\rangle$ into the $|D_{5/2}, -\frac{1}{2}\rangle$ state. Before the phase calibration for the 854 nm atom-photon entanglement is done, the relative strength of both frequency components of the bichromatic laser are calibrated to obtain an atom-photon state with balanced components (see Section 7.1 and Figure 7.7).

Projection of a detection time dependent superposition

In case of a detection time dependent superposition state

$$|\Psi\rangle(t) = \frac{1}{\sqrt{2}}\left(|\uparrow\rangle + e^{i(\phi + \varphi(t))}|\downarrow\rangle\right), \tag{4.8}$$

one can utilize the time dependence $\varphi(t)$ to determine the projections onto different atomic superpositions. Analog to the the previous case, after the projection pulse with phase θ the population

$$P_{|\uparrow\rangle} = \frac{1}{2}\left(1 + \sin(\phi + \varphi(t) - \theta)\right) \qquad \text{respective} \qquad P_{|\downarrow\rangle} = \frac{1}{2}\left(1 - \sin(\phi + \varphi(t) - \theta)\right) \tag{4.9}$$

is found in the energy eigenstates. Thus, the population that is mapped into the energy eigenstates has the same detection time dependence on the phase $\varphi(t)$ as the superposition $|\Psi\rangle(t)$. Consequently, the time dependence of the state can be determined directly from the time dependent population in the energy eigenstates. For the further evaluation the projection is interpreted differently. A detection time independent state with phase ϕ is projected with a detection time dependent projection pulse with phase $\tilde{\theta}(t) = \theta - \varphi(t)$. Therefore, for different detection times t superposition states with phase $\phi = \tilde{\theta}(t) + \frac{\pi}{2}$ are mapped into the energy eigenstates. This provides the projections required for the quantum state tomography.

This method to project the created state is applied in the evaluation of the monochromatic 393 nm atom-photon entanglement (see Section 7.2.1). For this scheme, the frequency difference of the spectral components results in a detection time dependent phase $\varphi(t) = 2\pi\nu t$ of the created atom-photon state. For a projection onto a linear polarization and an atomic superposition the detection time dependent phase leads to oscillation in the correlation between atomic state and polarization that are observed in the wave packet of the detected photon (see Figure 4.17 (a)). From the measured wave packets, the average frequency $\bar{\nu}$ is determined. With this
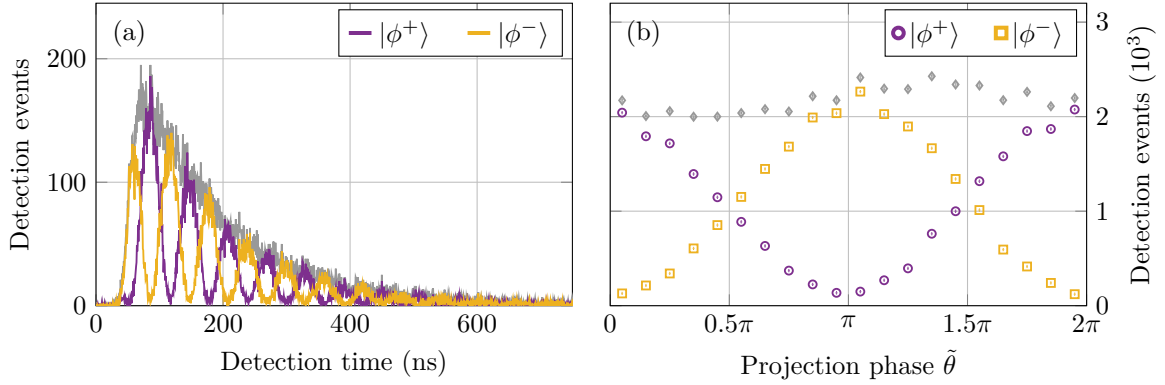
Figure 4.17.: (a) Wave packets and (b) phase histograms of the created 393 nm atom-photon state for a projection onto $|A\rangle$ and a atomic superposition. Gray curves are detection events without atomic state projection.

frequency, the detection events are sorted into phase bins according to their detection time (see Figure 4.17 (b)). The obtained detection events in each phase bin correspond to the detection events for the different phases of the projection pulse. In a calibration phase histogram, a phase offset is subtracted to obtain a maximum for $\tilde{\theta} = 0$ for the population mapped into the $|\uparrow\rangle$ energy eigenstate. A name is assigned to the superposition state, that is mapped into the $|\uparrow\rangle$ energy eigenstate with this projection phase. Consequently, for a phase $\tilde{\theta} = \pi$ the same superposition state is mapped into the $|\downarrow\rangle$ energy eigenstate. Thus, an even number of phase bins enables to add the detection events mapped into both energy eigenstates (with a phase shift of π). For the chosen example, the displayed phase histogram for $|A\rangle$ polarization is taken for the calibration and the atomic state $|+\mathrm{i}\rangle$ is assigned to the superposition projected for $\tilde{\theta}_{|\uparrow\rangle} = 0$ and $\tilde{\theta}_{|\downarrow\rangle} = \pi$. As in the method with two projection pulses, this assignment defines the phase of the reconstructed state.

It should be noted, that a single detection time independent atom-photon state is reconstructed with this method, as the detection time dependence is used to obtain the necessary projection values. The atom-photon state reconstructed with this method corresponds to the atom-photon state for detection times that are sorted into the phase bin $\tilde{\theta} = 0$. For other detection times, the created atom-photon state has a different phase according to $\varphi(t)$.

4.6.3. Quantum state tomopgraphy

The density matrix ρ describes the state of a quantum system. It allows to calculate properties as the fidelity $\mathcal{F}$ and purity $\mathcal{P}$ of the quantum state. Unfortunately the density matrix cannot be measured directly, but only projections to different bases. The reconstruction of the underlying density matrix from the projection outcomes is called quantum state tomography.

If the measured projections are described with a positive operator valued measure (POVM) Π_k, the measurement outcome are the probabilities

$$p_k = \text{Tr}\left\{\rho\Pi_k\right\}. \tag{4.10}$$

If the POVM Π_k is tomographically complete and the exact probabilities p_k are known, the equation can be inverted to calculate the density matrix ρ [7]. However, in an experimental situation one has no access to the exact probabilities p_k, but only estimates f_k that are measured by creating many identical copies of the same state that are projected with Π_k. From the detected signal events S_k for each projection basis the probabilities f_k are calculated.

Because the estimated probabilities differ from the exact probabilities p_k Equation 4.10 cannot be inverted for the estimates f_k. Thus a different approach has to be chosen. The chosen maximum likelihood approach reconstructs the estimated density matrix ρ_{est} that matches the estimated probabilities f_k the best and maximizes the likelihood measure

$$\mathcal{L}\left[f_k, \rho_{\text{est}}\right] = \sum_k f_k \, \text{Tr}\left\{\rho\Pi_k\right\}. \tag{4.11}$$

A particular challenge here is to reconstruct a physical density matrix (positive semidefinite, hermitian and $\text{Tr}\left\{\rho_{\text{est}}\right\} = 1$). The implemented algorithm [85] ensures that the reconstructed density matrix ρ_{est} is physical. Starting from a mixed state, in each iteration the next density matrix $\rho_{(n+1)}$ is calculated with the equations

$$R_{(n)} = \sum_k \frac{f_k}{p_{k,(n)}}\Pi_k, \quad \mu_{(n)} = \sqrt{\text{Tr}\left\{R_{(n)}\rho_{(n)}R_{(n)}\right\}}, \quad \text{and} \quad \rho_{(n+1)} = \mu_{(n)}^{-2}R_{(n)}\rho_{(n)}R_{(n)}. \tag{4.12}$$

The algorithm stops if the difference between the old and new density matrix is smaller than a given tolerance. The algorithm implemented in MATLAB reconstructs the density matrix of a two qubit state in less than one second (for a POVM with 36 projections).

In this work, quantum state tomography is done for atom-photon states where the POVM $\Pi_k = \Pi_u^{(at)} \otimes \Pi_v^{(ph)}$ that describes the measured projections (see Section 4.6.2) is composed of a POVM

$$\Pi^{(ph)} = \left\{\left|\text{L}\right\rangle\!\left\langle\text{L}\right|; \left|\text{R}\right\rangle\!\left\langle\text{R}\right|; \left|\text{H}\right\rangle\!\left\langle\text{H}\right|; \left|\text{V}\right\rangle\!\left\langle\text{V}\right|; \left|\text{D}\right\rangle\!\left\langle\text{D}\right|; \left|\text{A}\right\rangle\!\left\langle\text{A}\right|\right\} \tag{4.13}$$

that describes the polarization projection and the POVM $\Pi_u^{(at)}$ that describes the atomic projection. In the case of two projection $\frac{\pi}{2}$-pulses, the atomic POVM contains the operators

$$\Pi^{(at,1)} = \left\{\left|\uparrow\right\rangle\!\left\langle\uparrow\right|; \left|\downarrow\right\rangle\!\left\langle\downarrow\right|; \left|-\right\rangle\!\left\langle-\right|; \left|+\right\rangle\!\left\langle+\right|; \left|-\text{i}\right\rangle\!\left\langle-\text{i}\right|; \left|+\text{i}\right\rangle\!\left\langle+\text{i}\right|\right\}. \tag{4.14}$$

If the projection is done with a single projection $\frac{\pi}{2}$-pulse and the time dependence of the state,

---

[7]One calculates $\rho = \sum_k \text{Tr}\left\{\rho\Pi_k\right\} \tilde{\Pi}_k$, where $\tilde{\Pi}_k$ are the operators from the dual frame.

the POVM contains the operators

$$\Pi^{(at,2)} = \left\{ |\uparrow\rangle\langle\uparrow| \, ; |\downarrow\rangle\langle\downarrow| \, ; \frac{2}{M} |\tilde{\theta}_1\rangle\langle\tilde{\theta}_1| \, ; \frac{2}{M} |\tilde{\theta}_2\rangle\langle\tilde{\theta}_2| \, ; \frac{2}{M} |\tilde{\theta}_3\rangle\langle\tilde{\theta}_3| \, ; \cdots \right\}, \tag{4.15}$$

where M is the number of phase bins and $|\tilde{\theta}_w\rangle$ are the atomic superposition states projected in the phase bins $\tilde{\theta}_w$. All three POVM span the four-dimensional space of Hermitian operators and are therefore tomographically complete [86]. The measured projections described by these operators can therefore be taken to reconstruct the density matrix of the generated state. It should be noted, that the used POVM are not normalized to 1 but 2 or 3. This corresponds to the experimental situation that the atomic state is only measured after a photon with the chosen polarization was detected. The factors 2 and 3 compensate the random choice of the two respective three possible projection bases. This common factor in all projection operators can be factored out in Equations 4.12 and therefore has no influence on the reconstructed density matrix.

From the detected signal events S_k for each projection setting I calculate the estimated probability f_k fort this projection setting with

$$f_k = C \frac{S_k + 1}{N + \sum_k S_k}, \tag{4.16}$$

where N ist the number of projections in the POVM. The factor $C = 6$ or $C = 9$ accounts for the normalization of the POVM. Details on the necessary extension of Bayesian inference from a coin flip to the roll of a dice are discussed in Appendix B. The probabilities f_k are put in the algorithm that reconstructs the density matrix of the generated atom-photon state. To estimate the uncertainty in the reconstructed density matrix and the deduced properties I perform a Monte Carlo simulation. Under the assumption of Poissonian statistics for the involved detection events new sets of frequencies f_k are simulated with Poissonian-distributed random numbers for simulated detection events. For each set I reconstruct the density matrix and from all simulated sets, I calculate the mean value and the standard deviation of the properties of interest.

As example, In Figure 4.18 I show an overview over the measured signal events S_k, the estimated probabilities f_k, and the reconstructed density matrix of the created entangled atom-photon state for the bichromatic 393 nm atom-photon entanglement scheme presented in Section 7.2.2. I display the density matrix as color coded bar plots for the real and imaginary part, where the height and color of the bars encode the value of each entry of ρ as shown there. Such an overview is listen in Appendix D for almost all atom-photon entanglement measurements discussed in this work. In Chapter 7 I only display the density matrix.

	$\left|+\frac{1}{2}\right\rangle$	$\left|-\frac{1}{2}\right\rangle$	$\left|-\right\rangle$	$\left|+\right\rangle$	$\left|-i\right\rangle$	$\left|+i\right\rangle$
$\left|A\right\rangle$	632	656	663	601	35	1184
$\left|D\right\rangle$	708	595	666	620	1093	39
$\left|V\right\rangle$	660	553	1172	8	599	600
$\left|H\right\rangle$	558	593	55	1144	628	603
$\left|R\right\rangle$	20	1215	578	554	557	626
$\left|L\right\rangle$	1143	38	664	597	593	641

Sequence repetitions: 1080 M

Average repetition rate: 14 kHz

Total photon events: 26839

Estimated background: 4948

Signal events: **21891**

$\left|A\right\rangle$	0.260	0.270	0.273	0.247	0.015	0.486
$\left|D\right\rangle$	0.291	0.245	0.274	0.255	0.449	0.016
$\left|V\right\rangle$	0.271	0.227	0.481	0.004	0.246	0.247
$\left|H\right\rangle$	0.229	0.244	0.023	0.470	0.258	0.248
$\left|R\right\rangle$	0.009	0.499	0.238	0.228	0.229	0.257
$\left|L\right\rangle$	0.470	0.016	0.273	0.245	0.244	0.264
	$\left|+\frac{1}{2}\right\rangle$	$\left|-\frac{1}{2}\right\rangle$	$\left|-\right\rangle$	$\left|+\right\rangle$	$\left|-i\right\rangle$	$\left|+i\right\rangle$

$\langle\cdot|\rho|\cdot\rangle$	$\left|+\frac{1}{2},L\right\rangle$	$\left|+\frac{1}{2},R\right\rangle$	$\left|-\frac{1}{2},L\right\rangle$	$\left|-\frac{1}{2},R\right\rangle$
$\left\langle+\frac{1}{2},L\right|$	0.498	0.011	−0.011	−0.470
$\left\langle+\frac{1}{2},R\right|$	0.011	0.009	−0.003	−0.009
$\left\langle-\frac{1}{2},L\right|$	−0.011	−0.003	0.016	−0.011
$\left\langle-\frac{1}{2},R\right|$	−0.470	−0.009	−0.011	0.477

$\langle\cdot|\rho|\cdot\rangle$	$\left|+\frac{1}{2},L\right\rangle$	$\left|+\frac{1}{2},R\right\rangle$	$\left|-\frac{1}{2},L\right\rangle$	$\left|-\frac{1}{2},R\right\rangle$
$\left\langle+\frac{1}{2},L\right|$	−0.000	0.007	−0.006	−0.001
$\left\langle+\frac{1}{2},R\right|$	−0.007	−0.000	0.002	−0.001
$\left\langle-\frac{1}{2},L\right|$	0.006	−0.002	0.000	−0.011
$\left\langle-\frac{1}{2},R\right|$	0.001	0.001	0.011	0.000

Figure 4.18.: (top) Measurement info and Signal events S_k for all projection bases. (middle) Estimated probabilities f_k for all projection bases listed as numeric values and color coded map. (bottom) Density matrix of the created 393 nm atom-photon state reconstructed from the estimated probabilities f_k. Background corrected values are shown. Values without background correction are shown in Appendix D.2.3.

Results

5. Modeling the Raman scattering of a single photon

Raman scattering is the inelastic scattering of light. This means that the scattered light has a different frequency than the incident light. Depending on the frequency of the emitted light, the process is more detailed called Stokes-Raman scattering, if the scattered light has a smaller frequency than the incident light, or anti-Stokes-Raman scattering if the scattered light has a larger frequency than the incident light.

To scatter Raman photons an atomic system with at least three levels is needed. In this atomic system the initial state before the scattering process and the final state after the scattering process are different. Two cases are distinguished. The first case is stimulated Raman scattering, where the scattering process is stimulated by an external cavity or light field. In contrast to this case, in the second case no external light field or cavity is near resonance of the final transition. This case, called spontaneous Raman scattering is of interest in this work and treated here. In this chapter I develop a model to describe the spectral properties of a single photon that is generated by spontaneous Raman scattering.

The simplest system where Raman scattering can happen is a three level system with an initial state $|i\rangle$, an excited state $|e\rangle$ and an final state $|f\rangle$ (see Figure 5.1). The initial and final state are treated as stable thus there is no difference whether the initial or final state has a higher energy. The excited state decays with the decay rates Γ_i and Γ_f into the initial respective final state on transitions I therefore call initial and final transition. The system is prepared in the initial state $|i\rangle$ and excited by an incident light field into the excited state from where a Raman photon is released on the transition into the final state. Additionally to the decay into the final state also a decay back into the initial state can happen. If the system is excited by a single
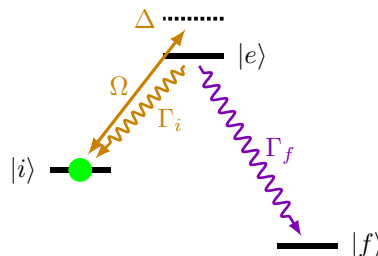
Figure 5.1.: Raman scattering process in a three level system. The properties of the photon emitted on the transition into the final state $|f\rangle$ are studied.

photon, the decay back into the initial state terminates the process without scattering a Raman photon. A laser, on the other hand, excites the system again until finally a Raman photon is released. In all cases, the scattering of a Raman photon terminates the process, because the final state is not coupled to the excited state. As an important consequence, there is always only a single Raman photon emitted on the transition into the final state.

The incident light field that excites the initial state can be a laser or single photon. Here, I focus on the excitation by a laser field [1]. I study how the emitted spectrum depends on the Rabi frequency Ω and detuning Δ of the laser as well as the decay rates Γ_f and Γ_i of the excited state. Therefore, I measure spectra of single Raman-scattered photons, generated with a single $^{40}Ca^+$ ion. To model the scattering process in this system, the model developed by my colleague Philipp Müller [20, 25] is extended to describe the $^{40}Ca^+$ ion. Additionally, the presented model covers modulated laser fields as for example a time dependent Rabi frequency. I start with a model that describes the Raman scattering in the three level system in Figure 5.1. I model the decay on the final transition as spontaneous decay and apply the Weisskopf-Wigner approximation to solve Schrödinger's equation. This approach leads to the same result for the three level system as the resolvent method in [20, 25]. However, a direct solution of the Schrödinger equation enables an easier treatment of arbitrary time dependent Rabi frequencies. Furthermore it is better suited for the extensions that are done in the next steps. These extensions pave the way to the model that describes the $^{40}Ca^+$ ion. I discuss

- additional decay channels including several final states,

- different initial states, and

- multiple excited states that decay into the same final state.

After the derivation, the model is applied to discuss various quantum interference effects that affect the spectrum of the scattered photon.

The model is based on the work of Zhu, Narducci and Scully [87] for a similar system. Additionally, it is influenced by the work of Yuana and Gao [88], the textbooks from Cohen-Tannoudji, Dupont-Roc & Grynberg [89], the lecture notes from Steck [43] as well as the work of Philipp Müller [20, 25].

5.1. Theoretical description of the Raman scattering

5.1.1. Model for the spontaneous decay

The spontaneous decay out of the excited state $|e\rangle$ is the central part of the Raman scattering process. Therefore, I start the development of the model with a description of this spontaneous decay in a two level system with the states $|e\rangle$ and $|f\rangle$. These states form a subsystem in the

---

[1]The excitation by a single photon is discussed in [20, 25].

three level system where the Raman scattering takes places. If one sets the energy of the excited state to zero, the internal Hamilton of this subsystem becomes

$$\hat{H}_0 = -\hbar\omega_f \left|f\right\rangle\left\langle f\right| + \hbar \int_0^\infty \omega b_f^\dagger(\omega)b_f(\omega)\,\mathrm{d}\omega. \tag{5.1}$$

The first part describes the energy of the final state, while the second part describes the energy of the field that is resonant with the transition. The spontaneous decay is modeled by an operator

$$\hat{S}_f = \hbar \int_0^\infty g_f \left|e\right\rangle\left\langle f\right| b_f(\omega) + g_f \left|f\right\rangle\left\langle e\right| b_f^\dagger(\omega)\,\mathrm{d}\omega, \tag{5.2}$$

where $g_f = \sqrt{\frac{\Gamma_f}{2\pi}}$. Therein Γ_f is the decay rate of the excited state given by the Weisskopf-Wigner approximation.

For all times, the system is assumed to be in one of two states. Before the decay, the system is in the excited state and no photon is present. I write this state $\left|e, 0_\omega\right\rangle$, where 0_ω indicates the vacuum mode. For simplicity the vacuum mode is dropped from the description in the following and the state is simply written as $\left|e\right\rangle$. After the decay, the system is in the final state with one photon distributed over all possible frequency modes. I write these states as $\left|f, 1_\omega\right\rangle$, where 1_ω indicates a photon in the mode with frequency ω. Consequently, the state $\left|\Psi(t)\right\rangle$ of the system is given by a superposition

$$\left|\Psi(t)\right\rangle = C_e(t)\left|e\right\rangle + \int_0^\infty C_{f,\omega}(t)\left|f, 1_\omega\right\rangle\,\mathrm{d}\omega \tag{5.3}$$

of both states. This state is inserted into the Schrödinger equation with the Hamilton $\hat{H} = \hat{H}_0 + \hat{S}_f$ to derive the coupled differential equations

$$\dot{C}_{f,\omega} = -\mathrm{i}(\omega - \omega_f)C_{f,\omega} - \mathrm{i}g_f C_e, \tag{5.4}$$

$$\text{and} \qquad \dot{C}_e = -\mathrm{i}\int_0^\infty g_f C_{f,\omega}\,\mathrm{d}\omega. \tag{5.5}$$

To solve these equations one introduces the slowly varying amplitude $C_{f,\omega} = \tilde{C}_{f,\omega}e^{-\mathrm{i}\delta t}$, where $\delta = \omega - \omega_f$ is the detuning of the photon mode with respect to the transition. With this amplitude Equation 5.4 and Equation 5.5 become

$$\dot{\tilde{C}}_{f,\omega} = -\mathrm{i}g_f C_e e^{\mathrm{i}\delta t}, \tag{5.6}$$

$$\text{and} \qquad \dot{C}_e = -\mathrm{i}\int_0^\infty g_f \tilde{C}_{f,\omega}e^{\mathrm{i}\delta t}\,\mathrm{d}\omega. \tag{5.7}$$

These equations are solved with the approach of Weisskopf and Wigner [90]. One integrates Equation 5.6 and substitutes the result in Equation 5.7 to obtained

$$\dot{C}_e = -\frac{\Gamma_f}{2}C_e, \tag{5.8}$$

which describes the decay of the amplitude in the excited state. I replace Equation 5.5 by this

equation. Consequently, the differential equations describing the time evolution of the state $|\Psi(t)\rangle$ become

$$\dot{C}_{f,\delta} = -\mathrm{i}\delta C_{f,\delta} - \mathrm{i}g_f C_e, \tag{5.9}$$

$$\text{and} \qquad \dot{C}_e = -\frac{\Gamma_f}{2} C_e. \tag{5.10}$$

These equations describe the dynamic of the spontaneous decay into a single frequency mode that has a detuning $\delta = \omega - \omega_f$ from the atomic transition. In these equations the evolution of the state $|e\rangle$ is independent from the state $|f, 1_\delta\rangle$. This corresponds to the emission into free space, where a photon emitted from the atomic system can not be reabsorbed. Therefore the dynamic of the excited state can be modeled as an independent subsystem. From the solution of Equation 5.9 and Equation 5.10 one calculates the amplitude spectrum of the emitted photon as $A(\delta) = C_{f,\delta}(t \to \infty)$.

One obtains the same equations as in Equation 5.9 and Equation 5.10 if the spontaneous decay is modeled with the non-Hermitian operator

$$\hat{W}_{f,\delta} = -\mathrm{i}\hbar\frac{\Gamma_f}{2} |e\rangle \langle e| + \hbar g_f |f, 1_\delta\rangle \langle e| \tag{5.11}$$

instead of the operator $\hat{S}_f$. This operator summarizes the Weisskopf-Wigner approach in the imaginary energy contribution $-\mathrm{i}\hbar\frac{\Gamma_f}{2}$ that depopulates the excited state. The imaginary energy contribution replaces the part $|e\rangle \langle f, 1_\delta|$ that brings population from the final state back into the excited state. The missing coupling back into the excited state corresponds to the above mentioned emission of a photon that can not be reabsorbed. In this case one can model the time evolution of the amplitude in the state $|e\rangle$ as independent subsystem. Also the internal Hamilton can be shortened to the Hamilton

$$\hat{H}_{0,\delta} = -\hbar\delta |f, 1_\delta\rangle \langle f, 1_\delta|, \tag{5.12}$$

that describes only the dynamic of the state that contains the photon mode 1_δ. The operators $\hat{W}_{f,\delta}$ in Equation 5.11 and $\hat{H}_{0,\delta}$ in Equation 5.12 build the basis of the model for the Raman scattering of a single photon developed in this chapter.

An additional decay channel out of the excited state $|e\rangle$ is modeled analog to the decay into the final state $|f\rangle$. For a decay into the state $|i\rangle$ an operator $\hat{W}_i$ analog to Equation 5.11 is used. In the subsystem containing only the states $|e\rangle$ and $|f, 1_\delta\rangle$, this operator becomes

$$\hat{W}_i = -\mathrm{i}\hbar\frac{\Gamma_i}{2} |e\rangle \langle e|, \tag{5.13}$$

where Γ_i is the decay rate of the additional decay channel. As consequence of this additional decay from the excited state one obtains the slightly changed equation

$$\dot{C}_e = -\frac{\Gamma}{2} C_e \tag{5.14}$$

for the amplitude in the excited state. Therein $\Gamma = \Gamma_f + \Gamma_i$ is the total decay rate of the excited state. Equation 5.9 that describes the dynamic of the final state is not affected by the additional decay channel. If one solves the differential equations and calculates the spectrum $A(\delta)$ of the photon emitted by a spontaneous decay into the final state one finds the known result, that the width of the spectrum only depends on the total decay rate Γ of the excited state while the ratio of the decay rates Γ_f and Γ_i affects the population of the spectrum emitted on the transition into the state $|f\rangle$

5.1.2. Raman scattering in a three level system

To describe the Raman scattering in a three level system, the initial state $|i\rangle$ and the excitation on the initial transition have to be added to the previous described two level system. The system is prepared in the initial state $|i\rangle$ and is excited by a laser into the excited state $|e\rangle$. From the excited state the system decays into the final state $|f\rangle$ by releasing a Raman photon or back into the initials state $|i\rangle$ from where it is excited again. In the frame rotating with the frequency ω_L of the laser interaction and for the energy of the excited state set to zero, the internal Hamilton becomes

$$\hat{H}_{0,\delta} = \hbar\Delta \, |i\rangle \, \langle i| + \hbar\delta \, |f, 1_\delta\rangle \, \langle f, 1_\delta| , \tag{5.15}$$

where $\Delta = \omega_L - \omega_i$ is the detuning of the laser from the excited transition while $\delta = \omega - \omega_f$ is the detuning of the scattered Raman photon from the transition into the final state. The laser interaction driving the Raman scattering process is described by the operator

$$\hat{V} = \hbar \left(\frac{\Omega}{2} \, |e\rangle \, \langle i| + \frac{\Omega^*}{2} \, |i\rangle \, \langle e| \right) , \tag{5.16}$$

where Ω is the on resonance Rabi frequency.

The spontaneous decay in the subsystem consisting of the excited state $|e\rangle$ and the final state $|f\rangle$ was discussed in the previous section. This decay is described by the operator

$$\hat{W}_{f,\delta} = -i\hbar\frac{\Gamma_f}{2} \, |e\rangle \, \langle e| + \hbar g_f \, |f, 1_\delta\rangle \, \langle e| , \tag{5.17}$$

where $g_f = \sqrt{\Gamma_f/(2\pi)}$ is given by the decay rate Γ_f on the final transition. The decay back to the initial state needs a more detailed treatment, because the system is excited again after such a decay happened. Therefore, it can not be treated with a single photon mode. I discuss the treatment of the decay back into the initial state more detailed later. At first, I model it as a loss of population from the system with the operator

$$\hat{W}_i = -i\hbar\frac{\Gamma_i}{2} \, |e\rangle \, \langle e| , \tag{5.18}$$

where Γ_i is the decay rate on the transition. This treatment corresponds to the case, that the

system is not excited again, after a back decay happened, as it is the case for the excitation by a single photon.

Analog to the spontaneous decay, I solve the Schrödinger equation for the state

$$|\Psi(t)\rangle = C_i(t)\,|i\rangle + C_e(t)\,|e\rangle + \int_{-\infty}^{\infty} C_{f,\delta}(t)\,|f, 1_\delta\rangle\,\mathrm{d}\delta \tag{5.19}$$

of the system. Due to the additional decay on the initial transition, this state is not normalized after the dynamic started. I insert the state $|\Psi(t)\rangle$ into the Schrödinger equation to get the coupled differential equations

$$\dot{C}_{f,\delta} = -\mathrm{i}\delta C_{f,\delta} - \mathrm{i}g_f C_e, \tag{5.20}$$

$$\dot{C}_e = -\frac{\Gamma}{2}C_e - \mathrm{i}\frac{\Omega}{2}C_i, \qquad \text{and} \tag{5.21}$$

$$\dot{C}_i = -\mathrm{i}\Delta C_i - \mathrm{i}\frac{\Omega^*}{2}C_e, \tag{5.22}$$

for the coefficients of the state. It should be noted, that the first Equation 5.20 only describes the dynamic into a single frequency mode. The other two equations are independent from this equation and can be solved first to obtain $C_e(t)$ and $C_i(t)$. For the initial condition $C_i(0) = 1$ one obtains

$$C_e(t) = \frac{\Omega}{2(\omega_+ - \omega_-)}e^{-\mathrm{i}\omega_+ t} - \frac{\Omega}{2(\omega_+ - \omega_-)}e^{-\mathrm{i}\omega_- t}. \tag{5.23}$$

With the result obtained for $C_e(t)$ one calculates

$$C_{f,\delta}(t) = \frac{g_f\Omega}{2}\left(\frac{e^{-\mathrm{i}\omega_+ t}}{(\omega_- - \omega_+)(\delta - \omega_+)} + \frac{e^{-\mathrm{i}\omega_- t}}{(\omega_+ - \omega_-)(\delta - \omega_-)} + \frac{e^{-\mathrm{i}\delta t}}{(\delta - \omega_+)(\delta - \omega_-)}\right). \tag{5.24}$$

In both coefficients ω_+ and ω_- are the frequencies of the dressed states, created by the laser interaction. These dressed state frequencies are given by

$$\omega_\pm = \frac{1}{2}\left(\Delta - \mathrm{i}\frac{\Gamma}{2}\right) \pm \frac{1}{2}\sqrt{\left(\Delta + \mathrm{i}\frac{\Gamma}{2}\right)^2 + |\Omega|^2} \tag{5.25}$$

which can be written as

$$\omega_+ = \Delta + \Delta_{\mathrm{AC}} - \mathrm{i}\frac{\kappa}{2} \qquad \text{and} \qquad \omega_- = -\Delta_{\mathrm{AC}} - \mathrm{i}\frac{\Gamma - \kappa}{2} \tag{5.26}$$

with the AC Stark shift

$$\Delta_{\mathrm{AC}} = -\frac{\Delta}{2} + \frac{\mathrm{sgn}\,\Delta}{2\sqrt{2}}\sqrt{|\Omega|^2 + \Delta^2 - \frac{\Gamma^2}{4} + \sqrt{\left(|\Omega|^2 + \Delta^2 - \frac{\Gamma^2}{4}\right)^2 + \Delta_1^2\Gamma^2}} \tag{5.27}$$

and the parameter

$$\kappa = \Gamma\frac{\Delta_{\mathrm{AC}}}{\Delta + 2\Delta_{\mathrm{AC}}}. \tag{5.28}$$

From the equations for the coefficients of the state, one calculates the spectrum and the wave packet of the scattered Raman photon. The amplitude of the wave packet of the photon is given by

$$R(t) = \sqrt{\Gamma_f} C_e(t) e^{-i\delta_f t} = \frac{\Omega \sqrt{\Gamma_f} \Theta(t)}{2(\omega_+ - \omega_-)} \left(e^{-\frac{\kappa}{2}t - i(\delta_f + \Delta + \Delta_{\mathrm{AC}})t} - e^{-\frac{\Gamma - \kappa}{2}t - i(\delta_f - \Delta_{\mathrm{AC}})t} \right) \quad (5.29)$$

with a phase factor $e^{-i\delta_f t}$ given by the detuning δ_f of the transition from the rotating frame. The spectral amplitude of the photon is given by the coefficient of the final state. Usually one is interested in the spectral amplitude after the emission process is over. This spectral amplitude is given by $C_{f,\delta}(t \to \infty)$. Due to the imaginary part of the dressed state frequencies ω_+ and ω_- only the last component from Equation 5.24 remains and the spectral amplitude becomes

$$R(\delta) = \frac{i\Omega \sqrt{\frac{\Gamma_f}{8\pi}}}{(\omega_+ - \omega_-)} e^{-i\delta t} \left(\frac{1}{\delta - \Delta - \Delta_{\mathrm{AC}} + i\frac{\kappa}{2}} - \frac{1}{\delta + \Delta_{\mathrm{AC}} + i\frac{\Gamma - \kappa}{2}} \right). \quad (5.30)$$

The scattered Raman photons contains two spectral components [25]. The Raman component (red) with spectral width or decay rate κ dominates for small Rabi frequencies $\Omega < \Gamma$ and the spectrum becomes close to a Lorentzian shape. For larger Rabi frequencies, the spontaneous component (blue) with spectral width or decay rate $\Gamma - \kappa$ poses a significant contribution to the spectral shape which then features two peaks of the Autler-Towns splitting [91] caused by the dressed states.

Treatment of the decay back into the initial state

In the above derivation, the decay back into the initial state was treated as loss of population from the system. However, due to the laser interaction, the system is re excited after each decay into the initial state $|i\rangle$ until finally the decay into the final state $|f\rangle$ terminates the process. Therefore a treatment of the back decay has to take all possible cases of $N = 0, 1, 2, ...$ back-decays into account. This can be done in two different ways.

The first approach is to calculate the dynamic for each possible number of back decays, as described in [20]. The spontaneous decay into the initials state is thereby modeled analog to the decay into the final state. The decay into the initial state creates a photon distributed over all frequency modes 1_{ω_i} of the corresponding transition. However, in contrast to the final state $|f\rangle$, the initial state $|i\rangle$ is excited again after a decay into this state happened. After each re excitation a further decay back into the initial state is possible. Consequently, for each back-decay a photon is created distributed over the modes 1_{ω_i} and not only the state $|i, 0_{\omega_i}\rangle$, but also the states $|i, 1_{\omega_i}^{(1)}\rangle$, ... and $|i, 1_{\omega_i}^{(1)}, ..., 1_{\omega_i}^{(N)}\rangle$ are possible. Therein $1_{\omega_i}^{(k)}$ describes the photon that is created by the k-th back decay. For each of these initial states, an excited state $|e, 1_{\omega_i}^{(1)}, ..., 1_{\omega_i}^{(N)}\rangle$ and a final state $|f^{(N)}\rangle = |f, 1_{\omega_f}, 1_{\omega_i}^{(1)}, ..., 1_{\omega_i}^{(N)}\rangle$ have to be added to the system. One then calculates the dynamic into each of the final states $|f^{(N)}\rangle$ as before. To remove the frequency information of the photons emitted on the transition into the initial state one has to

sum over all frequency modes of these photons. The full spectrum $S(\delta)$ and the wave packet $A(t)$ of the scattered Raman photon are then given by the sum

$$S(\delta) = \sum_{N=0}^{\infty} p_N S_N(\delta) \qquad \text{and} \qquad A(t) = \sum_{N=0}^{\infty} p_N A_N(t) \qquad (5.31)$$

of the spectrum $S_N(\delta)$ respective wave packet $A_N(t)$ of the Raman photon scattered after exactly N back decays. The spectra and wave packets are weighted by the probability

$$p_N = \frac{\Gamma_f}{\Gamma} \left(\frac{\Gamma_f}{\Gamma}\right)^N \qquad (5.32)$$

that exactly N back decays happened before the photon on the final transition was scattered. It was shown [20], that the power spectrum $S_N(\delta)$ is the same for each possible number N of back decays into the initial state. Thus the back decay has no influence on the photon spectrum in a three level system. It was also shown, that the wave packet $A_N(t)$ of the photon emitted after N back decays is given by a convolution of the previous wave packet with the wave packet $A_0(t)$ of the photon emitted without back decay. All together, the photon wave packet $A(t)$ is elongated by the back decay by a factor $\frac{\Gamma}{\Gamma_f}$.

While this first approach is feasible for a three level system and a small number of back decays it becomes almost impossible for other systems because all possible paths that lead to a Raman-scattered photon have to be taken into account. Therefore a different approach has to be taken in a model for other systems. Nevertheless, the result that the back decay in a three level system does not affects the spectral shape of the emitted photon is important for later discussions. The same result is also found with the following description.

The chosen approach is to describe the system with a density matrix ρ instead of the state vector $|\Psi\rangle$. This enables to describe the spontaneous decay back into the initial state as a relaxation. But also other relaxations as for example the line width of the excitation laser can be modeled. At the same time, the spontaneous decay into the final state $|f\rangle$ is treated as before. Due to the imaginary energy contribution to the excited state, the changed optical Bloch equations

$$\dot{\rho}_\delta = -\frac{i}{\hbar}\left(\hat{H}_\delta \rho - \rho \hat{H}_\delta^\dagger\right) + \frac{1}{2}\sum_k \left(2\hat{c}_k \rho \hat{c}_k^\dagger - \hat{c}_k^\dagger \hat{c}_k \rho - \rho \hat{c}_k^\dagger \hat{c}_k\right). \qquad (5.33)$$

have to be used [89]. Therein, the effective non-Hermitian Hamilton $\hat{H}_\delta = \hat{H}_{0,\delta} + \hat{V} + \hat{W}_f$ describes the coherent dynamic. The relaxation operators $\hat{c}_k$ describe the incoherent dynamic of the system that is caused by relaxation effects. The spontaneous decay is modeled by

$$\hat{c}_i = \sqrt{\Gamma_i}\, |i\rangle\langle e|, \qquad (5.34)$$

where Γ_i is the decay rate on this transition. Together with the imaginary energy contribution in the operator $\hat{W}_f$ the excited state is depopulated with the total decay rate $\Gamma = \Gamma_f + \Gamma_i$. The

line width of the excitation laser is introduced as a relaxation of type T_2 [92] by the operator

$$\hat{c}_L = \sqrt{\frac{\Delta\omega_L}{2}} \left(|i\rangle\langle i| - |e\rangle\langle e| \right), \tag{5.35}$$

where $\Delta\omega_L$ is the line width of the laser.

To calculate the spectrum or the wave packet of the emitted Raman photon Equation 5.33 is solved. This equation is the basis of further extensions of the model presented in the next section. There I discuss how the individual components of the Hamilton $\hat{H}_\delta$ and the relaxations $\hat{c}_k$ change in a more complex system.

5.1.3. Extension on the way to a model for the ^{40}Ca$^+$ ion

The model for the Raman scattering in a three level system builds the basis for all models that describe more complex systems. In the next sections, I guide through the extension that pave the way to the model that describes the Raman scattering in the ^{40}Ca$^+$ ion. The necessary extensions are (see Figure 5.2 (a) - (d)):

(a) Additional decays into a parasitic state $|p\rangle$ and multiple final states $|f_1\rangle$ and $|f_2\rangle$.

(b) Two initial states $|i_1\rangle$ and $|i_2\rangle$ that are both coupled to the excited state $|e\rangle$.

(c) Two excited state $|e_1\rangle$ and $|e_2\rangle$ that decay into the same final state $|f\rangle$. The excited states are populated from individual initial states $|i_1\rangle$ and $|i2\rangle$.

(d) The final state $|f\rangle$ is coupled to a level $|a\rangle$.

These four extensions are discussed in the following paragraphs. Afterwards, I combine the extensions to the model that describes the Raman scattering of a single photon with the ^{40}Ca$^+$ ion (see Section 5.1.4).
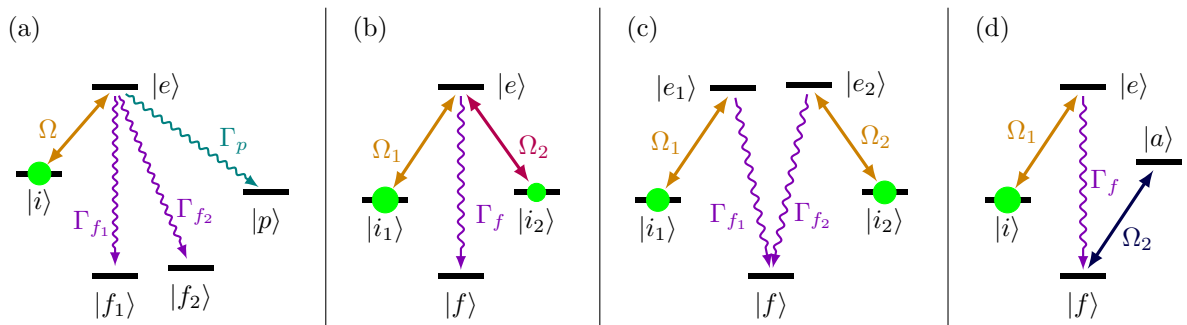
Figure 5.2.: Extensions of the three level scheme to model a more complex system. (a) Decay into a parasitic state $|p\rangle$ or into multiple final states. (b) Several states are coupled to the same excited state. (c) Decay from different excited states to the same final state. (d) The final state is coupled to an additional state. In all cases, the decay back into the initial states is not drawn for simplicity.

(a) Additional decay channels

Additional decay channels out of the excited state $|e\rangle$ are the first extension of the model (see Figure 5.2 (a)). These decay channels go into a final parasitic state $|p\rangle$ and to a second final state. Consequently, the system has two final states $|f_1\rangle$ and $|f_2\rangle$. I define a parasitic decay thereby as a final state of the scattering process, where the spectrum is not of interest. If the $D_{5/2}$ state of the $^{40}Ca^+$ ion is the initial state for the generation of a single 393 nm photon, the 850 nm decay is a parasitic decay. At the same time, the two Zeeman levels of the $S_{1/2}$ state correspond to multiple final states.

The parasitic decay is modeled analog to Equation 5.18 with the operator

$$\hat{W}_p = -i\hbar\frac{\Gamma_p}{2}|e\rangle\langle e|, \tag{5.36}$$

where Γ_p is the decay rate on the parasitic transition. As result, the parasitic decay appears as a loss of population from the system.

The decay into multiple final states is modeled analog to the decay into a single final state. Thereby, each of the final states is directly connected to a photon emitted on the corresponding transition. For this reason, there are only the final states

$$|f_1, 1_\delta^{(1)}\rangle \,\hat{=}\, |f_1, 1_\delta^{(1)}, 0_\delta^{(2)}\rangle \qquad \text{and} \qquad |f_2, 1_{\delta_2}^{(2)}\rangle \,\hat{=}\, |f_2, 0_\delta^{(1)}, 1_{\delta 2}^{(2)}\rangle \tag{5.37}$$

where $1_\delta^{(1)}$ describes a photon emitted on the transition into the state $|f_1\rangle$ while $1_\delta^{(2)}$ describes a photon emitted on the transition into the state $|f_2\rangle$. For both photon modes I use the same detuning δ with respect to a reference energy. Compared to this reference energy, the final states $|f_1\rangle$ and $|f_2\rangle$ are shifted by the energy ϵ_1 respectively ϵ_2. Thus the internal Hamilton of the system becomes

$$\hat{H}_{0,\delta} = \hbar\Delta|i\rangle\langle i| + \hbar(\delta + \epsilon_1)|f, 1_\delta^{(1)}\rangle\langle f, 1_\delta^{(1)}| + \hbar(\delta + \epsilon_2)|f, 1_\delta^{(2)}\rangle\langle f, 1_\delta^{(2)}|. \tag{5.38}$$

Due to the energy shifts ϵ_1 and ϵ_2 of the final states, the resonances of both individual decay channels are found at the positions $\delta = -\epsilon_1$ and $\delta = -\epsilon_2$.

The spontaneous decay on both transitions into the final states is modeled analog to Equation 5.11 by the operators

$$\hat{W}_{f_1,\delta} = -i\hbar\frac{\Gamma_{f_1}}{2}|e\rangle\langle e| + \hbar g_{f_1}|f_1, 1_\delta^{(1)}\rangle\langle e| \quad \text{and} \quad \hat{W}_{f_2,\delta} = -i\hbar\frac{\Gamma_{f_2}}{2}|e\rangle\langle e| + \hbar g_{f_2}|f_2, 1_\delta^{(2)}\rangle\langle e|, \tag{5.39}$$

where $g_{f_1} = \sqrt{\Gamma_{f_1}/(2\pi)}$ and $g_{f_1} = \sqrt{\Gamma_{f_2}/(2\pi)}$ are given by the decay rates Γ_{f_1} and Γ_{f_2} on the respective transition. The energy of all other states, the laser interaction and the decay back into the initial state are not affected by the additional decay channels.

Finally, the same approach can be taken to extend the three level system to a system with many additional decay channels from the same excited state. This situation would apply in case of a system with multiple parasitic states or more than two final states. An example is

the generation of a 854 nm photon, where each of the excited $|P_{3/2}\rangle$ Zeeman levels decays into three Zeeman levels of the $|D_{5/2}\rangle$ manifold

(b) Two initial states coupled to the same excited state

The next extension is a system with two initial states $|i_1\rangle$ and $|i_2\rangle$ that are coupled to the same excited state $|e\rangle$ (see Figure 5.2 (b)). The lasers that excite the transitions have the Rabi frequencies Ω_1 respective Ω_2 and detunings $\Delta_1 = \omega_{L_1} - \omega_{i_1}$ respective $\Delta_2 = \omega_{L_2} - \omega_{i_2}$. For both transitions an independent rotating frame transformation is done. Thus the internal Hamilton becomes

$$\hat{H}_{0,\delta} = \hbar\Delta_1 |i_1\rangle \langle i_1| + \hbar\Delta_2 |i_2\rangle \langle i_2| + \hbar\delta |f, 1_\delta\rangle \langle f, 1_\delta| . \tag{5.40}$$

The operator that describes the laser interaction has to cover both laser interactions. It becomes

$$\hat{V}_1 = \hbar \left(\frac{\Omega_1}{2} |e\rangle \langle i_1| + \frac{\Omega_1^*}{2} |i_1\rangle \langle e| \right) + \hbar \left(\frac{\Omega_2}{2} |e\rangle \langle i_2| + \frac{\Omega_2^*}{2} |i_2\rangle \langle e| \right) . \tag{5.41}$$

The decay on both excited transitions is modeled by the relaxation operators

$$\hat{c}_{i_1} = \sqrt{\Gamma_{i_1}} |i_1\rangle \langle e| \qquad \text{and} \qquad \hat{c}_{i_2} = \sqrt{\Gamma_{i_2}} |i_2\rangle \langle e| , \tag{5.42}$$

where Γ_{i_2} and Γ_{i_2} are the decay rates on both transitions. As there is only a single decay channel into the final state, the operator that describes this spontaneous decay is the same as for the three level system.

It should be noted that the above treatment assumes phase stability between the Rabi frequencies Ω_1 and Ω_2. This is ensured, if a single laser excites both transitions. In this case the individual detunings Δ_1 and Δ_2 can be expressed as

$$\Delta_1 = \Delta + \nu_1 \qquad \text{and} \qquad \Delta_2 = \Delta + \nu_2, \tag{5.43}$$

where ν_1 and ν_2 are the energy shifts of both initial states with respect to an energy reference point. The global detuning Δ is the detuning of the excitation laser from this reference point. When the lasers are not phase stable, the dynamic has to be calculated as an incoherent sum of all possible relative phases between Ω_1 and Ω_2.

(c) Two initial states coupled to different excited states

The third extension of the three level system is a system, where two excited states $|e_1\rangle$ and $|e_2\rangle$ decay into the same atomic state $|f\rangle$ (see Figure 5.2 (c)). The excited states, which are assumed to be from the same atomic manifold, are populated from two initial states $|i_1\rangle$ and $|i_2\rangle$ that are different states from the same atomic manifold, too. As the two emission channels from the states $|e_1\rangle$ and $|e_2\rangle$ happen on different atomic transitions, the photons scattered on the transitions are distinguishable, even if they have the same frequency. In an atomic system both decay channels emit the photon into different polarization modes (a σ^+ and σ^-

transition for example) and can therefore be distinguished with the right setup. Consequently, both transitions are treated as emission into different final states analog to the extension (a), but in contrast to the extension (a) both final states are connected to the same atomic level $|f\rangle$.

The two final states in the system connected to the decays from the excited states $|e_1\rangle$ and $|e_2\rangle$ are

$$|f, 1_\delta^{(1)}\rangle \triangleq |f, 1_\delta^{(1)}, 0_\delta^{(2)}\rangle \qquad \text{and} \qquad |f, 1_{\delta_2}^{(2)}\rangle \triangleq |f, 0_\delta^{(1)}, 1_\delta^{(2)}\rangle \qquad (5.44)$$

where $1_\delta^{(1)}$ and $1_\delta^{(2)}$ are the photon modes from the decay channels starting in the states $|e_1\rangle$ and $|e_2\rangle$. Both frequency modes have the same detuning δ with respect to a reference point.

In contrast to the other cases where the energy of the excited state was set to zero, in this case the excited states can have energy shifts η_1 respective η_2. Additionally, the initial states $|i_1\rangle$ and $|i_2\rangle$ are shifted by ν_1 and ν_2 with respect to an energy reference. Thus the internal Hamilton of this system becomes

$$\begin{aligned} \hat{H}_{0,\delta} = {} & \hbar(\Delta_1 + \nu_1)\,|i_1\rangle\,\langle i_1| + \hbar\eta_1\,|e_1\rangle\,\langle e_1| + \hbar\delta\,|f, 1_\delta^{(1)}\rangle\,\langle f, 1_\delta^{(1)}| \\ & + \hbar(\Delta_2 + \nu_2)\,|i_2\rangle\,\langle i_2| + \hbar\eta_2\,|e_2\rangle\,\langle e_2| + \hbar\delta\,|f, 1_\delta^{(2)}\rangle\,\langle f, 1_\delta^{(2)}|, \end{aligned} \qquad (5.45)$$

where Δ_1 and Δ_2 are the detunings of the excitation laser. This laser interaction is modeled by the operator

$$\hat{V} = \hbar\left(\frac{\Omega_1}{2}\,|e_1\rangle\,\langle i_1| + \frac{\Omega_1^*}{2}\,|i_1\rangle\,\langle e_1|\right) + \hbar\left(\frac{\Omega_2}{2}\,|e_2\rangle\,\langle i_2| + \frac{\Omega_2^*}{2}\,|i_2\rangle\,\langle e_2|\right), \qquad (5.46)$$

where Ω_1 and Ω_2 are the coupling strengths on both transitions. As in the previous extension (b) relative phase stability is assumed for both lasers.

The spontaneous decay channels into the final state are modeled by the operators

$$\hat{W}_{f1,\delta} = -i\hbar\frac{\Gamma_{f_1}}{2}\,|e_1\rangle\,\langle e_1| + \hbar g_{f_1}\,|f, 1_\delta^{(1)}\rangle\,\langle e_1| \quad \text{and} \quad \hat{W}_{f2,\delta} = -i\hbar\frac{\Gamma_{f_2}}{2}\,|e_2\rangle\,\langle e_2| + \hbar g_{f_2}\,|f, 1_\delta^{(2)}\rangle\,\langle e_2| \qquad (5.47)$$

with the coupling coefficients $g_{f_1} = \sqrt{\Gamma_{f_1}/(2\pi)}$ and $g_{f_2} = \sqrt{\Gamma_{f_2}/(2\pi)}$ given by the respective decay rates. The decay back into the initial states is described by the relaxation operators

$$\hat{c}_{i_1} = \sqrt{\Gamma_{i_1}}\,|i_1\rangle\,\langle e_1| \qquad \text{and} \qquad \hat{c}_{i_2} = \sqrt{\Gamma_{i_2}}\,|i_2\rangle\,\langle e_2|, \qquad (5.48)$$

where Γ_{i_1} and Γ_{i_2} are the respective decay rates.

An other option to describe such a five level system is to split the system into two smaller independent subsystems. The "left" subsystem contains the states $|i_1\rangle$, $|e_1\rangle$ and $|f, 1_\delta^{(1)}\rangle$ while the "right" subsystem contains the states $|i_2\rangle$, $|e_2\rangle$ and $|f, 1_\delta^{(2)}\rangle$. As there is no coupling between these system they can be treated independently from each other as three level system. Depending on whether both decay paths into the final state are distinguishable or indistinguishable both scattering amplitudes have to be summed up coherently or incoherently.

If both excited states are coupled to the same initial state, the description is analog but one has to replace the initial states $|i_1\rangle$ and $|i_2\rangle$ by the single initial state $|i\rangle$ in all terms. In this case both systems can not be separated anymore, because the ratio of the Rabi frequencies Ω_1 and Ω_2 determines the relative population in both sides.

(d) The final state is coupled to a further state

The last extension covers the case where the final state is coupled to an additional level $|a\rangle$ (see Figure 5.2 (d)). Since the formalism only covers the case were a single photon is scattered on the final transition, the state $|a\rangle$ may not be coupled to the excited or initial level. If the final state is coupled to the excited level resonance fluorescence is observed which is described differently. The coupling between the states $|a\rangle$ and $|f\rangle$ is done by a field with coupling strength Ω_2 and detuning Δ_2 from the transition. In the corresponding rotating frame, the interaction is described by

$$\hat{V}_2 = \hbar \left(\frac{\Omega_2}{2} |a\rangle \langle f| + \frac{\Omega_2^*}{2} |f\rangle \langle a| \right). \tag{5.49}$$

As the Raman scattering happens into a photon mode which is connected with the final state, also the state $|a\rangle$ is connected with this photon mode and becomes $|a, 1_\delta\rangle$ and the photon energy is added to this state in analogy to the final state $|f, 1_\delta\rangle$. Thus the internal Hamilton becomes

$$\hat{H}_{0,\delta} = \hbar\Delta_1 |i\rangle \langle i| + \hbar\delta |f, 1_\delta\rangle \langle f, 1_\delta| + \hbar(\delta - \Delta_2) |a, 1_\delta\rangle \langle a, 1_\delta|. \tag{5.50}$$

The interaction Hamilton that describes the spontaneous decay on the Raman transition and the operator that describes the decay into the initial state are the same as in the description for the three level system. In the same way as the decay on the initial transition, I describe the decay from the state $|a\rangle$ back into the state $|f\rangle$ with the relaxation $\hat{c}_a = \sqrt{\Gamma_a} |f, 1_\delta\rangle \langle a, 1_\delta|$. As for all other cases the spectrum of the photon is given by the amount of population in the photon mode 1_δ. As this mode is distributed over two states, the population in both states has to be summed up to get the power spectrum

$$S(\delta, t) = |C_{f,\delta}(t)|^2 + |C_{a,\delta}(t)|^2 \tag{5.51}$$

of the scattered photon.

If the state $|a\rangle$ decays to a further state $|b\rangle$, the decay has to be introduced in the same way as the decay back into the initial state to keep the population in the system. In this case, also the state $|b\rangle$ is connected with the emitted photon mode. If the initial or excited state decays into the states $|a\rangle$ or $|b\rangle$, additional states $|a, 0_\delta\rangle$ and $|b, 0_\delta\rangle$ that are not connected to the photon mode 1_δ have to be introduced to describe the system. In such a case the model contains the states $|a, 1_\delta\rangle$ and $|b, 1_\delta\rangle$ which are populated by the path including the Raman scattering as well as the states $|a, 0_\delta\rangle$ and $|b, 0_\delta\rangle$ which are populated directly from the initial and excited state. The decays populating the states $|a, 0_\delta\rangle$ and $|b, 0_\delta\rangle$ have to be introduced by operators $\hat{c}$ analogue to the decay back into the initial state.

5.1.4. Model for the Raman scattering of single 393 nm photons from $^{40}\text{Ca}^+$

The four extensions (a)-(d) are combined to model the Raman scattering of single photons with $^{40}\text{Ca}^+$. Here, I combine the first three extensions (a)-(c) to model the Raman scattering of 393 nm photons from the $\text{D}_{5/2}$ manifold, where the 854 nm transition is excited. Therefore the 850 nm decay into the $\text{D}_{3/2}$ manifold is treated as parasitic decay. The Zeeman levels of the $\text{S}_{1/2}$ state are not coupled to other states.

The system to model the spectrum of scattered 393 nm photons contains six initial states corresponding to the Zeeman levels of the $\text{D}_{5/2}$ manifold. These states are coupled to four excited states in the $\text{P}_{3/2}$ manifold by the 854 nm laser. From the excited states the ion decays into the two Zeeman levels in the $\text{S}_{1/2}$ ground state. Because there are six possible decay channels these Zeeman levels are connected to six final states. Thus the model contains a total number of sixteen levels. Nevertheless, I refer to the model by the number of atomic levels, which is in this case twelve Zeeman levels.

The internal Hamilton of the system becomes

$$
\begin{aligned}
\hat{H}_{0,\Delta_{393,\text{m}}} = {}& \hbar \sum_{m_\text{D}} \left(\Delta_{854,\text{m}} + g_\text{D} m_\text{D} \mu_\text{B} B \right) |\text{D}_{m_\text{D}}\rangle \langle \text{D}_{m_\text{D}}| \\
& + \hbar \sum_{m_\text{P}} g_\text{P} m_\text{P} \mu_\text{B} B |\text{P}_{m_\text{P}}\rangle \langle \text{P}_{m_\text{P}}| \\
& + \hbar \sum_{m_\text{S}} \sum_{k} \left(\Delta_{393,\text{m}} + g_\text{S} m_\text{S} \mu_\text{B} B \right) |\text{S}_{m_\text{S}}, 1^k_{\Delta_{393,\text{m}}}\rangle \langle \text{S}_{m_\text{S}}, 1^k_{\Delta_{393,\text{m}}}|,
\end{aligned}
\tag{5.52}
$$

where $g_\text{D} \approx \frac{6}{5}$, $g_\text{P} \approx \frac{4}{3}$ and $g_\text{S} \approx 2$ are the Landé factors of the atomic manifolds. Together with the magnetic quantum numbers m_D, m_P and m_S they determine the energy shift due to the applied magnetic field B. The index $k \in \{\sigma^-, \pi, \sigma^+\}$ denotes the different decay channels into the same Zeeman level of the final $\text{S}_{1/2}$ state. The detuning $\Delta_{854,\text{m}}$ of the 854 nm laser and the detuning $\Delta_{393,\text{m}}$ of the 393 nm frequency mode are with respect to the transition line centers defined by $B = 0\,\text{G}$.

The spontaneous 393 nm decay is described by the operator

$$
\hat{W}_{393} = \hbar \sum_{m_\text{P}} \sum_{m_\text{S}} \left(C_{m_\text{P},m_\text{S}} \sqrt{\frac{\Gamma_{393}}{2\pi}} |\text{S}_{m_\text{S}}, 1^k_{\Delta_{393,\text{m}}}\rangle \langle \text{P}_{m_\text{P}}| - \text{i} \frac{\Gamma_{393}}{2} C^2_{m_\text{P},m_\text{S}} |\text{P}_{m_\text{P}}\rangle \langle \text{P}_{m_\text{P}}| \right)
\tag{5.53}
$$

with the 393 nm decay rate Γ_{393} and the individual Clebsch-Gordan coefficients $C_{m_\text{P},m_\text{S}}$. In all cases only the Clebsch-Gordan coefficients for $\Delta m = m_\text{P} - m_\text{S} = 0, \pm 1$ are non-zero.

The parasitic 850 nm decay is introduced by the operator

$$
\hat{W}_{850} = -\text{i}\hbar \frac{\Gamma_{850}}{2} \sum_{m_\text{P}} |\text{P}_{m_\text{P}}\rangle \langle \text{P}_{m_\text{P}}|.
\tag{5.54}
$$

The 854 nm decay back into the initial $|D_{5/2}\rangle$ levels is introduced by relaxation operators

$$\hat{c}_{\Delta m} = \sum_{m_D} C_{m_P, m_D + \Delta m} \sqrt{\Gamma_{854}} |D_{m_D}\rangle \langle P_{m_D + \Delta m}| . \quad (5.55)$$

Each of the relaxation operators $\hat{c}_{\Delta m}$ covers all decay channels with $\Delta m = m_P - m_D$ that carry the same polarization. The factor C_{m_P, m_D} is the Clebsch-Gordan coefficient of the individual decay path. Again only the Clebsch-Gordan coefficients for $\Delta m = 0, \pm 1$ are non-zero.

Each of the 854 nm decay paths is excited with the 854 nm laser that is modeled by the operator

$$\hat{V} = \hbar \sum_{m_D} \sum_{m_P} g_{\Delta m} C_{m_P, m_D} \left(\frac{\Omega_{854}}{2} |P_{m_P}\rangle \langle D_{m_D}| + \frac{\Omega_{854}^*}{2} |D_{m_D}\rangle \langle P_{m_P}| \right) . \quad (5.56)$$

The strength of the individual interaction is determined by the Clebsch-Gordaon coefficient C_{m_P, m_D} and the coupling strength $g_{\Delta m}$ which takes the polarization and direction of the laser with respect to the quantization axis into account. More details on the description of the laser direction with respect to the quantization axis and polarization can be found in [25].

The line width $\Delta \omega$ of the laser is introduced by a relaxation operator

$$\hat{c}_L = \sqrt{\frac{\Delta \omega}{2}} \left(\sum_{m_D} |D_{m_D}\rangle \langle D_{m_D}| - \sum_{m_P} |P_{m_P}\rangle \langle P_{m_P}| \right) . \quad (5.57)$$

The operators for the internal Hamilton, the decay on the three dipole transitions, the laser interaction and the laser line width are inserted into equation 5.33. Two different approaches are taken to solve the generated differential equations using Matlab. The first approach for a time independent Rabi frequency Ω_{854} is to transform the density matrix ρ into a vector $\vec{\rho}$ with the same entries to write the equation of motion as $\dot{\vec{\rho}} = \hat{L} \cdot \vec{\rho}$, with the Liouville super operator $\hat{L}$ (for details see [25]). This equation can be integrated with the solution

$$\vec{\rho}(t) = e^{\int \hat{L} dt} \vec{\rho}(0). \quad (5.58)$$

For a time dependent Rabi frequency $\Omega_{854} = \Omega_{854}(t)$ the second approach is taken as each time step has to be calculated after each other. In this case Equation 5.33 is solved by direct numerical integration.

The model for spectra of 854 nm photon is build analogously to the 393 nm model. In this case the $S_{1/2}$ Zeeman levels are the initial states, while the $D_{5/2}$ Zeeman levels become the final states. Since there are more decay channels into the $D_{5/2}$ Zeeman levels, the resulting system has a total number of eighteen levels, including twelve levels connected to individual 854 nm decay channels.

5.2. Quantum interference effects in Raman-scattered photons

The model developed in the previous sections enables a theoretical study of the spectrum of a scattered Raman photon. For a detailed theoretical study on the spectrum of a photon generated in a three level system I refer to [25]. Here, I briefly discuss several interference effects that occur in more complex systems and affect the spectrum of the scattered photon. I discuss interference in absorption, in emission or caused by coupling to a further level. For all cases I consider systems which are found similar in the ^{40}Ca$^+$ ion for the scattering of a 393 nm Raman photon out of the D$_{5/2}$ manifold. I chose branching rations similar to the branching ratios of the 393 nm, 854 nm and 850 nm transition in the ^{40}Ca$^+$ ion. For simplicity, here, I omit the Clebsch-Gordan coefficients or effects due to laser polarization. In the second part of the following Chapter 6 this brief discussion is complemented by a study on measured spectra showing these interference effects.

5.2.1. The upper level coupling case

In the upper level coupling case (see Figure 5.3) the excited state is coupled to a second initial state $|i_2\rangle$. This case is similar to the upper level coupling discussed for spontaneous emission in [87] and therefore referred to by the same name. Also the effect on the spectrum is comparable.

All population is prepared in the first initial state $|i_1\rangle$. This level is excited by a laser with Rabi frequency Ω_1 and detuning Δ_1 to the excited state $|e\rangle$. Additionally a second level $|i_2\rangle$ is coupled to the excited state by a laser with Rabi frequency Ω_2 and detuning Δ_2. From the excited state, the system decays into the final state $|f\rangle$ by emitting a Raman photon or back into the initial states from where the system is excited again. I set the branching ratio of the involved decay rates to $\Gamma_f/\Gamma = 0.935$, $\Gamma_{i_1}/\Gamma = 0.058$ and $\Gamma_{i_2}/\Gamma = 0.007$. These values correspond the the branching ratios of the 393 nm, 854 nm and 850 nm decays out of the P$_{3/2}$ manifold of the ^{40}Ca$^+$ ion. The coupling on the transition out of the initial state $|i_1\rangle$ has a Rabi frequency $\Omega_1 = \Gamma$ and a detuning $\Delta_1 = 0$. I vary the coupling on the second transition in two ways to discuss the effect of this coupling.
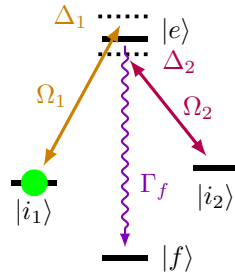
Figure 5.3.: Upper level coupling. All population is prepared in the initial state $|i_1\rangle$. A second state $|i_2\rangle$ is coupled to the excited state.
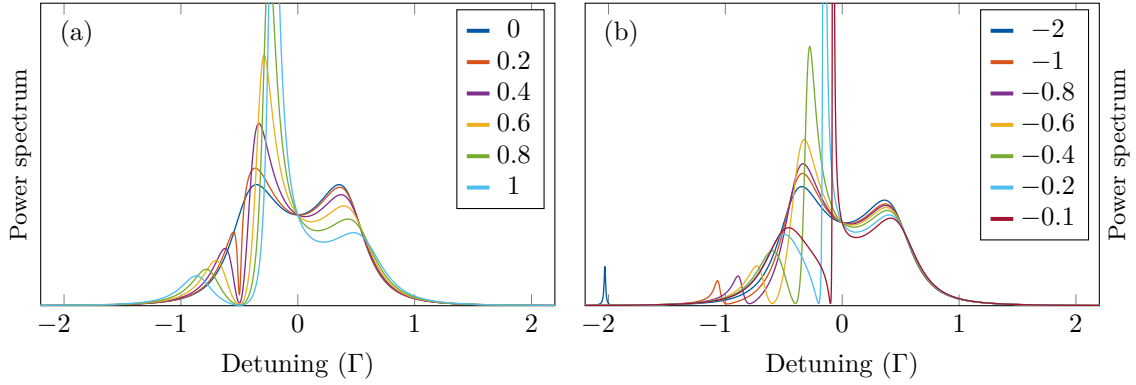
Figure 5.4.: Effect of the upper level coupling on the spectrum of a Raman photon. (a) Different values of Ω_2/Γ for a fixed detuning $\Delta_2 = -\Gamma/2$. (b) Different detunings Δ_2/Γ for a fixed Rabi frequency $\Omega_2 = \Gamma/2$. The values $\Omega_1 = \Gamma$ and $\Delta_1 = 0$ are fixed in all cases.

The first case is a scanned Rabi frequency Ω_2 for a fixed detuning $\Delta_2 = -\Gamma/2$. The second case is a scanned detuning Δ_2 for a fixed Rabi frequency $\Omega_2 = \Gamma/2$. For both cases, the emitted spectrum has a hole at the frequency mode with detuning Δ_2. For an increasing Rabi frequency Ω_2, the hole becomes broader (see Figure 5.4 (a)). If the detuning Δ_2 is changed, the position of the hole changes accordingly (see Figure 5.4 (b)).

As in the upper level coupling case for spontaneous emission [87, 88, 93] I attribute the hole in the spectrum to destructive interference of the involved scattering amplitudes. The decay back into the initial states $|i_1\rangle$ and $|i_2\rangle$ affects the depth of the hole. For a system without back decays the model predicts a complete suppression of the emission into the frequency mode at the position of the hole. Furthermore, the model predicts, that the relative phase between both Rabi frequencies Ω_1 and Ω_2 does not influence the upper level coupling effect. Reason is, that all population is prepared in the initial state $|i_1\rangle$. Thus there is no initial phase information between both coupled transitions.

An example of the upper level coupling are two Zeeman levels of the same atomic manifold, that are coupled to the same excited state. This is the case for a system prepared in any of the $D_{5/2}$ Zeeman levels that are excited by a vertically polarized $854\,\mathrm{nm}$ laser perpendicular to the magnetic field. The levels $|D_{5/2}, m\rangle$ and $|D_{5/2}, m \pm 2\rangle$, are coupled to the same $P_{3/2}$ Zeeman level. As both transitions are coupled by the same laser, the ratio of both Rabi frequencies is given directly by the corresponding Clebsch-Gordan coefficients. Similar, the detuning of the laser with respect to both transitions is given by the energy splitting in the $D_{5/2}$ state. Therefore, the relative detuning $\Delta_1 - \Delta_2$ is only given by this energy splitting. To change the relative detuning, the strength of the applied field has to be changed. I observe the described case in the spectra shown in Figure 6.3, where the ion is prepared in the $|D_{5/2}, +\frac{5}{2}\rangle$ level. A dip in the spectrum is caused by the additional coupling of the $|P_{3/2}, +\frac{3}{2}\rangle$ level to the $|D_{5/2}, +\frac{1}{2}\rangle$ level with the same laser. Due to vibration side bands, broadening of the measurement apparatus and the decay back into the initial state, the depth of the hole is reduced.

5.2.2. The lower level coupling case

In the lower level coupling case, the final state $|f\rangle$ of the Raman scattering process is coupled to a level $|a\rangle$ (see Figure 5.5). A similar scheme for the spontaneous decay is discussed in [87]. Therefore I refer to the scheme by the same name.

The system is prepared in the initials state $|i\rangle$. A laser (Ω_1, Δ_1) excites the system into the excited state $|e\rangle$ and a Raman photon is emitted on the transition into the final state $|f\rangle$. This final state is coupled by a second laser (Ω_2, Δ_2) to the state $|a\rangle$ from where the system decays either back into the final state or into a further state $|b\rangle$. I set the branching ratios for the decays from the excited state to $\Gamma_f/\Gamma = 0.941$ and $\Gamma_i/\Gamma = 0.059$. In several sets, I change the coupling on the initial transition, the coupling on the second transition and the decay rate of the state $|a\rangle$. If the final state $|f\rangle$ is not coupled to the state $|a\rangle$ ($\Omega_2 = 0$), the presence of the state $|a\rangle$ in the system has no effect on the spectrum.

The coupling of the final state to an additional level leads to dressed states, which are observed as an Autler-Townes splitting in the spectrum if the coupling strength is big enough. The splitting increases with increasing Rabi frequency Ω_2 (see Figure 5.6 (a)). For a strong coupling on the initial transition ($\Omega_1 > \Gamma/2$), there are dressed states created out of the initial and excited states. Consequently, the spectrum shows an Autler-Townes splitting without the coupling Ω_2. An additional strong coupling Ω_2 creates dressed states out of the states $|f\rangle$ and $|a\rangle$ that lead to an additional Autler-Townes splitting so that the spectrum has a double Autler-Townes splitting (see Figure 5.6 (b)). Each of the spectral components generated by the coupling Ω_1 is again split due to the coupling Ω_2.

For a detuning $\Delta_2 = 0$ (a,b) both dressed states generated by Ω_2 are split symmetrical around the original state $|f\rangle$ and thus equally populated. If the lower level coupling is off resonant ($\Delta_2 \neq 0$), the dressed states are shifted in direction of the detuning. For a blue detuned lower level coupling ($\Delta_2 > 0$), the spectrum shifts to positive frequencies and becomes asymmetrical (see Figure 5.6 (c)). The peak closer to resonance is stronger populated. Additionally, the splitting increases as the absolute detuning $|\Delta_2|$ becomes larger. Because the dressed states of the lower level coupling are independent from Ω_1 and Δ_1 the spectrum remains symmetrical around the final state for all values of Δ_1, as long as the condition $\Delta_2 = 0$ is met.

To show the influence of the decay rate of the state $|a\rangle$, I compare spectra for different decay
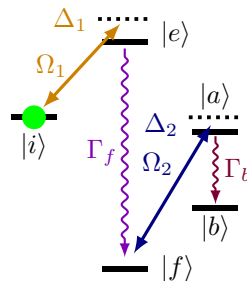
Figure 5.5.: Lower level coupling. The final state $|f\rangle$ is coupled to a state $|a\rangle$.
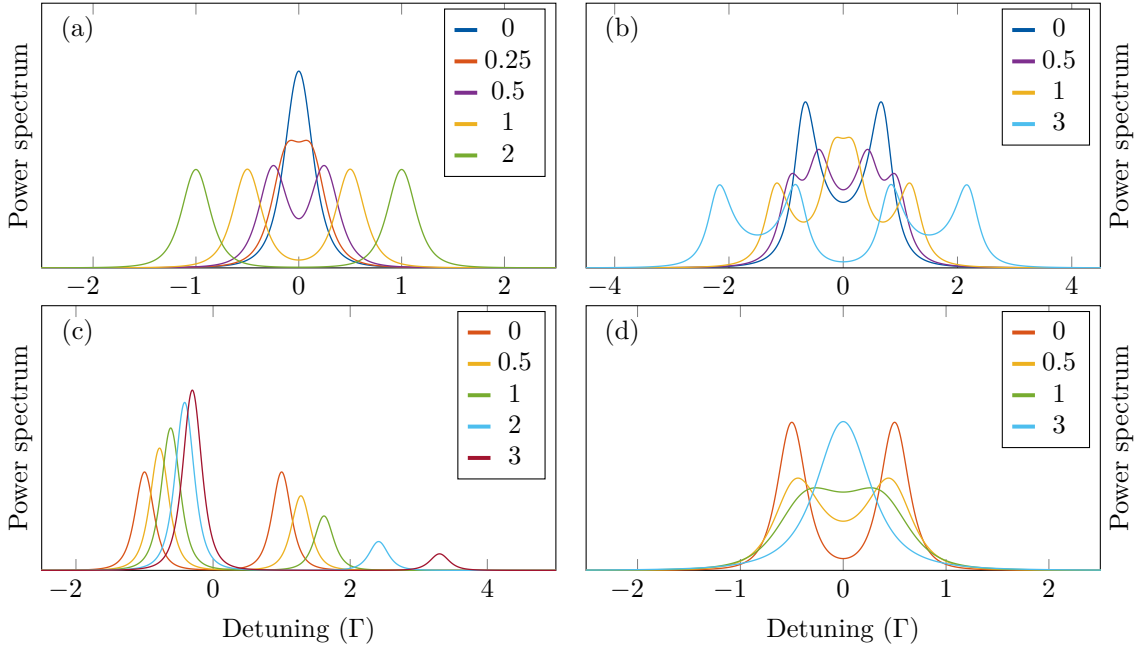
Figure 5.6.: Effect of the lower level coupling on the spectrum of a Raman photon. (a,b) The Rabi frequency Ω_2 of the coupling is scanned for a fixed detuning $\Delta_2 = 0$ and (a) $\Omega_1 = \Gamma/2$ or (b) $\Omega_1 = 1.5\Gamma$. (c) Scanned detuning Δ_2 for fixed Rabi frequencies $\Omega_2 = 2\Gamma$ and $\Omega_1 = \Gamma/2$. In all cases (a-c) the state $|a\rangle$ is treated as stable. (d) For fixed values $\Delta_2 = 0$, $\Omega_2 = \Gamma$ and $\Omega_1 = \Gamma/2$, the decay rate Γ_{af} of the state $|a\rangle$ into the final state $|f\rangle$ is scanned. The same detuning $\Delta_1 = 0$ is set in all cases.

rates (see Figure 5.6 (d)). The individual peaks of the Autler-Townes splitting vanishes as the decay rate Γ_a increases. Thereby, it is no difference whether the decay goes into the state $|f\rangle$ or into an other state $|b\rangle$. Both cases broaden the state $|a\rangle$ and with this the spectrum in the same way.

To realize the lower level coupling for 393 nm photons generated with the ^{40}Ca$^+$ ion, the final S$_{1/2}$ state has to be coupled to the P$_{1/2}$ state with a 397 nm laser or to the D$_{3/2}$ state with a 732 nm laser. Also a coupling on the transition between both Zeeman levels of the S$_{1/2}$ manifold is possible. While all of these cases are in principle possible, each of them has its own experimental challenges or limitations. In case of the coupling with the 397 nm laser one has to ensure, that the detector setup distinguishes 393 nm and 397 nm photons. At the moment the single mode coupling is optimized for 393 nm photons but also a few 397 nm photons are collected. The same holds for the coupling of the analysis cavity setup. A 732 nm laser that drives the transitions from the S$_{1/2}$ to D$_{3/2}$ state has to be set up from scratch. The RF coil to drive the transition in the ground state is in principal the easiest way, as it requires no additional setup or effort. In this case the parameter range is limited due to the low transition frequency of about 8 MHz. Thus, realizing the lower level coupling with the the 397 nm laser is the best option.

5.2.3. Quantum interference in absorption: The Λ-scheme

Quantum interference in absorption occurs, if two populated initial states are coupled to the same excited state. This is the case in a Λ-shaped level system, where, in contrast to the upper level coupling case, the population is distributed between both initial states $|i_1\rangle$ and $|i_2\rangle$ (see Figure 5.7). Here, I consider two initial states, that are both Zeeman levels of the same atomic manifold. The system is prepared in a balanced superposition between both initial states $|i_1\rangle$ and $|i_2\rangle$, which are energy shifted by $+\hbar\Gamma/2$ respective $-\hbar\Gamma/2$. Both initial states are coupled to the excited state by a laser with Rabi frequency Ω that is set on the line center between both excited transitions. The branching ratios are set to $\Gamma_f/\Gamma = 0.941$ for the decay to the final state and $\Gamma_i/\Gamma = 0.0295$ for the decays back into the initial states.

The spectral and temporal shape of a Raman photons scattered in the Λ-scheme depends on the phase ϕ of the initial superposition (see Figure 5.8). The spectrum of the photons created out of a superposition shows an enhancement and suppression of the emission into certain frequency modes compared to the spectrum of photons created out of a mixed state (a,b). The interference thereby depends on the spectral overlap of the components from the scattering paths that start in $|i_1\rangle$ or $|i_2\rangle$. For a large spectral overlap (a), the spectrum has a large central peak with two small peaks at the side or two peaks at the side and a hole in the middle. For a smaller Rabi frequency (b), the spectral components are almost separated and each spectrum has two peaks and a small plateau between the peaks. However, because the emission process is not affected by the interference all spectra carry the same population independently from the initial superposition. The wave packets show a modulation with a frequency that corresponds to the frequency splitting of the initial states $|i_1\rangle$ and $|i_2\rangle$. As fundamental interference mechanism a interference in the absorption process was found [19,56] that leads to an enhancement and suppression of the depopulation process of the initial states which can be observed as a stair-like population evolution in the initial states (e,f). Because the initial states are coupled with each other via the excited state, the excitation process has to be described in a system that contains the states $|i_1\rangle$, $|i_2\rangle$ as well as $|e\rangle$ and cannot be described separately in two three level systems as done in [20].
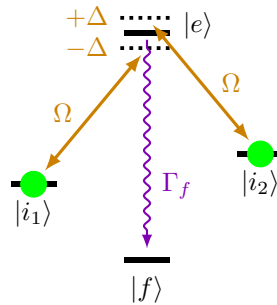
Figure 5.7.: Λ-scheme. The system is prepared in a superposition of two initial states $|i_1\rangle$ and $|i_2\rangle$ that are coupled to the same excited state.
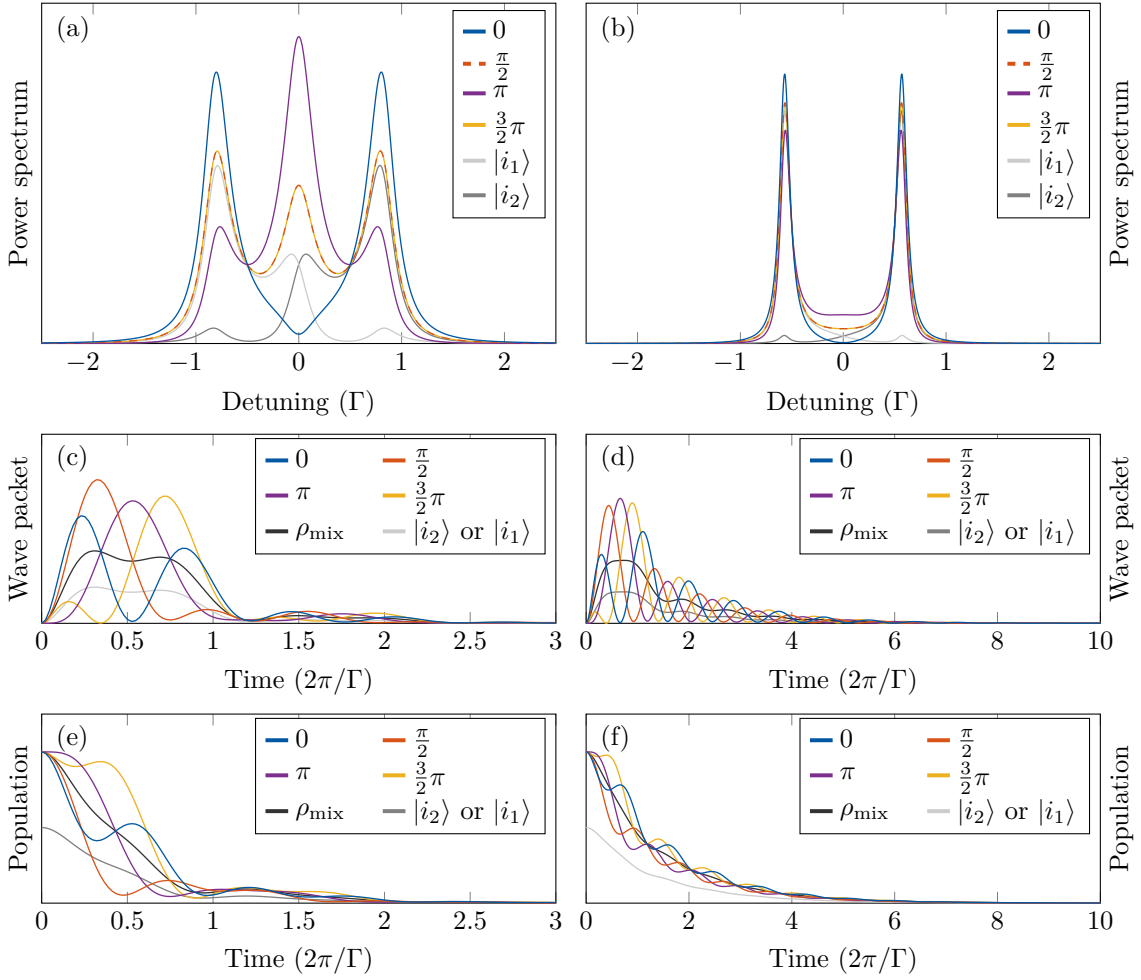
Figure 5.8.: Effect of quantum interference in absorption on the spectrum (a,b) and wave packet (c,d) of a Raman photon for different phases ϕ of the initial superposition. (e,f) Sum of the population in the initial states $|i_1\rangle$ and $|i_2\rangle$. (a,c,e) $\Omega = \Gamma$. This corresponds to the parameters discussed in [20]. (a,c,e) $\Omega = \Gamma/2$. For both cases, the initial states have an energy splitting of $\pm\hbar\Gamma$. The spectra for a mixed initial state and a phase $\phi = \frac{\pi}{2}$ or $\phi = \frac{3}{2}\pi$ are equal.

Similar to the upper level coupling case the initial superposition can be created between two Zeeman levels from different atomic states, for example from the $\mathrm{D}_{5/2}$ and $\mathrm{D}_{3/2}$ manifold. As the interference not only depends on the relative phase of the initial superposition but also the relative phase of both Rabi frequencies Ω_1 and Ω_2 two phase stable lasers are required in this case. If a single laser drives both transitions phase stability is ensured.

This interference effect is further discussed in Section 6.2.3 on the basis of measured spectra.

5.2.4. Quantum interference in emission: The V-scheme

Quantum interference in the emission process occurs, if two scattering paths that end in the same final state $|f\rangle$ are indistinguishable. An example is the V-shaped system shown in Figure 5.9. The system is prepared in a balanced superposition of the initial states $|i_1\rangle$ and $|i_2\rangle$ with a phase ϕ. This superposition is excited to the states $|e_1\rangle$ and $|e_2\rangle$ from where two σ decay channels, which are indistinguishable due to a collection perpendicular to the quantization axis and projection on vertically polarized photons, go to the final state $|f\rangle$. I consider a system, where both initial states are Zeeman levels of the same atomic manifold. The energies of the initial states are shifted by $+\hbar\Gamma/2$ respective $-\hbar\Gamma/2$. The excited states are Zeemen levels of a different atomic manifold which have the branching ratios $\Gamma_f/\Gamma = 0.941$ and $\Gamma_i/\Gamma = 0.059$. To compare the V-scheme and the Λ-scheme I set two different energy shifts for the excited states. In the first set, both excited states have the same energy. In the second set the energies of the excited states are shifted by $+\hbar\Gamma/4$ respective $-\hbar\Gamma/4$. For both sets, the initial states are coupled to the excited states with a Rabi frequency $\Omega = \Gamma$ on resonance with the line center between both transitions, what corresponds to $\Delta_1 = -\Delta_2$.

As for the Λ-scheme, the spectral and temporal shape of the photon depends on the phase of the initial superposition (see Figure 5.10). Each spectrum has two peaks that are caused by the "left" and "right" scattering path (a,b). Between the peaks the spectrum has a plateau or a peak depending on the phase of the initial superposition. In difference to the Λ-scheme each spectrum carries a different population what reveals the fundamental difference between both interference mechanisms. In case of the interference in emission, the emitted photon amplitudes interfere with each other what results in an emission pattern that rotates around the quantization axis [19, 56], where the initial phase depends on the phase of the prepared initial superposition. For a fixed position of the observer, this leads to a modulation in the wave packet with a frequency that corresponds to the energy difference of the initial states (c,d). As the duration of the photon wave packet is comparable with the rotation period of the emission pattern, the population in each spectrum and wave packet depends on the initial superposition. For a wave packet much longer than the oscillation period, what corresponds
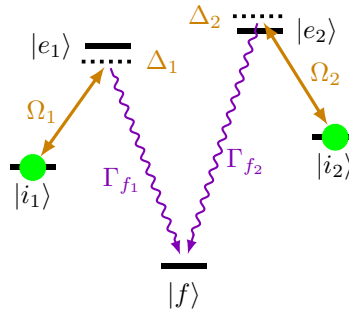
Figure 5.9.: V-scheme. The system is prepared in a superposition of two initial states $|i_1\rangle$ and $|i_2\rangle$, which are coupled to different excited states that decay to the same final state.
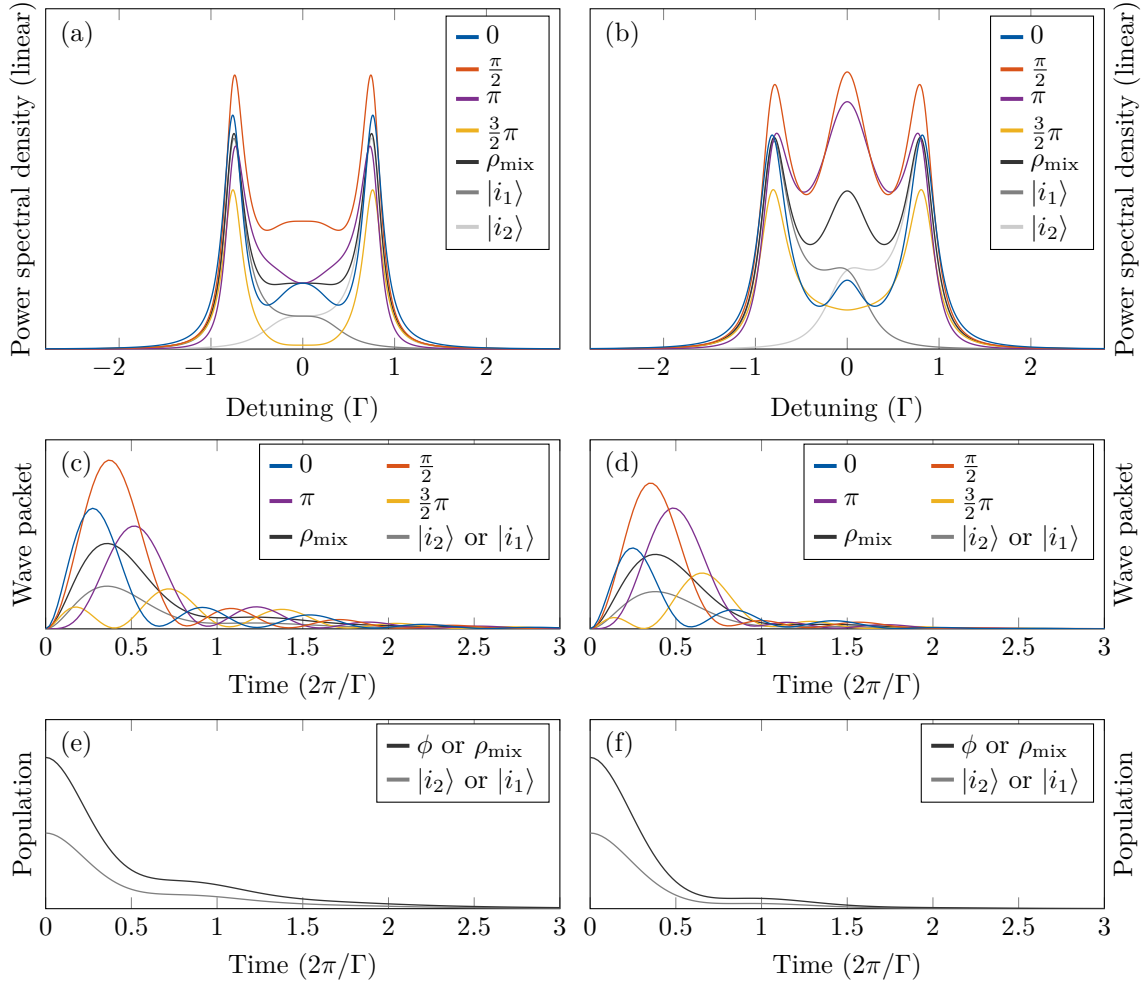
Figure 5.10.: Effect of quantum interference in emission on the spectrum (a,b) and wave packet (c,d) of a Raman photon for different phases ϕ of the initial superposition. (e,f) Sum of the population in the initial states $|i_1\rangle$ and $|i_2\rangle$. In both cases the initial states are separated by $\hbar\Gamma$ while the excited states have an energy splitting of (a,c,e) 0 or (b,d,f) $\hbar\Gamma/2$. The same Rabi frequency $\Omega = \Gamma$ and detunings $\Delta_1 = -\Delta_2$ are used in all cases.

to two separated spectral components and a spectral shape with almost no dependence on the initial superposition, the difference in the population vanishes. Because both scattering paths are independent from each other, the depopulation of the initial manifold (e,f) does not depend on the initial superposition and both scattering paths can be treated as independent three level system [2].

---

[2]This approach was chosen in [20] where both scattering amplitude of the Λ-scheme were calculated as independent three level systems and added afterwards with the relative phase of the initial atomic superposition. However, as discussed here this corresponds to the V-shaped system and not a Λ-shaped system. The spectra in Figure 5.10 (a) correspond to the spectra presented in [20]. In a Λ-shaped system both initial states and the excited states are coupled together and both scattering paths can not be calculated independently from each other.

In Section 6.2.4 I further discuss this interference effect on the basis of measured spectra. There I also argue how this interference builds the basis for the atom-photon entanglement schemes discussed in Chapter 7.

5.3. Summary

In this chapter I developed a model to calculate the spectrum of a single Raman-scattered photon. For a three level system and monochromatic excitation, the same results as in [20, 25] were found. However, the here presented model covers arbitrarily modulated laser fields as for example the rise time of an acousto-optic modulator or multiple frequency components. Additionally, the model covers multi level systems, initial superposition states and excitation on several transitions.
In the following two chapters, I apply the analytic model for a three level system (Equation 5.29 and Equation 5.30) and the twelve level model for the ^{40}Ca$^+$ ion (see Section 5.1.4). In case of the atom-photon entanglement and the quantum interference in emission, the system is approximated well by a three level system. I derive the observed interference effect and creation time dependence with the analytic three level model. With the twelve level model, I model the spectrum of scattered photons. It is used to calculate the expected spectrum shown in all spectrum measurements together with the measured data. Furthermore, I use the twelve level model to search for optimal experimental parameters. For the atom-photon entanglement schemes with a bichromatic laser excitation I optimize the detunings of both frequency components. For the quantum inferference in absorption, in emission and due to a bichromatic laser excitation, I optimize laser parameters and the prepared initial state.

6. The spectrum of single Raman photons

This chapter is devoted to the question how the spectrum of a Raman-scattered single photon looks like. To answer this question, I measure the spectrum of single Raman scattered photons. I study how the spectral shape depends on the Rabi frequency Ω, the detuning Δ and the pulse shape of the driving laser field. Afterwards, I explore the influence of quantum interference effects on the photon spectrum and thus tie in with the brief theoretical consideration in the previous chapter. The main focus of this chapter thereby lies on spectra of 393 nm photons, but also 854 nm photon spectra are measured to complement the analysis. The executed pulse sequences to generate the photons and the protocol to measure the spectra as well as the evaluation is presented detailed in Section 4.5.

6.1. Spectral properties of single Raman-scattered photons

To study the spectral shape of single Raman scattered photons, I generate 393 nm photons or 854 nm photons in systems, that are close to a three level system (see Figure 6.1). I generate photons for a large range of different Rabi frequencies Ω and detunings Δ and measure the power spectrum and power wave packet of the scattered Raman photon for each parameter set. From the measured spectrum and wave packet, I determine the spectral width, temporal duration and time-bandwidth product of the generated photon. Furthermore, I explore the effect of the ion temperature and incomplete photon generation on the spectrum.

To generate 393 nm photons, I prepare the $^{40}\text{Ca}^+$ ion in the $|\text{D}_{5/2}, -\frac{5}{2}\rangle$ Zeeman level as initial state of the Raman scattering process. The outer $\text{D}_{5/2}$ states offers the maximal intrinsic
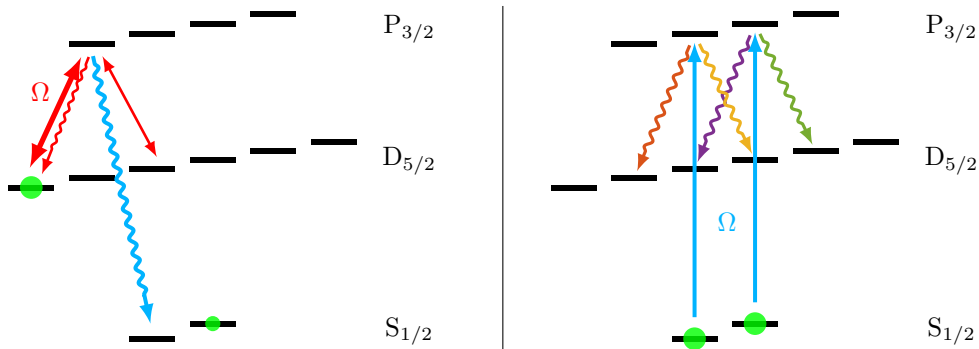
Figure 6.1.: Schemes to generate 393 nm (left) or 854 nm photons (right). I vary the parameters of the excitation laser to study properties of the generated photons.

efficiency due to the Clebsch-Gordan coefficients of the involved transitions. The $|D_{5/2}, -\frac{5}{2}\rangle$ state is favored compared to the $|D_{5/2}, +\frac{5}{2}\rangle$ state due to a partial optical pumping in the Doppler cooling period. A vertically polarized 854 nm laser perpendicular to the magnetic field, excites the initial state. By emitting a 393 nm photon the system returns to the $S_{1/2}$ ground state. I collect the generated 393 nm photons on quantization axis and couple them in a single mode or multi mode fiber. The photons in the single mode fiber are sent to the analysis cavity setup to measure the spectrum. The photons in the multi mode fiber are sent directly to a detector to measure the wave packet.

To generate 854 nm photons no state preparation is required. I excite a mixture in the $S_{1/2}$ ground state with a horizontally polarized 393 nm laser perpendicular to the magnetic field. This ensures a selective excitation of the π transitions. I collect the generated 854 nm photons on quantization axis and couple them into a single mode fiber. As for the 393 nm photons, the photons are sent to the analysis cavity setup to measure the photon spectrum or detected directly to measure the wave packet. Due to the photon collection on quantization axis, I detect only photons emitted on σ transitions. Together with a state detection after the photon detection and the polarization of the 393 nm laser that selectively excites π transitions, I am able to assign a scattering path to each detection event.

6.1.1. Dependence on the Rabi frequency Ω and detuning Δ

To study how the Rabi frequency Ω and detuning Δ of a monochromatic laser excitation affect the spectrum from the generated photon, I generate photons for different combinations of Ω and Δ. I generate 393 nm Raman photons with five different Rabi frequencies $\Omega_{854,t}$ on the excited $|D_{5/2}, -\frac{5}{2}\rangle$ to $|P_{3/2}, -\frac{3}{2}\rangle$ transition. For each Rabi frequency I set the excitation laser to different detunings $\Delta_{854,t}$ with respect to the excited transition. Measurements on 854 nm Raman photons complement the findings. There, I generate 854 nm Raman photons with two different Rabi frequencies $\Omega_{393,t}$ on the excited 393 nm transitions. The applied magnetic field shifts the involved Zeeman levels of the $S_{1/2}$ and $P_{3/2}$ state with respect to the transition line center. As result two different detunings $\Delta_{393,t}$ are applied to the "left" and "right" π transition (see Figure 6.1, right). An overview of the parameters is listed in Table 6.1. The measured 393 nm photon spectra are shown in figures 6.2 and 6.3. The spectra of the 854 nm photons are shown in Figure 6.4.

393 nm photon spectra

The 393 nm photons generated with $\Omega_t = 2.68(2)$ MHz have two sidebands located at ± 2.1 MHz. The spectrum becomes broader for larger Rabi frequencies and the sidebands merge with the carrier. However, the sidebands are still visible in some spectra of the photons generated with $\Omega_t = 8.03(3)$ MHz and $\Omega_t = 12.69(5)$ MHz. For larger Rabi frequencies $\Omega_t = 28.1(3)$ MHz and $\Omega_t = 53.0(3)$ MHz the sidebands are no longer resolved. I determine the relative strength $c_{sb} = 0.44(6)$ of the sidebands from the spectra measured with $\Omega_t = 2.68(2)$ MHz

Table 6.1.: Parameters of the 854 nm and 393 nm excitation laser that I use to generate 393 nm and 854 nm Raman photons from which the spectra are discussed in this Section 6.1.1. A detailed overview over the experimental parameters is given in Appendix C.1.

	393 nm photons					854 nm photons	
Ω (MHz)	2.68(2)	8.03(3)	12.69(5)	28.1(3)	53.0(3)	5.51(6)	9.5(2)
Δ_{min} (MHz)	-22.5	-24.2	-45.1	-45.0	-45.5	-11.1	-1.5
Δ_{max} (MHz)	$+22.0$	$+22.1$	$+44.8$	$+44.8$	$+45.8$	-8.4	1.2
Measurements	9	9	9	9	5	4	4
Figure	6.2 (a)	6.2 (b)	6.2 (c)	6.3 (d)	6.3 (e, f)	6.4 (a)	6.4 (b)
Appendix	C.1.1	C.1.2	C.1.3	C.1.4	C.1.5	C.1.6	C.1.6

and $\Omega_{\text{t}} = 8.03(3)$ MHz. This value for c_{sb} is used to model the 393 nm spectra of photons generated with larger Rabi frequencies.

The spectrum of the generated photon shifts with the detuning $\Delta_{854,\text{t}}$ of the 854 nm laser pulse. I indicate the applied detuning with a vertical dashed line in the displayed spectra (see Figure 6.2 and Figure 6.3). For a small Rabi frequency $\Omega_{\text{t}} = 2.66(2)$ MHz the spectrum is located at the 393 nm detuning that corresponds to the detuning of the 854 nm laser excitation. For larger Rabi frequencies the position of the spectrum is shifted. The shift increases with the Rabi frequency and for an excitation closer to the resonance. I attribute this shift to the AC Stark shift Δ_{AC}, which is caused by the excitation laser, and that can be calculated for a three level system with Equation 5.27. I list the calculated values for the measured 393 nm spectra in Appendix C.1.

With increasing Rabi frequency the spectrum of the generated photon becomes broader. For a Rabi frequency $\Omega_{\text{t}} > \Gamma_{\text{P}_{3/2}}$ and excitation near resonance, the spectrum does not feature a single peak but shows the Autler-Townes splitting [91] (see Figure 6.3 d,e). This Autler-Towns splitting is caused by the dressed states that are created by the laser interaction on the excited transition. The visibility of the Autler-Towns splitting is reduced by the sidebands and the broadening effect of the measurement apparatus. Also the rise time of the acousto-optic modulator has a significant effect. For large Rabi frequencies, a large fraction of the photon is generated while the laser power is still increasing. Thus a part of the spectrum is created with a smaller Rabi frequency and therefore narrower. This leads to a further reduction of the Autler-Towns splitting.

Some spectra, for example the spectrum measured with $\Omega_{\text{t}} = 53.0(3)$ MHz and $\Delta_{\text{t}} = -0.2$ MHz, have a hole that is not related to the Autler-Towns splitting. This hole is created by the additional coupling of the excited $|\text{P}_{3/2}, -\frac{3}{2}\rangle$ state to the $|\text{D}_{5/2}, -\frac{1}{2}\rangle$ state with the vertically polarized 854 nm laser. This upper level coupling is discussed more detailed in Section 6.2.1. As for the Autler-Towns splitting the visibility of the hole is reduced due to the vibration sidebands and the analysis cavity line width.
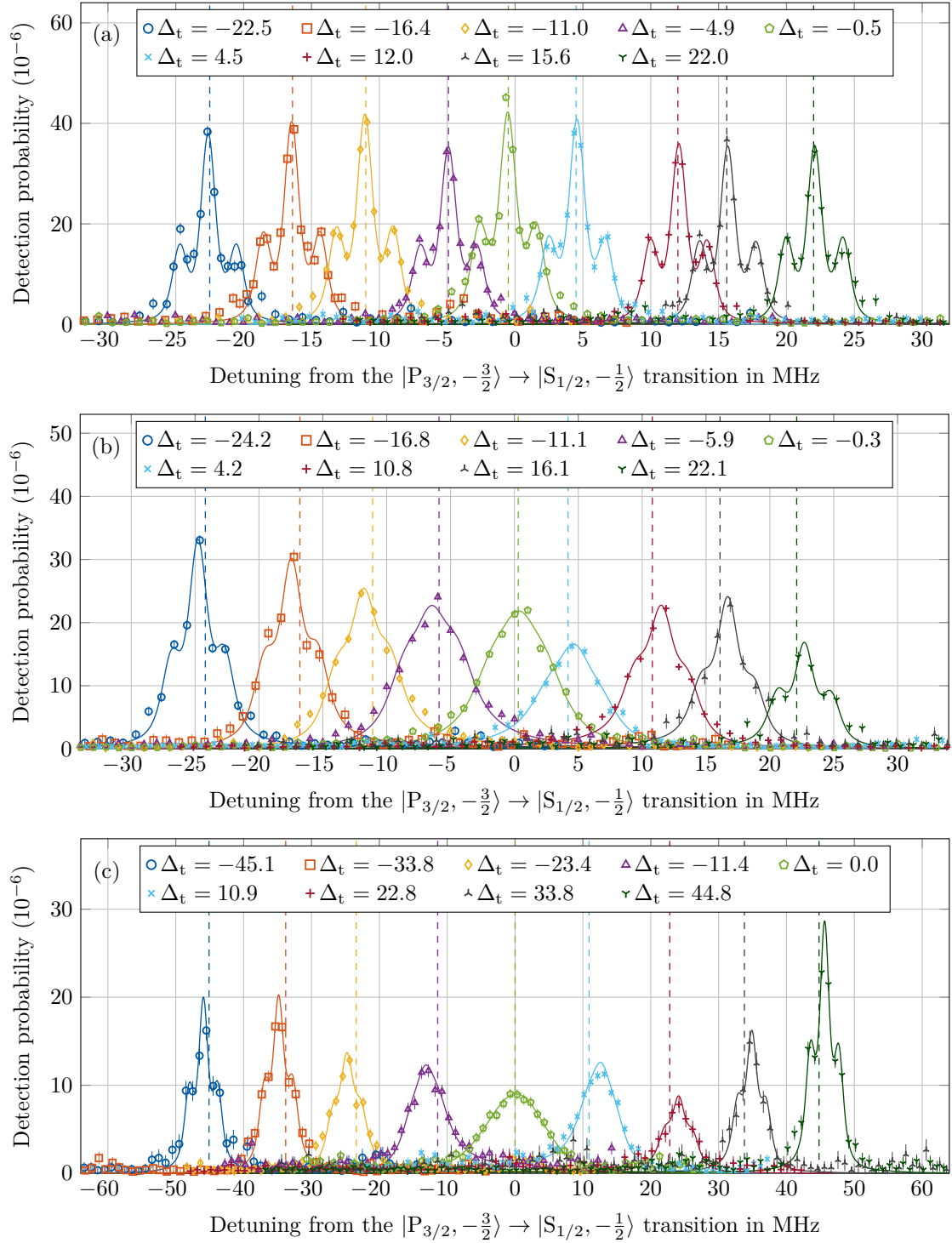
Figure 6.2.: Spectra of 393 nm Raman photons generated with different average Rabi frequencies $\bar{\Omega}_t$ and detunings Δ_t of the 854 nm excitation. (a) $\bar{\Omega}_t = 2.68(2)$ MHz. (b) $\bar{\Omega}_t = 8.03(3)$ MHz. (c) $\bar{\Omega}_t = 12.69(5)$ MHz. The corresponding *ideal* and *emitted* spectrum, the measured wave packets and measurement details are shown in Appendix C.1.1, C.1.2 and C.1.3.
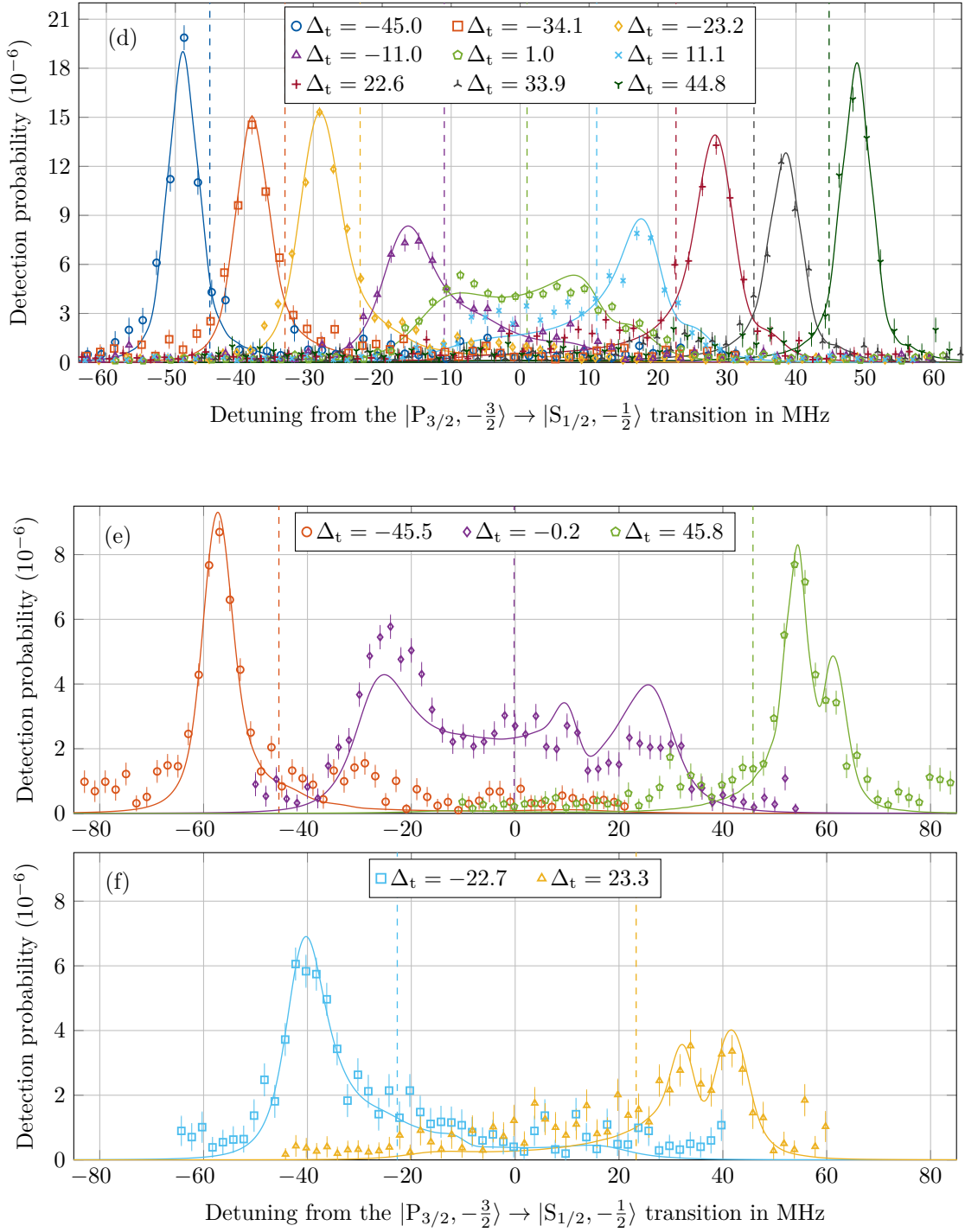
Figure 6.3.: Spectra of 393 nm Raman photons generated with different average Rabi frequencies $\bar{\Omega}_t$ and detunings Δ_t of the 854 nm excitation. (d) $\bar{\Omega}_t = 28.1(3)$ MHz. (e, f) $\bar{\Omega}_t = 53.0(3)$ MHz. The detection probability of the $\Delta_t = -0.2$ spectrum in (e) is multiplied by a factor 2. The corresponding *ideal* and *emitted* spectrum, the measured wave packets and measurement details are shown in Appendix C.1.4 and C.1.5.
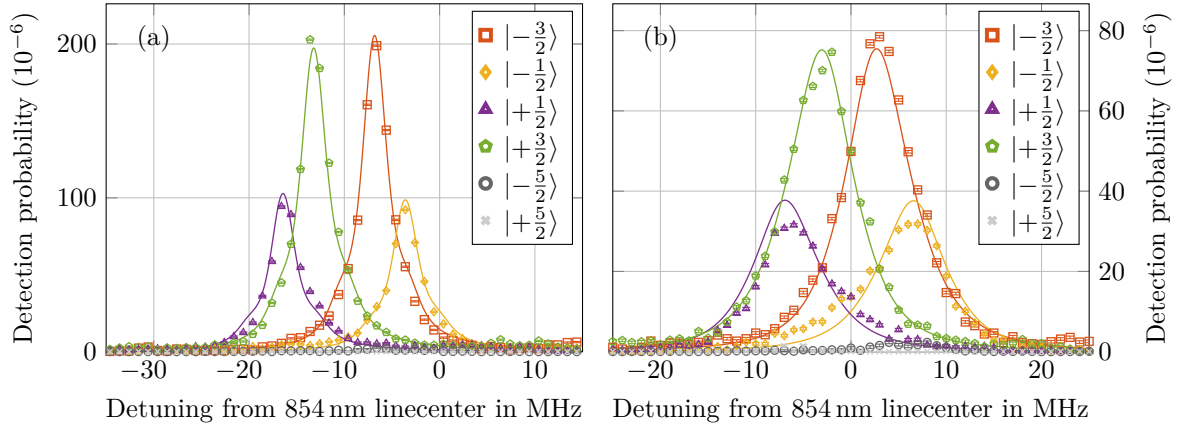
Figure 6.4.: Spectra of 854 nm Raman photons created with different laser parameter. (a) $\Omega_t = 5.51(6)\,\text{MHz}$, $\Delta_{393,\text{LC}} = -9.72\,\text{MHz}$. (b) $\Omega_t = 9.5(2)\,\text{MHz}$, $\Delta_{393,\text{LC}} = -0.15\,\text{MHz}$. The measured wave packets are shown in Appendix C.1.6.

854 nm photon spectra

The generated 854 nm photons have four spectral components (see Figure 6.4), which correspond to the four decay channels on the σ transitions into the $|D_{5/2}, +\frac{3}{2}\rangle$, $|D_{5/2}, -\frac{3}{2}\rangle$, $|D_{5/2}, +\frac{1}{2}\rangle$ and $|D_{5/2}, -\frac{1}{2}\rangle$ Zeeman levels. The small population found in the $|D_{5/2}, +\frac{5}{2}\rangle$ and $|D_{5/2}, -\frac{5}{2}\rangle$ states indicates that the 393 nm laser almost exclusively excites the π-transitions. Due to the energy splittings of the involved atomic states, the photons scattered on the four paths have different frequencies. The difference between the $|D_{5/2}, -\frac{3}{2}\rangle$ and $|D_{5/2}, +\frac{1}{2}\rangle$ spectrum as well as the difference between the $|D_{5/2}, -\frac{1}{2}\rangle$ and $|D_{5/2}, +\frac{3}{2}\rangle$ spectrum is caused by the energy splitting in the $D_{5/2}$ manifold. The states in the $D_{5/2}$ manifold are separated by 9.6 MHz. This frequency splitting is found between the spectral components that are created on the paths through the same $P_{3/2}$ Zeeman levels. The shift between the spectral components created on the paths through the $|P_{3/2}, +\frac{1}{2}\rangle$ and $|P_{3/2}, -\frac{1}{2}\rangle$ levels is caused by the different Zeeman splittings in the $S_{1/2}$, $P_{3/2}$ and $D_{5/2}$ manifold. The 393 nm π transition are shifted by $-1.33\,\text{MHz}$ ($|S_{1/2}, +\frac{1}{2}\rangle \rightarrow |P_{3/2}, +\frac{1}{2}\rangle$, B=2.86 G) and $+1.33\,\text{MHz}$ ($|S_{1/2}, -\frac{1}{2}\rangle \rightarrow |P_{3/2}, -\frac{1}{2}\rangle$) with respect to the 393 nm line center. The 854 nm transitions between the $|P_{3/2}, +\frac{1}{2}\rangle \rightarrow |D_{5/2}, +\frac{3}{2}\rangle$ and $|P_{3/2}, -\frac{1}{2}\rangle \rightarrow |D_{5/2}, +\frac{1}{2}\rangle$ transitions are shifted by $+0.53\,\text{MHz}$ with respect to each other. Both shifts sum up to a difference of 3.2 MHz between the spectral components scattered on the transition into the $|D_{5/2}, +\frac{3}{2}\rangle$ and $|D_{5/2}, +\frac{1}{2}\rangle$ respective $|D_{5/2}, -\frac{1}{2}\rangle$ and $|D_{5/2}, -\frac{3}{2}\rangle$ Zeeman level. Additionally the components carry different population ($\propto$ height), which is caused by the Clebsch-Gordan coefficients of the involved 854 nm decay channels. The ratio of $\sqrt{2}$ is between the Clebsch-Gordan coefficients is squared in the ratio between the height of the spectra.

The 854 nm spectra show the same dependence on the detuning of the excitation laser as the 393 nm spectra. The spectra of the photons generated with a detuning $\Delta_{393,\text{LC}} = -9.72\,\text{MHz}$ with respect to the 393 nm line center are centered around this detuning, while the spectra of the photons generated with a detuning $\Delta_{393,\text{LC}} = -0.15\,\text{MHz}$ are centered around this

detuning. Additionally, the spectra of the photons generated with the smaller Rabi frequency ($\Omega = (2\pi)\, 5.51(6)\,\mathrm{MHz}$) are narrower than the spectra of photons generated with the larger Rabi frequency ($\Omega = (2\pi)\, 9.5(2)\,\mathrm{MHz}$). At the same time the four spectra of photons generated with the same laser parameters have approximately the same width, independently from the scattering path.

Spectral width, duration and time-bandwidth product off the generated photons

The spectral width $\Delta\nu$ and duration $\Delta\tau$ of the created $393\,\mathrm{nm}$ photons, calculated from the measured spectrum and wave packet, strongly depend on the parameters of the excitation laser (see Figure 6.5). For a larger Rabi frequency the photon becomes shorter. A photon created with off-resonant excitation is elongated compared to a photon created with resonant excitation. The opposite is found for the spectral width. Increasing the Rabi frequency results in wider photon spectra. For an excitation away from resonance the photon becomes narrower. For large Rabi frequencies, the wave packet shows Rabi oscillation (see Appendix C.1), while the spectrum features the above discussed Autler-Townes splitting. Therefore, a comparison of the obtained values with the width of a photon created by spontaneous decay has some weakness. Nevertheless, the width of most generated photons is much smaller than the natural line width $\Gamma = (2\pi)\, 22.99\,\mathrm{MHz}$ of the $\mathrm{P}_{3/2}$ decay of the $^{40}\mathrm{Ca}^+$ ion. This shows, that the width of a Raman photon is not limited by the decay rate of the excited state, but depends on the Rabi frequency of the excitation laser. The model predicts, that the width of the photon becomes arbitrarily small for a correspondingly small Rabi frequency if no broadening effects are present. In case of the generated photons, the line width of the excitation laser and the sidebands broaden the photon spectrum. With an optimized setup, both broadening effects are reduced.
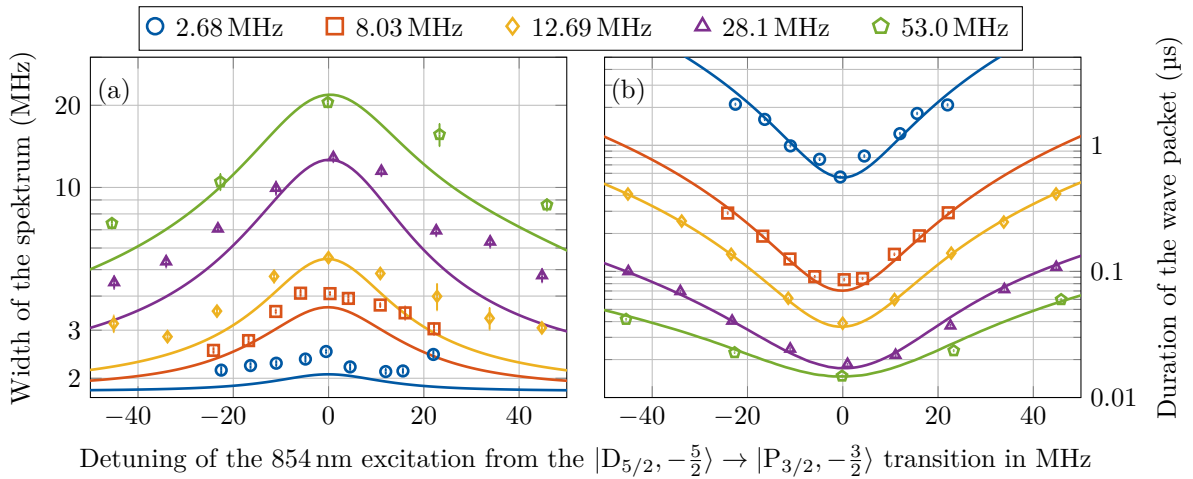
Figure 6.5.: Spectral width (a) and duration (b) of generated $393\,\mathrm{nm}$ Raman photons. The solid lines are model curves for the average Rabi frequencies.

A further broadening that affects the measured spectral width of the generated photon is the transfer function of the measurement apparatus. The measured spectrum is a convolution of the spectrum emitted by the ion and the transfer function of the analysis cavity setup (see Figure 4.12 and Section 2.6). This broadening affects all measured spectra, but the relative effect becomes larger for narrower photon spectra. As result the spectral width of photons generated with $\Omega_{854,t} = 2.68(2)$ MHz shows no dependence on the detuning. For larger Rabi frequencies the dependence on the detuning is visible. To reduce the effect of the broadening by the analysis cavity, a narrower analysis cavity is required. However, this broadening is caused by the measurement setup and no property of the generated photon. Therefore, the measured spectral width represents an upper bound of the actual spectral width of the generated photons, especially for small Rabi frequencies.

As for the 393 nm photons, I calculate the spectral width and duration of the generated 854 nm photons (see Table 6.2). For the first parameter set an average spectral width $\Delta\nu = 5.34(4)$ MHz and average wave packet duration $\Delta\tau = 0.79(5)$ µs is found. For the second parameter set an average spectral width $\Delta\nu = 3.34(2)$ MHz and average duration $\Delta\tau = 3.3(3)$ µs is measured. For both settings of the excitation laser, the spectral width and duration is similar for all four scattering paths. Because the decay rates on the individual 854 nm transitions differ by a ratio of 2 due to the Clebsch-Gordan coefficients, I conclude that the spectral width does not depend on the decay rate on the final transition, but only on the total decay rate of the excited state. Furthermore, I conclude that the wave packets have the same duration because the branching ratio between the 854 nm and 393 nm transition is the same for all four scattering paths.

From the spectral widths $\Delta\nu$ and durations $\Delta\tau$, I calculate the time-bandwidth products tbp $= 2\pi\Delta\nu\Delta\tau$ of the generated photons. As the spectral width and duration, the obtained time bandwidth product depends on the Rabi frequency of the excitation laser (393 nm photon see Figure 6.6; 854 nm photons see Table 6.2). For the 393 nm photons, the smallest measured value is 1.35(6) for a Rabi frequency $\Omega = (2\pi)\,12.40(2)$ MHz and detuning $\Delta = 0.0$ MHz. For smaller Rabi frequencies or off resonant excitation larger values are found. For the 854 nm photons the average time-bandwidth product of 27(2) respective 70(7) are found. In both

Table 6.2.: Spectral width, duration and time-bandwidth product of generated 854 nm Raman photons.

$\Omega_{393,t}$ (MHz)	5.51(6)				9.5(2)			
$D_{5/2}$ level	$\left|-\frac{3}{2}\right\rangle$	$\left|+\frac{1}{2}\right\rangle$	$\left|-\frac{1}{2}\right\rangle$	$\left|+\frac{3}{2}\right\rangle$	$\left|-\frac{3}{2}\right\rangle$	$\left|+\frac{1}{2}\right\rangle$	$\left|-\frac{1}{2}\right\rangle$	$\left|+\frac{3}{2}\right\rangle$
$\Delta_{393,t}$ (MHz)	-11.1	-11.1	-8.4	-8.4	-1.5	-1.5	1.2	1.2
$\Delta\nu$ (MHz)	3.011(9)	3.55(2)	3.48(2)	3.304(9)	5.27(2)	5.15(5)	5.65(5)	5.32(2)
$\Delta\tau$ (µs)	3.20(7)	3.2(5)	3.5(1)	3.4(6)	0.76(1)	0.76(7)	0.82(2)	0.83(8)
tbp	61(1)	70(10)	76(3)	70(10)	25.2(4)	25(2)	29.2(7)	28(3)
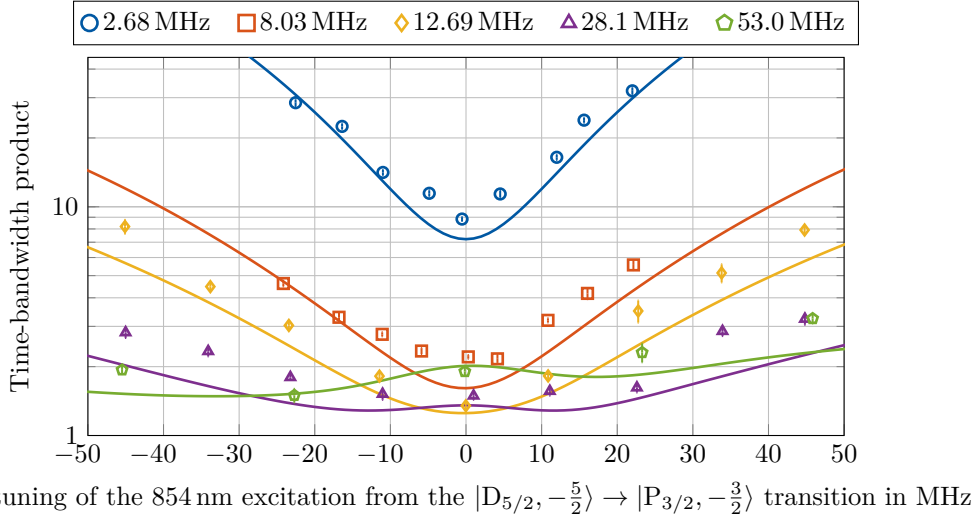
Figure 6.6.: Measured time-bandwidth-product of 393 nm photons together with model curves calculated for the average Rabi frequencies.

cases, the measured values are influenced by the cavity line width and can therefore be seen as an upper bound of the actual time-bandwidth product of the generated photons. This influence becomes larger as the spectrum becomes narrower and leads to the big difference of the measured time-bandwidth products for the photons of the same wavelengths. However, the time-bandwidth product of the 854 nm photons is still significantly larger than the time-bandwidth product of the 393 nm photons. This difference is caused by the different branching ratios of the 854 nm and 393 nm decay channels. The larger line width of 1.6 MHz from the 854 nm cavity compared to 0.6 MHz for the 393 nm analysis cavity does not significantly changes this result, even though I expect a larger broadening due to the measurement apparatus in case of the 854 nm photons.

To further study the influence of the branching ratio, I directly compare the spectral width, the duration and the time-bandwidth product of 393 nm photons and 854 nm photons that are generated with similar excitation parameters (detuning Δ and Rabi frequency Ω, see Table 6.3). For both parameter sets, the spectral width of the 854 nm photons is comparable with the spectral width of the 393 nm photons. At the same time, the photon duration differs by an order of magnitude. This large difference in the photon duration results in the large difference of the time bandwidth product of the photons. From this comparison I conclude, that the branching ratio does not affect the spectral width but elongates the wave packet. This experimental result confirms the prediction from the model. To test this result more precisely, further measurements have to be performed on 854 nm and 393 nm photons that are created with the same parameters of the excitation laser. Furthermore, the influence of the line width of the analysis cavity has to be considered. Optimally, you measure 393 nm and 854 nm spectra with cavities that have the same line width and stability. Nevertheless, I draw the conclusion, that the spectral width of a Raman photons depends on the Rabi frequency Ω and the detuning

Table 6.3.: Spectral width, duration and time-bandwidth product of 393 nm and 854 nm Raman photons generated with similar parameters of the excitation laser.

	Photon Wavelength	Ω (MHz)	Δ (MHz)	$\Delta\nu$ (MHz)	$\Delta\tau$ (µs)	tbp
	393 nm	2.80(1)	-11.0	2.27(5)	0.991(9)	14.1(4)
A	**854 nm**	5.51(6)	-9.75 ± 1.3	3.34(1)	3.3(3)	70(7)
	393 nm	8.06(3)	-11.1	3.51(6)	0.125(1)	2.77(6)
	393 nm	7.66(2)	0.3	4.08(6)	0.086(1)	2.21(4)
B	**854 nm**	11.6(3)	-0.15 ± 1.3	5.42(4)	0.79(5)	27(2)
	393 nm	12.40(2)	0.0	5.5(2)	0.0388(2)	1.35(6)

Δ of the excitation laser, as well as the total decay rate Γ of the excited state but is independent from the branching ratio that determines the number of decays back into the initial state. On the other hand, the duration of the wave packet is influenced by the branching ratio that leads to an elongation of the wave packet. This elongation affects the time-bandwidth product of the scattered Raman photon.

To show the influence of the branching ratio on the duration, spectral width and time bandwidth product, I calculate these properties for a photon generated in a three level system with a total decay rate $\Gamma = \Gamma_{393} + \Gamma_{854}$ of the excited state. I compare an ideal system without back-decay and two systems with decay rates Γ_{854} respective Γ_{393} into the initial state for the average Rabi frequencies from the 393 nm photon generation. The obtained values (see Figure 6.7) match the findings from the measurement. The back-decay elongates the photon wave packet (a,b,c) while the spectral width is not affected (d,e,f). The elongation of the wave packet then leads to an increased time-bandwidth product (g,h,i) for a system with back-decay. For the system without back-decay a time-bandwidth product between 0.8 and 1.3 is found [1]. The decay back into the initial state increases the time-bandwidth product by a factor 1.06 to 1.09 for 393 nm photons respective a factor between 16.98 and 24.45 for 854 nm photons. Both values are in range of the branching ratio $\Gamma/\Gamma_{393} = 1.0628$ respectively $\Gamma/\Gamma_{393} = 16.93$. Independently from the parameters of the excitation laser the time-bandwidth product of 854 nm photons is at least a factor ten larger than the time-bandwidth product of 393 nm photons. The measured (minimal) time-bandwidth products of 1.35(6) for 393 nm photons and 27(2) for 854 nm photons confirm this ratio and thus the influence of the branching ratio on the photon generation (see Table 6.3).

A consequence of this increased time-bandwidth product due to the back-decay is a reduced purity of the photon state which is relevant in quantum information applications, if the generated photons interferes with other photons. In this case the visibility of the interference pattern depends on the purity of the photon. The purity of an entangled atom-photon state

---

[1] A time-bandwidth product smaller than 1 is an artifact of the Süßmann measure (see Section 2.7).
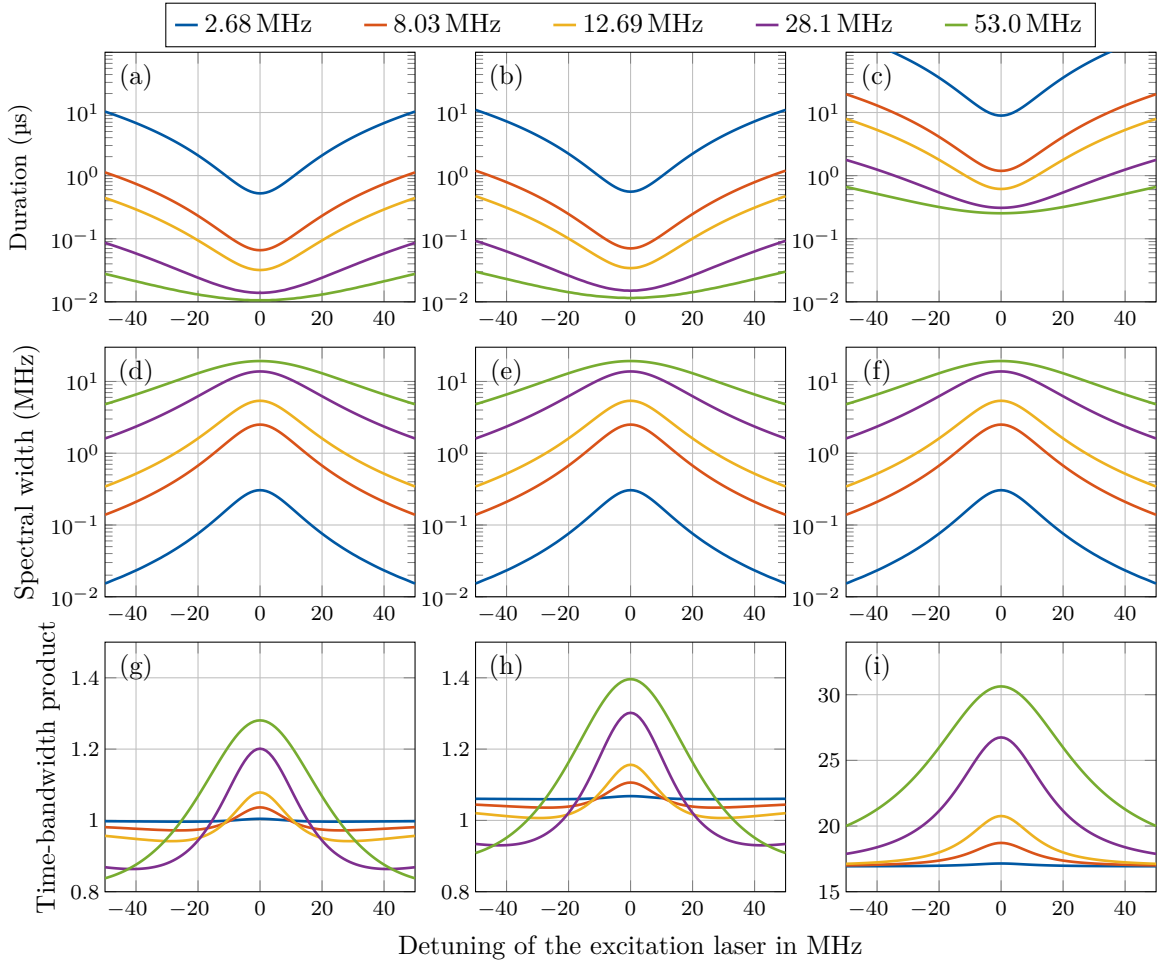
Figure 6.7.: (a,b,c) Duration, (d,e,f) spectral width and (g,h,i) time-bandwidth-product for a three level system with total decay rate $\Gamma = \Gamma_{393} + \Gamma_{854}$. (a,d,g) Without back decay ($\Gamma_f = \Gamma$, $\Gamma_i = 0$, see Figure 5.1). (b,e,f) 393 nm photon generation with $^{40}\text{Ca}^+$ ($\Gamma_f = \Gamma_{393}$, $\Gamma_i = \Gamma_{854}$). (c,f,i) 854 nm photon generation with $^{40}\text{Ca}^+$ ($\Gamma_f = \Gamma_{854}$, $\Gamma_i = \Gamma_{393}$).

as discussed in the next section is not directly affected by the purity of the generated photon. As the time-bandwidth product of a photon with several spectral components depends on the superposition of these components (see Section 2.7) the measured time bandwidth products can not be taken to calculate the purity of the created photons. However, from the comparison with an ideal three level system the conclusion can be drawn, that the 393 nm photons are in an almost pure quantum state. On the other hand, I expect a mixed state for 854 nm photons.

6.1.2. Effect of the ion temperature

The spectra of 393 nm photons presented in the previous section feature two sidebands symmetrical around the carrier with a distance that corresponds to the radial trap frequency ν_{rad}. Thus, I assume that the sidebands are caused by the radial motion of the ion in the trap, which lies in direction of the photon collection. To verify this assumption I compare the spectra of photons, that were generated for different radial trap frequencies. I compare spectra measured for radial trap frequencies of $\nu_{\text{rad}} = 2.14$ MHz, $\nu_{\text{rad}} = 3.39$ MHz, $\nu_{\text{rad}} = 3.67$ MHz, and $\nu_{\text{rad}} = 3.81$ MHz (examples see Figure 6.8). The radial trap frequency is measured precisely with a 729 nm spectroscopy. To study the influence of the ion temperature on the strength of the side bands I compare the spectra of photons generated for different directions of the 397 nm cooling laser. If the 397 nm laser is coupled in trough the $90\,^{\circ}$ or $45\,^{\circ}$ view port it has a different projection on the radial motion of the ion in the trap and the radial motion is differently cooled (see Section 4.1.1).

For each photon spectrum I fit the frequency ν_{sb} and population c_{sb} of the sidebands. The obtained values are listed in Table 6.4. The position of the sidebands changes accordingly to the radial trap frequency ν_{rad}. I attribute the deviation between the measured frequencies and the trap frequency to the frequency resolution of the spectrum measurement. Additionally one finds, that the population in the sidebands decreases for an increasing trap frequency. For a higher trap frequency, the energy difference between vibration states becomes larger what results in a smaller mean vibration number of the vibration mode. I attribute the lower population in the side bands to this smaller mean vibration number analog to the vibration sidebands in other spectroscopies that becomes smaller for lower mean vibration numbers [2].
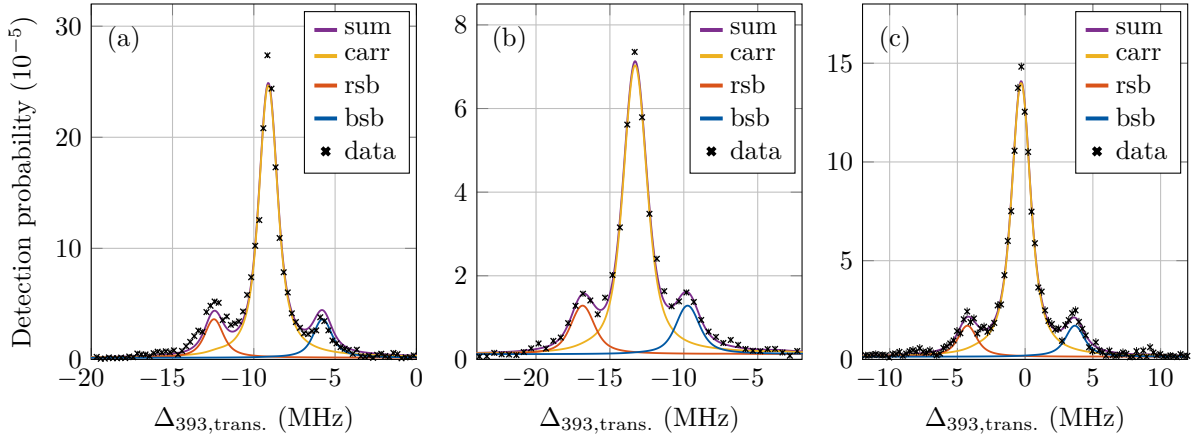
Figure 6.8.: Spectra of 393 nm Raman photons for a radial trap frequency of (a) 3.39 MHz, (b) 3.67 MHz and (c) 3.81 MHz. The spectra were measured at the bright trap (a) and dark trap (b,c) for cooling laser coupled through the 90° view port onto the ion. Additional spectra and the measurement parameter are shown in Appendix C.2.

---

[2]This can be used to determine the mean vibration number of the vibration mode.

Table 6.4.: Position and population in the spectral sidebands for different trap frequencies and cooling directions.

ν_{rad} (MHz)	2.14	3.39	3.39	3.67	3.67	3.81	3.81
Cooling	$90\,°$	$90\,°$	$45\,°$	$90\,°$	$45\,°$	$90\,°$	$90\,°$
ν_{sb} (MHz)	2.12(3)	3.34(7)	3.34(7)	3.55(5)	3.42(7)	3.8(1)	3.96(4)
c_{sb}	0.39(2)	0.142(12)	0.135(12)	0.168(8)	0.138(10)	0.092(9)	0.113(5)

This explanation is confirmed by comparing the spectra of photons generated with Doppler cooling from 90 ° or 45 °. The sidebands in the spectra measured with 45° cooling are smaller than the sidebands in the spectra measured with 90° cooling because the 45° cooling laser has a better projection on the radial trap frequency and therefore cools this direction better. From these observations, I conclude that the sidebands in the spectrum are caused by the radial motion of the ion in the trap.

To further reduce the strength of the sidebands, the mean vibration number in the radial motion of the ion has to be reduced. The first approach is to increase the radial trap frequency with a stronger confinement of the ion in the trap. This is achieved by a higher power of the radio frequency drive of the trap. Unfortunately, the applied power in both traps was limited due to a shortcut in the trap near one of the trap electrodes [3]. The second possibility is a second laser cooling scheme that is applied after the Doppler cooling as for example resolved sideband cooling. Disadvantage is the much longer cooling time compared to Doppler cooling that results in a significant lower repetition rate. This reduction of the repetition rate affects all sequences where photons are generated with a high repetition rate, as for example the spectrum measurements that become an almost impossible task. In the case of a small back decay a solution could be to apply sideband cooling not during every sequence repetition but only frequently enough to keep the ion in a low vibration state while maintaining a sufficiently high repetition rate.

6.1.3. Incomplete photon generation

To show the effect of an incomplete photon generation on the spectrum, I switch the laser off, before the full wave packet of the photon is generated. I set the 854 nm Rabi frequency to $\Omega_{\mathrm{t}} = (2\pi)\,4.4(1)\,\mathrm{MHz}$ for a detuning of $\Delta_{854,t} = -16.2\,\mathrm{MHz}$ from the $|\mathrm{D}_{5/2}, -\frac{5}{2}\rangle \to |\mathrm{P}_{3/2}, -\frac{3}{2}\rangle$ transition. These laser parameters are chosen, to get a relatively narrow spectrum, if the full wave packet is generated. I switch the radio frequency that is applied to the acousto-optic modulator to generate the excitation pulse off after 5 µs, 1 µs, 500 ns, 200 ns, and 100 ns. For an applied pulse of 5 µs duration, the full wave packet is generated. For the other pulse durations the wave packet is truncated at the end.

---

[3]The shortcut in the bright trap triggered the remodeling of the dark trap.
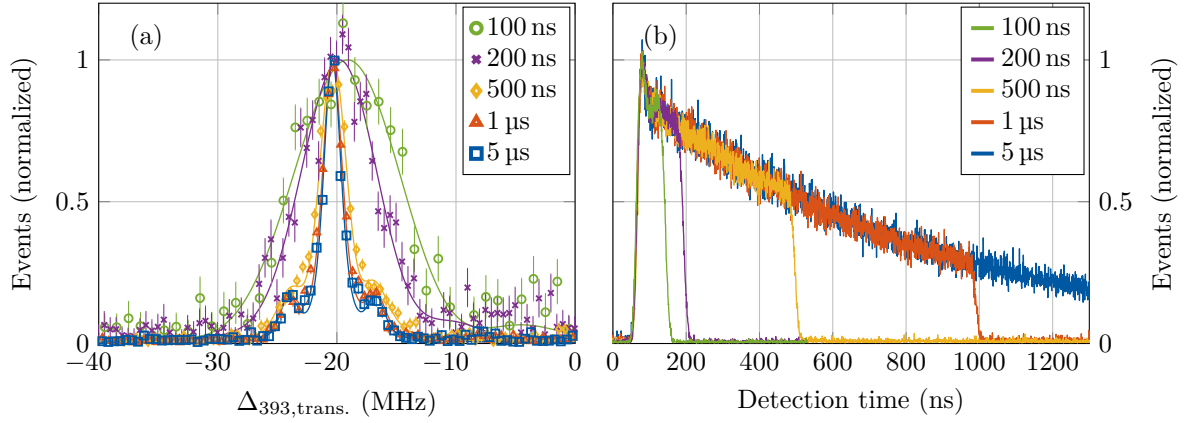
Measurement	5 µs	1 µs	500 ns	200 ns	100 ns
τ_{pulse} (ns)	5000	926(1)	429(1)	125(1)	79(1)
$\Delta\tau$ (ns)	815(1)	420.2(5)	214.6(2)	68.4(1)	45.0(1)
$\Delta\nu$ (MHz)	1.91(4)	2.05(3)	2.55(5)	4.8(2)	5.9(3)
tbp	9.8(2)	5.42(8)	3.44(6)	2.05(8)	1.66(9)

Figure 6.9.: (a) Spectra and (b) wave packets of truncated Raman photons. For a better comparison, the data is scaled to have the same maximum. For a pulse duration of 5 µs the full wave packet is generated. (bottom) Spectral properties of the generated photons. The exact pulse duration τ_{pulse} is determined from the measured wave packet. Not scaled data and measurement parameter are shown in Appendix C.3.

I determine the rise and fall time of the acousto-optic modulator and the pulse duration τ_{pulse} from the generated wave packets (see Figure 6.9 b). Due to the working principle of the acousto-optic modulator, the laser pulse is shorter than the applied radio frequency pulse. I model the expected spectrum taking the rise and fall time of the acousto-optic modulator and the laser pulse duration into account. From the measured spectra (see Figure 6.9 a) and wave packets, I calculate the duration ($\Delta\tau$), the spectral width ($\Delta\nu$) and the time-bandwidth product of the generated photon (tbp).

The photon spectrum becomes broader if the Raman photon generation is stopped, before the full wave packet is generated (see table in Figure 6.9). The following applies: The earlier the photon generation is stopped, the wider the spectrum becomes. This is analogue to the spectral broadening of a short laser pulse. Due to the influence of the measurement apparatus, the time-bandwidth product becomes smaller for a shorter photon (see Section 6.1.1). Furthermore, the influence of the measurement apparatus, the vibration sidebands and the switching time of the acousto-optic modulator (about 20 ns) suppresses spectral features that are expected for a rectangular laser pulse.

The measurement further shows that measurable broadening of the spectrum only occurs, if the photon generation or detection is stopped before a large portion of the photon wave packet is generated. Consequently, the broadening effect can be neglected in most experiments, where the photon wave packet is truncated. This usually happens to increase the signal to background ratio or the repetition rate at the expense of a reduced photon generation efficiency.

If instead of the laser, the detector is switched of during the photon generation, the model predicts almost the same spectrum. The difference is caused by the population that is in the excited state at the time when the laser is switched off. If the laser is switched off, the population remaining in the excited state decays spontaneously into the final state and contributes to the photon spectrum. If the detector is switched off, this population no longer contributes to the spectrum. The contribution of the spontaneous decay in the first case leads to the small difference. As the analysis cavity introduces a time uncertainty to the detection time of the photon, the second case and therefor the difference between both cases can not be studied with the current setup.

6.2. Quantum interference effects in Raman-scattered photons

If different paths of the Raman scattering process are indistinguishable, the scattering amplitudes superimpose coherently and quantum interference occurs. For the generation of a Raman photon, there are several possibilities that lead to indistinguishable scattering paths. The first example is photon generation out of a superposition state. In this case quantum interference may occur in the absorption or emission process what was already studied on the basis of the wave packet of the generated photon [19, 56]. The second example is a bichromatic laser excitation from a single initial state. But not only different scattering paths lead to interference effects, also the coupling of the excited state to an other level leads to interference that affects the photon spectrum. In this section I discuss these four interference phenomena on the basis of the spectrum of the generated photon.

6.2.1. Upper level coupling

If the excited state is coupled to a further level interference occurs that results in a hole in the spectrum. The same effect was studied theoretical for the spontaneous decay in a three level system and called upper level coupling [87, 88, 93]. Due to the coupling, the photon spectrum contains two amplitudes which interfere destructively and the photon emission into a specific frequency mode is completely suppressed. This lead to a hole in the spontaneous emission spectrum. The position and width of the hole depends on the parameters of the coupling. A similar effect is expected for the Raman photon generation, where three scattering amplitudes superimpose. For a certain frequency mode these amplitudes interfere destructively and the spectrum features a hole as in the case for the spontaneous emission. Analog to the spontaneous decay, I call this interference effect upper level coupling. With simulations (see Section 5.2.1), I found that the position of the hole depends on the detuning of the second laser, while the width depends on the Rabi frequency of the coupling to the second transition.
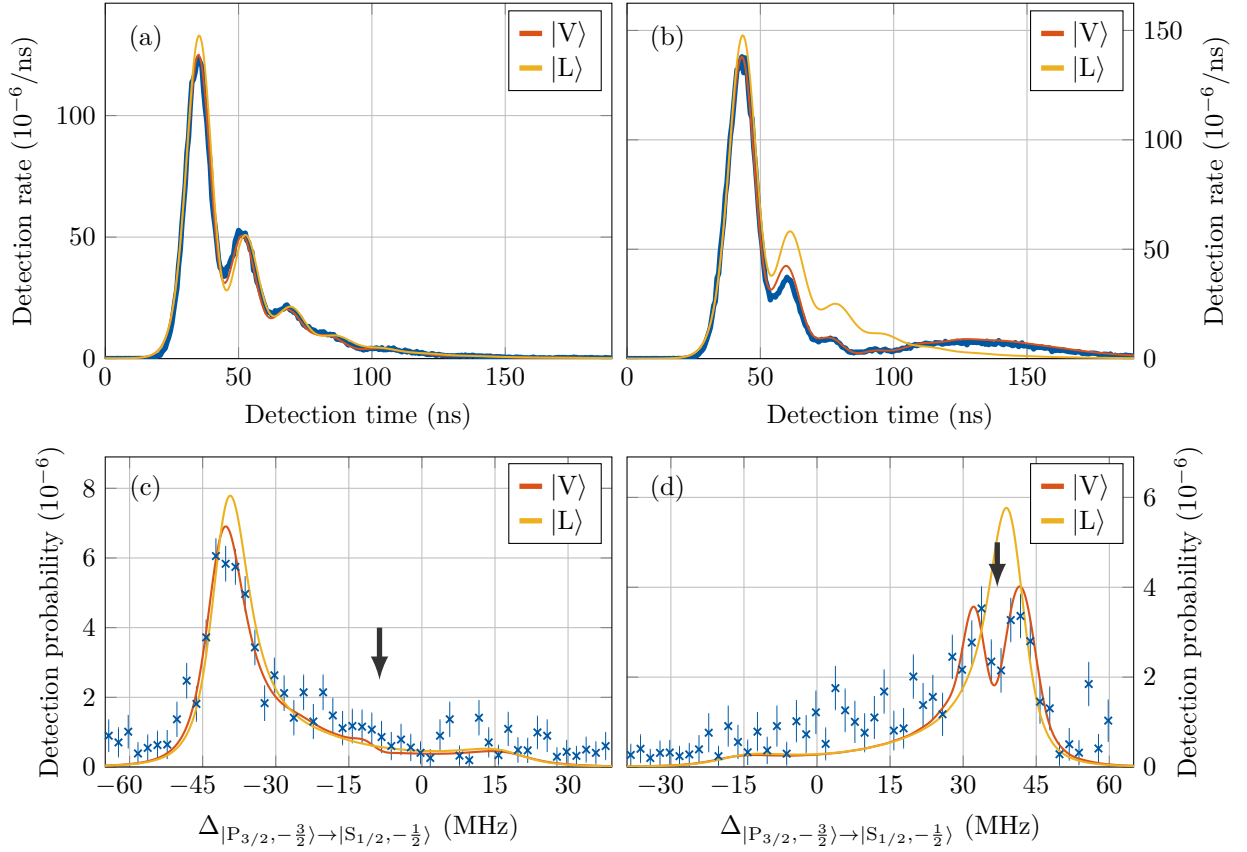
Figure 6.10.: Wave packets (a,b) and spectra (c,d) of Raman photons, that show the upper level coupling caused by a vertically polarized laser excitation ($|V\rangle$). The arrow marks the hole created by the coupling to the second transition. For comparison, the simulated spectra of photons generated with a left circularly polarized laser are shown. In this case no further level is coupled to the excited state and no hole is expected in the spectrum.

To generate 393 nm Raman photons, of which the spectra were discussed in Section 6.1.1, a vertically polarized 854 nm laser perpendicular to the magnetic field excites the initially prepared $|D_{5/2}, -\frac{5}{2}\rangle$ state. This 854 nm laser couples to all 854 nm σ transitions. Consequently, not only the initially prepared $|D_{5/2}, -\frac{5}{2}\rangle$ level is coupled to the $|P_{3/2}, -\frac{3}{2}\rangle$ level but also the $|D_{5/2}, -\frac{1}{2}\rangle$ level (see Figure 6.1). For small Rabi frequencies this coupling does not affect the shape of the photon spectra (see Figure 6.2). In this case, the system is well approximated by a three level system. However, for large Rabi frequencies the coupling significantly changes the shape of the photon spectrum (see Figure 6.3) and has to be taken into account.

To show the effect of the upper level coupling, I compare two spectra measured with the detunings $\Delta_{854,1,t} = -22.7\,\text{MHz}$ and $\Delta_{854,2,t} = +23.3\,\text{MHz}$ from the excited $|D_{5/2}, -\frac{5}{2}\rangle$ to $|P_{3/2}, -\frac{3}{2}\rangle$ transition (see Figure 6.10). For the applied magnetic field of 2.86 G, the transition from the $|P_{3/2}, -\frac{3}{2}\rangle$ state into the $|D_{5/2}, -\frac{1}{2}\rangle$ level is shifted by $-9.6\,\text{MHz}$ compared to the excited transition out of the initial state. Thus the 854 nm laser is detuned by $\Delta_{\text{up}} = \Delta_{854,t} + 9.6\,\text{MHz}$

from this transition, where $\Delta_{854,t}$ is the detuning of the laser with respect to the transition out of the $|D_{5/2}, -\frac{5}{2}\rangle$ level. Therefore, the spectrum features a hole at a 393 nm detuning that is blue detuned from the applied 854 nm detuning $\Delta_{854,t}$ (see Figure 6.10, indicated by an arrow) [4]. The width of the hole is given by the applied Rabi frequency. As the same laser couples to both transitions, the Rabi frequencies on both transitions are proportional to each other with a ratio $\frac{1}{\sqrt{10}}$ that is given by the Glebsch-Gordan coefficients. For a blue detuned 854 nm laser, the hole is located in the main part of the spectral peak and well visible. For a red detuned 854 nm laser, the hole is expected at the side of the spectrum and strongly suppressed. In both cases, the depth of the hole is reduced due to the vibration side bands and the width of the analysis cavity [5]. In case of the red detuned 854 nm laser therefore the hole is strongly suppressed.

For comparison, I show the simulated expected spectrum for a circularly polarized laser that excites the initial state with the same Rabi frequency. In this case, the laser does not couple to the second transition and the system is approximated well by a three level system. Therefore, the spectrum has no hole and is mirror inverted for detunings with an opposite sign. The spectrum of the photon generated with the negative 854 nm detuning is similar to the expected spectrum of a three level system, while the photon generated with a positive detuning differs significantly from the corresponding three level spectrum due to the hole. The same is also found for the wave packets, where the wave packet created with a positive detuning $\Delta_{854,2,t}$ is elongated.

6.2.2. Bichromatic laser excitation

If two scattering paths that start in the same initial state end in the same final state, they form a Mach-Zender like interferometer. Such an interferometer is created by a bichromatic laser excitation of the form

$$A = A_1 \sin(2\pi\Delta_1 t) + A_2 \sin(2\pi\Delta_2 t + \phi) \tag{6.1}$$

that creates two scattering paths into the same final atomic level through two virtual states. Therefore, both paths are intrinsically indistinguishable and interference happens between both scattering amplitudes depending on the phase ϕ between both bichromatic components.

I prepare the system in the $|D_{5/2}, -\frac{5}{2}\rangle$ state that is excited with a vertically polarized 854 nm laser perpendicular to the magnetic field (see Figure 6.1). The laser has two frequency components that are detuned $\Delta_{1,t} = +5.1\,\text{MHz}$ and $\Delta_{2,t} = -4.9\,\text{MHz}$ from the excited $|D_{5/2}, -\frac{5}{2}\rangle$ to $|P_{3/2}, -\frac{3}{2}\rangle$ transition. I set the initial phase difference between both frequency components to $\phi_1 = 0$, $\phi_2 = 90°$, $\phi_3 = 180°$ and $\phi_4 = 270°$ to study the effect on the generated photon. For comparison, I generate two photons where the (monochromatic) excitation has only one of both frequency components. The average Rabi frequencies of both components is set to $\Omega_{1/2,t} = (2\pi)\,10.25(4)\,\text{MHz}$.

---

[4]Due to the AC-Stark shift the position of the hole is shifted.

[5]Additionally, the back decay limits the depth of the hole. However, this effect is small compared to the

In case of the bichromatic laser excitation the shape of the spectrum and wave packet depends strongly on the relative phase between both frequency components of the bichromatic excitation (see Figure 6.11, a) as the scattering paths through both virtual levels interfere with each other. This interference leads to an enhanced and suppressed emission into different frequency modes and to a modulation in the wave packet. For the spectrum, the relative phase between both frequency components determines the relative phase of the spectral amplitudes of both scattering components. The components created with a monochromatic laser pulse are separated by about 12 MHz. This separation is caused by the 10 MHz frequency difference of both frequency components and an additional light shift caused by the laser excitation (see Section 6.1.1) that pushes the spectral components outwards. The spectral components created with the bichromatic excitation that interfere with each are similar to the monochromatic spectra. Depending on the relative phase between the bichromatic components the spectral amplitudes interfere constructively or destructively and the spectrum of the created photon has two separated peaks ($\phi = 0°$ and $\phi = 90°$) or a single central peak ($\phi = 180°$ and $\phi = 270°$).

In case of the wave packet a different picture is used. The bichromatic laser beam corresponds to an amplitude modulated monochromatic laser beam. This amplitude modulation is imprinted on the wave packet that becomes modulated accordingly. The relative phase between both frequency components sets the initial phase of the amplitude modulation and by this the initial dynamic of the wave packet. The frequency difference of 10 MHz results in a modulation period of 100 ns that can be identified in the wave packets generated with a relative phase difference of $\phi = 180°$ or $\phi = 270°$. In the wave packets of the photons created with a relative phase of $\phi = 0°$ or $\phi = 90°$ the distance between the first two maxima is smaller. This is an
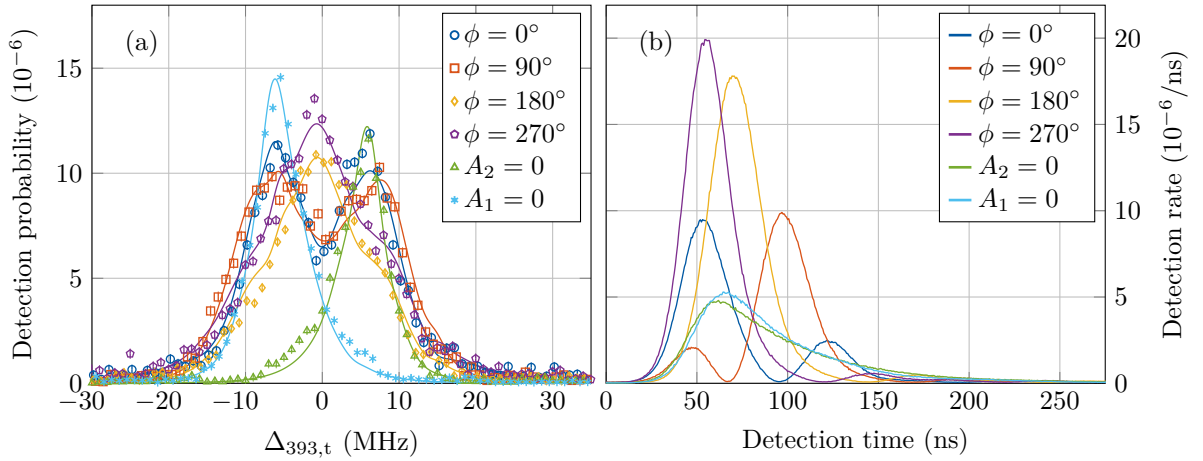
Figure 6.11.: (a) Spectra and (b) wave packets of Raman photons generated with a monochromatic (scaled by 0.5) or bichromatic laser pulse. The monochromatic laser pulse contains one frequency component of the bichromatic pulse. The corresponding *ideal* and *emitted* spectra, as well as the measurement parameter are listed in Appendix C.4.

---

other effects that reduce the visibility of the hole.

artifact caused by the start of the dynamic at the maximum or during the falling slope of the amplitude modulation. For a smaller Rabi frequency, the photon wave packet covers several oscillation periods and the modulation period can be identified for all relative phases.

The model curves are in good agreement with the measured spectra from what I conclude that the model developed in Chapter 5 also covers modulated laser fields. This case is not covered by the model introduced in [20,25] and one result of this section [6]. The bichromatic laser excitation forms the basis of the detection time independent atom-photon entanglement scheme discussed in Chapter 7 and the ability to model the bichromatic laser excitation is a prerequisite to optimize parameters for the atom-photon entanglement generation. Furthermore, the presented measurement shows full control over the phase between both frequency components and how this phase affects the spectrum. In the atom-photon entanglement scheme, the relative phase appears as relative phase between both components of the generated atom-photon state. Thus, I assume that I can control the phase between both components of the generated atom-photon state with the phase between both frequency components of the bichromatic laser excitation.

6.2.3. Quantum interference in the absorption process

Quantum interference in the absorption process occurs, if a superposition that is prepared in two initial states is excited to the same excited state. The scheme is called the Λ-scheme after the appearance of the two interfering transitions in the atomic system. The effect of the quantum interference in absorption on the wave packet of the scattered Raman photon was studied previously for $393\,\text{nm}$ photon generated by a ${}^{40}\text{Ca}^+$ ion [19, 56]. A modulation of the wave packet with the frequency difference of the initial states was found. As fundamental interference mechanism leading to this modulation, a suppression and enhancement of the depopulation process from the initial state was identified. I complement the results found with a study of the spectra of the scattered photons and show, that interference in absorption also affects the spectrum of the scattered photon.
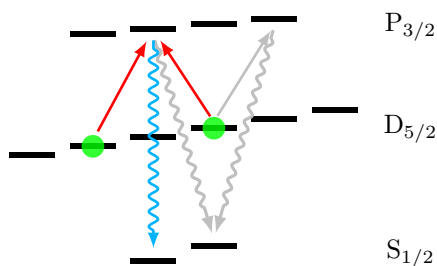
Figure 6.12.: Λ-scheme that shows quantum interference in the absorption process. Colored arrows indicate wanted transitions. Gray arrows show parasitic $854\,\text{nm}$ absorption and unwanted $393\,\text{nm}$ emission that is filtered out by polarization projection. The $854\,\text{nm}$ decay and additional paths introduced thereby are not shown.

---

[6] The analytic model does not cover time dependent Rabi frequencies.

To study the effect of quantum interference in absorption on the spectrum of the scattered Raman photon, I prepare the superposition

$$|i\rangle = \frac{1}{\sqrt{2}} \left(|D_{5/2}, +\tfrac{1}{2}\rangle + e^{i\phi} |D_{5/2}, -\tfrac{3}{2}\rangle \right) \tag{6.2}$$

with different phases ϕ in the $D_{5/2}$ manifold of the $^{40}Ca^+$ ion (see Figure 6.12). I excite the initial superposition with a linearly polarized 854 nm laser pulse on quantization axis. This 854 nm pulse is "seen" by the atom ion as polarization

$$\mathbf{e}_{\mathrm{pol}} = \frac{1}{\sqrt{2}} \left(\mathbf{e}_{\sigma+} + e^{i\theta} \mathbf{e}_{\sigma-} \right), \tag{6.3}$$

where the polarization angle θ defines the linear polarization (H, D, V, A, ...). From this polarization, the $\mathbf{e}_{\sigma+}$ part couples to the σ^+ transitions while the $\mathbf{e}_{\sigma-}$ parts couples to the σ^- transitions. Thus changing the linear polarization does not change the coupling strength on both transitions but the relative phase between both couplings. In the same way, the initial phase ϕ of the superposition changes the relative phase between both coupled transitions. The 854 nm laser excites the ion into the state

$$|e\rangle = A_{+\frac{3}{2}} |P_{3/2}, +\tfrac{3}{2}\rangle + A_{-\frac{1}{2}}(\phi, \theta) |P_{3/2}, -\tfrac{1}{2}\rangle, \tag{6.4}$$

with the amplitudes $A_{+\frac{3}{2}}$ and $A_{-\frac{1}{2}}(\phi, \theta)$. These amplitudes contain the normalization, the Clebsch-Gordan coefficients and the detuning-dependent atomic response. The amplitude in the state $|P_{3/2}, -\tfrac{1}{2}\rangle$ depends on the phase of the initial superposition and the polarization of the laser. From the excited state, the ion decays into the final state

$$|f\rangle = R_{+\frac{1}{2},\sigma+} |S_{1/2}, +\tfrac{1}{2}\rangle |\sigma^+\rangle + R_{-\frac{1}{2},\sigma-}(\phi, \theta) |S_{1/2}, -\tfrac{1}{2}\rangle |\sigma^-\rangle + R_{+\frac{1}{2},\pi}(\phi, \theta) |S_{1/2}, +\tfrac{1}{2}\rangle |\pi\rangle \tag{6.5}$$

that contains the amplitudes $R_{+\frac{1}{2},\sigma+}$, $R_{+\frac{1}{2},\sigma-}(\phi, \theta)$ and $R_{-\frac{1}{2},\pi}(\phi, \theta)$ of the scattered 393 nm Raman photon. The states $|\sigma^+\rangle$, $|\sigma^-\rangle$ and $|\pi\rangle$ describe the 393 nm photon emitted on the σ and π decay channels. For emission perpendicular to the magnetic field, the σ decays translate into vertically polarized photons while the π decay is seen as a horizontally polarized photon. A polarization filter set up to transmit horizontally polarized photons removes the σ components. Thus only the photon amplitude of the state

$$|f_\Lambda\rangle = R_{-\frac{1}{2},\pi}(\phi, \theta) |S_{1/2}, -\tfrac{1}{2}\rangle |H\rangle = R_\Lambda(\phi, \theta) |S_{1/2}, -\tfrac{1}{2}\rangle |H\rangle \tag{6.6}$$

is transmitted through the polarization filter and detected.

The Raman amplitude $R_\Lambda(\phi, \theta)$ of the 393 nm photon in this state depends on the phase ϕ of the superposition and the polarization angle θ of the laser. These two phases set the relative phase of the involved scattering amplitudes that interfere with each other depending on the relative phase of the prepared superposition. In the wave packet $P_\Lambda(t) = |R_\Lambda(t)|^2$ of the scattered photon, the interference is observed as quantum beats with a period τ that corresponds to the

time evolution of the phase $\phi = \phi_0 + 2\pi\nu t$ of the initial superposition due to Larmor precession with the frequency ν of the energy splitting [19]. The initial phase ϕ_0 of the superposition and the polarization angle θ of the laser thereby give the initial phase of the quantum beat. It should be noted that in general, the amplitudes $A_{-\frac{1}{2}}(\phi, \theta)$ respective $R_{+\frac{1}{2}, \pi}(\phi, \theta)$ can not be calculated independently from each other for both absorption paths as formulated in [19, 56] (for details see the comparison of the Λ- and V-scheme in Sections 5.2.3 and 5.2.4) due to the coupling of both initial states to the respective other state via the excited state. This coupling is neglected if each absorption path is calculated independently from each other. However, for small Rabi frequencies the error becomes small and can be neglected. For larger Rabi frequencies, that are needed to observe a significant effect on the photon spectrum, the coupling cannot be neglected and the absorption has to be calculated taking all involved states into account.

To generate 393 nm photons with the Λ-scheme, the magnetic field is rotated in direction of the $90\,^\circ$ and $270\,^\circ$ view port what enables optical pumping with the 397 nm laser. The phase ϕ of the initial superposition is set by adjusting the phase φ of the second 729 nm pulse that transfers population into the $|D_{3/2}, -\frac{3}{2}\rangle$ state (the pulse sequence is presented in Section 4.5.2). I generate photons with two different parameter sets. In the first set, the phase of the second 729 nm pulse is set to $\varphi \in \{81°, 171°, 261°, 351°\}$ and I apply an 854 nm pulse with an average Rabi frequency $\Omega_{854} = (2\pi)\,45.3(1)\,\text{MHz}^7$ and detuning $\Delta_{854,\text{m}} = -5\,\text{MHz}$ with respect to the 854 nm line center. In the second parameter set, the phase of the second 729 nm pulse is set to $\varphi \in \{15°, 105°, 195°\,285°\}$. The 854 nm laser was applied with a Rabi frequency $\Omega_{854} = (2\pi)\,30.74(8)\,\text{MHz}$ and a detuning $\Delta_{854,\text{m}} = 0\,\text{MHz}$ with respect to the 854 nm line center.

The emitted 393 nm photons are collected perpendicular to the magnetic field. A polarization setup adjusted to transmit horizontal polarization selects photons emitted on the π transitions. Photons that are scattered on the σ transitions are removed by the polarization projection. The transmitted photons are coupled into a single mode fiber and sent to the analysis cavity setup. A small fraction of the beam is cut out with a D-shaped mirror, coupled into a multi mode fiber and detected directly to measure the wave packet. From a fit to the wave packet I determine the phase offset of the initial superposition state.

For both parameter sets the photon spectrum and wave packet shows a significant dependence on the phase of the initial superposition (see Figure 6.13). For the first parameter set (a,b) and a superposition state created with a phase $\varphi = 171°$, the largest fraction of the wave packet is emitted in the first 50 ns. In contrast to this, the wave packet of the photon generated from the superposition state created with $\varphi = 351°$ is "delayed" by approximately 25 ns. This delay is caused by the periodical enhancement and suppression of the excitation rate caused by the quantum interference of both scattering amplitudes [56]. Because the duration of all wave packets is shorter than the Larmor period of 104 ns the periodical enhancement and suppression

---

[7]To translate the Rabi frequency in the model to the Rabi frequency as seen by the individual transitions, the laser polarization and direction as well as the Clebsch Gordan coefficients have to be taken into account. As example the Rabi frequency seen by the $|D_{5/2}, -\frac{3}{2}\rangle \rightarrow |P_{3/2}, -\frac{1}{2}\rangle$ transition is $\Omega_t = \frac{1}{\sqrt{5}}\Omega_{854} = (2\pi)\,20.26(4)\,\text{MHz}$.
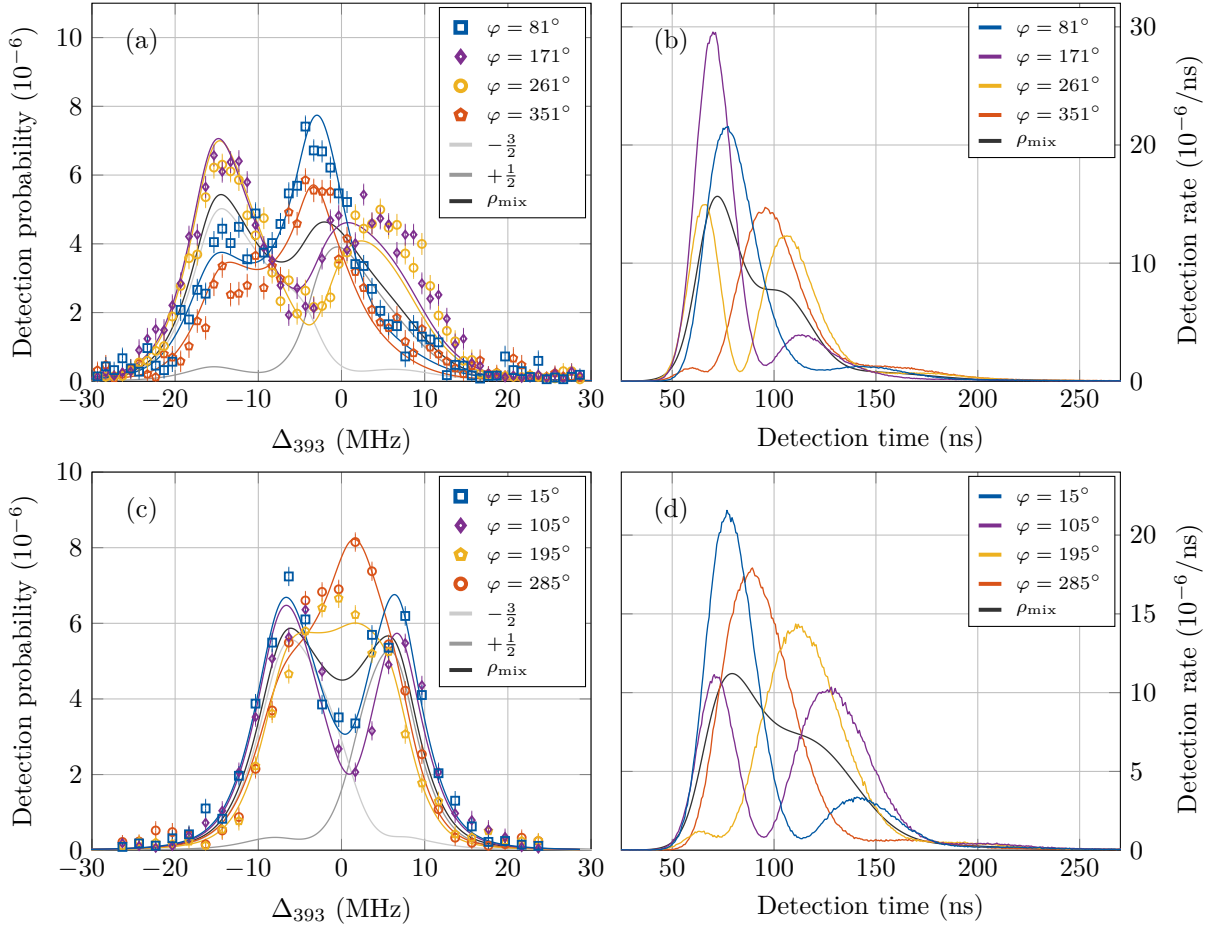
Figure 6.13.: Spectra (a,c) and wave packets (b,d) of photons generated in a Λ-type system for different phases of the initial superposition. Additional, I show model curves for a system that is prepared in either of the initial Zeeman levels or a mixed initial state. (a,b): $\Omega_{854} = (2\pi)\,45.3(1)\,\text{MHz}$, $\Delta_{854} = -5\,\text{MHz}$; (c,d): $\Omega_{854} = (2\pi)\,30.74(8)\,\text{MHz}$, $\Delta_{854} = 0\,\text{MHz}$. The *ideal* and *emitted* spectra as well as measurement parameters are listed in Appendix C.5.

of the excitation rate is not visible as oscillation but a shifted maximum of the wave packet. In the spectrum the emission into certain frequency modes is enhanced or suppressed. Compared to the spectrum of a mixed state, the spectra of photons generated from the superposition states created with the phases $\varphi = 171°$ or $\varphi = 261°$ have a stronger left peak and a weaker right peak. For the other two phases, the right peak is stronger. For frequency modes in these peaks, the scattering amplitudes interfere constructively or destructively. This interference leads to the different height of both peaks, depending on the phase of the initial superposition.

Due to the smaller Rabi frequency in the second parameter set, the wave packet becomes longer. Nevertheless, the wave packet is still to short to cover more than one period of the quantum beat modulation and the wave packets look similar to the wave packets measured in the first parameter set. The spectra are narrower due to the smaller Rabi frequency and

shifted accordingly to the different laser detuning. For this parameter set, the spectra of photons created from the $\varphi = 15°$ and $\varphi = 105°$ superposition have two well separated peaks. These peaks are located at the expected position of the spectrum of both individual scattering paths. Compared to the mixed state, the hole between both peaks is deeper. At the central frequency modes, both scattering paths interfere destructively and the emission is suppressed. For the other two phases a constructive interference happens at the central frequency modes. The result is a plateau ($\varphi = 195°$) or a single deformed peak ($\varphi = 285°$) in the spectrum.

In all cases, the model curves are in a good agreement with the measured spectra. This confirms that for interference in the absorption process, the two scattering amplitudes out of the initial superposition cannot be calculated separately, but have to be calculated in a single system. This is a fundamental difference to the interference in the emission process which is discussed in the next section.

6.2.4. Quantum interference in the emission process

If two indistinguishable scattering paths end in the same final state, quantum interference occurs in the emission process. The scheme is called *V*-scheme after the appearance of the two atomic transitions that emit the interfering photons. As the the interference in the absorption process, the interference in the emission process was previously studied on the basis of the wave packet of $393\,\text{nm}$ photon generated with a $^{40}\text{Ca}^+$ ion [19,56], where the interference leads to a modulation in the wave packet. However, compared to the Λ-scheme a fundamentally different interference mechanism causes the modulation. For the interference in the emission process, the modulation is caused by a time dependent emission pattern. Here I show, that this time dependent emission patterns also affects the spectrum of the photon.

To study the interference in emission, I prepare the $^{40}\text{Ca}^+$ ion in the initial superposition

$$|i\rangle = \frac{\sqrt{3}}{2}\,|\text{D}_{5/2},+\tfrac{3}{2}\rangle + \frac{1}{2}e^{\mathrm{i}\phi}\,|\text{D}_{5/2},-\tfrac{5}{2}\rangle \tag{6.7}$$
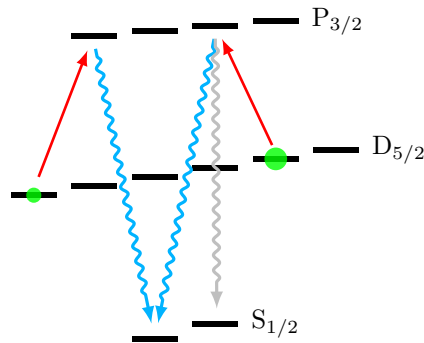
Figure 6.14.: *V*-scheme that shows quantum interference in the emission process. Colored arrows indicate wanted transition. Gray arrows show unwanted $393\,\text{nm}$ decay channels that are filtered out with a polarization projection. Additional channels introduced due to the $854\,\text{nm}$ decay are not shown.

in the $D_{5/2}$ manifold (see Figure 6.14). The imbalance in the superposition compensates the additional 393 nm decay channel out of the $|P_{3/2}, +\frac{1}{2}\rangle$ level. The initial state is excited with a linearly polarized 854 nm laser on quantization axis, analog to the Λ-scheme. This laser drives two independent scattering paths from the initial superposition $|i\rangle$ into the same final $|S_{1/2}, -\frac{1}{2}\rangle$ level. As the scattering paths are independent from each other they are described in a three level system [8]. In each of these three level systems a Raman photon is created with the temporal and spectral Raman amplitude $R(\Delta_{854}, \Omega_{854})$. The Raman amplitude in the "left" part of the scheme is connected to a 393 nm photon emitted on a σ^- transition, while the amplitude in the "right" part is connected to a 393 nm photon emitted on a σ^+ transition. If these photons are observed perpendicular to the quantization axis both photons are seen as vertically polarized photons and therefore indistinguishable. In this case both scattering amplitudes add coherently and interfere with each other. At the same time, the photon emitted on the $|P_{3/2}, +\frac{1}{2}\rangle$ to $|S_{1/2}, +\frac{1}{2}\rangle$ π transition is seen as horizontally polarized photon and is filtered out with a polarization filter. Thus only photons with the joint scattering amplitude

$$R_V(\Delta_{854}, \Omega_{854}) = R_{\sigma^+}(\Delta_{854}, \Omega_{854}) + e^{i\phi}e^{i\theta}R_{\sigma^-}(\Delta_{854}, \Omega_{854}) \tag{6.8}$$

are transmitted through the polarization filter. In this amplitude the components $R_{\sigma^+}(\Delta_{854}, \Omega_{854})$ and $R_{\sigma^-}(\Delta_{854}, \Omega_{854})$ describe the scattering amplitude from the initial $|D_{5/2}, +\frac{3}{2}\rangle$ respective $|D_{5/2}, -\frac{5}{2}\rangle$ Zeeman level into the final $|S_{1/2}, -\frac{1}{2}\rangle$ state. Due to the second, removed 393 nm decay channel out of the $|P_{3/2}, +\frac{1}{2}\rangle$ state, the imbalance from the initial state disappears in the joint scattering amplitude. Depending on the phase ϕ of the initial superposition and the polarization phase θ of the 854 nm laser, the scattering amplitudes of both σ transitions interfere constructively or destructively. As for the Λ-scheme the quantum interference is observed in the wave packet $P_V(t) = |R_V(t)|^2$ as modulation with a time period caused by the Larmor precession of the superposition in the initial states.

I generate 393 nm photons with the same pulse sequence as for the Λ-scheme but project the emitted 393 nm photons to vertical polarization. This polarization projection removes the unwanted π-decay out of the $|P_{3/2}, +\frac{1}{2}\rangle$ state so that both indistinguishable σ-decay channels, which are observed as vertical polarization, remain. I generate photons with two different settings of the 854 nm excitation laser. In both cases the laser has a Rabi frequency $\Omega_{854,m} = (2\pi)\,30.55(9)\,\text{MHz}$ and is applied on resonance ($\Delta_{854,m} = 0\,\text{MHz}$) of the 854 nm line center. For the first set I apply a vertically polarized 854 nm laser. In the second set, I apply a horizontally polarized 854 nm laser. For each setting I prepare four different initial superposition states by changing the phase φ of the second 729 nm laser pulse. In the first parameter set, the 729 nm pulse is applied with the phases $\varphi \in \{10°, 100°, 190°, 280°\}$. In the second parameter set, the 729 nm pulse is applied with the phases $\varphi \in \{175°, 265°, 355°, 85°\}$.

The measured wave packets show an oscillation with a period that matches the expected period of 52.1 ns calculated from the frequency difference of both initial Zeeman levels (see Figure 6.15

---

[8] I neglect the coupling of both scattering paths via the $|D_{5/2}, -\frac{1}{2}\rangle$ level
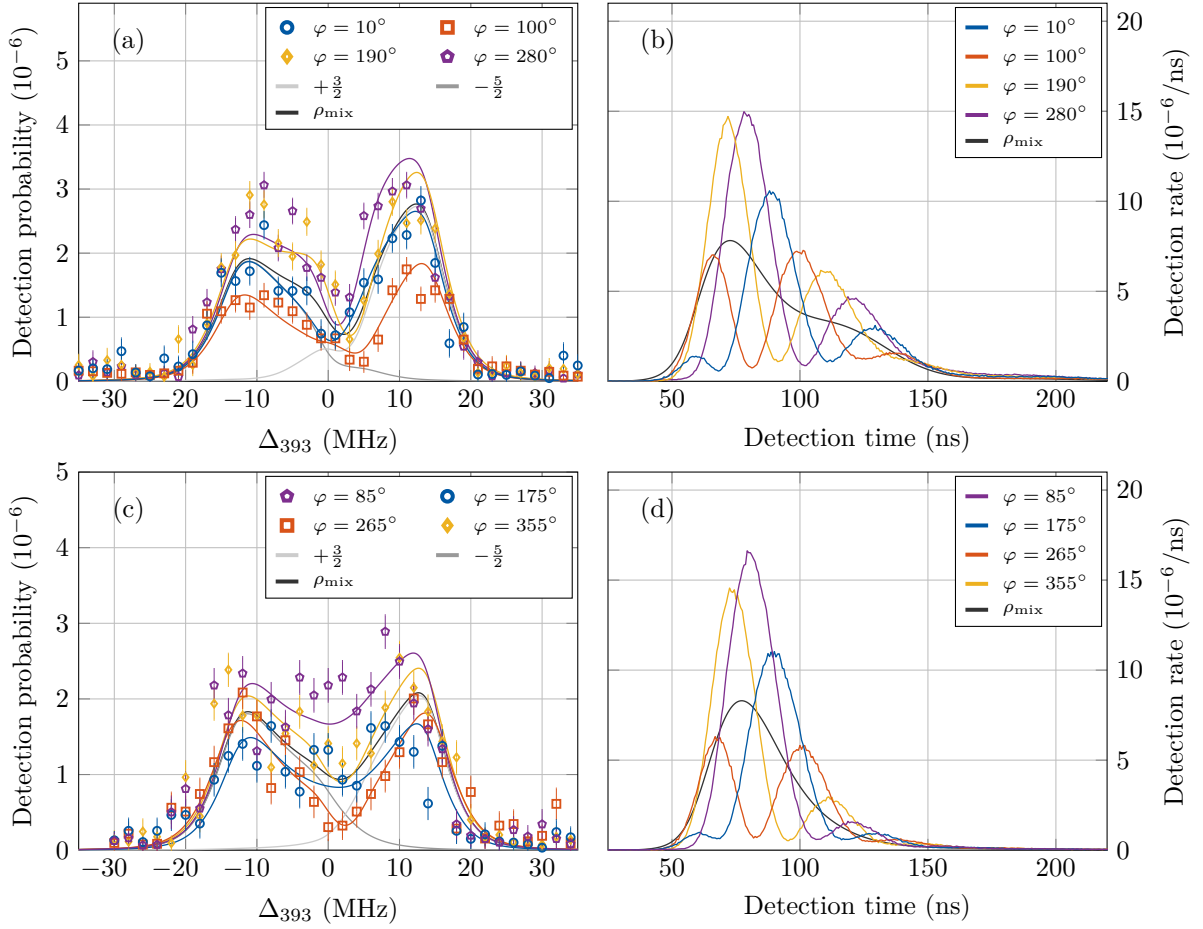
Figure 6.15.: Spectra and wave packets of photon created in a *V*-scheme with vertically (a,b) or horizontally (c,d) polarized 854 nm excitation. Model curves for the different initial phases and for a system prepared in one of the Zeeman levels or a mixed state are also shown for the spectrum measurements. Excitation with: $\Omega_{854,\mathrm{m}} = (2\pi)\,30.55(9)\,\mathrm{MHz}$ and $\Delta_{854,\mathrm{m}} = 0\,\mathrm{MHz}$. The *ideal* and *emitted* spectra, as well as detailed parameter are listed in Appendix C.6.

(b,d)). Due to the higher frequency difference between both initial states compared to the Λ-scheme, the wave packets covers more than one oscillation period. In both measurement sets, all spectra show two peaks separated by approximately 20 MHz corresponding to the individual scattering paths from the left and right part of the *V*-scheme (see Figure 6.15 (a,c)). The spectral overlap of both spectral components is small what results in a small difference between individual spectra due to interfering spectral components. However, a significant difference is found in both measurement set between individual spectra. The shape and population of the spectrum changes depending on the phase of the initial superposition. This is caused by the constructive or destructive interference of both spectral components, which leads to an emission pattern that rotates around the quantization axis. As result, the emission into certain solid angles is enhanced or suppressed for a short photon [56]. Due to the fixed position of

the photon collection optics perpendicular to the quantization axis this leads to the observed modulation in the wave packets and the different shapes and population of the spectra. This is a fundamental difference to the previously discussed Λ-scheme, where the photon generation itself is enhanced and suppressed.

If one compares the spectra of the photons that were created with vertical respective horizontal 854 nm polarization one sees a difference between both measurement sets, even though similar phases of the initial atomic superposition were prepared. The spectra of photons generated with vertical 854 nm polarization have a narrow dip in between two asymmetric broad peaks while the dip in the spectra of photons generated with horizontal polarization is broader and the peaks are more symmetric. The same is found for the model spectrum of a photon generated from a mixed state. This polarization dependence is not expected by the simple derivation that leads to Equation 6.8 because the coupling from both initial states to the $|D_{5/2}, -\frac{1}{2}\rangle$ level, which causes this difference, was neglected. Also both initial states are coupled with each other through this level. Due to this coupling additional interference effects occur, which affect the spectrum. The twelve level model takes this coupling into account and describes the measured data well. If the initial transition is excited with a small Rabi frequency, the coupling from both states to the $|D_{5/2}, -\frac{1}{2}\rangle$ level can be neglected and the difference vanishes. In this case also the spectral overlap between both scattering paths becomes small so that almost no difference in the measured spectra is expected.

An application of the quantum interference in emission is the generation of atom-photon entanglement. Therefore, the initial state is changed to the superposition

$$|i\rangle = \frac{1}{\sqrt{2}} \left(|D_{5/2}, +\tfrac{5}{2}\rangle + e^{i\phi} |D_{5/2}, -\tfrac{5}{2}\rangle \right). \tag{6.9}$$

As the involved scattering paths are symmetric, a balanced superposition is prepared. Raman scattering of a single photon from both initial states results in the final state

$$|f\rangle = \frac{1}{\sqrt{2}} \left(R_+ |\sigma^+\rangle |S_{1/2}, +\tfrac{1}{2}\rangle + e^{i\phi} e^{i\theta} R_- |\sigma^-\rangle |S_{1/2}, -\tfrac{1}{2}\rangle \right). \tag{6.10}$$

In this state, the amplitudes of the Raman photons emitted on both decay channels are described by R_+ and R_-. As both decay channels end in a different atomic level, they are distinguishable. However, if the ion is projected onto the atomic superposition states $|+\rangle = \frac{1}{\sqrt{2}} \left(|S_{1/2}, +\tfrac{1}{2}\rangle + |S_{1/2}, -\tfrac{1}{2}\rangle \right)$ and $|-\rangle = \frac{1}{\sqrt{2}} \left(|S_{1/2}, +\tfrac{1}{2}\rangle - |S_{1/2}, -\tfrac{1}{2}\rangle \right)$ the final state is seen as

$$|f_2\rangle = \frac{1}{2} \left[\left(R_+ |\sigma^+\rangle + e^{i\phi} e^{i\theta} R_- |\sigma^-\rangle \right) |+\rangle + \left(R_+ |\sigma^+\rangle - e^{i\phi} e^{i\theta} R_- |\sigma^-\rangle \right) |-\rangle \right]. \tag{6.11}$$

If the photon is collected in direction of the quantization axis and projected on a linear polarization, both decay channels become indistinguishable and the amplitudes R_+ and R_- interfere with each other. This interference is observed as a correlation between the atomic superposition and linear polarization that depends on the phase ϕ of the initial superposition, the polarization phase θ and the projection setting. For a monochromatic excitation, the correlation oscillates

with the frequency difference of the initial and final states and is observed as modulation of the wave packet. For a bichromatic excitation, however, the frequency components can be chosen so that spectral components of the generated photon amplitude overlap which then lead to a complete suppression of the emission of these components. This interference builds the basis for the atom-photon entanglement scheme with a bichromatic excitation that I discuss detailed in the following Chapter 7. With this scheme I create an entangled atom-photon state with a phase that is independent from the detection time of the photon.

6.3. Summary

In this chapter, I discussed the spectrum of Raman-scattered photons. The first part focused on the spectral properties where I studied the position and spectral width of the generated photons in dependence from the parameters of the laser excitation. I showed that the photon spectrum becomes broader, if the Rabi frequency of the excitation laser is increased. If the laser is detuned from resonance, for a fixed Rabi frequency, the spectrum becomes narrower. It was shown, that for a Rabi frequency $\Omega \ll \Gamma$ a photon is created with a spectrum much narrower than the natural line width Γ of the excited state. From a comparison of measured spectral widths and durations of 393 nm and 854 nm photons, I concluded two central properties of Raman scattered photons: The spectral width only depends on the Rabi frequency Ω and the detuning Δ of the excitation laser as well as the total decay rate Γ of the excited state. In contrast to the spectral width, the duration of the wave packet is influenced by the decay back into the initial state that elongates the wave packet. Furthermore, I measured the time-bandwidth product of generated 393 nm and 854 nm photons. The values of 1.31(5) and 27(2) for 393 nm respective 854 nm photons confirm the influence of the branching ratio on the scattered photon.

Finally, interference effects that affect the spectral shape and the wave packet of the photons were discussed. Interference occurs in the absorption process if two initial states are coupled to the same excited state, between scattering paths into the same final state, between two scattering paths created by a bichromatic laser excitation, or due to the coupling of additional levels to the excited state. In all cases the interference effects alters the photon spectrum as it affects the photon wave packet. Due to the constructive and destructive interference of different scattering amplitudes, the emission into different frequency modes of the scattered photon is enhanced or suppressed.

For all measured spectra the developed model matches the measured data well. I assume small differences in the polarization and laser parameters as reasons for deviations. Effects due to the micro- or macro-motion of the ion in the trap are neglected or only covered rudimentary. Nevertheless, the model describes all performed experiments and predicts results for further experimental situations as for example the atom-photon entanglement generation in Chapter 7. In this chapter, I apply the model to find optimized excitation parameters for the atom-photon entanglement generation.

7. Larmor-precession-free atom-photon entanglement

A sender-based quantum repeater scheme requires the generation of atom-photon entanglement. In this chapter, I present schemes to create atom-photon entanglement with a bichromatic laser excitation. I create a 393 nm or 854 nm photon, which carries a polarization qubit that is entangled with the state of the $^{40}Ca^+$ ion encoded in two Zeeman levels. An external spectral filter removes unwanted components from the created atom-photon state, which makes the phase of the created state independent from the creation time of the photon. I compare the created atom-photon entanglement with atom-photon entanglement that is created with monochromatic excitation in schemes that were already presented in [57, 59, 60].

This chapter is organized as follows. In the first section I give a generalized overview on the creation of atom-photon entanglement with monochromatic or bichromatic laser excitation. The overview is focused on the relation between spectral components of the scattered photon and the phase of the created atom-photon state. I show how photons with controlled spectral components create an atom-photon state with a phase that is independent from the detection time of the photon. In the next step I adapt the general overview to the experimental situation for the 393 nm and the 854 nm atom-photon entanglement scheme. In the following two sections I discuss the 393 nm respective 854 nm atom-photon entanglement created in the presented schemes.
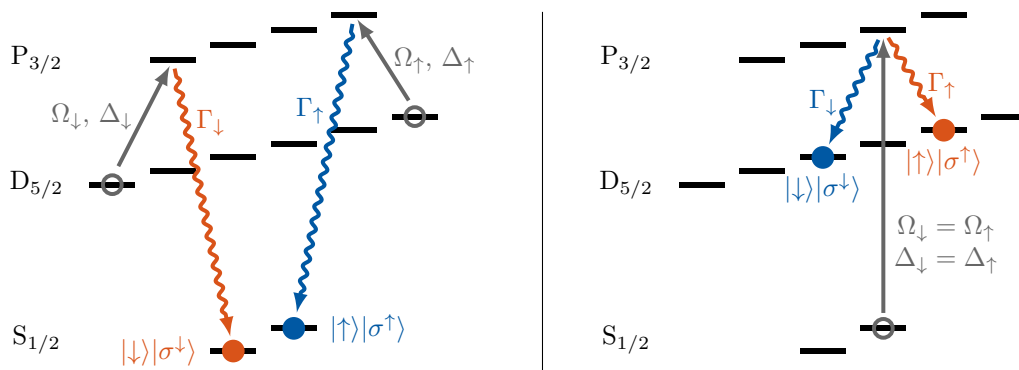
Figure 7.1.: Schemes to create 393 nm (left) or 854 nm (right) atom photon entanglement.

7.1. Atom-photon entanglement creation schemes

The atom-photon entanglement schemes implemented in this work create atom-photon entanglement by Raman scattering of a single photon, which takes place on a σ^+ and σ^- transition into two different final states $|\uparrow\rangle$ and $|\downarrow\rangle$ that are Zeeman levels of the same atomic manifold (see Figure 7.1). According to the final states $|\uparrow\rangle$ and $|\downarrow\rangle$, all quantities that are involved the Raman scattering processes (Detuning Δ, Rabi frequency Ω, decay rate Γ, ...) are labeled with $\uparrow$ and $\downarrow$. The implemented schemes create an entangled atom-photon state of the form

$$|\Psi\rangle = R_\uparrow |\uparrow\rangle |\sigma^\uparrow\rangle + R_\downarrow |\downarrow\rangle |\sigma^\downarrow\rangle , {}^1 \tag{7.1}$$

where $|\uparrow\rangle$ and $|\downarrow\rangle$ denote the Zeeman levels that encode the atomic qubit, while $|\sigma^\uparrow\rangle$ and $|\sigma^\downarrow\rangle$ denote the created photonic polarization qubit. For collection of the photons in direction of the quantization axis, the σ decays translate into $|R\rangle$ or $|L\rangle$ circularly polarized photons. The Raman amplitudes $R_\uparrow$ and $R_\downarrow$ describe the Raman scattering of the single photon on the transitions into the two states $|\uparrow\rangle$ and $|\downarrow\rangle$. They contain a constant relative phase offset ϕ that is given by the experimental realization. This phase depends on the initial state, the phase of the laser excitation and timings in the pulse sequence.

The Raman amplitudes $R_\uparrow$ and $R_\downarrow$ play the central role in this chapter, as they contain the temporal and spectral information of the generated photon and by this define the generated atom-photon state. I describe the Raman amplitudes with the models derived in Chapter 5. Because the scattering paths into the final atomic states $|\uparrow\rangle$ and $|\downarrow\rangle$ are independent from each other, I can describe the Raman scattering on both paths by two independent three level systems. This is utilized for the following analytic derivation and comparison of the monochromatic and bichromatic scheme. All simulations and model calculations, for example to find optimal experimental parameters or to describe measured spectra, were performed with the model for the twelve atomic states of the $S_{1/2}$, $P_{3/2}$ and $D_{5/2}$ manifold of the ${}^{40}Ca^+$ ion.

Monochromatic laser excitation

For a monochromatic excitation, the temporal Raman amplitude $R(t)$ of the scattered photon becomes (see Section 5.1)

$$R(t) = \frac{\Omega\sqrt{\Gamma_f}}{N}\Theta(t)\left[e^{-\frac{\kappa}{2}t-\mathrm{i}(\delta_f+\Delta+\Delta_{AC})t} - e^{-\frac{\Gamma-\kappa}{2}t-\mathrm{i}(\delta_f-\Delta_{AC})t}\right]. \tag{7.2}$$

This amplitude depends on the parameters of the excitation laser (detuning Δ and Rabi frequency Ω), the detuning δ_f of the final transition with respect to the chosen rotating frame, the total decay rate Γ of the excited state, the decay rate Γ_f on the transition into the final state, the AC stark shift Δ_{AC} and the decay rate κ of the Raman component [25]. The AC

---

[1]The state $|\Psi\rangle$ is expressed in a system that rotates with the energy difference of the states $|\sigma^\uparrow\rangle$ and $|\sigma^\downarrow\rangle$, as the Raman amplitudes $R_\uparrow$ and $R_\downarrow$ contain only the phase evolution of the photon. In a frame rotating with the frequency of the Raman transition, the generated state becomes $|\Psi\rangle = R_\uparrow e^{-\mathrm{i}\varepsilon_\uparrow t} |\uparrow\rangle |\sigma^\uparrow\rangle + R_\downarrow e^{-\mathrm{i}\varepsilon_\downarrow t} |\downarrow\rangle |\sigma^\downarrow\rangle$, where $\hbar\varepsilon_\uparrow$ and $\hbar\varepsilon_\downarrow$ are the energy shifts of the states $|\sigma^\uparrow\rangle$ respectively $|\sigma^\downarrow\rangle$.

Stark shift Δ_{AC} and the decay rate κ depend on Δ, Ω and Γ (see Equation 5.27 and Equation 5.28). As all these parameters depend on the Zeeman levels of the involved atomic transitions they are different for the scattering paths into the states $|\uparrow\rangle$ and $|\downarrow\rangle$. The normalization N accounts for the population in the initial state of the Raman scattering process.

In the following, I consider a weak excitation $\Omega \ll \Gamma$. In this case the AC stark shift becomes $\Delta_{\text{AC}} \approx 0$ and can be neglected. Furthermore, one gets $\kappa \ll \Gamma$ what means that the second part of the sum decays much faster and can therefore be neglected, too. Thus the scattered photon is described by the Raman amplitude

$$R(t) = \sqrt{\Gamma_f} a e^{-\mathrm{i}(\delta_f + \Delta)t}. \tag{7.3}$$

This Raman amplitude contains two parts. The first part $\sqrt{\Gamma_f} a$ with the coefficient

$$a = \frac{\Omega}{N} \Theta(t) e^{-\frac{\kappa}{2}t} \tag{7.4}$$

describes the envelope of the photon wave packet. The second part $e^{-\mathrm{i}(\delta_f + \Delta)t}$ describes the phase of the scattered photon, which depends on the detuning δ_f of the final transition from the rotating frame and the detuning Δ of the excitation laser with respect to the excited transition. I put this Raman amplitude into equation 7.1 to obtain the joint atom-photon state

$$|\Psi(t)\rangle = \left(\sqrt{\Gamma_\uparrow} a_\uparrow e^{-\mathrm{i}(\delta_\uparrow + \Delta_\uparrow)t} |\uparrow\rangle |\sigma^\uparrow\rangle + \sqrt{\Gamma_\downarrow} a_\downarrow e^{-\mathrm{i}(\delta_\downarrow + \Delta_\downarrow)t} |\downarrow\rangle |\sigma^\downarrow\rangle \right) \tag{7.5}$$

that is detected at the time t. The phase of both components of this state depends on the detection time t of the photon and the frequencies $\nu_\uparrow = \delta_\uparrow + \Delta_\uparrow$ respective $\nu_\downarrow = \delta_\downarrow + \Delta_\downarrow$ that are given by the detunings $\delta_\uparrow$ and $\delta_\downarrow$ of the final transition from the chosen rotating frame and the detunings $\Delta_\uparrow$ and $\Delta_\downarrow$ of the excitation laser from the excited transition. The amplitudes $\sqrt{\Gamma_\uparrow} a_\uparrow$ and $\sqrt{\Gamma_\downarrow} a_\downarrow$ describe the envelopes of the photons created on both scattering paths. If the condition $|\sqrt{\Gamma_\uparrow} a_\uparrow| = |\sqrt{\Gamma_\downarrow} a_\downarrow|$ is met, the created atom photon state

$$|\Psi(t)\rangle = \sqrt{\Gamma_\uparrow} a_\uparrow \left(e^{-\mathrm{i}(\delta_\uparrow + \Delta_\uparrow)t} |\uparrow\rangle |\sigma^\uparrow\rangle + e^{\mathrm{i}\phi} e^{-\mathrm{i}(\delta_\downarrow + \Delta_\downarrow)t} |\downarrow\rangle |\sigma^\downarrow\rangle \right) \tag{7.6}$$

is maximally entangled. The time-dependent phases, however, lead to oscillations in the correlation between atomic state and photon polarization, which result in a dependence of the atom-photon entanglement on the detection time of the photon. The frequency $|\nu_\downarrow - \nu_\uparrow|$ of this oscillation corresponds to the frequency difference $|\nu_i - \nu_f|$, where ν_i is the atomic Larmor precession of a superposition in the initial state[2] and ν_f is the atomic Larmor precession of a superposition in the final states $|\uparrow\rangle$ and $|\downarrow\rangle$ (ν_f). The phase offset ϕ is given by experimental parameters and the relative phase between both Raman amplitudes. If you ignore the detection time of the photon[3] the phase information between both components is blurred and a mixed atom-photon state is created.

---

[2]If the scheme starts from an energy eigenstate you get $\nu_i = 0$.

[3]This corresponds to a sum over all possible detection times.

In the case

$$\nu_\uparrow = \delta_\uparrow + \Delta_\uparrow = \delta_\downarrow + \Delta_\downarrow = \nu_\downarrow \tag{7.7}$$

the frequency difference becomes zero, the oscillation vanishes and the atom-photon state

$$|\Psi(t)\rangle = e^{-\mathrm{i}(\delta_\uparrow + \Delta_\uparrow)t}\left(\sqrt{\Gamma_\uparrow}a_\uparrow |\uparrow\rangle |\sigma^\uparrow\rangle + e^{\mathrm{i}\phi}\sqrt{\Gamma_\downarrow}a_\downarrow |\downarrow\rangle |\sigma^\downarrow\rangle\right) \tag{7.8}$$

is created, which has a phase that is independent from the detection time of the photon. However, the necessary condition $\nu_\uparrow = \nu_\downarrow$, formulated in Equation 7.7, which means that the spectra of the photons created on the $\uparrow$ and $\downarrow$ scattering paths overlap, is usually hard to fulfill in the monochromatic scheme. The detunings $\delta_\uparrow$ and $\delta_\downarrow$ are given by the involved atomic transitions while the detunings $\Delta_\uparrow$ and $\Delta_\downarrow$ cannot be chosen independently from each other, for a single monochromatic laser that excites both scattering paths. As a consequence, the case formulated in Equation 7.7 is usually not found in experiments and the phase of the atom-photon state created with monochromatic laser excitation depends on the detection time of the photon.

The situation changes if two laser beams are used. One laser beam excites the $\uparrow$ branch, while the second independent laser excites the $\downarrow$ branch. In this case the detunings $\Delta_\uparrow$ and $\Delta_\downarrow$ can be chosen independently from each other to satisfy the condition formulated in Equation 7.7. Consequently, the detection time dependence of the phase in Equation 7.5 vanishes. This is for example the case for $\Delta_\uparrow = -\delta_\uparrow$ and $\Delta_\downarrow = -\delta_\downarrow$. However, a closer look reveals that this approach poses two experimental challenges. The relative phase encode in the phase of $\Omega_\uparrow$ and $\Omega_\downarrow$ enters the phase of the created state. Therefore, phase-stability between both laser beams driving the $\uparrow$ and $\downarrow$ branch is required, which poses the first challenge. The second challenge is to selectively drive the $\uparrow$ and $\downarrow$ branch with the respective laser beam. In case of the 393 nm entanglement scheme the excited transitions are a σ^-- and a σ^+-transition (see Figure 7.1) and a selective excitation is possible with circularly polarized laser beams in direction of the quantization axis. In case of the 854 nm entanglement scheme, only a single transition is excited that is part of the $\uparrow$ and $\downarrow$ branch (see Figure 7.1). Therefore, it is not possible to selectively excite the $\uparrow$ and $\downarrow$ branch. Instead, the $\uparrow$-laser also excites the $\downarrow$ branch and vice versa. Consequently, four scattering paths are created from whom two have the same frequency (condition in Equation 7.7). The other two scattering paths have different frequencies and can be removed by spectral filtering.

Instead of two individual phase-stable laser beams that excite the same transition, a single bichromatic laser beam can be used to ensure the required phase stability. The same can be applied in the 393 nm scheme where the bichromatic laser beam excites both transitions. As in the 854 scheme a spectral filter removes the unwanted frequency components. This approach taken here, a bichromatic laser excitation together with a spectral filter, is presented in more detail in the following.

Bichromatic laser excitation

In case of a bichromatic laser excitation with the Rabi frequencies Ω_1 and Ω_2 no common rotating frame can be found for both components. However, for small Rabi frequencies Ω_1 and Ω_2 the Raman amplitude R can be approximated by a sum of the Raman amplitudes R_1 and R_2. These amplitudes treat both components of the bichromatic laser beam as independent, phase-stable monochromatic laser beams. Together with the same approximations as for the monochromatic case ($\Omega_{1,2} \ll \Gamma$, $\Delta_{AC} \approx 0$), the Raman amplitude of the photon scattered in each branch becomes

$$R(t) = R_1(t) + R_2(t) = \sqrt{\Gamma_f}e^{-i\delta_f t}\left(a_1 e^{-i\Delta_1 t} + a_2 e^{-i\Delta_2 t}\right). \tag{7.9}$$

In analogy to the monochromatic case (see Equation 7.4) the coefficients

$$a_1 = \frac{\Omega_1}{N_1}\Theta(t)e^{-\frac{\kappa_1}{2}t} \qquad \text{and} \qquad a_2 = \frac{\Omega_2}{N_2}\Theta(t)e^{-\frac{\kappa_2}{2}t} \tag{7.10}$$

describe the envelope of the wave packet. They depend on the Rabi frequencies Ω_1 respectively Ω_2 and the detunings Δ_1 respectively Δ_2 and describe the relative strengths of both scattering paths created by the bichromatic laser excitation. By adjusting Ω_1, Ω_2, Δ_1 and Δ_2 the relative strength can be controlled. I utilize this to compensate different decay rates $\Gamma_\uparrow$ and $\Gamma_\downarrow$ (see Equation 7.8). In the following I will assume positive Rabi frequencies Ω_1 and Ω_2. This corresponds to two frequency components with the same phase. For different phases you have to replace $\Omega_1 \to e^{i\phi_1}\Omega_1$ and $\Omega_2 \to e^{i\phi_2}\Omega_2$ what leads to an additional phase offset in the created atom-photon state.

For the experimental implementation two special cases are relevant that allow to further simplify the Raman amplitude. First, for symmetric detuning $\Delta_1 = -\Delta_2 = \Delta$ one finds $\kappa_1 = \kappa_2 = \kappa$ and $N_1 = N_2 = N$ and the Raman amplitude becomes

$$R(t) = \sqrt{\Gamma_f}e^{-i\delta_f t}\frac{\Theta(t)}{N}e^{-\frac{\kappa}{2}t}\left(\Omega_1 e^{-i\Delta t} + \Omega_2 e^{+i\Delta t}\right). \tag{7.11}$$

In this case, the relative strength of both components is directly given by the ratio of the Rabi frequencies Ω_1 and Ω_2. This case is applied in the $854\,\text{nm}$ atom-photon entanglement scheme. Second, for equal Rabi frequencies $\Omega_1 = \Omega_2 = \Omega$ one finds

$$R(t) = \sqrt{\Gamma_f}e^{-i\delta_f t}\left(\tilde{a}_1 e^{-i\Delta_1 t} + \tilde{a}_2 e^{-i\Delta_2 t}\right) \tag{7.12}$$

with the coefficients $\tilde{a}_k = a_k(\Omega = \Omega_k, \Delta_k)$ that are only different due to the different detunings Δ_k. Consequently, the relative strength in both components is only given by the detunings Δ_1 and Δ_2 of both frequency components from the excited transition. This case of equal Rabi frequencies Ω_1 and Ω_2 is applied in the $393\,\text{nm}$ atom-photon entanglement scheme where one additionally has $\Delta_{\uparrow 1} = -\Delta_{\downarrow 2}$ and $\Delta_{\uparrow 2} = -\Delta_{\downarrow 1}$ for the excited transitions in the $\uparrow$ and $\downarrow$ branch what results in $\tilde{a}_{\uparrow 1} = \tilde{a}_{\downarrow 2}$ respective $\tilde{a}_{\uparrow 2} = \tilde{a}_{\downarrow 1}$.
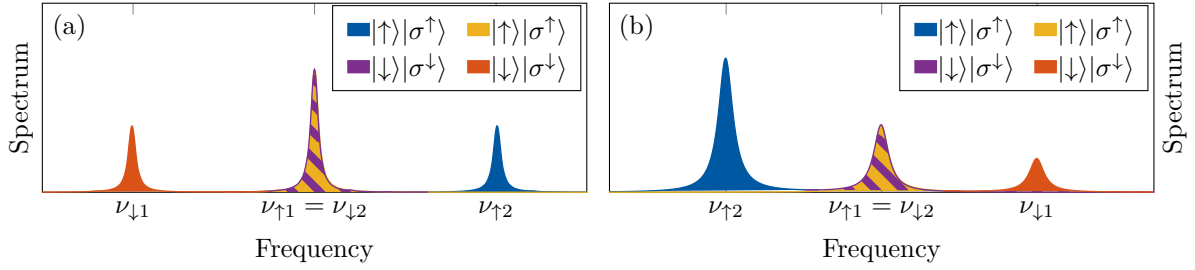
Figure 7.2.: Exemplary power spectrum of the four components of an atom-photon state created with a bichromatic laser excitation that satisfies the conditions in Equation 7.15. The not overlapping spectral components carry the same (a) or different population (b). These cases appear in the schemes that generate 393 nm (a) respective 854 nm (b) photons (See the measured spectra in Figure 7.4 and Figure 7.6.).

I put the Raman amplitude for a bichromatic laser excitation in Equation 7.9 into Equation 7.1 to obtain the created atom-photon state

$$\begin{aligned}|\Psi\rangle = \sqrt{\Gamma_\uparrow}e^{-\mathrm{i}\delta_\uparrow t}\left(a_1 e^{-\mathrm{i}\Delta_{\uparrow 1}t} + a_2 e^{-\mathrm{i}\Delta_{\uparrow 2}t}\right)|\uparrow\rangle\,|\sigma^\uparrow\rangle \\ + \sqrt{\Gamma_\downarrow}e^{-\mathrm{i}\delta_\downarrow t}\left(a_1 e^{-\mathrm{i}\Delta_{\downarrow 1}t} + a_2 e^{-\mathrm{i}\Delta_{\downarrow 2}t}\right)|\downarrow\rangle\,|\sigma^\downarrow\rangle\,.\end{aligned} \tag{7.13}$$

This state contains four components, two from each scattering path that have the frequencies

$$\nu_{\uparrow 1} = \delta_\uparrow + \Delta_{\uparrow 1}, \qquad \nu_{\uparrow 2} = \delta_\uparrow + \Delta_{\uparrow 2}, \qquad \nu_{\downarrow 1} = \delta_\downarrow + \Delta_{\downarrow 1}, \qquad \text{and} \qquad \nu_{\downarrow 2} = \delta_\downarrow + \Delta_{\downarrow 2}. \tag{7.14}$$

These frequencies correspond to the position of the spectral components of the generated photon amplitudes. If the frequency components of the bichromatic laser field are chosen so that the conditions

$$\nu_{\uparrow 1} = \delta_\uparrow + \Delta_{\uparrow 1} = \delta_\downarrow + \Delta_{\downarrow 2} = \nu_{\downarrow 2} \qquad \text{and} \qquad \sqrt{\Gamma_\uparrow}a_1 = \sqrt{\Gamma_\downarrow}a_2, \tag{7.15}$$

are satisfied, the created atom-photon state becomes

$$\begin{aligned}|\Psi\rangle = a_1\sqrt{\Gamma_\uparrow}e^{-\mathrm{i}\nu_{\uparrow 1}t}\left(|\uparrow\rangle\,|\sigma^\uparrow\rangle + |\downarrow\rangle\,|\sigma^\downarrow\rangle\right) \\ + \left(a_2\sqrt{\Gamma_\uparrow}e^{-\mathrm{i}\nu_{\uparrow 2}t}|\uparrow\rangle\,|\sigma^\uparrow\rangle + a_1\sqrt{\Gamma_\downarrow}e^{-\mathrm{i}\nu_{\downarrow 1}t}|\downarrow\rangle\,|\sigma^\downarrow\rangle\right)\,.\end{aligned} \tag{7.16}$$

In this state, the four spectral components form two parts: The first part (yellow and purple) contains the photon amplitudes where the spectral components have the same frequency ($\nu_{\uparrow 1} = \nu_{\downarrow 2}$, see Figure 7.2). The second part (blue and red) contains the photon amplitudes where the spectral components have different frequencies ($\nu_{\uparrow 2}$, $\nu_{\downarrow 1}$, see Figure 7.2). Because the two photon amplitude components in the first part have the same frequency, the phase of this part is independent from the detection time of the photon. In the second part, the frequencies

are different and the phase of this part depends on the detection time of the photon, as for the monochromatic case (cf. Equation 7.6). If additionally to the condition in Equation 7.15 the condition $a_1\sqrt{\Gamma_\downarrow} = a_2\sqrt{\Gamma_\uparrow}$ is met (see Figure 7.2 (a)), the generated state is maximally entangled, if one takes the detection time of the photon into account. This is analog to the monochromatic case. In contrast to the monochromatic case, a partially entangled state is created, if the detection time of the photon is ignored. In this case, the phase information in the detection time dependent part (blue and red) is lost, which reduces the entanglement of the created atom-photon state. Then, the relative population between the detection time independent part (yellow and purple) and the detection time dependent part determines the amount of entanglement in the generated atom-photon state. If one is able to remove the detection time dependent part from the generated state one creates a maximal entangled atom photon state, that is independent from the detection time of the photon.

As the photon amplitudes of the detection time independent part are linked to overlapping spectral components, which are separated from the spectral components of the time dependent part, the time dependent part can be removed with a spectral filter that is set to the frequency $\nu_{\uparrow 1} = \nu_{\downarrow 2}$. For photons transmitted through this spectral filter, the generated atom photon state becomes [4]

$$|\Psi\rangle = \frac{1}{\sqrt{2}} \left(|\uparrow\rangle \, |\sigma^\uparrow\rangle + |\downarrow\rangle \, |\sigma^\downarrow\rangle \right). \tag{7.17}$$

This is a maximal entangled state that is independent from the detection time of the photon. The constant phase offset ϕ in this state depends on the phase between the frequency components of the bichromatic laser beam and the experimental realization.

In the following sections I adapt the above derivation to the 393 nm and the 854 nm atom-photon entanglement schemes. Afterwards, I characterize the generated atom-photon entanglement for the monochromatic and the bichromatic schemes. In case of the bichromatic scheme the atom-photon state created with and without spectral filtering is compared. With this I show how the spectral filter acts as quantum eraser [94] that increases the entanglement of the generated state.

7.1.1. The 393 nm entanglement creation schemes

To create 393 nm atom-photon entanglement I prepare the ion in a superposition of the $|D_{5/2}, +\frac{5}{2}\rangle$ and $|D_{5/2}, -\frac{5}{2}\rangle$ Zeeman levels. A vertically polarized 854 nm laser, perpendicular to the magnetic field, excites the prepared initial superposition into the $|P_{3/2}, +\frac{3}{2}\rangle$ and $|P_{3/2}, -\frac{3}{2}\rangle$ Zeeman levels. By emitting a 393 nm Raman photon the ion returns into the $|S_{1/2}, +\frac{1}{2}\rangle$ and $|S_{1/2}, -\frac{1}{2}\rangle$ state. The polarization of the 393 nm Raman photon created in this process is entangled with the atomic state in the Zeeman levels of the $S_{1/2}$ ground state. I collect the created 393 nm photon in direction of the magnetic field, thus the photons scattered on the

---

[4]The atom-photon state corresponds to the case, that a photon was detected. The amplitude of the components that are reflected at the cavity have been separated off. The same is done throughout the whole discussion with atom-photon amplitudes created by a decay into other atomic states (e.g. $D_{3/2}$).

σ transitions are circularly polarized and I get the following mapping for the involved atomic and polarization states:

$$|\uparrow\rangle \to |S_{1/2}, +\tfrac{1}{2}\rangle = |+\tfrac{1}{2}\rangle, \quad |\downarrow\rangle \to |S_{1/2}, -\tfrac{1}{2}\rangle = |-\tfrac{1}{2}\rangle, \quad |\sigma^+\rangle \to |L\rangle, \quad \text{and} \quad |\sigma^-\rangle \to |R\rangle. \quad (7.18)$$

Monochromatic laser excitation

I set the detuning of the monochromatic $854\,\mathrm{nm}$ laser to the line center of the $854\,\mathrm{nm}$ transition ($\Delta = 0$). This results in the detunings

$$\Delta_\uparrow = \Delta - (g_P m_{P\uparrow} - g_D m_{D\uparrow})\mu_B B = +\mu_B B \qquad \text{and} \qquad \Delta_\downarrow = -\mu_B B \qquad (7.19)$$

on the individual excited $854\,\mathrm{nm}$ transitions, using $g_P = \frac{6}{5}$, $g_D = \frac{4}{3}$ and the magnetic quantum numbers $m_{P\uparrow} = +\frac{3}{2}$, $m_{P\downarrow} = -\frac{3}{2}$, $m_{D\uparrow} = +\frac{5}{2}$ and $m_{D\downarrow} = -\frac{5}{2}$. Because the detunings fulfill the condition $\Delta_\uparrow = -\Delta_\downarrow$ the envelopes of the wave packets of both scattering paths (see Equation 7.4) are the same and therefore a constant common factor that is not written down in the further analysis. With the frequency shifts

$$\delta_\uparrow = (g_P m_{P\uparrow} - g_S m_{S\uparrow})\mu_B B = +\mu_B B \qquad \text{and} \qquad \delta_\downarrow = -\mu_B B \qquad (7.20)$$

of the $393\,\mathrm{nm}$ transitions, where $g_S = 2$, $m_{S\uparrow} = +\frac{1}{2}$ and $m_{S\downarrow} = -\frac{1}{2}$, and the $854\,\mathrm{nm}$ laser detunings $\Delta_\uparrow$ and $\Delta_\downarrow$ I calculate the frequencies

$$\nu_\uparrow = +2\mu_B B = +8\,\mathrm{MHz} \qquad \text{and} \qquad \nu_\downarrow = -2\mu_B B = -8\,\mathrm{MHz} \qquad (7.21)$$

of both components of the scattered $393\,\mathrm{nm}$ photon. With theses frequencies, the joint atom-photon state detected at a time t becomes

$$|\Psi(t)\rangle = \frac{1}{\sqrt{2}}\left[e^{-2i\mu_B B t}\,|+\tfrac{1}{2}\rangle\,|L\rangle + e^{2i\mu_B B t + i\phi}\,|-\tfrac{1}{2}\rangle\,|R\rangle\right]. \qquad (7.22)$$

The phase of this state depends on the detection time t of the $393\,\mathrm{nm}$ photon, with a constant phase offset ϕ given by the experimental realization that contains the phase of the prepared initial superposition, the phase of the $854\,\mathrm{nm}$ laser and timings in the experimental pulse sequence. The frequency $\nu_\Psi = 4\mu_B B$ of the oscillation in the correlation between the atomic state and photon polarization corresponds to the frequency difference of the Larmor precession in the $|D_{5/2}, +\tfrac{5}{2}\rangle$ and $|D_{5/2}, -\tfrac{5}{2}\rangle$ Zeeman levels ($\nu_D = 6\mu_B B$) and the Larmor precession in the $|S_{1/2}, +\tfrac{1}{2}\rangle$ and $|S_{1/2}, -\tfrac{1}{2}\rangle$ Zeeman levels ($\nu_S = 2\mu_B B$).

I show this monochromatic scheme in Figure 7.3, where horizontal lines indicate the energy shifts of involved levels in units of $\mu_B B$, here $4\,\mathrm{MHz}$. Additionally, I show the measured spectrum of photons scattered from a mixed initial state in the $|D_{5/2}, +\tfrac{5}{2}\rangle$ and $|D_{5/2}, -\tfrac{5}{2}\rangle$ Zeeman level (without any state or polarization projection). The $854\,\mathrm{nm}$ laser is applied with the excitation parameters I use for the monochromatic atom-photon entanglement generation presented in Section 7.2.1. Therefore, the measured spectrum is the same as the spectrum of
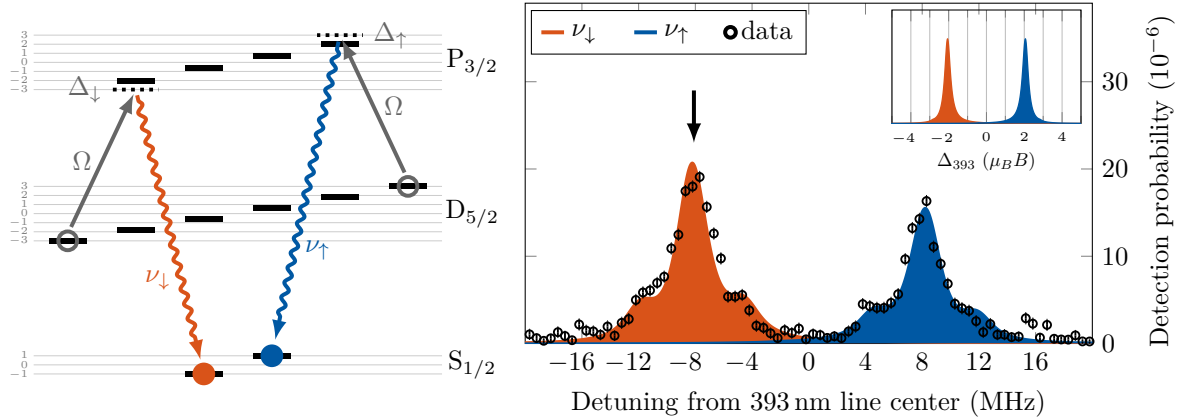
Figure 7.3.: Scheme to create 393 nm atom-photon entanglement with a monochromatic laser and spectrum of the created 393 nm photon (from a mixed initial state). Excitation parameter: $\tau = 2\,\mu s$, $\Omega_{854} = (2\pi)\,9.88(1)\,\text{MHz}$, $\Delta_{854} = 0\,\text{MHz}$ ($0 \to 0$ horizontal line). The inset contains the ideal spectrum (without sidebands and measurement apparatus) that is emitted on both scattering paths from a balanced superposition state. The arrow indicates the position of the filter cavity during the entanglement measurement in Section 7.2.1.

photons created during the atom-photon-entanglement scheme (except for the imbalance).

The photon spectrum has two peaks at $\pm 8\,\text{MHz}$ that correspond to the frequencies $\nu_\uparrow$ and $\nu_\downarrow$. The different height of both components is an artifact from the initial state prepared in the spectrum measurement. Because the spectrum was measured without any optical pumping (pulse sequence see Section 4.5) the initial state is imbalanced towards the $|D_{5/2}, -\frac{5}{2}\rangle$ Zeeman level. In the atom-photon entanglement scheme presented in Section 7.2.1 the state preparation includes optical pumping so that a balanced initial superposition is created.

The shift of both spectral components with respect to the 393 nm line center can be found in the following way in the depicted level scheme. The initial $|D_{5/2}, -\frac{5}{2}\rangle$ level has an energy shift of $-3\mu_\text{B}B$. The 854 nm laser (resonant with the line center of the 854 nm transition) excites this state to a virtual level with an energy shift of $-3\mu_\text{B}B$. This virtual level lies below the $|P_{3/2}, -\frac{3}{2}\rangle$ state, which is shifted by $-2\mu_\text{B}B$. The distance of the virtual level to the $|P_{3/2}, -\frac{3}{2}\rangle$ state corresponds to the detuning $\Delta_\downarrow = -\mu_\text{B}B$ of the 854 nm laser from the $|D_{5/2}, -\frac{5}{2}\rangle$ to $|P_{3/2}, -\frac{3}{2}\rangle$ transition. From the virtual level, the ion decays into the $|S_{1/2}, -\frac{1}{2}\rangle$ state. Because the virtual level has an energy shift of $-3\mu_\text{B}B$ and the final level has an energy shift of $-\mu_\text{B}B$, the frequency of the photon is shifted by $-2\mu_\text{B}B$ compared to the 393 nm line center. The scattering path out of the $|D_{5/2}, +\frac{5}{2}\rangle$ is mirror inverted what leads to the shift of $+2\mu_\text{B}B$ compared to the 393 nm line center. The additional small shift visible in the spectrum is caused by the AC stark shift of the excited level ($\Delta_{\text{AC},\downarrow} \approx -0.26\,\text{MHz}$ respective $\Delta_{\text{AC},\uparrow} \approx +0.26\,\text{MHz}$, calculated with Equation 5.27; Details see Section 6.1) that is neglected in the simplified calculation. Additional features in the measured spectrum are identified as radial sidebands ($\pm 3.7\,\text{MHz}$ from the carrier) and micromotion sidebands ($\pm 24\,\text{MHz}$ from the carrier).

Bichromatic laser excitation

The frequency components of the bichromatic laser beam are calculated from the frequency shifts of the involved atomic transitions. I calculate the detunings $\Delta_1 = -2\mu_B B$ and $\Delta_2 = +2\mu_B B$ of the bichromatic frequency components. Together with the frequency shifts of the 854 nm transitions and the frequency shifts of the 393 nm transitions I get the positions

$$\nu_{\downarrow 1} = -4\mu_B B, \qquad \nu_{\uparrow 1} = 0, \qquad \nu_{\downarrow 2} = 0, \qquad \text{and} \qquad \nu_{\uparrow 2} = +4\mu_B B. \qquad (7.23)$$

of the spectral components of the generated 393 nm photon (see Figure 7.2 (a)). Because the system is symmetric, I set the same Rabi frequencies Ω_1 and Ω_2 for both frequency components of the bichromatic 854 nm laser. Due to the symmetry of the scheme ($\Gamma_\uparrow = \Gamma_\downarrow$, $\Delta_{\uparrow 1} = -\Delta_{\downarrow 2}$ and $\Delta_{\uparrow 2} = -\Delta_{\downarrow 1}$) one can summarize all parts that describe the envelope in two coefficients $\alpha = \Gamma_\uparrow \tilde{a}_{\uparrow 1} = \Gamma_\downarrow \tilde{a}_{\downarrow 2}$ and $\beta = \Gamma_\uparrow \tilde{a}_{\uparrow 2} = \Gamma_\downarrow \tilde{a}_{\downarrow 1}$ (see paragraphs around Equation 7.10 and Equation 7.12). Altogether one gets the generated atom-photon state

$$|\Psi(t)\rangle = \alpha \left(|+\tfrac{1}{2}\rangle\,|\text{L}\rangle + e^{i\phi_1}|-\tfrac{1}{2}\rangle\,|\text{R}\rangle \right) + \beta \left(e^{-4i\mu_B Bt}|+\tfrac{1}{2}\rangle\,|\text{L}\rangle + e^{i\phi_2}e^{+4i\mu_B Bt}|-\tfrac{1}{2}\rangle\,|\text{R}\rangle \right), \quad (7.24)$$

where the constant offset phases ϕ_1 and ϕ_2 depend on the experimental realization (initial superposition, bichromatic phase, experimental timings). The phase of the first part (yellow and purple) that is formed by the spectral components that overlap at the line center of the 393 nm transition is independent from the detection time of the photon. The second part (blue and red) has a phase that depends on the detection time of the photon. This part is formed by outer spectral components at the frequencies $\nu_{\uparrow 2}$ and $\nu_{\downarrow 1}$. I remove the outer spectral components with a spectral filter that is set to the frequency of the overlapping spectral components ($\nu_{\uparrow 1} = \nu_{\downarrow 2}$) . This spectral filter transmits only photons that form the first part (yellow and purple) of the created atom photon state. Therefore, for photons transmitted through the spectral filter the atom-photon state

$$|\Psi(t)\rangle = \frac{1}{\sqrt{2}} \left(|+\tfrac{1}{2}\rangle\,|\text{L}\rangle + e^{i\phi_1}|-\tfrac{1}{2}\rangle\,|\text{R}\rangle \right) \qquad (7.25)$$

is created. This maximally entangled state is independent from the detection time of the 393 nm photon.

I show the bichromatic scheme in Figure 7.4. In analogy to the monochromatic scheme, horizontal lines indicate the energy shifts of the involved levels in units of $\mu_B B$, here 4 MHz. The bichromatic laser creates virtual levels above and below the excited states in the $P_{3/2}$ manifold. For comparison, I show the virtual state from the monochromatic case (light gray). From each virtual level a decay path goes into the respective $S_{1/2}$ Zeeman level. As it can be seen in the scheme, the photon emitted from the virtual level above the $|P_{3/2}, -\tfrac{3}{2}\rangle$ state and the photon emitted from the virtual level below the $|P_{3/2}, +\tfrac{3}{2}\rangle$ state have the same frequency. The decays from the other two virtual levels are shifted by the frequency difference of the bichromatic
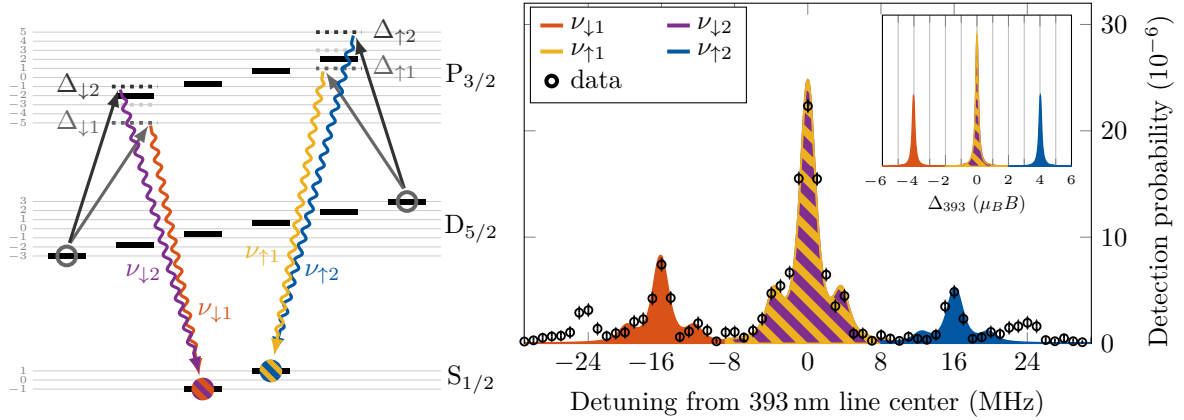
Figure 7.4.: Scheme to generate 393 nm atom photon entanglement with a bichromatic 854 nm laser pulse (left) and spectrum of the created 393 nm photons (right). Excitation parameter: $\tau = 3\,\mu s$, $\Omega_{1,2} = (2\pi)\,5.56(1)\,MHz$, $\Delta_{1,2} = \pm 8.05\,MHz$. The inset contains the ideal spectrum (without sidebands and measurement apparatus) that is emitted from a balanced superposition.

components. Additionally, the sketch shows that the first mentioned virtual levels are closer to the respective $P_{3/2}$ Zeeman level and therefore become stronger populated. Consequently, the spectral components with the frequencies $\nu_{\uparrow 1}$ and $\nu_{\downarrow 2}$ are stronger.

I measure the spectrum of photons created out of a mixed initial state with the bichromatic 854 nm excitation that is used for the atom-photon entanglement scheme in Section 7.2.2. Therefore, the photons created in the atom-photon entanglement scheme have the same spectral shape as the measured spectrum (except for the imbalance). The photon spectrum has three peaks that correspond to the frequency components created by the bichromatic laser excitation, a large component at the 393 nm line center and two smaller components located at $\pm 16\,MHz$. The spectral component at the line center corresponds to the overlapping scattering paths with the frequencies $\nu_{\uparrow 1}$ and $\nu_{\downarrow 2}$. The component at $-16\,MHz$ is located at the frequency $\nu_{\downarrow 1}$. The component at $+16\,MHz$ is located at the frequency $\nu_{\uparrow 2}$. The central peak has more than twice the height of the outer spectral components. This is caused by the different distance of the virtual levels from the excited $P_{3/2}$ Zeeman level. As for the monochromatic case, the measured spectrum contains radial sidebands (at $\pm 3.7\,MHz$) and micromotion sidebands (at $\pm 24\,MHz$) of each carrier.

7.1.2. The 854 nm entanglement creation schemes

Schemes to generate 854 nm atom-photon entanglement are a focus of further research in our research group towards a quantum network. One reason for this is the availability of a quantum frequency converter [60, 95] to convert the generated 854 nm photons to telecommunication wavelengths. This is a requirement to distribute the created atom-photon entanglement over large distances. Furthermore, the schemes create atom-photon entanglement at a higher rate compared to the 393 nm atom-photon entanglement schemes.

The scheme to generate 854 nm atom-photon entanglement [59] starts from a mixture in the $S_{1/2}$ ground state. A horizontally polarized 393 nm laser, perpendicular to the magnetic field axis, selectively excites the π transitions into the $|P_{3/2}, +\frac{1}{2}\rangle$ and $|P_{3/2}, -\frac{1}{2}\rangle$ Zeeman levels. The selective excitation of the π transitions is a crucial part of this scheme. From the excited $P_{3/2}$ levels, the ion decays into the $D_{5/2}$ manifold by emitting a 854 nm photon, back into the $S_{1/2}$ ground state or into the $D_{3/2}$ manifold. The decay into the $D_{3/2}$ manifold reduces the efficiency of the scheme. Additionally it has to be taken into account in the state detection scheme. Although the unwanted decay back into the $S_{1/2}$ state happens more frequently than the desired decay into the $D_{5/2}$ state, the continuous excitation of the ground state into the $P_{3/2}$ state ensures, that finally the decay into the $D_{5/2}$ state happens. The 854 nm decay out of the $|P_{3/2}, +\frac{1}{2}\rangle$ and $|P_{3/2}, -\frac{1}{2}\rangle$ levels can happen on a σ^+, π or σ^- transition. Photon collection along the quantization axis selects the photons emitted on the σ-transitions. With this the polarization of a detected 854 nm photon is entangled with the atomic state in the $D_{5/2}$ Zeeman levels. However, there are two possibilities for the generated atom-photon state. The 393 nm laser excites both π transitions and therefore the 854 nm decay happens out of the $|P_{3/2}, +\frac{1}{2}\rangle$ and $|P_{3/2}, -\frac{1}{2}\rangle$ levels into four different $D_{5/2}$ levels. Thus the scheme can be divided into two independent schemes that are distinguished post-selectively by atomic state detection. I call the scheme involving the $|P_{3/2}, -\frac{1}{2}\rangle$ level the "left" side and the scheme involving the $|P_{3/2}, +\frac{1}{2}\rangle$ level the "right" side. To generate 854 nm atom-photon entanglement only one side is needed while the other side is considered a loss channel. Because both sides are mirror-inverted from each other, all arguments for one side can be made analogously for the other side. Here, I focus on the right side to compare the case of a monochromatic or bichromatic 393 nm laser excitation. For this side I get the following mapping of the involved atomic and polarization states [5]:

$$|\uparrow\rangle \to |D_{5/2}, +\tfrac{3}{2}\rangle = |+\tfrac{3}{2}\rangle, \quad |\downarrow\rangle \to |D_{5/2}, -\tfrac{1}{2}\rangle = |-\tfrac{1}{2}\rangle, \quad |\sigma^+\rangle \to |R\rangle, \quad \text{and} \quad |\sigma^-\rangle \to |L\rangle. \quad (7.26)$$

Monochromatic laser excitation

In the 854 nm entanglement scheme the same 393 nm transition is excited for both scattering paths of the 854 nm photon. Therefore, the detunings $\Delta_\uparrow$ and $\Delta_\downarrow$ are the same and the frequency difference of both scattering paths is given by the frequency difference of both final Zeeman levels. I use the individual 393 nm and 854 nm transitions between the $|S_{1/2}, +\frac{1}{2}\rangle$, $|P_{3/2}, +\frac{1}{2}\rangle$ and $|D_{5/2}, +\frac{1}{2}\rangle$ state as reference for all detunings. For a monochromatic 393 nm laser excitation, I get the frequencies

$$\nu_\downarrow = \Delta_{393} + g_D \mu_B B \qquad \text{and} \qquad \nu_\uparrow = \Delta_{393} - g_D \mu_B B \qquad (7.27)$$

of the scattered photons, where Δ_{393} is the detuning of the 393 nm laser.

---

[5]Because the photons are collected anti parallel to the magnetic field the σ decays translate into the orthogonal polarization compared to the 393 nm atom-photon entanglement schemes (see Equation 7.18).
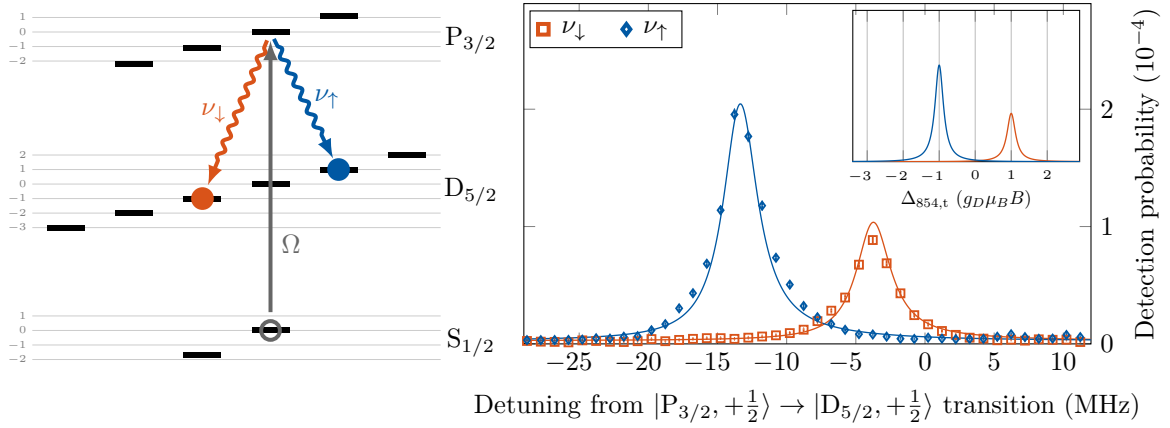
Figure 7.5.: Scheme to generate 854 nm atom-photon entanglement with a monochromatic laser (left) and spectrum of the generated photons (right). Excitation parameter: $\tau = 20\,\mu\text{s}$, $\Omega_{393} = (2\pi)\,5.51(1)\,\text{MHz}$, $\Delta_{393} = -8.4\,\text{MHz}$. The inset contains the ideal emitted spectrum (without sidebands and measurement apparatus) in units of the $D_{5/2}$ state splitting.

I put the frequencies of the scattered photons in Equation 7.5 to obtain the created imbalanced atom-photon state

$$|\Psi(t)\rangle = \sqrt{\tfrac{2}{3}}e^{+ig_D\mu_B Bt}\,|+\tfrac{3}{2}\rangle\,|\text{L}\rangle + \sqrt{\tfrac{1}{3}}e^{i\phi}e^{-ig_D\mu_B Bt}\,|-\tfrac{1}{2}\rangle\,|\text{R}\rangle, \tag{7.28}$$

where the phase ϕ depends on the experimental realization. The factors $\sqrt{\tfrac{2}{3}}$ and $\sqrt{\tfrac{1}{3}}$, are caused by the Clebsch-Gordan coefficients of the respective 854 nm decay channel. To obtain a balanced state, half of the population in the $|+\tfrac{3}{2}\rangle\,|\text{L}\rangle$ state has to be removed. Experimentally, this can be done either by introducing a polarization dependent loss or by removing population from the $|D_{5/2}, +\tfrac{3}{2}\rangle$ level with an additional laser pulse [6]. The latter method is chosen in the experimental realization. The balancing changes the created atom-photon state to

$$|\Psi(t)\rangle = \frac{1}{\sqrt{2}}\left[e^{+ig_D\mu_B Bt}\,|+\tfrac{3}{2}\rangle\,|\text{L}\rangle + e^{i\phi}e^{-ig_D\mu_B Bt}\,|-\tfrac{1}{2}\rangle\,|\text{R}\rangle\right]. \tag{7.29}$$

As for the 393 nm monochromatic case, the phase of this state depends on the detection time of the 854 nm photon. The frequency of the oscillation in the correlation between photon polarization and atomic superposition state is given by the frequency of the Larmor precession of a superposition in the $|+\tfrac{3}{2}\rangle$ and $|-\tfrac{1}{2}\rangle$ Zeeman level.

I show the atom-photon entanglement scheme in Figure 7.5. Horizontal lines indicate frequency shifts with respect to the $m = +\tfrac{1}{2}$ Zeeman levels in units of the frequency splitting between two $D_{5/2}$ Zeeman levels ($g_D\mu_B B$, here 4.8 MHz). The frequency difference between the frequencies $\nu_\uparrow$ and $\nu_\downarrow$ is only given by the frequency difference of the final $D_{5/2}$ Zeeman levels. I measure

---

[6]The detuning Δ_{393} has no effect on the population because the same 393 nm transition is excited for both scattering paths.

the spectrum of photon generated in this scheme before the balancing operation is applied. The measured spectrum of the 854 nm photons (see Figure 7.5 right) shows the frequency difference of 9.6 MHz between both spectral components (details on the spectrum measurement see Section 4.5). Due to a detuning $\Delta_{393} = -8.4$ MHz of the 393 nm laser from the excited $|S_{1/2}, +\frac{1}{2}\rangle$ to $|P_{3/2}, +\frac{1}{2}\rangle$ transition, the spectra of the generated photons are red-shifted with respect to the $|P_{3/2}, +\frac{1}{2}\rangle$ to $|D_{5/2}, +\frac{1}{2}\rangle$ transition. The different height and population of both spectral components corresponds to the square of the Clebsch-Gordan coefficients of the decay into the $|D_{5/2}, +\frac{3}{2}\rangle$ and $|D_{5/2}, -\frac{1}{2}\rangle$ Zeeman level, which were not compensated in the spectrum measurement.

Bichromatic laser excitation

The frequency components of the bichromatic laser excitation are set to compensate the frequency difference of both decay channels out of the $|P_{3/2}, +\frac{1}{2}\rangle$ state. Thus, the frequency components have the detunings

$$\Delta_1 = g_D\mu_B B \qquad \text{and} \qquad \Delta_2 = -g_D\mu_B B. \tag{7.30}$$

A laser pulse with these detunings excites the ion into two virtual levels above and below the $|P_{3/2}, +\frac{1}{2}\rangle$ level. From the virtual levels the ion decays into the final $|D_{5/2}, +\frac{3}{2}\rangle$ and $|D_{5/2}, -\frac{1}{2}\rangle$ Zeeman level. Therefore, the frequencies of the spectral components become

$$\nu_{\uparrow 2} = -2g_D\mu_B B, \qquad \nu_{\uparrow 1} = 0, \qquad \nu_{\downarrow 2} = 0, \qquad \text{and} \qquad \nu_{\downarrow 1} = 2g_D\mu_B B. \tag{7.31}$$

Additionally, I compensate the different Clebsch-Goarden coefficients of the 854 nm decay channels. For the symmetric detunings $\Delta_1 = -\Delta_2$ the relative strength of both scattering paths only depends on the ratio of the Rabi frequencies Ω_1 and Ω_2 of both frequency components (see Equation 7.11). For a ratio

$$\Omega_2 = \sqrt{2}\Omega_1 \tag{7.32}$$

the spectrally overlapping components become equally strong. Thus this ratio is chosen. The atom-photon state that is created with the discussed settings of the bichromatic laser components is

$$\begin{aligned} |\Psi\rangle = C\Big[&\sqrt{2}\,|+\tfrac{3}{2}\rangle\,|\text{L}\rangle + e^{i\phi_1}\sqrt{2}\,|-\tfrac{1}{2}\rangle\,|\text{R}\rangle \\ &+ 2e^{i\phi_2}e^{+2ig_D\mu_B Bt}\,|+\tfrac{3}{2}\rangle\,|\text{L}\rangle + e^{i\phi_3}e^{-2ig_D\mu_B Bt}\,|-\tfrac{1}{2}\rangle\,|\text{R}\rangle \Big], \end{aligned} \tag{7.33}$$

where C contains the normalization and the temporal envelope of the scattered photon. The created state has a part that does not depend on the detection time of the photon (yellow and purple) and a part that depends on the detection time of the photon (blue and red). As a result of the Rabi frequencies $\Omega_2 = \sqrt{2}\Omega_1$, the detection-time-independent part is balanced. In the detection-time-dependent part, the imbalance between both components is increased due
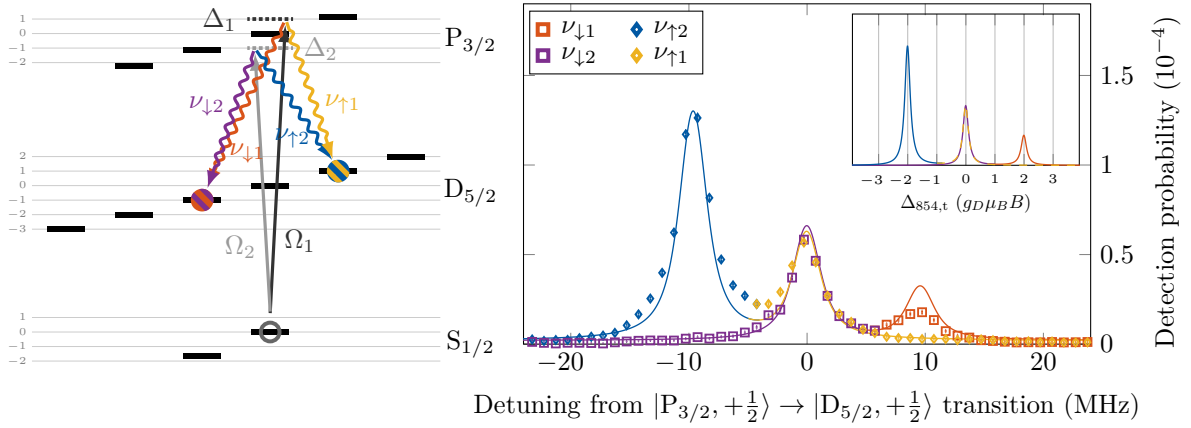
Figure 7.6.: Scheme to generate 854 nm atom-photon entanglement with a bichromatic 393 nm laser (left) and spectrum of the generated photon (right). Excitation parameter: $\tau = 3\,\mu s$, $\Omega_1 \approx (2\pi)\,2.5\,MHz$, $\Omega_2 \approx (2\pi)\,3.7\,MHz$, $\Delta_{1,2} = \pm 4.087\,MHz$. The inset contains the ideal emitted spectrum (without sidebands and measurement apparatus) in units of the $D_{5/2}$ state splitting.

to the different Rabi frequencies (compared to the monochromatic scheme). The phases ϕ_1, ϕ_2 and ϕ_3 between the individual components depend on the experimental realization. The time dependent part can be removed with a spectral filter that is set to the $|P_{3/2}, +\frac{1}{2}\rangle$ to $|D_{5/2}, +\frac{1}{2}\rangle$ transition. This filter transmits only photons linked to the detection-time-independent part of the atom-photon state. Thus the atom-photon state for photons transmitted through the cavity becomes

$$|\Psi\rangle = \frac{1}{\sqrt{2}} \left[|+\frac{3}{2}\rangle\,|L\rangle + e^{i\phi}\,|-\frac{1}{2}\rangle\,|R\rangle \right]. \tag{7.34}$$

I show the bichromatic scheme in Figure 7.6. As for the monochromatic case I indicate frequency shifts with respect to the $m = +\frac{1}{2}$ Zeeman levels in units of the frequency splitting between two $D_{5/2}$ Zeeman levels ($g_D \mu_B B$, here 4.8 MHz). This enables one to read the frequencies in Equation 7.31 directly from the depicted scheme. Due to the chosen detunings $\Delta_1 = -\Delta_2$ the frequencies $\nu_{\uparrow 1}$ and $\nu_{\downarrow 2}$ are equal. As a result the corresponding spectral components are located at the same frequency. The photon spectrum (see Figure 7.6, right) shows this overlap at the frequency of the $|P_{3/2}, +\frac{1}{2}\rangle$ to $|D_{5/2}, +\frac{1}{2}\rangle$ transition. The outer two spectral components correspond to the components of the frequencies $\nu_{\uparrow 2}$ (at -9.6 MHz) and $\nu_{\downarrow 1}$ (at $+9.6$ MHz). Additionally, the spectral components at the frequency of the $|P_{3/2}, +\frac{1}{2}\rangle$ to $|D_{5/2}, +\frac{1}{2}\rangle$ transition carry the same population, while the spectral component at $\nu_{\uparrow 2} = -9.6$ MHz and at $\nu_{\downarrow 1} = +9.6$ MHz) carries twice respectively half the population. This is a consequence of the chosen Rabi frequencies $\Omega_2 = \sqrt{2}\Omega_1$ (exact calibration see below) that compensate the Clebsch-Gordan coefficients of the involved 854 nm decay channels into the $|D_{5/2}, +\frac{1}{2}\rangle$ ($\sqrt{\frac{2}{5}}$) and $|D_{5/2}, -\frac{3}{2}\rangle$ ($\frac{1}{\sqrt{5}}$) Zeeman levels.
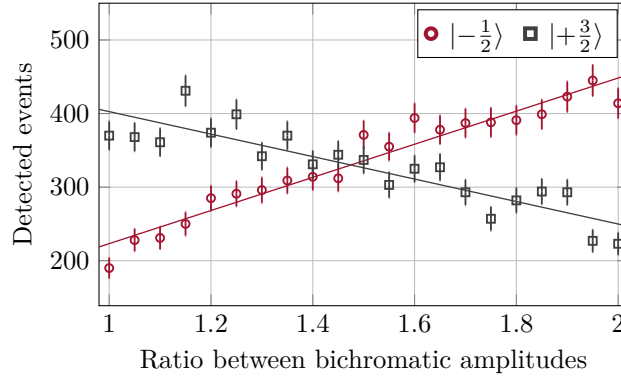
Figure 7.7.: Calibration of the amplitudes of the bichromatic frequency components for the bichromatic 854 nm atom-photon entanglement scheme.

To obtain an atom-photon state as in Equation 7.34, were the spectral overlapping components are equally strong, I calibrate the amplitudes of the frequency components of the bichromatic laser pulse. To balance the components of the created state, the lower virtual state has to be more strongly populated, thus the amplitude of the red-detuned component has to be larger. I set the amplitudes A_1 and A_2 of both radio frequency components that are applied to the acousto-optic modulator that generates the bichromatic 393 nm laser pulse to the same value $(A_1 = A_2)$. With the chosen amplitudes I obtain the Rabi frequencies $\Omega_1 = \Omega_2 \approx (2\pi)\, 2.5\,\mathrm{MHz}$. For this value the spectral components are narrow and I expect well-separated spectral components at the frequencies $\nu_{\uparrow 1} = \nu_{\downarrow 2}$, $\nu_{\uparrow 2}$ and $\nu_{\downarrow 1}$ [7]. I increase the amplitude of the second frequency component $(\Omega_k \propto A_k)$ and measure the population in the $|\mathrm{D}_{5/2}, +\frac{3}{2}\rangle$ and $|\mathrm{D}_{5/2}, -\frac{1}{2}\rangle$ Zeeman levels for each photon that is transmitted through the analysis cavity. I set the analysis cavity to the frequency of the central spectral components which corresponds to the frequency of to the $|\mathrm{P}_{3/2}, +\frac{1}{2}\rangle$ to $|\mathrm{D}_{5/2}, +\frac{1}{2}\rangle$ transition $(\Delta_{854,\mathrm{t}} = 0\,\mathrm{MHz}$ in Figure 7.6, right).

For an increasing Rabi frequency Ω_2, I find the atom more often in the $|\mathrm{D}_{5/2}, -\frac{1}{2}\rangle$ Zeeman level and less often in the $|\mathrm{D}_{5/2}, +\frac{3}{2}\rangle$ Zeeman level (see Figure 7.7). This is caused by a redistribution of the population in the virtual levels below (created by Ω_2) and above (created by Ω_1) the $|\mathrm{P}_{3/2}, +\frac{1}{2}\rangle$ state. Because the virtual level below the $|\mathrm{P}_{3/2}, +\frac{1}{2}\rangle$ state becomes more strongly populated, the components of the atom-photon state that are populated from this virtual state becomes more populated. This are the spectral components wit the frequencies $\nu_{\uparrow 2}$ and $\nu_{\downarrow 2}$. Consequently the spectral components with the frequencies $\nu_{\uparrow 1}$ and $\nu_{\downarrow 1}$ become less populated. The cavity transmits only atom-photon amplitude with the spectral components at the frequencies $\nu_{\downarrow 2} = \nu_{\uparrow 1}$ which results in the observed dependence of the atomic state population from the ratio of the bichromatic amplitudes. For a ratio of 1.47 between the amplitudes A_1 and A_2, the atom-photon amplitude of the spectral components at $\nu_{\downarrow 2} = \nu_{\uparrow 1}$ are equally strong. I attribute the deviation from $\sqrt{2}$ to the performance of the AOM and to

---

[7]The dependence of the Raman photon spectrum on the parameters of the excitation laser is discussed detailed in Section 6.1.

parts of the atom-photon amplitude from the outer spectral components that is transmitted through the cavity. Thus a value larger than $\sqrt{2}$ is required to get the same population in both atomic states [8]. I use the obtained ratio of both frequency components to generate the atom-photon entanglement that is presented in Section 7.3.2. The spectrum shown in Figure 7.6 was measured with the same parameters, therefore the photons created in the atom-photon entanglement scheme have the same spectrum.

7.2. 393 nm atom photon entanglement

7.2.1. Monochromatic excitation – spectral components of the created atom-photon state

To analyze the spectral components of the atom-photon state in Equation 7.22 that is created with monochromatic laser excitation, I remove one of the spectral components with a spectral filter. I prepare the ion in a superposition of the $|D_{5/2}, +\frac{5}{2}\rangle$ and $|D_{5/2}, -\frac{5}{2}\rangle$ Zeeman level. A vertically polarized 854 nm laser ($\tau = 2\,\mu s$, $\Omega_{854} = (2\pi)\,9.88(1)\,\text{MHz}$, $\Delta_{854} = 0\,\text{MHz}$) scatters a 393 nm photon on the transitions into the $|S_{1/2}, +\frac{1}{2}\rangle$ and $|S_{1/2}, -\frac{1}{2}\rangle$ Zeeman levels, where the polarization of the scattered 393 nm photon is entangled with the atomic state in the $|S_{1/2}, +\frac{1}{2}\rangle$ and $|S_{1/2}, -\frac{1}{2}\rangle$ Zeeman levels. The scattered 393 nm photons are collected in direction of the magnetic field and projected on different polarization. Most of the transmission of the polarization setup is coupled into a single mode fiber and send to the analysis cavity setup for spectral filtering. I set the spectral filter to $\Delta_{\text{cav}} = -8.1\,\text{MHz}$ from the 393 nm line center to select photons scattered on the $|P_{3/2}, -\frac{3}{2}\rangle$ to $|S_{1/2}, -\frac{1}{2}\rangle$ transition (see Figure 7.3). A small fraction of the projected photons is coupled into a multi mode fiber and detected directly to detect unfiltered photons scattered on both 393 nm transitions.

I project the polarization of the generated photons on the six polarization $|L\rangle$, $|R\rangle$, $|H\rangle$, $|D\rangle$, $|V\rangle$ respectively $|A\rangle$ and the atomic state on the energy eigenbasis, and a rotating superposition basis (details see Section 4.6.2). For each of the twelve projection settings I measure the wave packet of the scattered photons for $80 \cdot 10^6$ sequence repetitions. A total number of $563 \cdot 10^3$ photons are detected directly. Behind the filter cavity $18 \cdot 10^3$ individual photon events are detected.

If the photon is projected onto $|R\rangle$ polarization and the atom is projected on an energy eigenstate (example see Figure 7.8 (a,d)), the population is found almost exclusively in the $|S_{1/2}, -\frac{1}{2}\rangle$ state. If the atomic state is instead projected onto a superposition state, the atom is found equally frequent in both mapped atomic superposition states if the photon is detected directly (b) while the detector after the spectral filter only detects dark counts (e), because the $|+\frac{1}{2}\rangle |L\rangle$ component of the state is not transmitted through the filter. For projection onto linear polarization and the atomic superposition basis the direct detected wave packet is modulated (c) because the phase of the created atom-photon state depends on the detection time of the pho-

---

[8]The atom-photon amplitude from the outer spectral components that is transmitted through the cavity is one of the limitations of the 854 nm scheme. Details are discussed later.
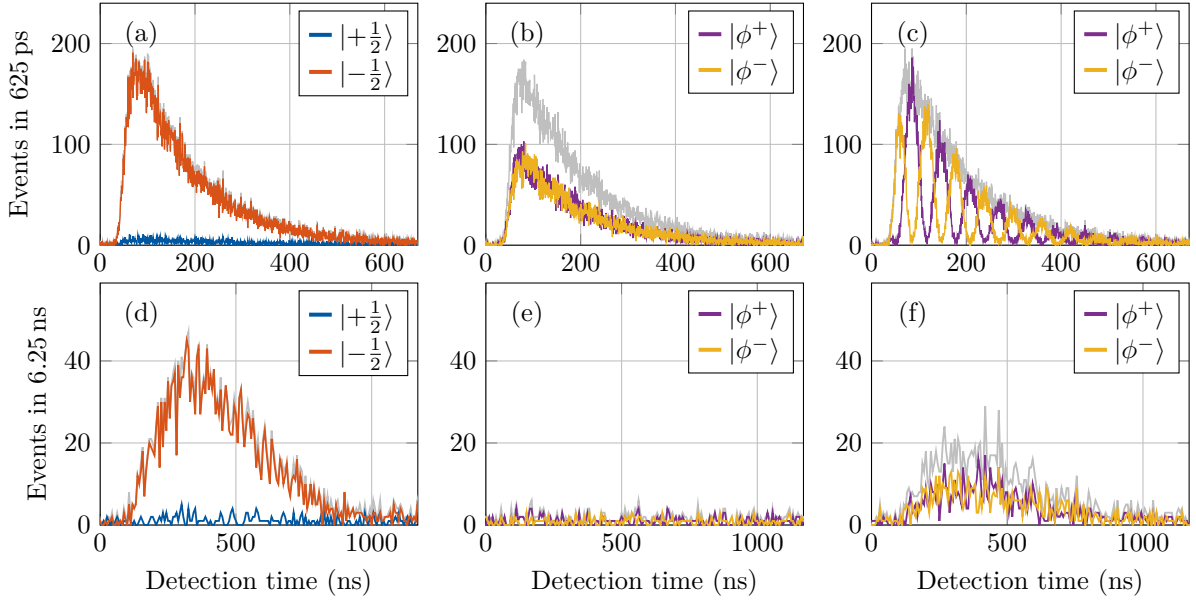
Figure 7.8.: Wave packets of directly detected (a-c) or spectrally filtered (d-f) photons for monochromatic excitation conditioned on the result of the atomic state projection. The wave packets without atomic state projection are shown in gray. The polarization projection is set to $|R\rangle$ (a,d), $|L\rangle$ (b,e) or $|A\rangle$ (c,f). The atom is projected onto the energy eigenbasis (a,d) or the rotating superposition basis (b,c,e,f).

ton. As only the $|-\frac{1}{2}\rangle\,|R\rangle$ component of the state is transmitted through the spectral filter, no modulation is found for the cavity filtered photons. Instead the atom is found equally frequent in both superposition states for all photon detection times (f).

From all modulated wave packets (linear polarization and atomic superposition) I determine the average frequency $\bar{\nu} = 16.37(9)\,\mathrm{MHz}$ of the modulation. This frequency corresponds to the frequency separation of the peaks in the spectrum of the created photons (see Figure 7.3). Together with an offset, this frequency determines the phase of the atom-photon state that is detected at a time t. With the frequency $\bar{\nu}$ I sort the photons into phase bins according to their detection time. These phase bins correspond to the projection onto an atomic superposition state with the respective phase (details see Section 4.6.2). The obtained phase histogram provides the estimated probabilities for the projection onto the atomic superposition states. The estimated probabilities for the projection onto the atomic energy eigenstates are obtained from all photon events in the respective wave packet.

I reconstruct the density matrix of the generated atom-photon state, from the estimated probabilities from all twelve projection settings (see Figure 7.9). In case of the direct detected photons an entangled atom-photon state with high purity is created. I calculate an overlap fidelity of $\mathcal{F} = 0.893(2)$ ($\mathcal{F}_c = 0.916(2)$) with respect to the maximal entangled state $|\Psi\rangle = \frac{1}{\sqrt{2}}(|+\frac{1}{2}, L\rangle - |-\frac{1}{2}, R\rangle)$. The values in brackets are for background corrected data. The generated atom-photon state has a purity of $\mathcal{P} = 0.809(4)$ ($\mathcal{P}_c = 0.850(4)$). Both values, the
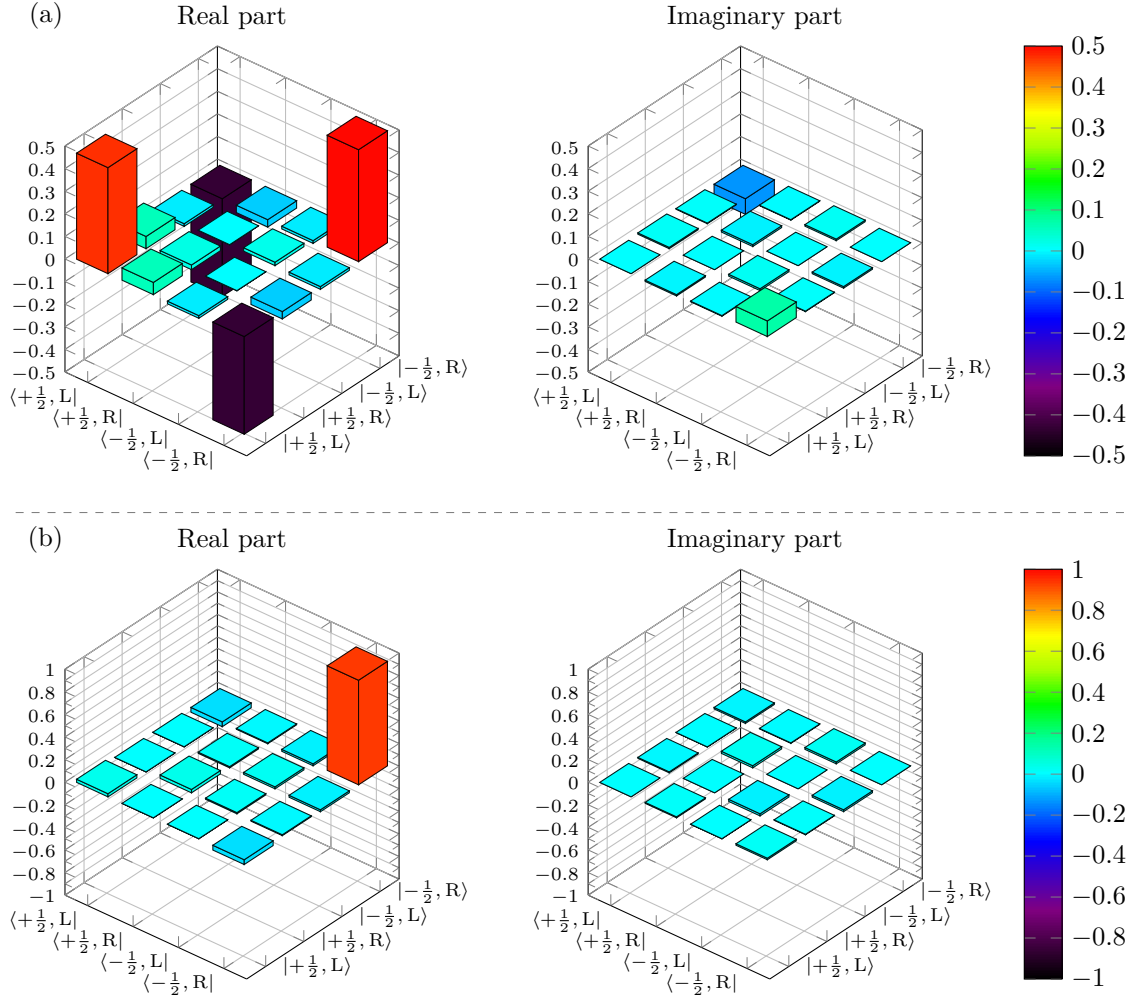
Figure 7.9.: Reconstructed density matrices of the generated atom-photon state for a monochromatic 854 nm laser excitation. (a) Unfiltered photons. (b) Photons filtered by a cavity set to the left spectral component of the emitted photons. Numeric values are listed in Appendix D.1.2 and Appendix D.1.4.

fidelity and purity are a slight improvement compared to previous work [57, 59]. Additionally, I calculate the Bell parameter $\mathcal{S} = 2.37(1)$ ($\mathcal{S}_c = 2.45(1)$) and the concurrence $\mathcal{C} = 0.788(5)$ ($\mathcal{C}_c = 0.836(4)$) from the reconstructed density matrix.

The cavity destroys the entanglement of this atom-photon state by removing the $|\Psi\rangle = |+\frac{1}{2}, \mathrm{L}\rangle$ component from the emitted atom-photon state because only photons emitted on the $|\mathrm{P}_{3/2}, -\frac{3}{2}\rangle$ to $|\mathrm{S}_{1/2}, -\frac{1}{2}\rangle$ transition are transmitted through the cavity. Consequently, only the component $|\Psi\rangle = |-\frac{1}{2}, \mathrm{R}\rangle$ of the created atom-photon state is transmitted through the cavity and the system is found almost excursively in the state $|\Psi\rangle = |-\frac{1}{2}, \mathrm{R}\rangle$. With respect to this state, the fidelity of the generated atom-photon state is $\mathcal{F} = 0.80(1)$ ($\mathcal{F}_c = 0.91(1)$) for a purity of $\mathcal{P} = 0.67(2)$ ($\mathcal{P}_c = 0.85(2)$).

The comparison of both atom-photon states shows, that both parts of the atom-photon state are linked to individual spectral components of the scattered photon. The frequency difference between both spectral components causes the detection time dependence of the phase of the state. For direct detected photons, the frequency information is erased and both scattering paths are only distinguishable by the polarization of the created photon. As result entanglement is created between the 393 nm photon polarization and the electronic state of the ^{40}Ca$^+$ ion, if the detection time of the photon is taken into account. If the spectral information is taken into account, both paths become distinguishable and no entanglement is created.

7.2.2. Bichromatic excitation – atom-photon entanglement with a detection time independent phase

To create an atom-photon state as in Equation 7.25 with a phase that is independent from the detection time of the 393 nm photon, I excite the superposition that is prepared in the $|D_{5/2}, +\frac{5}{2}\rangle$ and $|D_{5/2}, -\frac{5}{2}\rangle$ Zeeman level with a bichromatic laser with the Rabi frequencies $\Omega_1 = \Omega_2 = (2\pi)\,5.56(1)\,\text{MHz}$ ($\tau = 3\,\mu\text{s}$). I set the frequency components to the detunings $\Delta_1 = +8.05\,\text{MHz}$ and $\Delta_2 = -8.05\,\text{MHz}$ from the 854 nm line center. For the applied Rabi frequencies, these detunings lead to the best atom-photon entanglement in simulations with the model from Chapter 5. The experimental setup is the same as for the monochromatic case. I set the analysis cavity on resonance with the 393 nm line center ($\Delta_{393} = 0\,\text{MHz}$, see Figure 7.4). I project the polarization of the generated photons on six polarization $|L\rangle$, $|R\rangle$, $|H\rangle$, $|D\rangle$, $|V\rangle$ and $|A\rangle$. If a photon was detected, the atomic state is projected on the energy eigenstates or two superposition bases (detail see Section 4.6.2). For each of the eighteen projection settings I measure the created photon wave packet for $60 \cdot 10^6$ sequence repetitions. I obtain $638 \cdot 10^3$ directly detected photons and $27 \cdot 10^3$ spectrally filtered photons.

The wave packets of the directly detected photons (example in Figure 7.10 a-c) show a modulation caused by the bichromatic laser beam. The bichromatic laser beam can be seen as an amplitude modulated monochromatic beam. This amplitude modulation is imprinted on the wave packet. Consequently, no photons are detected at times, where the modulation crosses 0. This is the case for example at $t \approx 410\,\text{ns}$. Depending on the atomic state projection, the measured wave packet changes the shape. In case of a projection onto the energy eigenbasis (a) both wave packets have the same form. For projection onto the atomic *X*-basis (b) the wave packets are phase shifted with respect to each other, but the modulation is the same for both projection results. In case of projection onto the atomic *Y*-basis (c) the wave packets are differently modulated. The wave packet that is conditioned on the detection of the atomic superposition $|-i\rangle$ contains less detection events and is modulated with twice the frequency compared to the other wave packets. For this combination of state projections ($|A\rangle$ and $|-i\rangle$), the detection time independent parts from Equation 7.24 interfere destructively. The frequency difference of the remaining components corresponds to the difference of the outer two spectral components in Figure 7.4. This frequency is twice the frequency difference of the components of the bichromatic laser excitation what leads to the observed modulation. For a projection onto
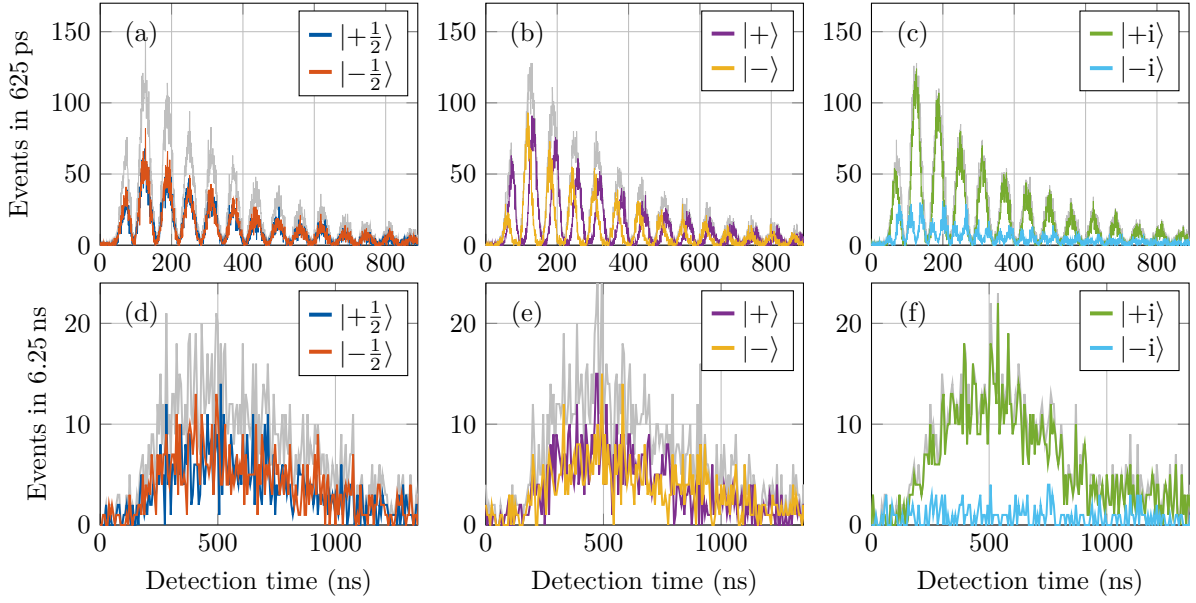
Figure 7.10.: Wave packets of the atom-photon state generated with a bichromatic laser pulse for unfiltered photons (a-c) or spectrally filtered photons (d-f) conditioned on the atomic state projection. The wave packets without atomic state projection are shown in gray. The photon is projected to $|A\rangle$ polarization in all cases.

the perpendicular atomic state $|+i\rangle$ the spectral overlapping components interfere constructively and the wave packet contains the population that is "missing" in the $|-i\rangle$ wave packet and thus contains more detection events than the other wave packets. The constructive and destructive interference happens between the overlapping spectral components in the central peak. These components are transmitted through the spectral filter, while the non interfering components are removed. As result the wave packet of the $|-i\rangle$ projection (Figure 7.10 (f)) is completely suppressed and the wave packet of the $|+i\rangle$ projection contains all photons transmitted through the cavity (for a projection on $|A\rangle$). For the other atomic bases (d,e), both wave packets contain the same population. As a further effect, the cavity elongates the wave packet and blurs the creation time of the photon. Due to this, the modulation of the bichromatic laser beam is no longer visible.

I integrate the photon wave packets to get the number of photon events for each of the 36 state projections. From the obtained photon events I calculate the estimated probabilities for all projections. With the estimated probabilities I reconstruct the density matrix of the atom-photon state that is created for direct detected or cavity filtered photons (see Figure 7.11). In case of the direct detected photons a partially entangled state is created what can be seen in the reduced coherences of the reconstructed density matrix. The direct detected state contains two components linked to the outer spectral components which have a detection time dependent phase. If one integrates over all possible detection times, the phase information of these components is lost. As consequence these components give a mixed contribution to
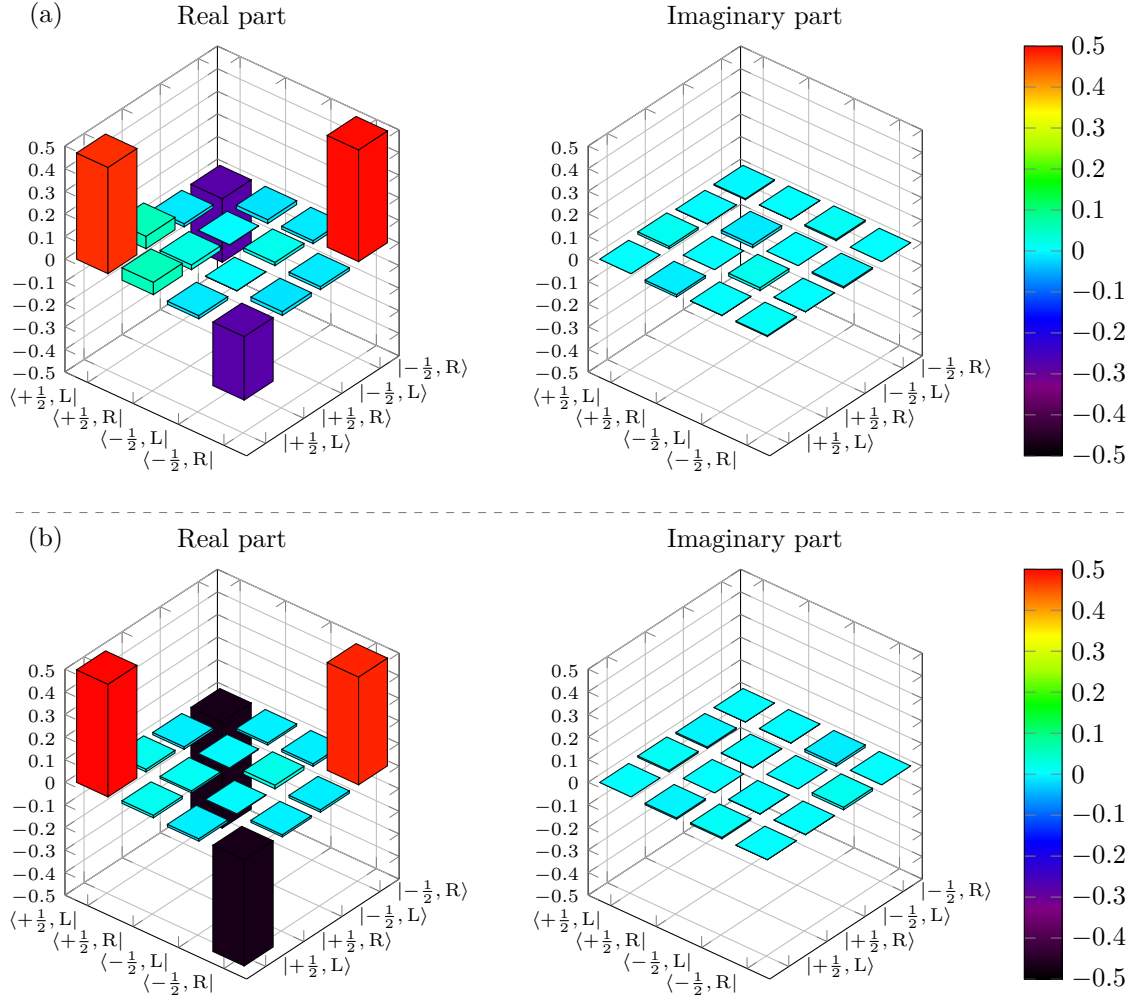
Figure 7.11.: Reconstructed density matrix of the created atom-photon state for a bichromatic laser excitation. (a) Directly detected photons. (b) Spectrally filtered photons by a cavity set to the central spectral component. Numeric values are listed in Appendix D.2.2 and Appendix D.2.4.

the created atom-photon state. The spectral filtering removes the outer spectral components and by this the mixed contribution to the generated state. Only detection time independent parts remain and the created atom-photon state is maximally entangled what results in the increased modulus of the coherences in the reconstructed density matrix of the cavity filtered atom-photon state. The comparison of both created states shows the influence of the spectral components on the created atom-photon state. Furthermore, it shows how the spectral filter acts as a quantum eraser, that increases the entanglement of the created state.

For both atom-photon states I calculate the fidelity with respect to the maximal entangle state $|\Psi\rangle = \frac{1}{\sqrt{2}}(|+\frac{1}{2}, \mathrm{L}\rangle - |-\frac{1}{2}, \mathrm{R}\rangle)$, the purity, the concurrence and the Bell parameter. The obtained values with and without background correction are listed in Table 7.1. The calculated

Table 7.1.: Properties of the 393 nm atom-photon states generated with a bichromatic laser excitation and direct detection or filtered photons.

Background	cavity filtered		unfiltered	
	uncorrected	corrected	uncorrected	corrected
Fidelity $\mathcal{F}$	0.820(5)	0.957(3)	0.732(1)	0.763(1)
Purity $\mathcal{P}$	0.686(8)	0.929(5)	0.586(1)	0.632(1)
Concurrence $\mathcal{C}$	0.64(1)	0.924(6)	0.467(3)	0.531(3)
Bell parameter $\mathcal{S}$	2.14(4)	2.66(3)	1.54(1)	1.64(1)

properties of the generated state confirm the observation made with the reconstructed density matrix. The large difference between the values of the cavity filtered photons obtained with and without background correction is caused by the small signal to noise ratio due to the small efficiency of the setup. Additional to this experimental limitation, a more fundamental limit is given by the decay back into the $D_{5/2}$ state on the 854 nm transition. The influence of this decay on the created state is discussed in the next section.

To compare the detection time dependence of the 393 nm atom-photon states generated with the monochromatic scheme and the bichromatic scheme, I infer the phase of the generated atom-photon state directly from the wave packets. The obtained phases of the three generated entangled states are shown in Figure 7.12 together with model curves. For the monochromatic scheme, the phase depends linear on the detection time of the photon. In case of the atom-photon state, which was created with a bichromatic 854 nm pulse and whose photons are not spectral filtered, the phase of the generated state also depends on the detection time of the
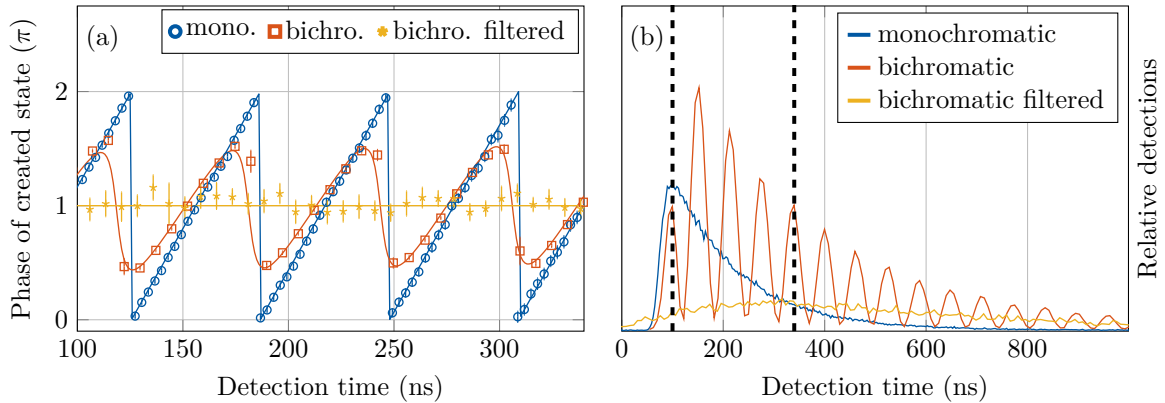
Figure 7.12.: (a) Phase of the atom-photon states generated by the presented schemes depending on the detection time of the photon. (b) Wave packet of the emitted photon without any projection. Only the phase of states where the photon is detected in the window marked in the wave packet is shown.

photon. In contrast to the monochromatic case, this atom-photon state contains only phases between $\frac{\pi}{2}$ and $\frac{3\pi}{2}$. As for the monochromatic case, the phase increase almost linearly but then jumps back to the smallest phase value every time the modulation in the photon wave packet has a minimum. The generated state with photons filtered by the cavity has a detection time independent phase.

7.2.3. Limits of the 393 nm schemes

In the presented experiments the dark counts induced by the photon detectors strongly affect the quality of the generated atom-photon state. If one eliminates these background events, for example with super conducting single photons detectors that have almost no dark counts, I expect to reach the back ground corrected values for the generated atom-photon state. Additional improvements of the experimental setup should further increase the quality of the generated atom-photon state. However, there is a fundamental limitation in the 393 nm atom-photon entanglement creation schemes. This limitation comes from the decay into the initial state on the 854 nm transition and the coupling to other levels of the ^{40}Ca$^+$ ion. Both effects can not be eliminated and therefore limit the quality of the generated atom-photon state. However, the coupling to other levels is negligible for small Rabi frequencies as in the presented experiments. Thus only the back decay remains.

The back decay destroys the phase information in the $D_{5/2}$ manifold. Consequently, all atom-photon states that are generated after a back decay happened have no phase information and are therefore mixed states. For the presented schemes the first back decay into a $D_{5/2}$ Zeeman level can happen on three different transitions which are shown in Figure 7.13 for the $|P_{3/2}, -\frac{3}{2}\rangle$ state. In the following I discuss the effect of these three decay channels. The back decay out of the $|P_{3/2}, +\frac{3}{2}\rangle$ is analog.

All three possible back decay channels have different Clebsch-Gordan coefficients (see Figure 2.5). The strongest decay channel goes back into the $|D_{5/2}, -\frac{5}{2}\rangle$ state (a). This decay channel reduces the phase information in the initial superposition state. As consequence the phase information and with this the purity of the generated atom-photon state is reduced. The
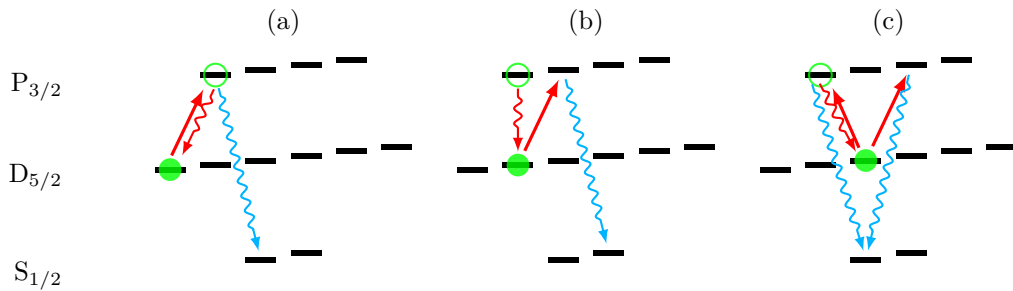
Figure 7.13.: Possibilities for a decay from the $|P_{3/2}, -\frac{3}{2}\rangle$ state on a 854 nm transition. With the analysis cavity as spectral filter only the decay back into the initial state (a) has a contribution to the final state.

second decay channel goes into the $|\text{D}_{5/2}, -\frac{3}{2}\rangle$ state (b). The 393 nm photon generated from this state has the same polarization as the photon generated from the $|\text{D}_{5/2}, -\frac{5}{2}\rangle$ state, but the final atomic state is different. As result, this decay adds an additional component to generated atom-photon state. Again this component carries no phase information. The last and weakest decay channel goes to the $|\text{D}_{5/2}, -\frac{1}{2}\rangle$ state (c). From this state, there are two scattering paths to generate a 393 nm photon. The first path through the $|\text{P}_{3/2}, -\frac{3}{2}\rangle$ Zeeman level creates a photon with the same polarization as the scattering path from the initial $|\text{D}_{5/2}, -\frac{5}{2}\rangle$ state. This path reduces the purity of the wanted components. The other path creates a photon with perpendicular polarization and therefor adds mixed population to an additional component of the atom-photon state. Additional to these cases where a 393 nm σ photon is emitted, the ion can also decay on 393 nm π transitions. Because the photons emitted on π transitions are not collected in direction of the magnetic field, the decay on π transitions has no effect on the generated atom photon state. Of course more than one back decay can happen. These cases are analog to the cases for a single back decay and are calculated with the population given after the previous back decay.

In case of the cavity filtered photons the spectrum of the photon scattered after a back decay has to be taken into account. Since the spectrum depends on the detuning of the excitation laser with respect to the individual levels, as well as the actual transition frequency, the 393 nm photons generated on all possible scattering paths have different frequencies. As a result the cavity transmits only photon generated on the scattering path that starts in the $|\text{D}_{5/2}, -\frac{5}{2}\rangle$ level. For this reason, only the decay back into the initial state has an effect on the atom-photon state created with a bichromatic laser excitation if the photons are spectrally filtered. As there are fewer scattering paths that corrupt the generated atom-photon state for the bichromatic scheme with spectrally filtered photons compared to the monochromatic scheme, the maximal achievable fidelity, purity and concurrence in the bichromatic scheme becomes larger.

To estimate the achievable quality of the generated atom-photon state, I calculate the density matrix of the expected state taking the above mentioned decays into account. In the performed calculation the 850 nm decay is neglected, as there is no 393 nm photon created afterwards. In the same way all decays on 393 nm π transitions are omitted, because these photons are not collected with the setup. Additionally the 854 nm laser is assumed to drive only the $\sigma^{\pm}$ transitions and that no population is transferred to other $\text{D}_{5/2}$ levels by Rabi oscillations. With these assumptions the achievable fidelity, purity and concurrence are calculated. For the monochromatic scheme, the back decay limits the quality of the generated atom-photon state to

$$\mathcal{F} = 0.973, \qquad \mathcal{P} = 0.954, \qquad \text{and} \qquad \mathcal{C} = 0.946. \tag{7.35}$$

In case of the bichromatic scheme and spectrally filtered photons, the back decay limits the quality of the generated atom-photon state to

$$\mathcal{F} = 0.980, \qquad \mathcal{P} = 0.961, \qquad \text{and} \qquad \mathcal{C} = 0.960. \tag{7.36}$$

It should be noted, that the higher quality of the state created with the bichromatic scheme comes at the cost of an intrinsic, unavoidable loss due to the components of the generated state that are removed with the spectral filtering. Additionally, the bichromatic scheme contains additional elements, that create further transmission loss. These losses have to be considered, if the rate of entanglement generation is relevant for the application.

7.3. 854 nm atom photon entanglement

7.3.1. Monochromatic excitation – detection time dependence of the atom-photon state

The results for the monochromatic scheme were obtained together with Stephan Kucera and Matthias Bock. In contrast to the scheme with a bichromatic 393 nm laser pulse discussed in the next section were the "right" scheme was used (see Figure 4.13), in the monochromatic scheme the mirror inverted "left" scheme was used. I expect similar results in the respective other scheme.

To create 854 nm atom-photon entanglement a monochromatic 393 nm laser excites the ^{40}Ca$^+$ ion from the S$_{1/2}$ ground state into the P$_{3/2}$ state ($\Delta = -11$ MHz, $\tau = 1.8$ µs). The laser is horizontally polarized and coupled in perpendicular to the magnetic field thus only the π-transitions are excited (details on the pulse sequence see Section 4.6.1). In the "left" scheme, the ion decays from the $|\text{P}_{5/2}, -\frac{1}{2}\rangle$ level into the $|\text{D}_{5/2}, -\frac{3}{2}\rangle$ and $|\text{D}_{5/2}, +\frac{1}{2}\rangle$ Zeeman levels. To compensate the Clebsch-Gordan coefficients of the 854 nm decay channels population is removed from the $|\text{D}_{5/2}, -\frac{3}{2}\rangle$ Zeeman level after a photon detection. The scattered 854 nm photon is collected on quantization axis and as result, the polarization of the scattered 854 nm photon is entangled with the electronic state of the ion. The generated 854 nm photons are projected onto the 3 polarization bases $\{|\text{R}\rangle, |\text{L}\rangle\}$, $\{|\text{H}\rangle, |\text{V}\rangle\}$ and $\{|\text{D}\rangle, |\text{A}\rangle\}$ and detected directly without spectral filtering. Both orthogonal polarization of the same basis are measured simultaneously at both outputs of a Wollaston prism. Therefore, the detection efficiencies of both outputs of the Wollaston prism have to be balanced. This is done by inserting loss in the stronger arm. If a photon was detected, the atomic state is projected. For each polarization projection, the atom is projected onto the bases $\{|-\frac{3}{2}\rangle, |+\frac{1}{2}\rangle\}$, $\{|+\rangle, |-\rangle\}$ and $\{|+\text{i}\rangle, |-\text{i}\rangle\}$. In total $60 \cdot 10^6$ sequence repetitions are done for each of the nine projection combinations what results in $556 \cdot 10^3$ photon events.

For each projection setting the wave packet of the created photon is measured conditioned on the state detection of the ion. For a projection on $|\text{L}\rangle$ polarization, the wave packets show an exponential decay that is truncated at the end (see Figure 7.14, a). At this point the 393 nm laser was switched off to achieve a higher sequence repetition rate without loosing to much efficiency. The wave packets for a projection on $|\text{H}\rangle$ polarization and an atomic state projection onto a superposition state are modulated what shows the detection time dependence of the created state. The oscillation period of 104 ns corresponds to the frequency splitting of 9.6 MHz found in the measured spectrum (see Figure 7.14, b). For each time bin I determine
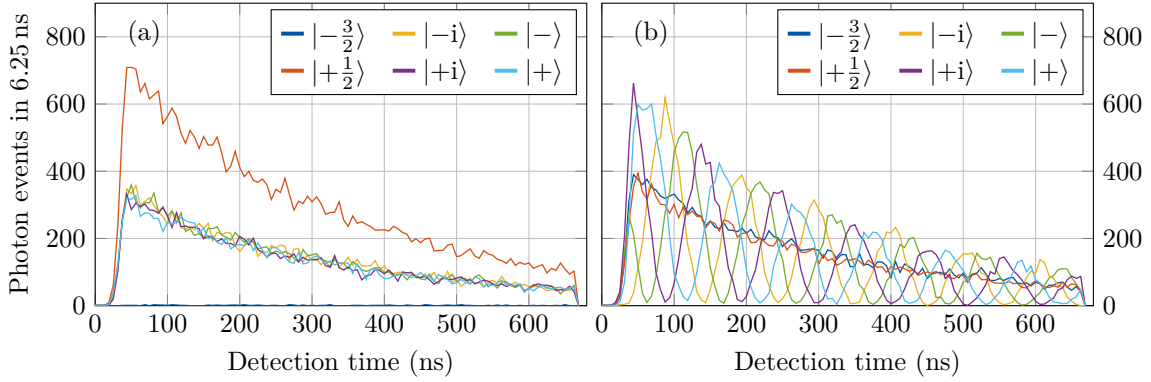
Figure 7.14.: Wave packets of unfiltered 854 nm photons created with a monochromatic 393 nm laser pulse conditioned on the atomic state projection. The polarization is projected to (a) $|L\rangle$ or (b) $|H\rangle$. To obtain a higher sequence repetition rate only a part of the photon wave packet is generated. The wave packets are displayed with the time bins that are applied for the further evaluation.

the estimated probability for all 36 projection combinations. With the obtained probabilities I reconstruct the density matrix of the created atom-photon state for a photon detected in this time bin.

The reconstructed density matrices of the atom-photon states that are detected in different time bins show maximally entangled states (see Figure 7.15). The phase of these states depends on the detection time of the 854 nm photon what can be identified in the coherence $|-\frac{3}{2}, R\rangle\langle+\frac{1}{2}, L|$. The value of this coherence oscillates with the same frequency as the modulation in the wave packet of the generated photon. This shows, that the modulation of the wave packet is directly linked to the phase of the created atom-photon state. From the diagonal entries I find, that the state is slightly imbalanced towards the $|-\frac{3}{2}\rangle|R\rangle$ part. This indicates, that the 729 nm balancing pulse did not remove enough population from this component. From the reconstructed density matrices for photons detected in the time window from 50 ns up to 600 ns I calculate the properties of the generated state. I find the populations $p(|+\frac{1}{2}\rangle|L\rangle) = 0.475(10)$ and $p(|-\frac{3}{2}\rangle|R\rangle) = 0.514(10)$ in the wanted components. The remaining population is stored in the other two components. I determine the frequency and phase offset of the phase of the created atom-photon state with a fit of the displayed coherence. The values $\nu_L = 9.605(3)\,\text{MHz}$ and $\phi_0 = 324.0(3)\,°$ are found. The found frequency matches the frequency difference of the $D_{5/2}$ levels. The frequency and phase offset values are put in the maximal entangled atom-photon state

$$|\Psi(t)\rangle = \frac{1}{\sqrt{2}}\left(|+\tfrac{1}{2}\rangle|L\rangle + e^{-2i\pi\nu_L t - i\phi_0}\,|-\tfrac{3}{2}\rangle|R\rangle\right) \tag{7.37}$$

to calculate the fidelity of the generated state with respect to this state. Furthermore I calculate the purity, concurrence and Bell Parameter of the generated state. I get

$$\mathcal{F}_\phi = 0.966(11), \qquad \mathcal{P} = 0.939(20), \qquad \mathcal{C} = 0.940(21), \quad \text{and} \quad \mathcal{S} = 2.67(5). \tag{7.38}$$
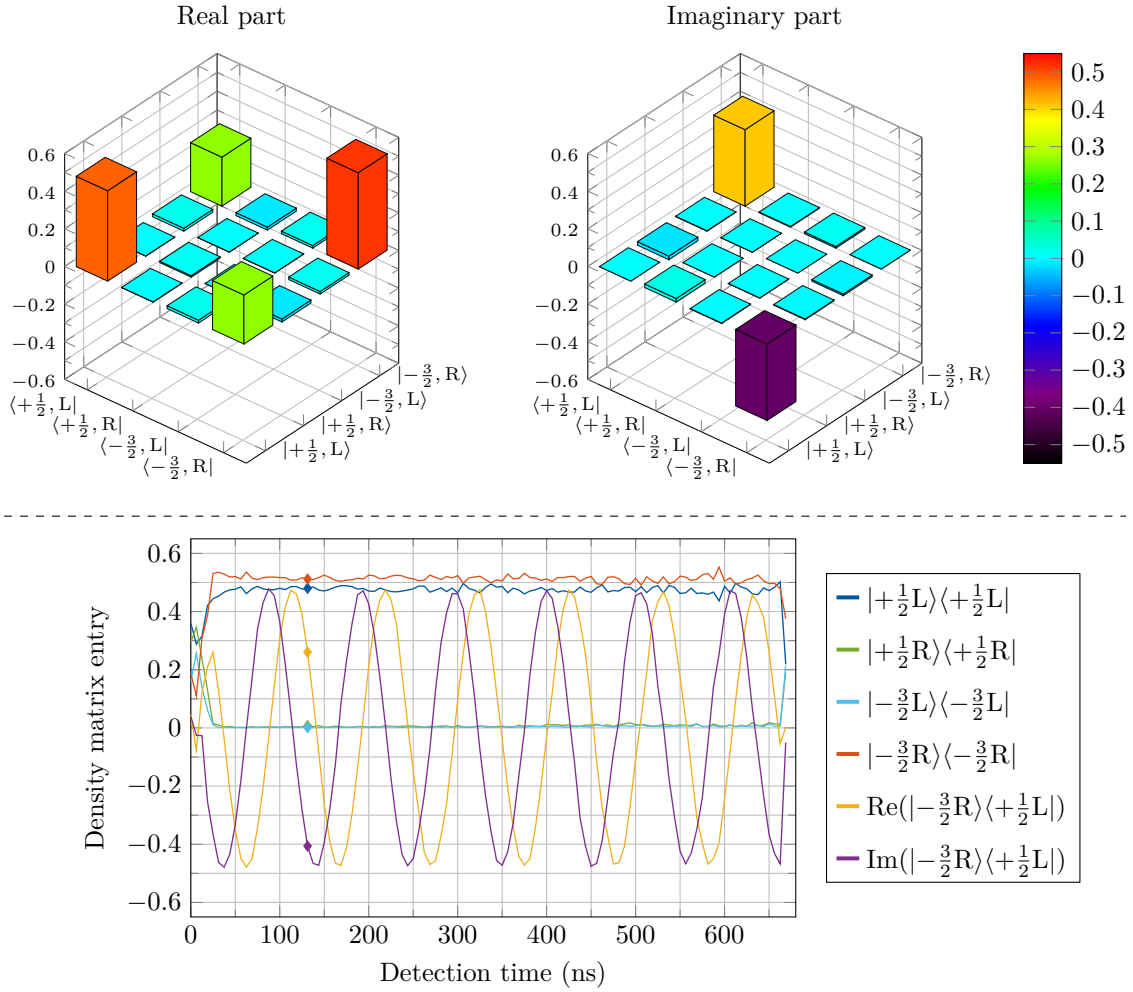
Figure 7.15.: Reconstructed density matrix of of the generated $854\,\mathrm{nm}$ atom-photon state for the $131\,\mathrm{ns}$ time bin (top) and entries of the density matrices for all reconstructed states (bottom). The values of the density matrix displayed on top are marked in the bottom graph with a rhombus.

Instead of reconstructing the density matrix for each time bin, one can determine the frequency ν_L from the measured wave packet and sort the detected photons into phase bins according to their detection time. These phase bins correspond to different phases of the created atom-photon state. The generated state can then be reconstructed for each phase bin. In this case I obtain the values

$$\mathcal{F} = 0.974(5), \qquad \mathcal{P} = 0.953(9), \qquad \mathcal{C} = 0.953(9), \qquad \text{and} \qquad \mathcal{S} = 2.70(3)$$

for the generated state. These values are slightly better compared to the values obtained for the time bins. The phase histogram samples only a single period of the oscillation wile the wave packet covers five periods. Consequently, there are more detection events in each bin and the oscillation can be sampled finer. This leads to the improved values.

7.3.2. Bichromatic excitation – atom-photon entanglement with a detection time independent phase

I create 854 nm atom-photon entanglement with a detection time independent phase with a bichromatic 393 nm laser in the "right" scheme that is shown in Figure 7.6. I set the frequency components of the bichromatic laser to the detunings $\Delta_1 = +4.087\,\text{MHz}$ and $\Delta_2 = -4.087\,\text{MHz}$ with respect to the excited $|S_{1/2}, +\frac{1}{2}\rangle \rightarrow |P_{3/2}, +\frac{1}{2}\rangle$ transition. I chose the right scheme because the 393 nm transition in this scheme has a smaller frequency than the 393 nm transition in the left scheme. As consequence the 393 nm laser is red detuned from the $|S_{1/2}, -\frac{1}{2}\rangle \rightarrow |P_{3/2}, -\frac{1}{2}\rangle$ transition and I expect no heating due to 393 nm photons scattered on this transition. The frequency splitting of the bichromatic laser corresponds to the frequency splitting of the final $|D_{5/2}, -\frac{1}{2}\rangle$ and $|D_{5/2}, +\frac{3}{2}\rangle$ Zeeman levels.

I generate and detect 854 nm atom-photon entanglement with a pulse sequence similar to the monochromatic case (details see Section 4.6.1). To compensate the Clebsch-Gordan coefficients of the 854 nm decay channels into the final $|D_{5/2}, -\frac{1}{2}\rangle$ and $|D_{5/2}, +\frac{3}{2}\rangle$ Zeeman levels I apply the birchromatic laser with two amplitudes $A_2 = 1.47 A_1$ (details see Figure 7.7, Figure 7.6 and corresponding paragraphs) what results in the Rabi frequencies ($\Omega_2 \approx 1.47\Omega_1 \approx 3.7\,\text{MHz}$). A smaller Rabi frequency compared to the monochromatic scheme is chosen to reduce the spectral overlap between individual components. To generate the full wave packet the pulse duration of the 393 nm laser is set to 10 μs.

I collect the scattered 854 nm photons anti parallel to the magnetic field axis and couple the photons into a single mode fiber. The photons are send directly to a polarization projection stage or previously to the analysis cavity setup for spectral filtering [9]. I project the photon polarization with a Wollaston prism and two wave plates at each output of the Wollaston prism to the six polarization $|R\rangle$, $|L\rangle$, $|H\rangle$, $|V\rangle$, $|D\rangle$ and $|A\rangle$. With this I can evaluate both outputs independently from each other or sum them up. Also, I do not need to induce a loss in one of the detection arms to balance the efficiencies in both arms. If a photon is detected the atomic state is projected onto the states $\{|+\frac{3}{2}\rangle, |-\frac{1}{2}\rangle\}$, $\{|+\rangle, |-\rangle\}$ or $\{|+i\rangle, |-i\rangle\}$ to reconstruct the density matrix of the generated state. For the projection onto a linear polarization, the atomic state is projected on two additional bases rotated by 45° with respect to the X and Y basis to measure the Bell parameter directly. To spectrally filter the photons, I set the analysis cavity to the central frequency between both decay channels. This corresponds to a detuning $\Delta_{854} = +0.27\,\text{MHz}$ with respect to the 854 nm line center.

I measure the wave packet of the created atom-photon state for directly detected photons and spectrally filtered photons in two independent runs with the same parameters. In case of the direct detected photons, I execute $16.5 \cdot 10^6$ sequence repetitions with an average repetition rate of 57 kHz for each of the 52 projection settings to detect a total number of $400 \cdot 10^3$ photon events. In case of the cavity filtered photons, I execute $12 \cdot 10^6$ sequence repetitions with an average repetition rate of 41 kHz to detect a total number of $36 \cdot 10^3$ photon events. I integrate

---

[9]Compared to the bichromatic 393 nm atom-photon entanglement scheme, in case of the 854 nm atom-photon entanglement scheme, the polarization projection is done behind the spectral filter.
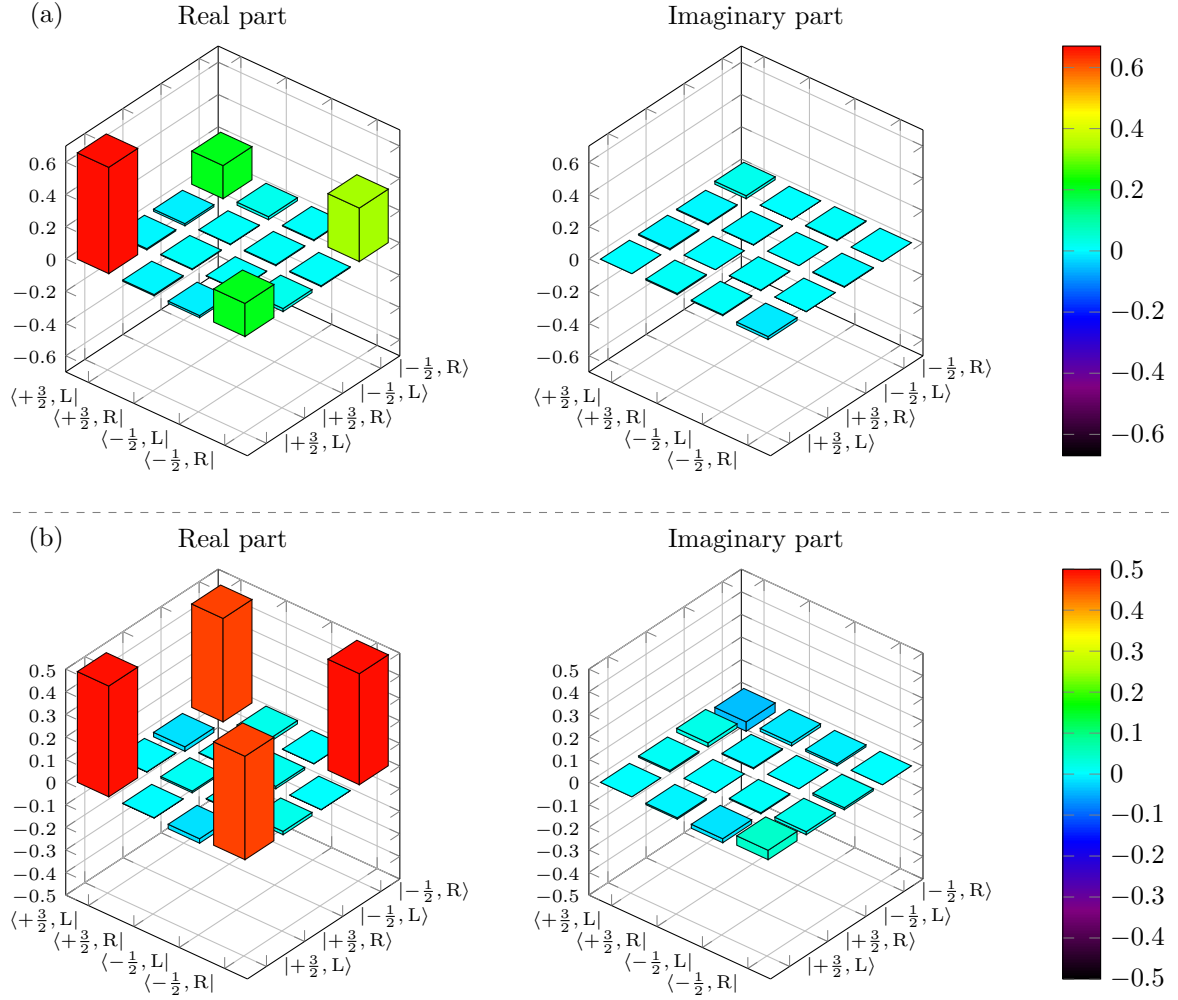
Figure 7.16.: Reconstructed density matrices for (a) directly detected photons and (b) photons filtered by the analysis cavity for the bichromatic 854 nm atom-photon entanglement scheme. Numeric values are listed in Appendix D.3.3 and Appendix D.3.6.

the photon events in each wave packet to obtain the number of events for each projection setting. From the events in each wave packet, I calculate the estimated probabilities for each projection setting.

I reconstruct the density matrix of the generated atom-photon states (see Figure 7.16) from the estimated probabilities calculated from the sum of the detection events obtained at both outputs of the Wollaston prism. In case of the direct detected photons, the density matrix shows an imbalance towards the $|+\frac{3}{2}\rangle|L\rangle$ part of the generated state caused by the different Clebsch-Gordan coefficients of both scattering paths. Furthermore, the coherences are reduced due to the remaining detection time dependence of the atom-photon state. This detection time dependence is ignored as I take only the total detection events for each projection setting into account. With this I integrate over all possible phases of the generated atom-photon state

Table 7.2.: Properties of the generated atom-photon states. Values for both outputs of the Wollaston prism as well as for the sum are listed.

	direct detection			filtered by cavity		
	DAQ0	DAQ2	sum	DAQ0	DAQ2	sum
Fidelity $\mathcal{F}$	0.687(2)	0.717(3)	0.700(2)	0.949(4)	0.949(4)	0.948(3)
Purity $\mathcal{P}$	0.646(2)	0.619(3)	0.630(2)	0.903(8)	0.910(8)	0.907(6)
Concurrence $\mathcal{C}$	0.377(5)	0.438(6)	0.403(4)	0.897(9)	0.905(9)	0.904(6)
Bell parameter $\mathcal{S}$	1.13(6)	1.24(7)	1.18(4)	2.59(15)	2.60(16)	2.60(11)

what results in the reduced coherences of a partially mixed state. By spectral filtering I remove the outer two components that are linked to the time dependent components of the generated state what makes the created atom-photon state that is transmitted through the spectral filter detection time independent. Hence, the reconstructed density matrix has larger coherences. The second effect of the spectral filtering is, that the generated atom-state becomes balanced. By adjusting the Rabi frequencies, the population in both spectral components that are linked to the time independent components of the state were balanced.

From the reconstructed density matrices I calculate the properties of the generated atom-photon states. The fidelity $\mathcal{F}$ is calculated with respect to the maximally entangled state

$$|\Psi\rangle = \frac{1}{\sqrt{2}} \left[|+\tfrac{3}{2}\rangle|\mathrm{L}\rangle + |-\tfrac{1}{2}\rangle|\mathrm{R}\rangle \right]. \tag{7.39}$$

The calculated values, as well as the purity $\mathcal{P}$, concurrence $\mathcal{C}$ and the Bell parameter $\mathcal{S}$ are listed in Table 7.2. The Bell parameter $\mathcal{S}$ is calculated directly from the photon events, where the polarization was projected to $\{|\mathrm{H}\rangle,|\mathrm{V}\rangle\}$ and $\{|\mathrm{D}\rangle,|\mathrm{A}\rangle\}$ and the atomic state was projected to $\{|\tfrac{\pi}{4}\rangle,|\tfrac{5}{4}\pi\rangle\}$ and $\{|\tfrac{3}{4}\pi\rangle,|\tfrac{7}{4}\pi\rangle\}$. The quality of the atom-photon state with direct detected photons is reduced due to the remaining time dependence and the imbalance. The quality of the entangled atom-photon state created with cavity filtered photons is comparable to the quality of the entangled atom-photon state created with the monochromatic scheme.

7.3.3. Limits of the 854 nm scheme

In the 393 nm atom-photon entanglement scheme, the decay back into the initial state is the main limiting factor for the quality of the generated state. Because the 854 nm atom-photon entanglement is created from a mixed initial state, the back-decay has no effect on the quality of the generated atom-photon state. On the other hand, in contrast to the 393 nm scheme there are several scattering paths that end in the same final state. To eliminate all paths except for one is a crucial requirement in this scheme. This sets requirements on the direction of the photon collection and the direction and polarization of the excitation laser. By probing the

population that is pumped into the $|\mathrm{D}_{5/2}, +\frac{5}{2}\rangle$ and $|\mathrm{D}_{5/2}, -\frac{5}{2}\rangle$ states with the 393 nm pulse, the polarization of the 393 nm laser can be adjusted. In a similar way the collection direction of the created photon can be adjusted. Therefore, these requirements are eliminated with the setup.

A more relevant limiting factor is the spectral shape of the generated photons and the properties of the spectral filter. Depending on the Rabi frequencies of both components of the bichromatic excitation, the spectral overlap between both components of the spectrum changes. This spectral overlap can be seen in the measured spectra in Figure 7.6. The spectral components are not separated perfectly. Consequently, a part of the unwanted component is transmitted through the filter cavity. As this part is linked to the detection time dependent part of the state, this reduces the quality of the atom-photon state. Reducing the Rabi frequency leads to narrower spectral components (see Chapter 6) and thus the spectral overlap between individual components reduces. This improves the quality of the generated atom-photon state.

Not affected by a reduced Rabi frequency is the transmission of the unwanted spectral components through the cavity due to the transmission spectrum of the cavity. In case of the presented scheme the unwanted components are located at $+10\,\mathrm{MHz}$ and $-10\,\mathrm{MHz}$ with respect to the central component. In this case a filter cavity with 2 MHz line width transmits about 1 % of the population in these components. Thus population of the unwanted time dependent part is present in the filtered photons. To reduce this transmission, there are two possible solutions. The first option is a larger magnetic field to increase the Zeeman splitting between the involved levels. For an increased Zeeman splitting the frequency difference between both components of the bichromatic laser beam has to be increased. With this the spectral components are further separated and the outer, unwanted spectral components shift to a position were the cavity transmission is smaller. This reduces the unwanted population transmitted through the cavity. If this approach is taken, the effect on other aspects of the scheme (Doppler cooling, efficiency of pulses, ...) have to be kept in mind.

The second option is a narrower filter cavity that has less transmission at the $+10\,\mathrm{MHz}$ and $-10\,\mathrm{MHz}$ components. Consequently, the population from the unwanted components in the created state reduces. However, a narrower cavity reduces the spectral overlap with the central component and with this the efficiency of the protocol. To increase the spectral overlap again, the Rabi frequency of the laser excitation has to be reduced as this reduces the spectral width of the created photons. At the same time, the photon wave packet becomes longer. This reduces the entanglement creation rate of the scheme.

To compare these effects, I simulate the quality of the generated atom-photon state and the achievable entanglement creation rates for different line widths of the spectral filter and Rabi frequencies of the laser excitation. The measure for the quality of the created entangled state is the concurrence $\mathcal{C}$. To quantify the achievable rate I assume an overhead of 2.5 µs in each sequence repetition. This overhead contains Doppler cooling and times required for the state readout and other operations. I chose the pulse duration depending on the Rabi frequency so that 60 % of the photon wave packet is generated. I assume a total detection efficiency
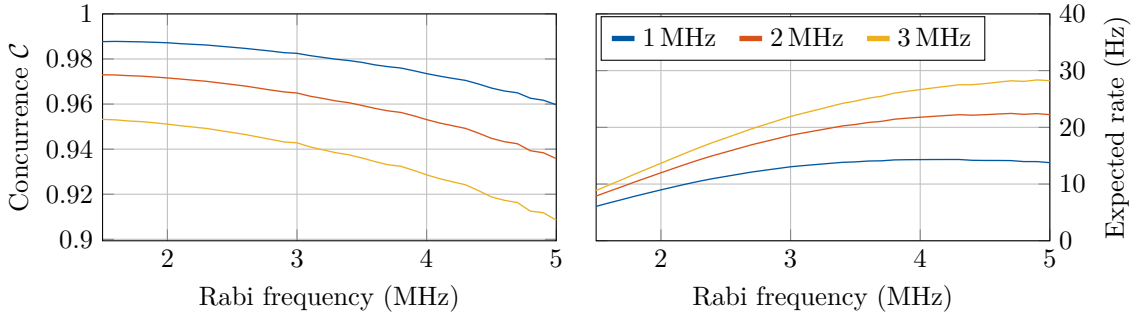
Figure 7.17.: Concurrence and entanglement creation rate for different line widths of the spectral filter.

of $5 \cdot 10^{-3}$ and $50\,\%$ on resonance transmission through the cavity setup comparable to the above presented experiment. For all Rabi frequencies the same detunings of both frequency components are chosen.

The simulation shows that the quality of the generated state is reduced for an increasing Rabi frequency and cavity line width (see Figure 7.17). Cause are the above discussed effects of the spectral overlap and the transmission of unwanted components through the cavity. On the other hand, the entanglement creation rate increases as there are more photons transmitted through the cavity. The achievable rate is thereby limited by the overhead of $2.5\,\mu s$ in the entanglement creation sequence. Both dependencies have to be considered, if the system is optimized for a specific application.

The effects discussed here that limit the creation of $854\,nm$ atom-photon entanglement in the bichromatic scheme also occur in the bichromatic $393\,nm$ atom-photon entanglement scheme. However, as the distance between the spectral components is almost twice as big the effect on the created state is smaller. Additionally, the branching ratios favor the $393\,nm$ decay what elongates the generated $854\,nm$ photon. As a result, $854\,nm$ photons with the same spectral width as $393\,nm$ photons are 17 times longer. Thus, if photons of the same duration are generated a higher Rabi frequency is required for the $854\,nm$ photon generation. As a further difference the $393\,nm$ sequence has a larger overhead time ($\approx 40\,\mu s$), which is needed to create the superposition in the $D_{5/2}$ manifold. As a result the achievable rate is mainly dominated by the overhead in the experimental sequence. As consequence the Rabi frequency can be chosen smaller without loosing to much (of the already smaller) repetition rate.

A further difference between the $393\,nm$ and $854\,nm$ scheme is the purity of the generated photon (not the purity of the atom-photon state). Due to the decay back into the initial state, the purity of the photon is reduced as the arrival time becomes blurred. In the $854\,nm$ scheme the decay back into the initial state does not affect the quality of the generated atom-photon entanglement but the ability of the generated photon to interfere with other photons created in the same way. In the $393\,nm$ scheme, the decay back into the initial state reduces the phase information in the initial superposition and therefore affects the purity of the created atom-photon state in the same way as the purity of the created photon is reduced. However, as

the branching ratio favors the 393 nm decay, the effect is smaller than for the 854 nm scheme. To reduce this problem there are two options. First a system with an initial state with a smaller back decay can be chosen as for example the $D_{3/2}$ manifold. The second option is a single excitation with a π-pulse instead of the excitation with a continuous laser pulse as in the presented schemes. In the latter case the time independence is given by the fact that the created photon is emitted during a fraction of the oscillation period given by the frequency difference of the final states.

7.4. Summary

In this chapter, I have discussed schemes to create 393 nm or 854 nm atom-photon entanglement. I have analyzed the influence of the spectral components on the atom-photon state created with monochromatic or bichromatic excitation. A monochromatic excitation creates a photon with two spectral components. As result, the phase of the atom-photon state depends on the detection time of the photon. The bichromatic excitation creates a photon with four spectral components. For the correct frequency difference of the bichromatic components two of the created spectral components overlap. In this case the created atom-photon state contains two parts. The first part is linked to the spectral overlapping components. The phase of this part is independent from the detection time of the photon. The second part is linked to the other two spectral components. Because they have different frequencies, the phase of the second part depends on the detection time of the photon. A spectral filter, that acts as quantum eraser [94], removes this time dependent part from the created atom-photon state. The result is an atom-photon state whose phase is independent of the creation time of the photon.

In case of the monochromatic 393 nm schemes, I create detection time dependent atom-photon entanglement with a concurrence $\mathcal{C} = 0.836(4)$ at an average rate of about 24 events per second for direct detected photons. The spectral filter removes one of the spectral components and thereby destroys the atom-photon entanglement. In case of the spectrally filtered photons I detected 0.6 events per second. With the bichromatic scheme I create detection time independent atom-photon entanglement with a concurrence $\mathcal{C} = 0.924(6)$ with an average rate of 0.5 events per seconds and partially entangled atom-photon states with a rate of 15 events per second. Because only a small fraction of the generated photons are detected directly, the rate of direct detected photons can be increased easily by an order of magnitude, if all photons are sent in this direction. The small rate for the cavity filtered photons are caused by the small overall efficiency of about $2 \cdot 10^{-5}$ of the whole setup. This efficiency contains the collection efficiency of the HALO (6 %), the single mode coupling (20 %), projection (50 %) and the quantum efficiency of the single photon detector (80 %). Additionally, the filter cavity influences the efficiency in two ways. The first influence is the on resonance transmission through the analysis cavity setup (5 %). The second influence is the spectral overlap of the spectral filter with the emitted photon spectrum. In case of the bichromatic scheme a spectral overlap of 30 % is expected, what means that from all photons only 30 % can be transmitted through

the cavity. As a comparison $60\,\%$ of the population of the generated photons are located in the central peak (see Figure 7.4). The actual spectral overlap is expected to be even smaller because the side bands are not taken into account in this calculation.

For the $854\,\text{nm}$ entanglement schemes larger event rates are reached. In the monochromatic scheme detection time dependent $854\,\text{nm}$ atom-photon entanglement with a concurrence $\mathcal{C} = 0.940(21)$ is created with an average rate of $180\,\text{Hz}$. This rate is a factor three larger compared to previously performed experiments with the setup, where 55 entangled atom-photon pairs were created each second [59,60]. The larger entanglement creation rate is caused mainly by the higher sequence repetition rate of $175\,\text{kHz}$ compared to $58\,\text{kHz}$ for the previous iteration of the experiment. In case of the bichromatic scheme partially entangled atom-photon pairs are created with a rate of 54 events per second. In case of cavity filtered photons, detection time independent atom-photon entanglement with a concurrence $\mathcal{C} = 0.904(6)$ is created with a rate of 4.7 events per second. The difference between the direct detection and filtered photons arises due to smaller efficiencies and a slightly lower sequence repetition rate. For direct detected photons a single shot efficiency of $9.5 \cdot 10^{-4}$ is achieved. This efficiency contains the collection efficiency of the HALO ($6\,\%$), the chance to generate a wanted σ photon on the wanted side ($23\,\%$), a correction factor of 0.9 due to the $D_{3/2}$ decay and coupling efficiencies. With the cavity as spectral filter, the total efficiency is further reduced by the overlap of the cavity with the spectrum of the generated photons ($25\,\%$, $40\,\%$ are emitted into the central peak) and the on resonance transmission of the cavity setup ($45\,\%$). The measured single shot efficiency of $1.1 \cdot 10^{-4}$ matches the expected efficiency calculated from the efficiency for direct detection.

For both wavelengths the quality of the atom-photon entanglement created with the bichromatic excitation is comparable to the quality of the atom-photon entanglement created with the monochromatic excitation. A difference between both scheme is the position of the filter in the setup. In case of the $393\,\text{nm}$ atom-photon entanglement, the spectral filtering is done after the polarization projection. For the $854\,\text{nm}$ atom-photon entanglement, the spectral filtering is done before the polarization projection. From this I infer, that the position of the filter has no effect on the generated atom-photon state. In the picture of a network it is thus not important if the spectral filter is located at the sender or receiver.

An other possibility to create an atom-photon state whose phase is independent of the detection time of the photon is to place the ion inside a cavity [96,97]. Together with a bichromatic laser excitation, the cavity ensures that an atom-photon state with spectral overlapping components is created. As result the phase of the state is time independent. For this system, it was shown that the phase of the created atom-photon state can be controlled with the relative phase of both frequency components of the bichromatic excitation. In the course of this work (see Section 6.2.2), I have showed the influence of the relative phase of both bichromatic frequency components on the spectrum and wave packet of a photon scattered in a three level system. I conclude, that the phase of the atom-photon state created with the bichromatic scheme presented here can be set by with the relative phase between both bichromatic frequency components. Simulations with the model developed in Chapter 5 confirm this conclusion.

8. Summary and Outlook

In this work I studied the spectral properties of a single Raman scattered photon generated from a single $^{40}\text{Ca}^+$ ion and the generation of atom-photon entanglement with such photons. For this, I set up to Fabry-Pérot resonators for $393\,\text{nm}$ and $854\,\text{nm}$ which act as single photon spectrometer to measure the spectra of single Raman-scattered photons or act as quantum eraser in schemes to create atom-photon entanglement, whose phase is independent from the detection time of the photon. To model the experimental situations, I developed a model that describes the laser induced Raman scattering with a $^{40}\text{Ca}^+$ ion.

In detail, I studied the spectral properties of single Raman scattered photons. I explored the dependence on the Rabi frequency Ω, the detuning Δ and the total decay rate Γ of the excited state. The found dependence of the spectral shape on the parameters of the excitation laser can be summarized as follows:

1. The spectral shape is complex and depends on the excitation parameters as well as the atomic level scheme and contains features as for example the Autler-Towns splitting.

2. The spectrum becomes wider for larger Rabi frequencies and narrower for an off-resonant excitation. The wave packet shows the opposite behavior.

3. The decay back into the initial state has no effect on the spectral width but the duration of the wave packet.

4. For an arbitrarily small Rabi frequency, the spectrum becomes arbitrarily narrow.

In further experiments I studied the effect of the ion temperature on spectral sidebands, how a truncated photon wave packet affects the spectral width and different quantum interference mechanisms that occur in the Raman scattering process. The different quantum interference effects can be observed as a modulation in the wave packet or in case of the spectrum as an enhancement and suppression of the photon emission into certain frequency modes.

As application of tailored spectral properties of single Raman-scattered photons, I presented a scheme to create atom-photon entanglement. A bichromatic laser excitation combined with a spectral filter creates an entangled atom-photon state whose phase is independent from the detection time of the photon. The spectral filter acts as quantum eraser that removes unwanted spectral components from the created atom-photon state and transforms a partially entangled state into a maximally entangled state. Furthermore, by adjusting the Rabi frequencies of the bichromatic frequency components different Clebsch-Gordan coefficients are compensated.

With the bichromatic atom-photon entanglement schemes I create 393 nm and 854 nm atom-photon entanglement with a fidelity of 0.95. Thereby, the scheme is similar to a scheme where the ion is positioned in a resonator [96]. In contrast to this scheme, I perform spectral filtering with an external resonator what makes the scheme easier to control and to implement into an existing setup.

With the presented work I showed that the setup is capable of studying spectra of single Raman-scattered photons and the generation of tailored atom-photon entanglement. At this point, further research can be done in various ways. The first option is to replace the laser excitation by the excitation with single photons as for example created with the down-conversion source in our group that creates entangled 854 nm photon pairs [58, 98]. In this context, the model needs to be further developed to describe this case. Furthermore, a slightly changed setup enables to study the upper level coupling in more detail. There are two options. As first option, two 854 nm beams can be set up that selectively couple to individual transitions. The second option is to set up a 850 nm laser that couples the $P_{3/2}$ state with the $D_{3/2}$ levels. Both options offer the possibility to set independent parameters for the coupling on the initial transition and the second transition what enables to study the upper level coupling for a broad range of parameters.

In case of the atom-photon entanglement schemes, the next step is an extension to multiple ions, where atom-photon entanglement is created for each ion. With the Mølmer-Sørensen gate [99, 100] the entanglement between the individual atom-photon pairs is then swapped to both photons to create an entangled photon-photon pair. This is the next step for the realization of a quantum repeater protocol with single ions as network nodes and photons as flying qubits that transport quantum information between these nodes.

Appendices

A. Dark ions in the bright trap

At the end of 2018 the ion storage time in the dark trap reduced drastically. The first guess were problems with the vacuum conditions that turned out to be unchanged. During further tests, it showed that the ions do not get lost but become dark instead. By recording videos of ion strings with the camera, we managed to observe calcium ions which became dark but remained in the trap. Such an event is captured in the pictures in Figure A.1. At the start, the string contains four $^{40}Ca^+$ ions. After some while one of the ions disappears and the remaining three ions take new equilibrium positions (12:29:11). A few seconds later the string changed twice in quick succession. A further calcium ion leaves the string (12:29:36) before a new dark ion enters the string (12:29:39). From the positions of the bright and dark ions we infer, that there are two bright $^{40}Ca^+$ ions in the string together with one dark ion other than $^{40}Ca^+$. After some while the dark ion became bright again (13:41:07).

This observation lead to the assumption that the calcium ion undergoes a chemical reaction and the created molecule is trapped. This molecule does not scatter 397 nm photons and is therefore dark. After some time the molecule decayed again and the calcium ion stayed in the trap. To specify the dark ion, we measured the vibration frequencies of the axial center of mass and axial breathing mode for two ions strings with either two calcium ions or one calcium ion and one dark ion. Unfortunately the ion crystals were not stable enough to perform a 729 nm spectroscopy to determine the frequencies. Instead a radio frequency oscillation was applied to the trap end tips to excite the motion of the ion string. To determine the resonance frequencies the ion fluorescence was observed on the camera. For an end tip voltage of 50 V we determined
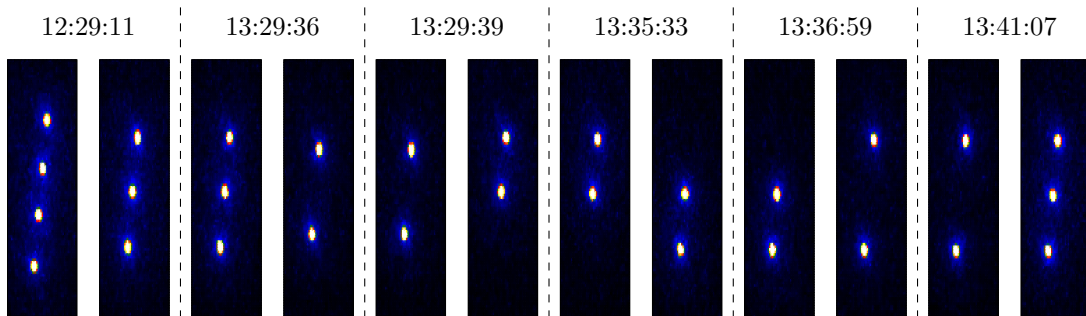
Figure A.1.: Ion string with four $^{40}Ca^+$ ions. One ion is lost at the beginning and another one reacts to form a molecule. Comparing the ion position allows to determine whether there are two $^{40}Ca^+$ ions or two $^{40}Ca^+$ ions and a dark molecule inside the string. Camera pictures show the 397 nm fluorescence in 100 ms integration time.
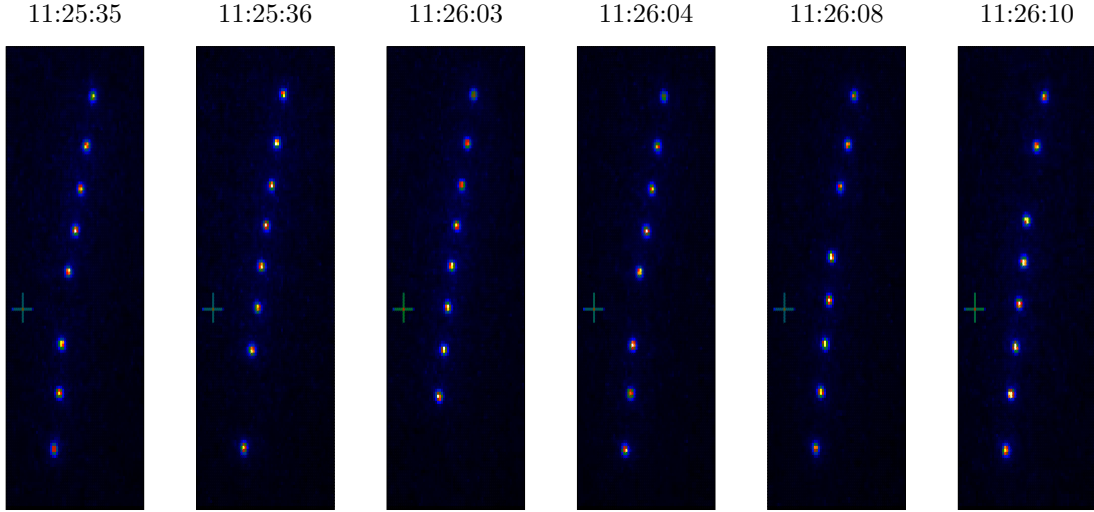
Figure A.2.: String of eight ^{40}Ca$^+$ ions and one dark molecule showing a kink at the position of the molecule. Camera pictures show the 397 nm fluorescence in 100 ms integration time.

the trap frequencies $\nu_{o,bb} = 420.1$ kHz, $\nu_{i,bd} = 228.1$ kHz and $\nu_{o,bd} = 378.5$ kHz. The indices i and o describe the oscillation **in** and **o**ut of phase. The indices *bb* and *bd* describe the ion string with two **b**right respective one **b**right and one **d**ark ion. At an other day we measured the trap frequencies $\nu_{i,bb} = 599.3$ kHz, $\nu_{i,bd} = 533.9$ kHz and $\nu_{o,bd} = 941.6$ kHz for an end tip voltage of 100 V. From these frequencies, I calculate the mass ratio μ of the ion string using the formulas from [101]. I obtain the values $\mu_{50\,V} = 1.52$ and $\mu_{100\,V} = 1.58$. With this mass ratio and the mass of the calcium ion, the mass of the dark ion (or molecule) is calculated to be $m_{50\,V} = 60.6$ amu. and $m_{100\,V} = 63.4$ amu. Event though the used method is to insensitive to determine the exact mass of the dark ion it strengthens the assumption that a chemical reaction changed the calcium ions to a heavier molecule.

Additionally to the different mass, the dark molecule causes a kink in a longer ion string. This is inferred from the observation of a string containing eight ^{40}Ca$^+$ ions and one dark molecule shown in Figure A.3. The position of the kink jumps with the position of the ion.

In further examinations to locate the cause of these dark ions, I found a shortcut in the trap between one of the blade electrodes and one of the micromotion compensation electrodes. For the typical power driving the trap, the shortcut could be observed as a glowing. The cause of the short circuit could not be determined with certainty. By reducing the trap power the glowing could be stopped. Increasing the trap power again lead to a new start of the glowing. The start of the glow at the shortcut also lead to a changed resonance condition of the helical resonator, which is used to generate the voltage needed to drive the trap. This change was observed as an increased reflection of the power coupled into the helical resonator. This also confirms, that the shortcut appeared at this time as this change of the resonance frequency was not observed before. Reducing the trap power to a point where the shortcut did not start to glow allowed us to continue to work with the bright trap with the disadvantage, that the trap frequencies
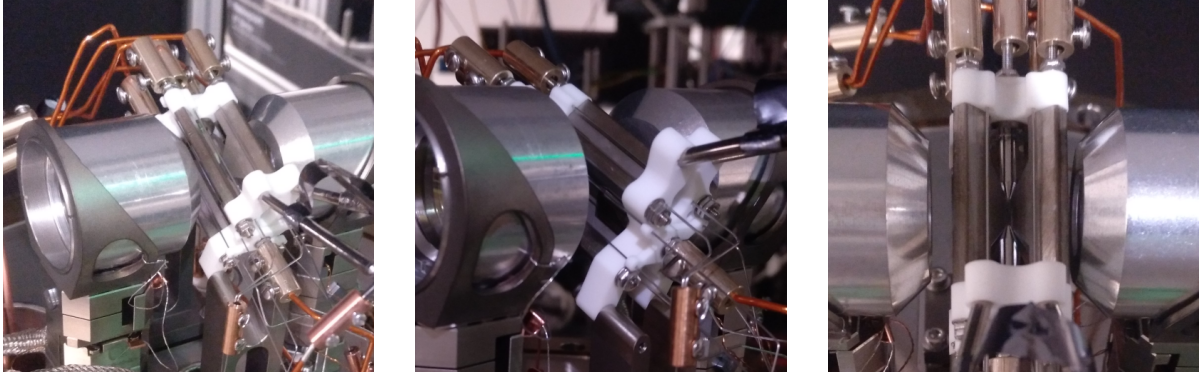
Figure A.3.: Pictures of the reconstructed dark trap with the additional compensation electrodes in HALO direction.

were lower and the storage time of an ion was reduced. As the trap was still functional we decided to modify the dark trap and keep the bright trap as a backup until the dark trap is fully functional. The modification targets the issue of the micromotion compensation due to the position of the compensation electrodes described in [52]. Additionally we decided to add a calcium target, to have the possibility for ablation loading of ions.

In the original design of the trap (see Figure 2.2 and Figure 3.1), four compensation electrodes are located above and below the radio frequency electrodes. It turned out, that these electrodes are not sufficient to compensate the micromotion, since the achievable shift in HALO direction is rather small. To solve this problem we mounted four additional compensation electrodes right and left of the radio frequency electrodes to have two compensation electrodes on each side (see Figure A.3). To keep the necessary changes small, no additional feed-through for the electrodes was installed. Instead we connected each pair of electrodes (top, left, right and bottom) to one of the already existing connections. Due to an unknown reason one of the electrode pairs seems to have no effect on the ion position. This was discovered after the full setup around the trap was done. Since the other electrode are sufficient to compensate the micromotion this problem was not fixed anymore.

To avoid problems with the vacuum conditions all parts that were added to the trap were cleaned and baked out before the reconstruction. The reconstruction of the trap took a few hours during which the vacuum vessel was closed and flooded with nitrogen. After the reconstruction the system was baked out again at about $120\,°C$ for about a week. It was no problem to reach the vacuum conditions we had before the reconstruction. In the later setup, the crucial step was to image the fluorescence of neutral calcium on the camera. This could be achieved only by mounting the camera in a close distance behind the view port. The observed fluorescence was then taken to setup fake ion beams as reference for the further steps.

Unfortunately, also in the dark trap a shortcut occurred shortly after the reconstruction. This shortcut limits the radio frequency power that is applied to operate the trap. With a laser that was bought for ablation loading of ions, I could reduce the occurrence of the glowing up to a point, where the trap could be operated sufficiently well.

B. Bayesian inference for a dice with F faces.

I reconstruct the density matrices of the generated atom-photon states with a quantum state tomography from the relative detection frequencies of each projection setting. To obtain the relative detection frequencies, the same state is generated many times and projected on F different atom-photon states. For each of these projection settings one measures k_i detection events. To determine estimates of the relative detection frequencies p_i from the measured detection events k_i, I extend the Bayesian inference method described in [57]. This extension corresponds to the transition from a coin flip to the roll of a dice. In both cases one wants to get estimates for the probabilities p_i for each measurement outcome.

If one rolls a dice with F faces a total of N times one can calculate the probability to get the signal $S = (k_1, k_2, ..., k_F)$ with the multinomial distribution

$$P(S|W(p_1, p_2, ..., p_F)) = \frac{N!}{k_1!k_2!...k_F!}p_1^{k_1}p_2^{k_2}...p_F^{k_F}, \tag{B.1}$$

if the probabilities p_i to land on each face are known. In the experiment, the inverted problem is of relevance. The dice was tossed N times and the outcome $S = (k_1, k_2, ..., k_F)$ is known. From this measured signal one wants to infer the underlying probabilities p_i. This is done with the probability distribution $P(W(p_1, p_2, ..., p_F)|S)$ that describes the probability for each realization of the dice under the condition that it led to the signal S. From this distribution the mean $\langle p_i \rangle$ and standard deviation Δp_i for each probability can be calculated.

With Bayes' theorem the wanted distribution can be written as

$$P(W(p_1, p_2, ..., p_F)|S) = \frac{P(S|W(p_1, p_2, ..., p_F))P(W)}{P(S)}, \tag{B.2}$$

where $P(W)$ describes the probability to have a dice with the probabilities p_k. The denominator

$$P(S) = \int P(S|W(p_1, p_2, ..., p_F))P(W)\mathrm{d}p_1\mathrm{d}p_2...\mathrm{d}p_{F-1} \tag{B.3}$$

is the probability to obtain the signal S. The integration is only done over $F-1$ probabilities, because the last probability is fixed by the condition $\sum p_i = 1$. This integral is solved using $P(W) = 1$ as prior, which corresponds to an uniform distribution of all possible realizations of the dice. This reflects no knowledge of the dice. Together with the probability to get the

signal S for a given dice, the integral

$$P(S) = \int_0^1 \mathrm{d}p_1 \int_0^{1-p_1} \mathrm{d}p_2 ... \int_0^{1-p_1-p_2-...-p_{F-1}} \mathrm{d}p_{F-1} \left[\frac{N!}{k_1!k_2!...k_F!} p_1^{k_1} p_2^{k_2} ... p_F^{k_F} \right] \qquad (B.4)$$

has to be solved.

Instead of this integral, I solve the more general Integral

$$I_m = \int_0^1 \mathrm{d}p_1 \int_0^{1-p_1} \mathrm{d}p_2 ... \int_0^{1-p_1-p_2-...-p_{F-1}} \mathrm{d}p_{F-1} \left[\frac{N!}{k_1!k_2!...k_F!} p_s^m p_1^{k_1} p_2^{k_2} ... p_F^{k_F} \right]. \qquad (B.5)$$

Therein an additional factor p_s^m is introduced to the probability p_s. This more general solution is needed later to calculate different moments of the distribution. The case $m = 0$ gives the integral in Equation B.4.

To solve this integral, first the probabilities p_s are substituted by u_s to get an upper limit of 1 for each integral. With this substitution the integrals become independent from each other and can be solved. The substitutions are:

$$p_1 \to u_1 \qquad (B.6)$$

$$p_2 \to (1-p_1)u_2 = (1-u_1)u_2 \qquad (B.7)$$

$$p_3 \to (1-p_1-p_2)u_3 = (1-u_1)(1-u_2)u_3 \qquad (B.8)$$

$$p_{F_1} \to (1-p_1-p_2-...p_{F-1})u_F = (1-u_1)(1-u_2)...(1-u_{F-2})u_F \qquad (B.9)$$

$$p_F \to (1-p_1-p_2-...p_{F-1}) = (1-u_1)(1-u_2)...(1-u_{F-1})(1-u_{F-1}). \qquad (B.10)$$

With these substitutions, the probabilities $p_i^{k_i}$ in the integral become

$$p_1^{k_1} = u_1^{k_1} \qquad (B.11)$$

$$p_2^{k_2} = (1-u_1)^{k_2}u_2^{k_2} \qquad (B.12)$$

$$p_s^{k_s+m} = (1-u_1)^{k_s+m}(1-u_2)^{k_s+m}...(1-u_{s-1})^{k_s+m}u_s^{k_s+m} \qquad (B.13)$$

$$p_{F-1}^{k_{F-1}} = (1-u_1)^{k_{F-1}}(1-u_2)^{k_{F-1}}...(1-u_{F-2})^{k_{F-1}}u_{F-1}^{k_{F-1}} \qquad (B.14)$$

$$p_F^{k_F} = (1-u_1)^{k_F}(1-u_2)^{k_F}...(1-u_{F-2})^{k_F}(1-u_{F-1})^{k_F}. \qquad (B.15)$$

Analog the differentials $\mathrm{d}p_k$ are replaced by

$$\mathrm{d}p_1 \to \mathrm{d}u_1 \qquad (B.16)$$

$$\mathrm{d}p_2 \to (1-u_1)\mathrm{d}u_2 \qquad (B.17)$$

$$\mathrm{d}p_s \to (1-u_1)(1-u_2)...(1-u_{s-1})\mathrm{d}u_s \qquad (B.18)$$

$$\mathrm{d}p_{F-1} \to (1-u_1)(1-u_2)...(1-u_{F-2})\mathrm{d}u_{F-1}. \qquad (B.19)$$

$$(B.20)$$

Altogether, the component $p_i^x \mathrm{d}p_i$ is substituted by the product

$$p_i^x \mathrm{d}p_i \to u_i^x \mathrm{d}u_i \prod_{n=1}^{i-1} (1 - u_n)^{x+1}. \tag{B.21}$$

These substitutions are put in the integral in Equation B.5. I then sort the variables and get integrals containing the factors u_i and $(1 - u_i)$ with the exponents k_i and $k_{i+1} + 1 + k_{i+2} + 1 + ... + k_{F-1} + 1 + k_F$. The second exponent is build by all the factors $(1 - u_i)$ coming from the substitution of the probabilities with an index bigger than i. The parts $+1$ in the sum add up to $F - 1 - i$. With these substitutions the integral in equation B.5 becomes

$$\begin{aligned}
I_m = {} & \frac{N!}{k_1! k_2! ... k_F!} \int_0^1 \mathrm{d}u_1 ... \int_0^1 \mathrm{d}u_{F-1} \left[u_1^{k_1} (1 - u_1)^{k_2 + k_3 ... + k_s + m + ... + k_F + F - 2} \right. \\
& u_2^{k_2} (1 - u_2)^{k_3 + k_4 + ... + k_s + m + ... + k_F + F - 3} ... u_s^{k_s + m} (1 - u_s)^{k_{s+1} + ... + k_F + F - 1 - s} ... \\
& \left. ... u_{F-1}^{k_{F-1}} (1 - u_{F-1})^{k_F} \right].
\end{aligned} \tag{B.22}$$

This integral is split in independent integrals $I_{m,r}$ with the solution

$$\begin{aligned}
I_{m,r} &= \int_0^1 \mathrm{d}u_r u_r^{k_r} (1 - u_r)^{k_{r+1} + ... + k_s + m + ... + k_F + F - r - 1} \\
&= \frac{k_r! (k_{r+1} + ... + k_s + m + ... + k_F + F - r - 1)!}{(k_r + k_{r+1} + ... + k_s + m + ... + k_F + F - r)!}
\end{aligned} \tag{B.23}$$

given by the Euler Beta function. These individual solutions are put into the integral I_m which is then given by the product $I_{m,1} I_{m,2} ... I_{m,F-1}$. In this product individual fractions are truncated in the following way

$$... I_{m,r-1} I_{m,r} I_{m,r+1} ... = ... \frac{(\cdots)(\diagup)}{(\cdots)} \frac{(\cdots)(\diagdown)}{(\diagup)} \frac{(\cdots)(\cdots)}{(\diagdown)} ... . \tag{B.24}$$

Thus from each fraction only the left factor $k_r!$ in the numerator remains, except for the first and last fraction. From the first fraction also denominator stays. From the last fraction, the full numerator remains. Thus the value of the wanted integral becomes

$$I_m = \frac{N!}{k_1! k_2! ... k_F!} \frac{k_1! k_2! ... (k_s + m)! ... k_{F-1} k_F)!}{(k_1 + k_2 + ... + k_s + m + ... + k_F + F - r)!} = \frac{N!}{k_s!} \frac{(k_s + m)!}{(N + F + m - 1)!} \tag{B.25}$$

From this one gets the probability

$$P(S) = I_0 = \frac{N!}{(N + F - 1)!}. \tag{B.26}$$

This probability is used to obtain the probability distribution for W given the result S

$$P(W(p_1, p_2, ..., p_F)|S) = \frac{(N+F-1)!}{N!} \frac{N!}{k_1!k_2!...k_F!} p_1^{k_1} p_2^{k_2} ... p_F^{k_F} = \frac{(N+F-1)!}{k_1!k_2!...k_F!} p_1^{k_1} p_2^{k_2} ... p_F^{k_F}.$$
(B.27)

The different moments of the distribution are calculated by

$$\langle p_s^m \rangle = \int ... \int p_s^m P(W(p_1, p_2, ..., p_F)|S) \mathrm{d}p_1 \mathrm{d}p_2 ... \mathrm{d}p_{F-1} = \frac{I_m}{I_0}$$
(B.28)

with the limits as discussed above. Using the result I_m for the integral one finds

$$\begin{aligned} \langle p_s^m \rangle &= \frac{(N+F-1)!}{N!} I_m = \frac{(N+F-1)!}{N!} \frac{N!}{k_s!} \frac{(k_s+m)!}{(N+F+m-1)!} \\ &= \frac{(N+F-1)!}{(N+F+m-1)!} \frac{(k_s+m)!}{k_s!} \end{aligned}$$
(B.29)

for the moments of the distribution. From the moments of the distribution, the wanted expectation value and the standard deviation of the probability p_s are calculated. For the expectation value one gets

$$\langle p_s \rangle = \langle p_s^{m=1} \rangle = \frac{k_s+1}{N+F}.$$
(B.30)

The standard deviation Δp_s becomes

$$\Delta p_s = \sqrt{\langle p_s^2 \rangle - \langle p_s \rangle^2},$$
(B.31)

where

$$\langle p_s^2 \rangle = \frac{(k_s+1)(k_s+2)}{(N+F)(N+F+1)}.$$
(B.32)

These are the wanted estimates for the relative frequencies and the uncertainty in the frequencies for each projection setting. For a coin flip on uses $F = 2$. This corresponds to the result found in [57].

C. Supplementary material to the spectrum measurements

In this appendix, I supply additional information to the spectrum measurements presented in this work. This includes the parameters of the excitation laser and other experimental parameters. Furthermore, I list the number of detected photons and properties of the Raman photon determined from the measured photon as for example the line width. For each measurement, I list a subset from the following quantities:

$\Delta_{\mathbf{m}}$: 854 nm or 393 nm detuning(s) with respect to the transition line center. I use the same index m for the detuning of the excitation laser and the frequency of the emitted photon to indicate a detuning with respect to the line center.

$\Omega_{\mathbf{m}}$: Rabi frequency of the excitation laser in the model.

$\Delta_{\mathbf{t}}$: 854 nm or 393 nm detuning(s) with respect to an individual atomic transition. Calculated from Δ_{m} and the shift η of the respective transition with $\Delta_{\mathrm{t}} = \Delta_{\mathrm{m}} - \eta$. For the applied magnetic field $B \approx 2.857\,\mathrm{G}$ one gets $\mu_{\mathrm{B}}B \approx 4\,\mathrm{MHz}$. Often used transitions are

- $|\mathrm{P}_{3/2}, -\frac{3}{2}\rangle \to |\mathrm{D}_{5/2}, -\frac{5}{2}\rangle$, where $\Delta_{\mathrm{t}} = \Delta_{\mathrm{m}} - 4\,\mathrm{MHz}$
- $|\mathrm{P}_{3/2}, -\frac{3}{2}\rangle \to |\mathrm{S}_{1/2}, -\frac{1}{2}\rangle$, where $\Delta_{\mathrm{t}} = \Delta_{\mathrm{m}} + 4\,\mathrm{MHz}$
- $|\mathrm{P}_{3/2}, -\frac{1}{2}\rangle \to |\mathrm{S}_{1/2}, -\frac{1}{2}\rangle$, where $\Delta_{\mathrm{t}} = \Delta_{\mathrm{m}} - 1.33\,\mathrm{MHz}$
- $|\mathrm{P}_{3/2}, +\frac{1}{2}\rangle \to |\mathrm{S}_{1/2}, +\frac{1}{2}\rangle$, where $\Delta_{\mathrm{t}} = \Delta_{\mathrm{m}} + 1.33\,\mathrm{MHz}$
- $|\mathrm{P}_{3/2}, +\frac{1}{2}\rangle \to |\mathrm{D}_{5/2}, +\frac{1}{2}\rangle$, where $\Delta_{\mathrm{t}} = \Delta_{\mathrm{m}} - 0.27\,\mathrm{MHz}$

I list the detuning with respect to an individual transition, if a single transition is excited, the photons are emitted mainly on a single transition, or the transition offers a good reference point.

$\Omega_{\mathbf{t}}$: Rabi frequency on an individual transition. Calculated from Ω_{m} together with the Clebsch-Gordan coefficient and the polarization of the excitation laser. Frequent cases are:

- $|\mathrm{D}_{5/2}, -\frac{5}{2}\rangle \to |\mathrm{P}_{3/2}, -\frac{3}{2}\rangle$, $|\mathrm{V}\rangle$ polarization perpendicular to B-field: $\Omega_{\mathrm{t}} = \sqrt{\frac{10}{15}}\sqrt{\frac{1}{2}}\Omega_{\mathrm{m}}$
- $|\mathrm{S}_{1/2}, \pm\frac{1}{2}\rangle \to |\mathrm{P}_{3/2}, \pm\frac{1}{2}\rangle$, $|\mathrm{H}\rangle$ polarization perpendicular to B-field: $\Omega_{\mathrm{t}} = \sqrt{\frac{2}{3}}\Omega_{\mathrm{m}}$

$\delta_{\mathbf{b}}$: Shift of the 393 nm frequency axis that is introduced to match the model curve to the measured data. The shifted position is calculated as $\Delta_{\mathrm{ion}} = \Delta_{\mathrm{cav}} + \delta_{\mathrm{b}}$, where Δ_{cav} are the frequency set points during the measurement.

Rep.: Sequence repetitions per frequency point. Given in multiples of one million.

Sig: Signal events in the spectrum after the dark count correction was applied.

ε**:** Total efficiency of the setup during the spectrum measurement. Contains the collection efficiency, the single mode coupling, the on resonance transmission through the cavity setup and the detection efficiency.

$\Delta_{\mathbf{AC}}$**:** Expected AC-Stark shift caused by the laser excitation. Calculated for a three level system with equation 5.27 from the Rabi frequency Ω_t and the detuning Δ_t of the laser excitation and the total decay rate $\Gamma_{P_{3/2}} = 22.99\,\text{MHz}$ of the excited state.

$\Delta\nu$**:** Spectral width of the scattered photon determined with Equation 2.51 and Equation 2.52.

$\Delta\tau$**:** Duration of the scattered photon determined with Equation 2.51 and Equation 2.52.

tbp: Time bandwidth product calculated as $\text{tbp} = 2\pi\Delta\nu\Delta\tau$

$c_{\mathbf{sb}}$**:** Strength of the vibrational side bands. Determined by a fit to narrow spectra.

Pop.: Population in the spectrum emitted by the ion. Reaches 1 in the optimal case. Reduced by the 850 nm decay, not observed transitions, and polarization projection.

$\nu_{\mathbf{rad}}$**:** Radial trap frequency. Measured with 729 nm spectroscopies.

$\tau_{\mathbf{pulse}}$**:** Duration of the radio frequency pulse applied to the acousto-optic modulator that switches the laser pulse.

Additionally I show the calculated **emitted** and **ideal** spectrum and the measured wave packet. The emitted spectrum contains vibration sidebands, which are not present in the ideal spectrum (detail see Section 4.5.3). In the first Section C.1, the emitted spectrum is drawn in dotted lines. The ideal spectrum is drawn in sold lines. Additionally, the applied 854 nm detuning is marked with a vertical dotted line to indicate the effect of the AC-Stark shift. In the other sections, the emitted spectra are shown on the left side, while the ideal spectra are shown on the right side (if displayed).

C.1. Spectral properties: dependence on Ω and Δ – Section 6.1.1

C.1.1. 500 nW 854 nm laser power – $\bar{\Omega}_t = 2.68(2)$ MHz – Figure 6.2 (a)

Δ_t/MHz	Ω_t/MHz	δ_b/MHz	Rep.	Sig.	$\varepsilon/10^{-4}$	Δ_{AC}/MHz	$\Delta\nu$/MHz	$\Delta\tau$/µs	tbp	c_{sb}
−22.5	2.97(3)	0.00(2)	27	7223	1.12(3)	−0.1	2.14(7)	2.12(2)	29(1)	0.38(2)
−16.4	2.75(2)	−0.07(2)	30	8991	1.26(3)	−0.1	2.23(6)	1.61(2)	22.5(6)	0.42(3)
−11.0	2.80(1)	−0.05(2)	30	8449	1.36(3)	−0.1	2.27(5)	0.991(9)	14.1(4)	0.42(2)
−4.9	2.49(1)	0.07(2)	18	4712	1.16(2)	−0.0	2.35(6)	0.78(1)	11.5(3)	0.40(2)
−0.5	2.695(8)	−0.07(2)	30	9676	1.49(2)	−0.0	2.51(4)	0.561(5)	8.8(2)	0.43(2)
4.5	2.39(2)	0.08(2)	18	5301	1.30(3)	0.0	2.20(6)	0.82(1)	11.4(3)	0.38(2)
12.0	2.59(2)	0.00(1)	57	13839	1.15(2)	0.1	2.12(5)	1.24(2)	16.5(4)	0.43(2)
15.6	2.50(3)	0.05(2)	51	13272	1.11(3)	0.1	2.13(5)	1.79(2)	23.9(6)	0.43(3)
22.0	2.95(3)	0.08(2)	27	7264	1.13(2)	0.1	2.44(8)	2.09(2)	32(1)	0.46(2)
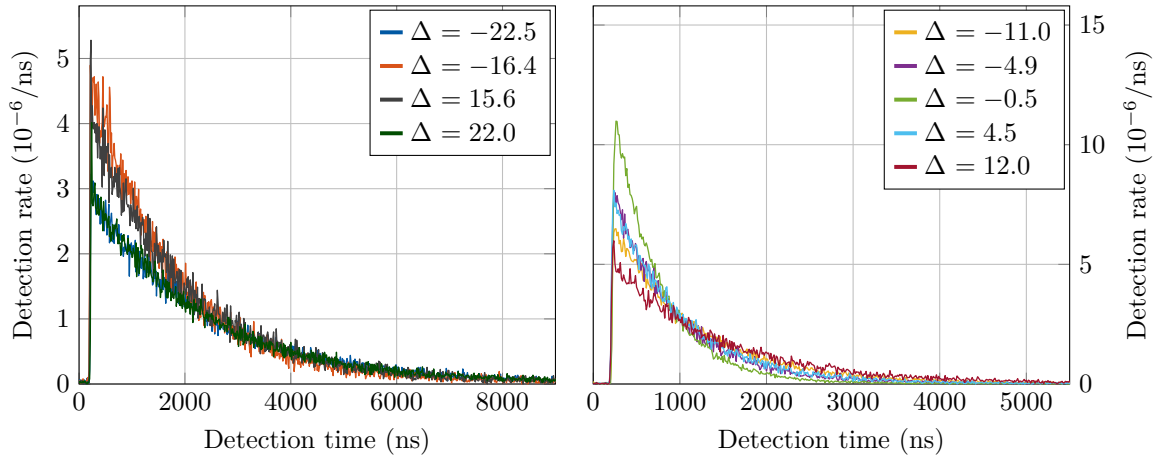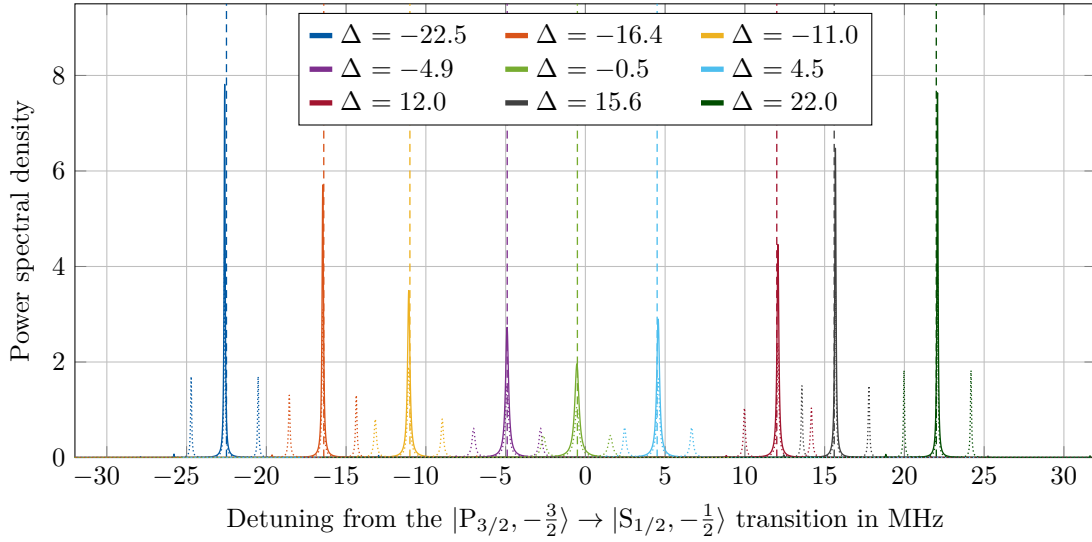
C.1.2. 5 µW 854 nm laser power − $\bar{\Omega}_\mathbf{t} = 8.03(3)$ MHz − Figure 6.2 (b)

Δ_t/MHz	Ω_t/MHz	δ_b/MHz	Rep.	Sig.	$\varepsilon/10^{-4}$	Δ_AC/MHz	$\Delta\nu$/MHz	$\Delta\tau$/µs	tbp	c_sb
−24.2	8.62(4)	−0.06(3)	70	12197	1.44(2)	−0.6	2.53(6)	0.291(4)	4.6(1)	0.39(2)
−16.8	8.21(3)	−0.26(5)	20	3872	1.52(3)	−0.7	2.7(1)	0.190(2)	3.3(1)	0.42(3)
−11.1	8.06(3)	0.11(4)	40	7186	1.52(2)	−0.7	3.51(6)	0.125(1)	2.77(6)	0.46(4)
−5.9	7.94(2)	0.17(7)	40	8177	1.66(3)	−0.7	4.1(1)	0.091(1)	2.34(7)	0.61(8)
0.3	7.66(2)	0.23(5)	55	10347	1.64(2)	0.1	4.08(6)	0.086(1)	2.21(4)	0.57(6)
4.2	7.88(3)	0.12(7)	40	5645	1.13(2)	0.6	3.9(1)	0.088(1)	2.16(9)	0.38(6)
10.8	7.81(3)	0.02(4)	70	10978	1.30(2)	0.7	3.71(6)	0.137(2)	3.19(7)	0.43(3)
16.1	8.00(5)	0.01(7)	15	2519	1.14(4)	0.7	3.5(2)	0.192(2)	4.2(2)	0.35(4)
22.1	8.08(5)	−0.13(5)	25	2912	0.79(3)	0.6	3.0(1)	0.292(4)	5.6(3)	0.48(5)
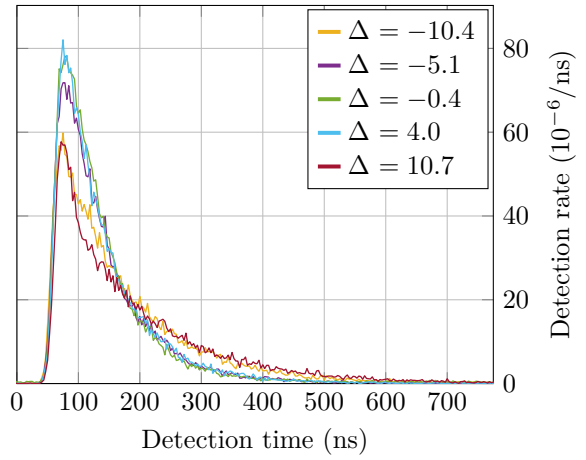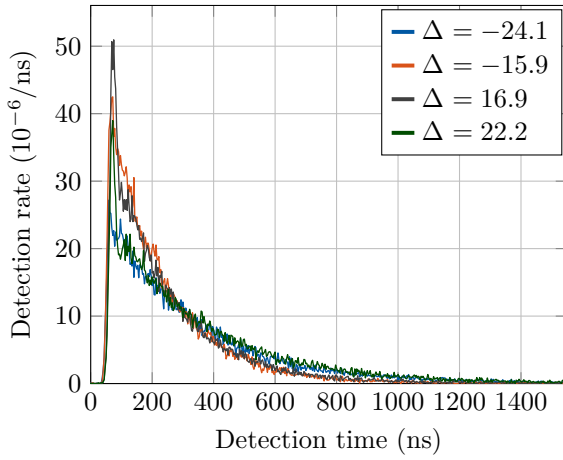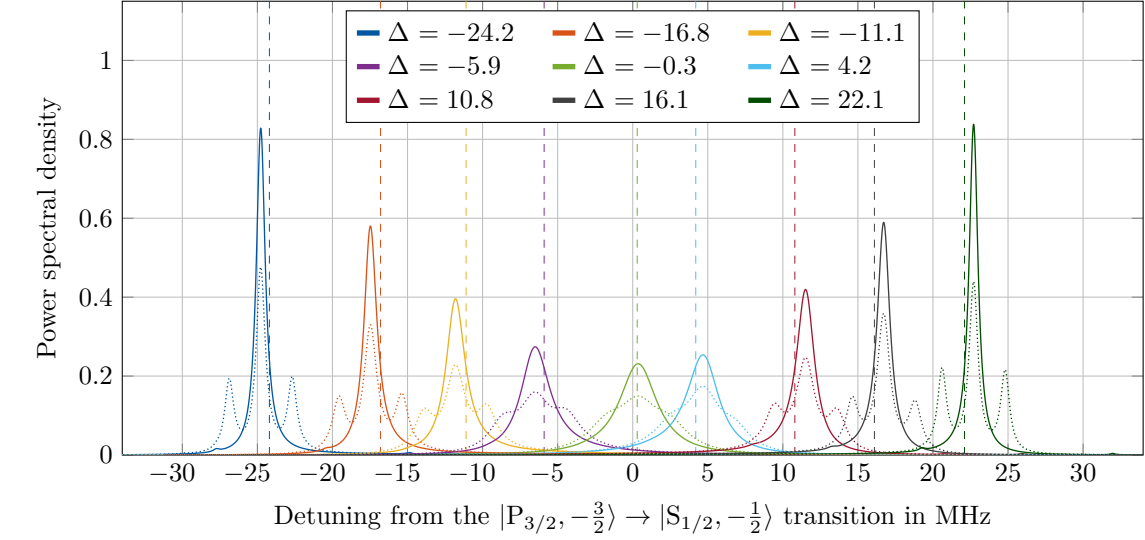
C.1.3. 13 µW 854 nm laser power − $\bar{\Omega}_{\mathbf{t}} = 12.69(5)$ MHz − Figure 6.2 (c)

Δ_t/MHz	Ω_t/MHz	δ_b/MHz	Rep.	Sig.	$\varepsilon/10^{-4}$	Δ_{AC}/MHz	$\Delta\nu$/MHz	$\Delta\tau$/µs	tbp
−45.1	12.75(5)	−0.05(5)	30	3774	0.86(3)	−0.8	3.2(2)	0.411(2)	8.2(6)
−33.8	12.62(5)	0.01(3)	66	7617	0.98(2)	−1.0	2.8(1)	0.251(2)	4.5(2)
−23.4	12.69(6)	0.03(7)	63	6715	0.81(2)	−1.4	3.5(2)	0.1368(8)	3.0(1)
−11.4	12.37(5)	−0.2(2)	39	5547	1.03(4)	−1.8	4.7(2)	0.0613(4)	1.82(9)
−0.0	12.40(2)	0.1(2)	66	8944	1.10(3)	−2.3	5.5(2)	0.0388(2)	1.35(6)
10.9	12.63(5)	0.5(1)	96	13303	1.08(3)	1.9	4.8(1)	0.0599(4)	1.82(6)
22.8	12.68(5)	0.3(1)	36	3409	0.52(2)	1.4	4.0(4)	0.1397(9)	3.5(4)
33.8	13.10(4)	−0.31(8)	20	3240	0.79(3)	1.1	3.3(3)	0.246(1)	5.1(5)
44.8	12.91(5)	−0.27(2)	65	11260	1.23(2)	0.9	3.1(1)	0.412(2)	7.9(3)
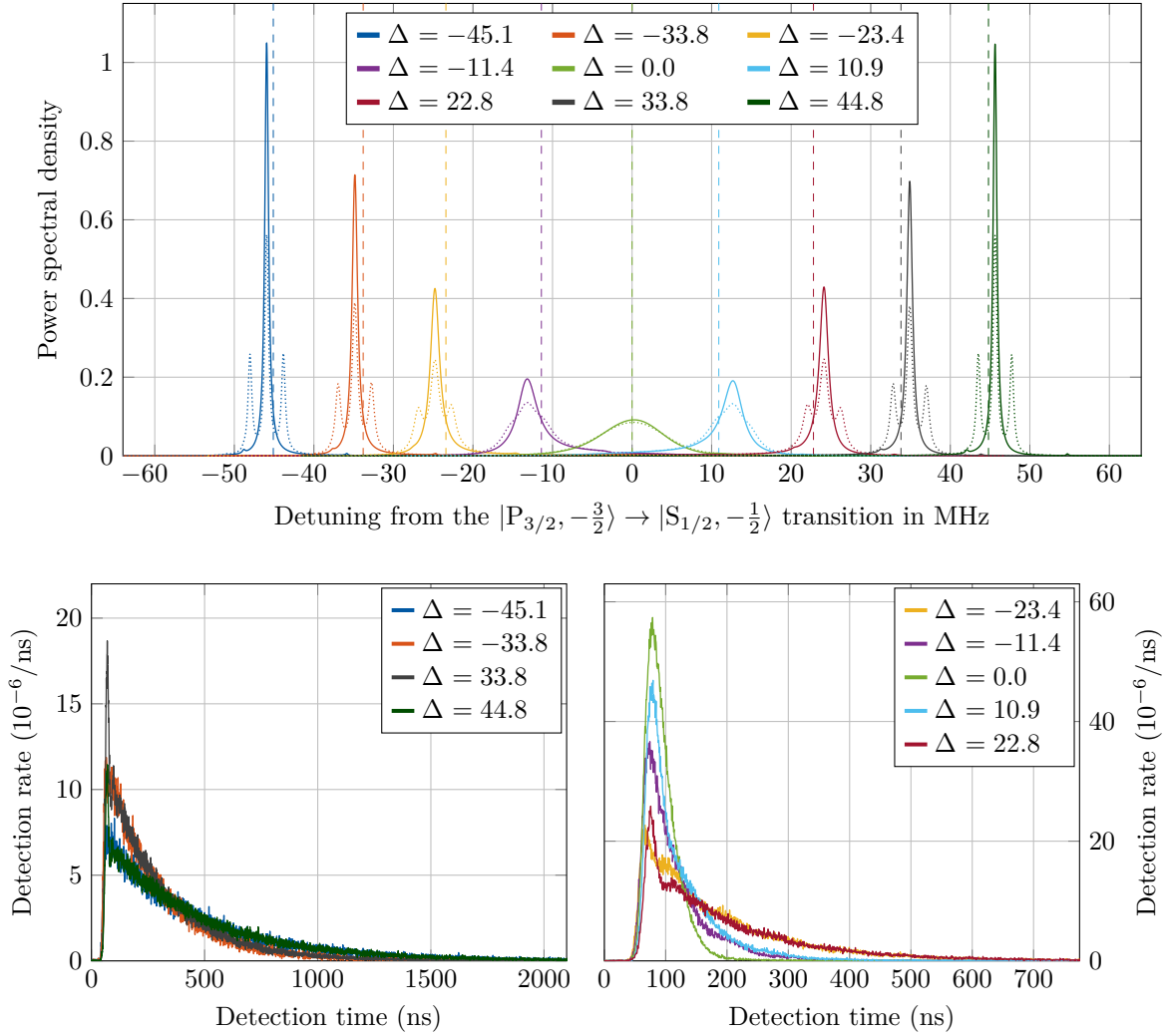
The wave packet for $\Delta = 33.8\,\text{MHz}$ and $\Delta = 44.8\,\text{MHz}$ are scaled by 0.5 to compensate a higher detection efficiency during these measurements.

C.1.4. 60 µW 854 nm laser power − $\bar{\Omega}_\mathbf{t} = 28.1(3)$ MHz − Figure 6.3 (d)

Δ_t/MHz	Ω_t/MHz	δ_b/MHz	Rep.	Sig.	$\varepsilon/10^{-4}$	Δ_{AC}/MHz	$\Delta\nu$/MHz	$\Delta\tau$/µs	tbp
−45.0	28.1(2)	−0.1(1)	35	3463	1.29(4)	−3.9	4.5(2)	0.100(1)	2.8(2)
−34.1	28.3(2)	−0.1(1)	45	4188	1.17(4)	−4.8	5.3(3)	0.0695(9)	2.3(1)
−23.2	27.9(4)	0.29(8)	100	9410	1.61(3)	−6.0	7.1(1)	0.0405(5)	1.80(4)
−10.2	23.8(4)	2.6(2)	60	4862	1.33(3)	−6.8	9.9(5)	0.0243(3)	1.52(9)
1.0	27.6(1)	1.3(3)	80	6665	1.56(4)	12.1	12.9(5)	0.01843(8)	1.49(6)
11.1	28.4(3)	1.2(2)	100	8269	1.41(5)	8.8	11.5(5)	0.0217(3)	1.56(7)
22.6	29.7(4)	1.2(1)	50	4760	1.52(4)	6.8	6.9(3)	0.0371(5)	1.62(8)
33.9	29.1(2)	0.6(1)	85	6240	1.01(3)	5.1	6.3(3)	0.0720(3)	2.9(1)
44.8	29.9(4)	1.0(1)	35	3474	1.26(4)	4.3	4.8(3)	0.108(1)	3.2(2)
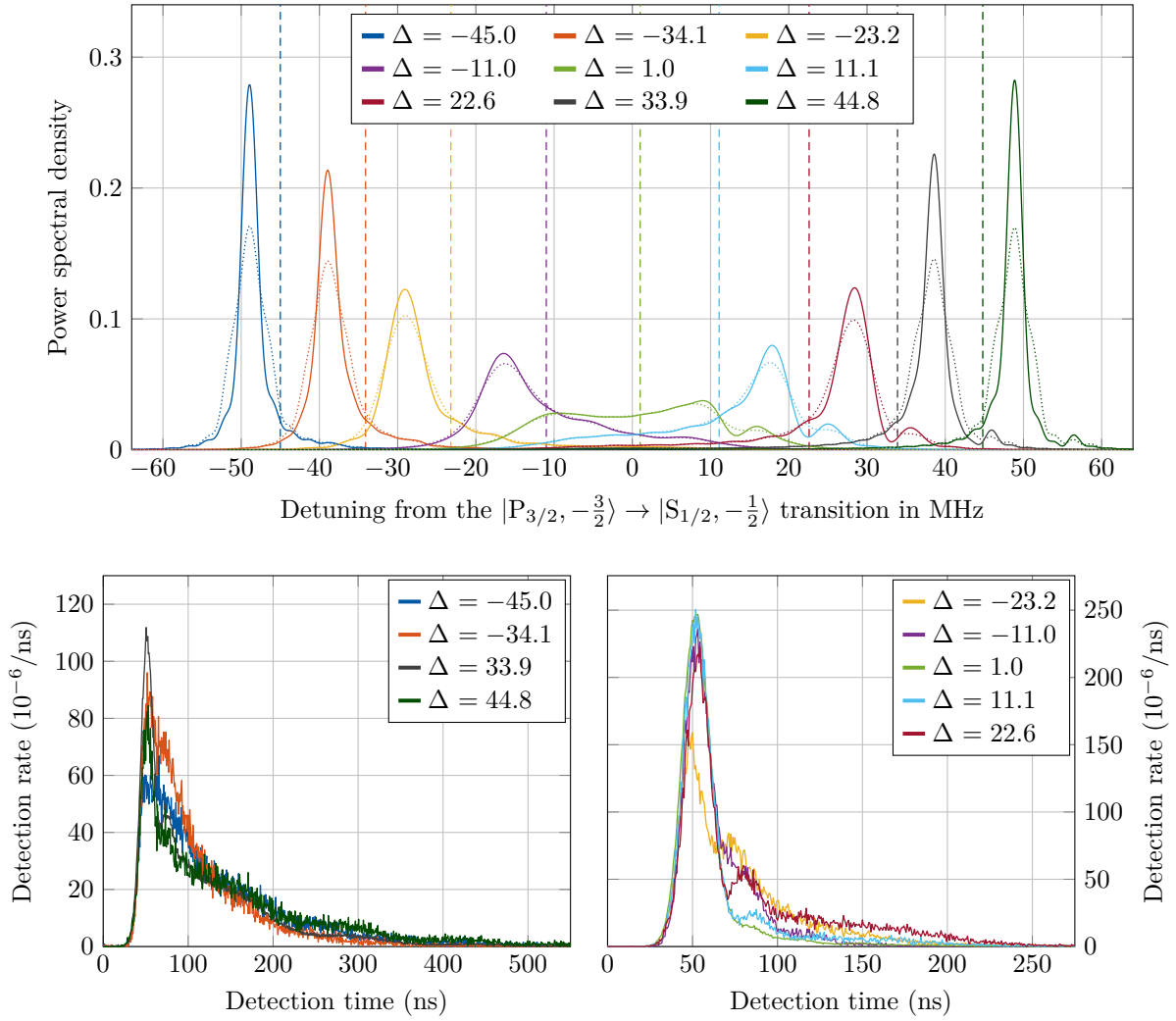
C.1.5. 660 µW 854 nm laser power − $\bar{\Omega}_\mathbf{t} = 53.0(3)$ MHz − Figure 6.3 (e, f)

Δ_t/MHz	Ω_t/MHz	δ_b/MHz	Rep.	Sig.	$\varepsilon/10^{-4}$	Δ_{AC}/MHz	$\Delta\nu$/MHz	$\Delta\tau$/µs	tbp
−45.5	51.8(3)	0.9(2)	75	5315	0.99(4)	−11.4	7.4(3)	0.0417(3)	1.94(8)
−22.7	53.9(3)	0.8(3)	45	3426	1.25(5)	−17.4	10.5(7)	0.0227(1)	1.5(1)
−0.2	53.5(3)	1.1(5)	350	18514	1.07(5)	−26.1	20.5(8)	0.0148(1)	1.90(8)
23.3	52.1(3)	0.2(3)	66	3920	0.88(6)	16.4	16(1)	0.0235(2)	2.3(2)
45.8	53.7(1)	1.2(1)	111	7117	1.03(4)	12.1	8.6(4)	0.0598(4)	3.2(2)
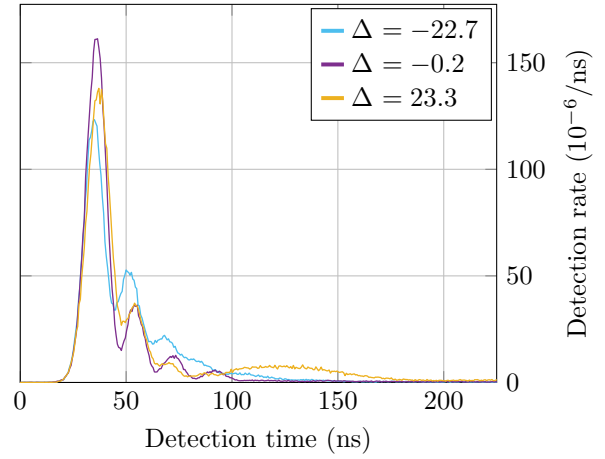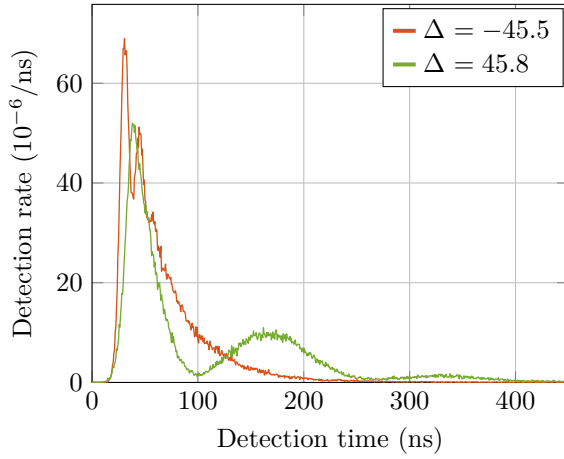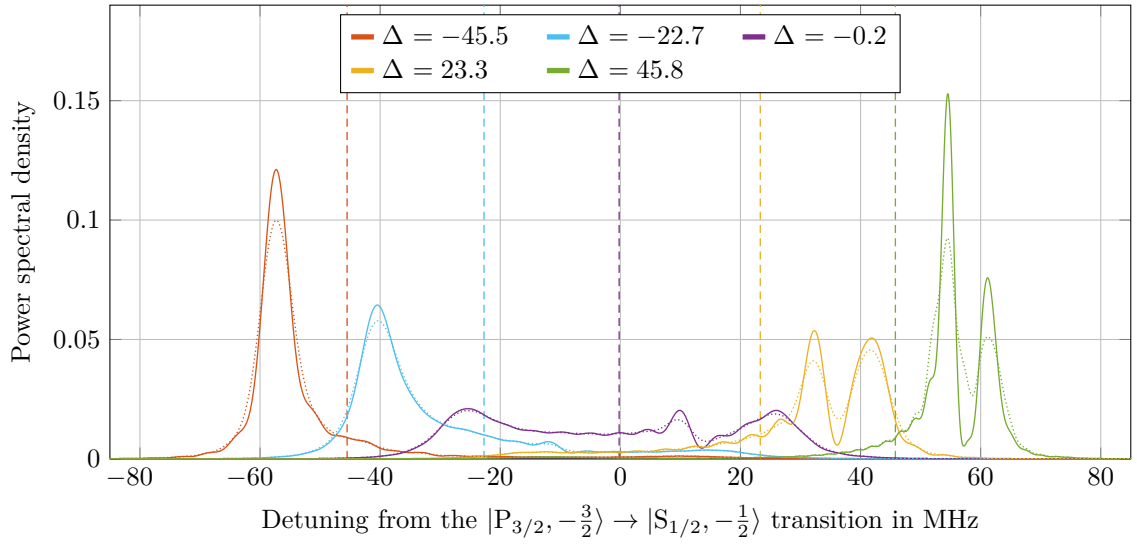
C.1.6. 854 nm spectra to study the dependence on Ω and Δ – Figure 6.4 (a, b)

		Δ_t/MHz	Ω_t/MHz	Rep.	Sig.	$\varepsilon/10^{-3}$	$\Delta\nu$/MHz	$\Delta\tau$/µs	tbp
(a)	$\left|-\frac{3}{2}\right\rangle$	-11.1	5.52(6)	10	11372	2.10(1)	3.011(9)	3.20(7)	61(1)
	$\left|-\frac{1}{2}\right\rangle$	-8.4	5.52(6)	10	6351	2.10(1)	3.48(2)	3.5(1)	76(3)
	$\left|+\frac{1}{2}\right\rangle$	-11.1	5.52(6)	10	6746	2.10(1)	3.55(2)	3.2(5)	70(10)
	$\left|+\frac{3}{2}\right\rangle$	-8.4	5.52(6)	10	12496	2.10(1)	3.304(9)	3.4(6)	70(10)
(b)	$\left|-\frac{3}{2}\right\rangle$	-1.5	10.1(1)	12	10674	1.48(1)	5.27(2)	0.76(1)	25.2(4)
	$\left|-\frac{1}{2}\right\rangle$	1.2	10.1(1)	12	5332	1.48(1)	5.65(5)	0.82(2)	29.2(7)
	$\left|+\frac{1}{2}\right\rangle$	-1.5	10.1(1)	12	4872	1.48(1)	5.15(5)	0.76(7)	25(2)
	$\left|+\frac{3}{2}\right\rangle$	1.2	10.1(1)	12	10196	1.48(1)	5.32(2)	0.83(8)	28(3)
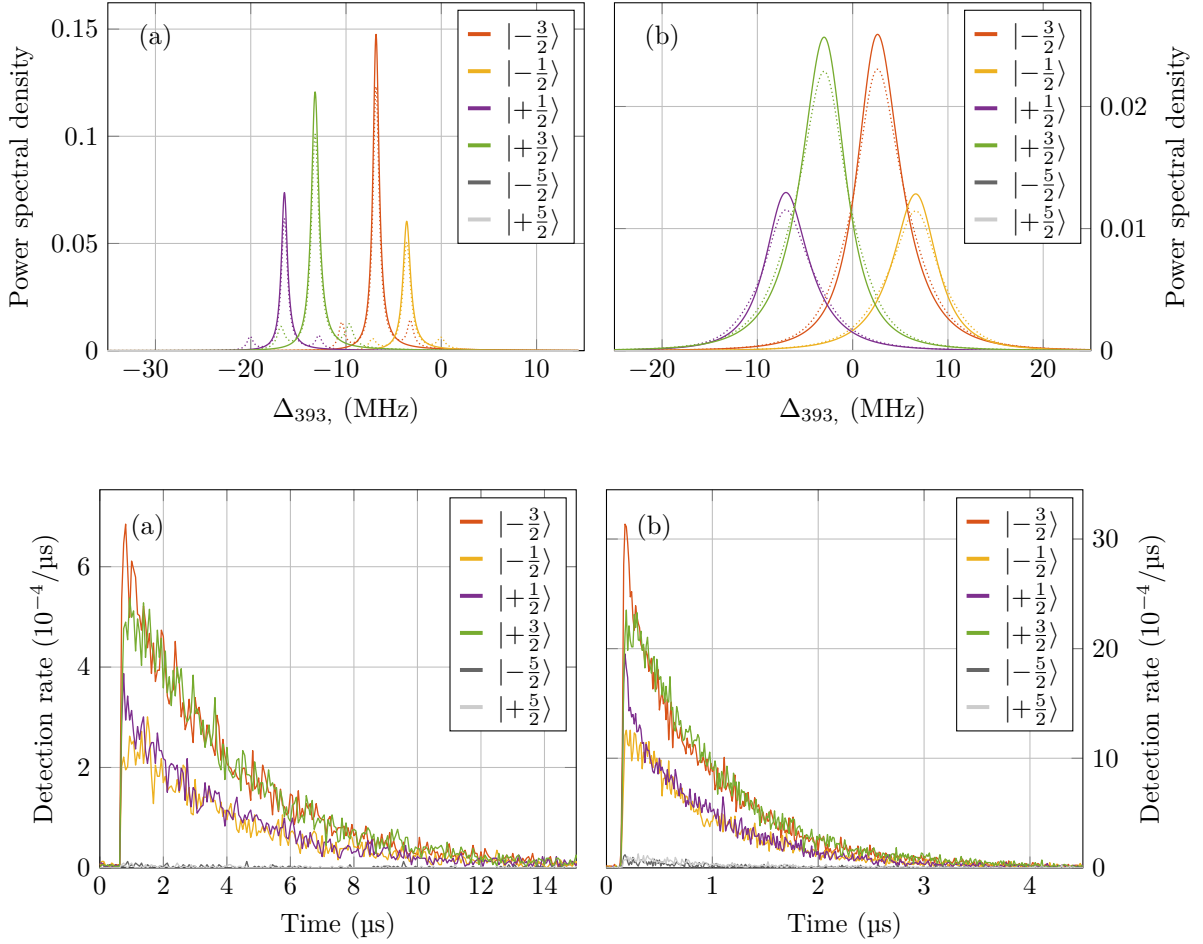
C.2. Spectral properties: sidebands – Section 6.1.2
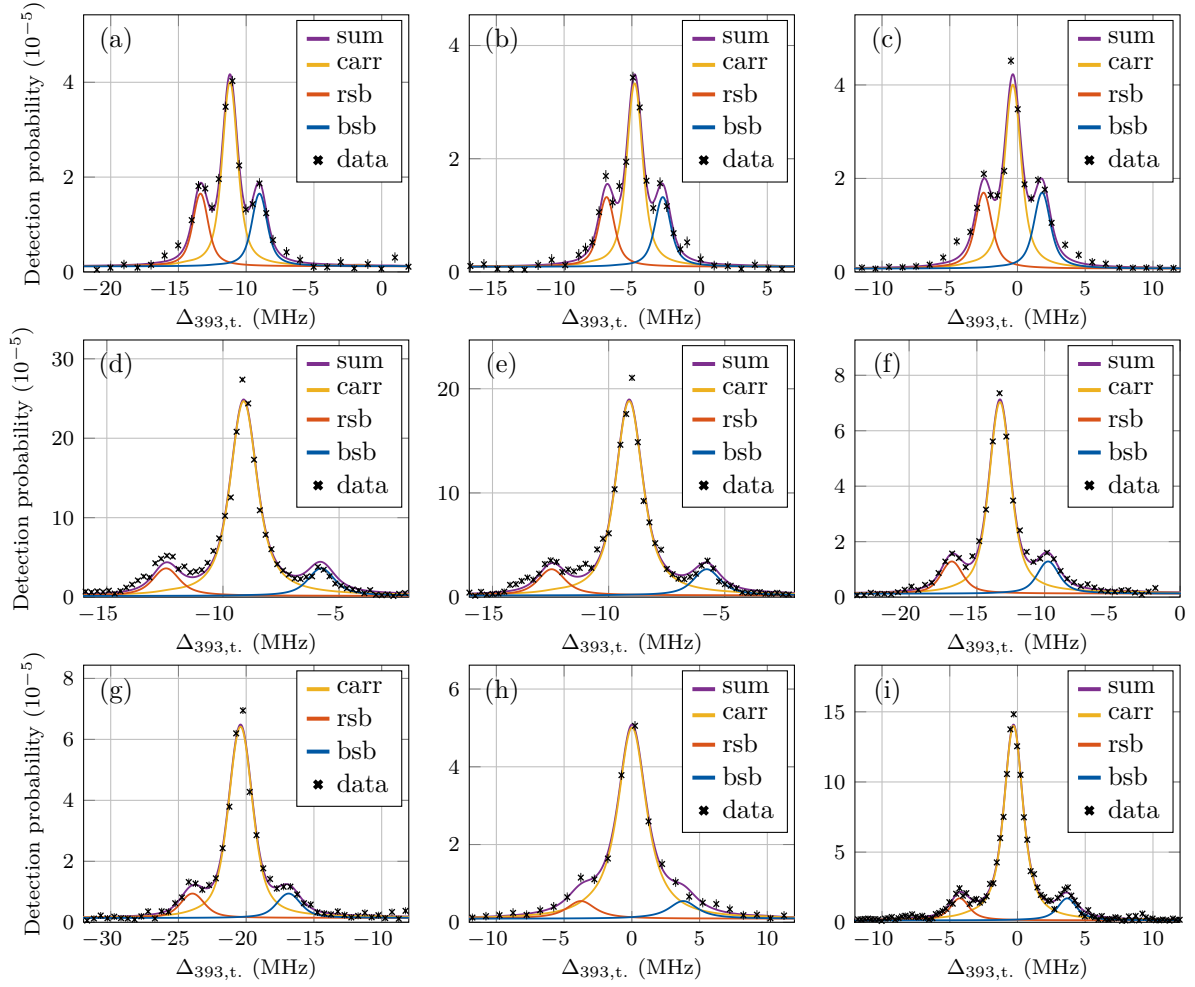
	ν_{rad}/MHz	Ω_{t}/MHz	Δ_{t} /MHz	Rep.	Sig.	$\varepsilon/10^{-4}$	ν_{sb}/MHz	c_{sb}
(a)	+2.14	2.81(1)	−11.1	30	8449	1.29(2)	2.18(2)	0.40(1)
(b)	+2.14	2.48(1)	−4.7	18	4712	1.09(2)	2.07(3)	0.38(2)
(c)	+2.14	2.69(1)	−0.3	30	9676	1.45(2)	2.16(3)	0.41(2)
(d)	+3.39	3.31(1)	−9.0	6	15150	6.7(2)	3.34(7)	0.14(1)
(e)	+3.39	3.39(1)	−9.0	4	7834	5.1(1)	3.34(7)	0.13(1)
(f)	+3.67	4.32(1)	−13.1	36	19203	2.25(3)	3.55(5)	0.168(8)
(g)	+3.67	4.39(1)	−20.2	18	9888	1.80(3)	3.55(9)	0.13(1)
(h)	+3.81	5.654(6)	+0.0	20	5489	2.09(3)	3.8(1)	0.092(9)
(i)	+3.81	3.322(6)	−0.3	12	21625	4.01(3)	3.96(4)	0.113(4)

C.3. Spectral properties: Truncated wave packet – Section 6.1.3
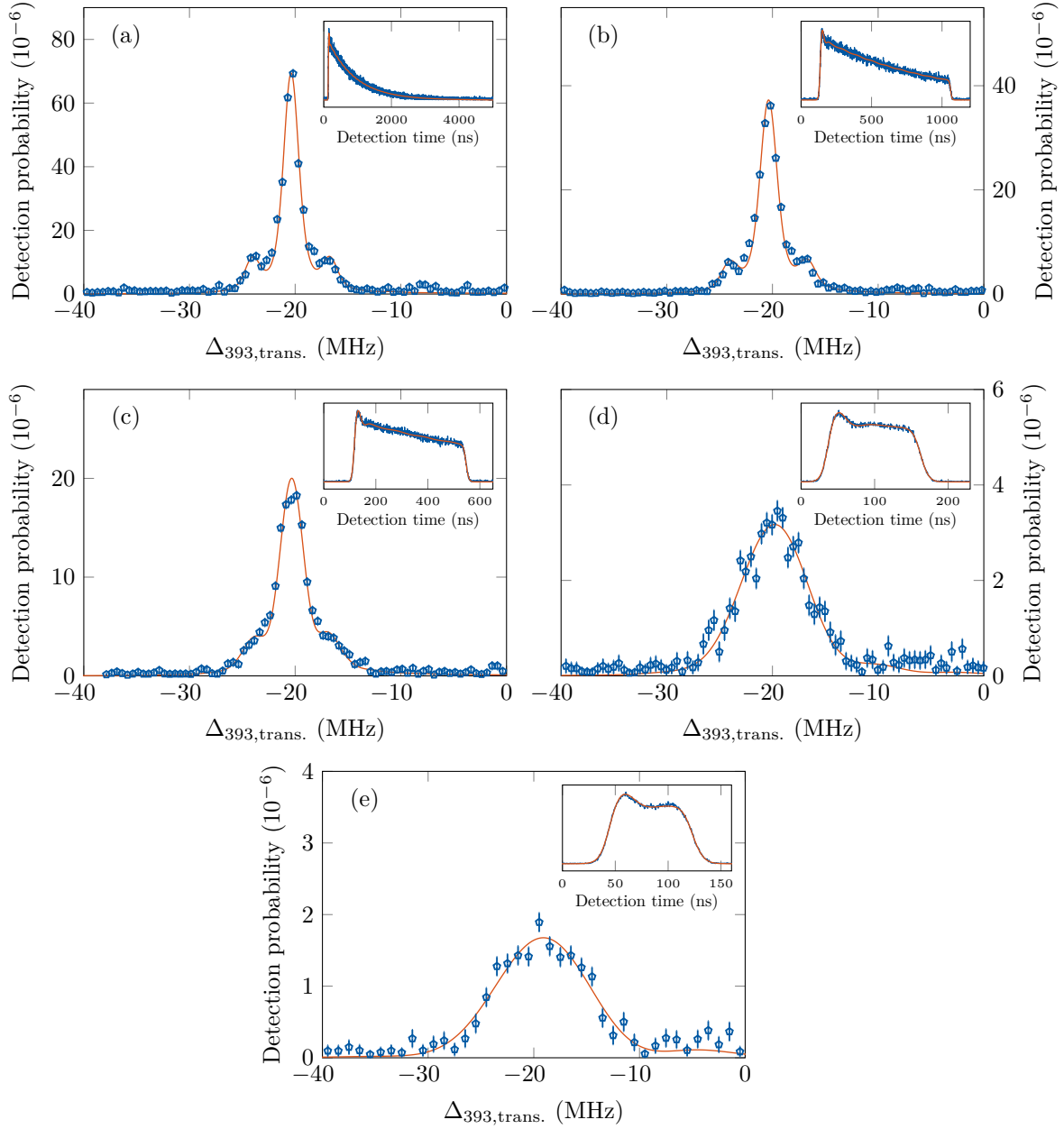
	τ_{pulse}/ns	δ_{b}/MHz	Rep.	Sig.	$\varepsilon/10^{-4}$	$\Delta\nu$/MHz	$\Delta\tau$/µs	tbp	Pop.
(a)	5000	$-0.10(2)$	18	8383	2.11(5)	1.91(4)	0.815(1)	9.8(2)	0.9750
(b)	926(1)	$-0.49(2)$	21	5627	1.85(3)	2.05(3)	0.4202(5)	5.42(8)	0.6609
(c)	429.3(5)	$-0.21(3)$	36	6804	2.19(3)	2.55(5)	0.2146(2)	3.44(6)	0.3903
(d)	125.0(4)	$-0.2(1)$	48	3362	2.58(7)	4.8(2)	0.06839(9)	2.05(8)	0.1061
(e)	78.9(3)	$-0.2(2)$	125	2961	3.5(1)	5.9(3)	0.04496(6)	1.66(9)	0.0541
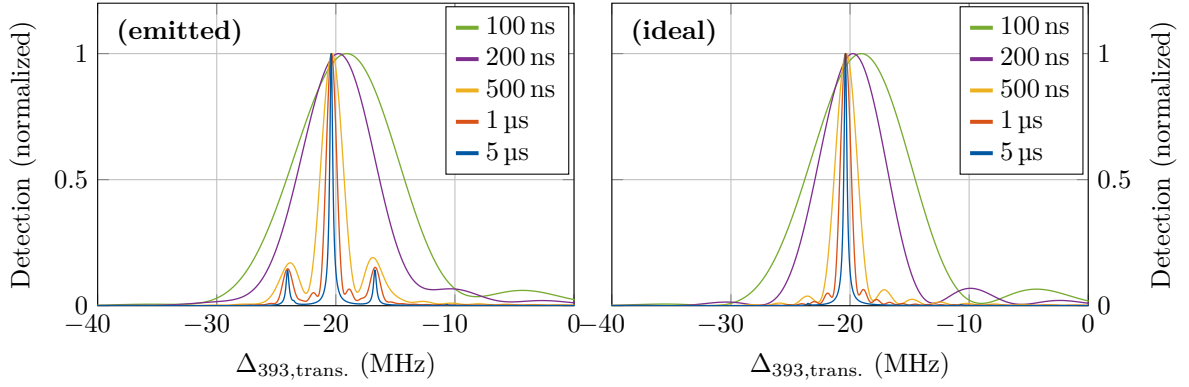
C.4. Quantum interference: bichromatic excitation – Section 6.2.2
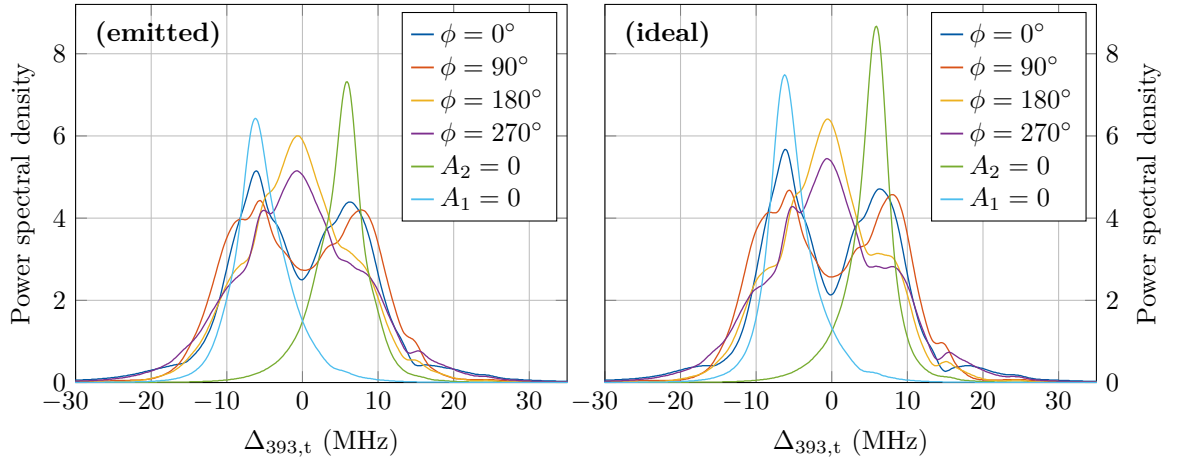
measurement	Ω_t/MHz	$\Delta_\mathrm{t,1}$/MHz	$\Delta_\mathrm{t,2}$/MHz	Rep.	Sig.	$\varepsilon/10^{-4}$
$\phi = 0°$	10.05(1)	+4.86	−5.14	48	11164	2.39(4)
$\phi = 90°$	9.736(9)	+4.93	−5.07	48	11336	2.39(4)
$\phi = 180°$	10.3(1)	+4.80	−5.20	72	13100	1.86(3)
$\phi = 270°$	10.29(4)	+4.82	−5.18	48	11476	2.48(4)
$A_2 = 0$	10.07(1)	+4.89	−5.11	24	4952	1.91(3)
$A_1 = 0$	11.03(3)	+4.98	−5.02	24	6312	2.51(3)

C.5. Quantum interference: Λ-scheme – Section 6.2.3
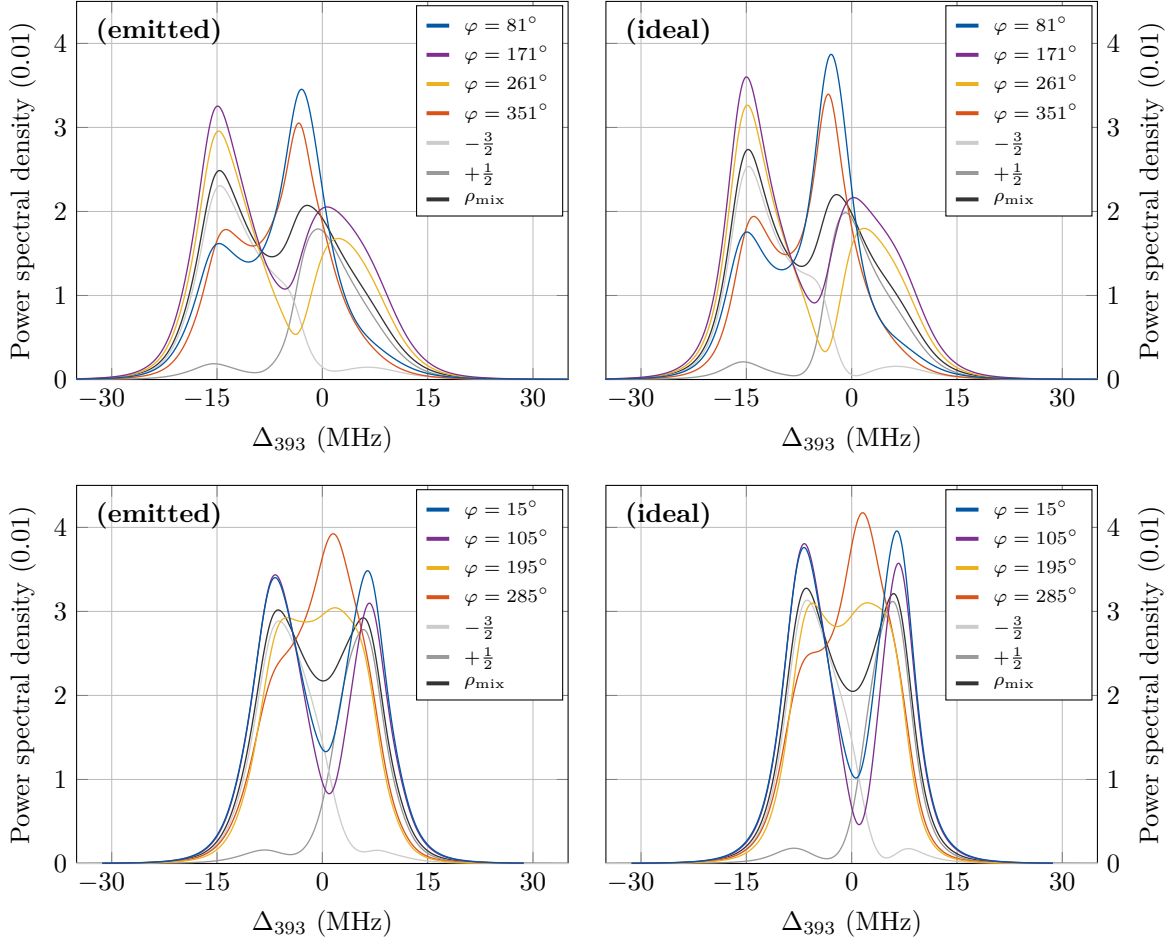
measurement	Ω_m/MHz	Δ_m/MHz	Rep.	Sig.	$\varepsilon/10^{-4}$	Pop.
$\phi = 81°$	26.40(5)	-5.0	36	4955	2.49(9)	0.5093
$\phi = 171°$	26.88(6)	-5.0	36	4559	2.38(7)	0.4871
$\phi = 261°$	26.46(6)	-5.0	36	5392	2.29(8)	0.6127
$\phi = 351°$	24.82(8)	-5.0	30	2997	2.00(7)	0.4483
$\phi = 15°$	18.46(8)	$+0.0$	44	2871	2.17(6)	0.5824
$\phi = 105°$	17.77(3)	$+0.0$	44	2838	2.07(7)	0.6015
$\phi = 195°$	17.79(3)	$+0.0$	44	2530	1.99(9)	0.5476
$\phi = 285°$	16.98(5)	$+0.0$	44	2490	2.00(6)	0.5449

C.6. Quantum interference: V-scheme – Section 6.2.4
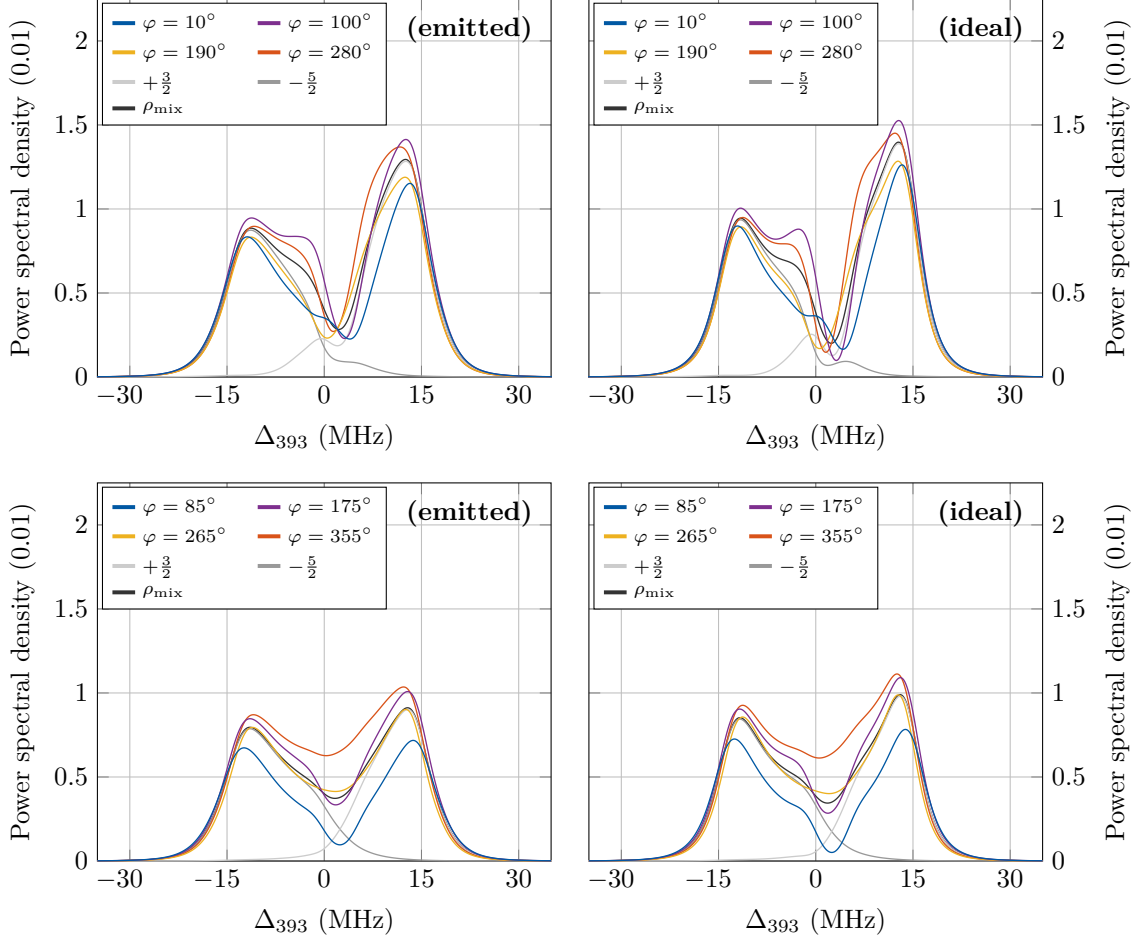
measurement	Ω_{m}/MHz	Δ_{m}/MHz	Rep.	Sig.	$\varepsilon/10^{-4}$	Pop.
$\phi = 10°$	17.37(6)	+0.0	39	1261	2.3(1)	0.2510
$\phi = 100°$	17.97(4)	+0.0	52	1154	1.7(1)	0.2365
$\phi = 190°$	17.75(4)	+0.0	48	1910	2.4(1)	0.3052
$\phi = 280°$	17.40(4)	+0.0	52	2209	2.6(1)	0.2970
$\phi = 85°$	16.81(8)	+0.0	38	910	1.9(2)	0.2167
$\phi = 175°$	18.72(6)	+0.0	38	940	2.6(2)	0.1704
$\phi = 265°$	17.82(4)	+0.0	38	1268	2.5(2)	0.2462
$\phi = 355°$	17.29(4)	+0.0	38	1458	2.6(2)	0.2718

D. Supplementary material to the atom-photon entanglement measurements

In this appendix, I list measurement details of the 393 nm monochromatic, 393 nm bichromatic, and 854 nm bichromatic atom-photon entanglement generation. For each measurement I list the **sequence repetitions**, the **average repetition rate**, the **total photon events**, the (total) **estimated background**, and the (total) **signal events** that were used for the evaluation. Because the background correction is done for each projection basis the difference between signal events and total events may differ from the total estimated background. Furthermore I list the projection events and the inferred probabilities for each measurement basis and finally, the density matrix including the numeric values for each entry reconstructed from these probabilities.

For the 393 nm atom-photon entanglement, for each individual measurement (monochromatic direct detected, monochromatic filtered, ...), I first list the values without background correction and afterwards the background corrected values. In case of the bichromatic 854 nm atom-photon entanglement scheme, I first list the values of both outputs of the Wollaston prism evaluated individually and then values after combining both outputs. No background correction was done in this case. For the 854 nm atom photon entanglement additional projection settings were measured to directly measure the Bell parameter. I additionally list the total sequence repetitions and total signal events for these additional bases.

The estimated probabilities from the bichromatic 854 nm atom-photon entanglement show an imbalance towards either the $|+\frac{3}{2}\rangle$ or $|-\frac{1}{2}\rangle$ state, depending on the output of the Wollaston prism (see Appendix D.3). If the photon events from both sides are taken into account to calculate the estimated probability of the projection, the imbalance vanishes. I could not identify the reason for this imbalance but can exclude a polarization dependent loss, the measurement sequence, the atomic state projection or an electronic artifact.

The density matrices that are displayed in Chapter 7 are found in the following sections of this appendix:

- The numeric values of the density matrix from the 393 nm monochromatic atom-photon entanglement scheme shown in Figure 7.9 are listed in Section D.1.2 and Section D.1.4.

- The numeric values of the density matrix from the 393 nm bichromatic atom-photon entanglement scheme shown in Figure 7.11 are listed in Section D.2.2 and Section D.2.4.

- The numeric values of the density matrix from the 854 nm bichromatic atom-photon entanglement scheme shown in Figure 7.16 are listed in Section D.3.3 and Section D.3.6.

D.1. 393 nm atom-photon entanglement: monochromatic scheme

D.1.1. Unfiltered photons, without background correction

Sequence repetitions:	960 M	
Total photon events:	563062	
Signal events:	**563062**	

Average repetition rate:	14 kHz	
Estimated background:	21019	

	$\lvert+\tfrac{1}{2}\rangle$	$\lvert-\tfrac{1}{2}\rangle$	$\lvert\theta_1\rangle$	$\lvert\theta_2\rangle$	$\lvert\theta_3\rangle$	$\lvert\theta_4\rangle$	$\lvert\theta_5\rangle$	$\lvert\theta_6\rangle$	$\lvert\theta_7\rangle$	$\lvert\theta_8\rangle$	$\lvert\theta_9\rangle$
$\lvert L\rangle$	43473	2136	2263	2154	2167	2130	2208	2085	2105	2248	2279
$\lvert R\rangle$	2931	45638	2533	2396	2468	2313	2319	2247	2221	2278	2390
$\lvert H\rangle$	17547	25889	2104	2674	3212	3519	3845	3902	3767	3705	3363
$\lvert D\rangle$	23956	23846	377	429	625	1047	1538	2231	2753	3334	3983
$\lvert V\rangle$	27799	23231	2604	1936	1329	809	481	381	421	743	1164
$\lvert A\rangle$	22195	22329	4387	3899	3693	3139	2568	1979	1306	866	546

	$\lvert\theta_{10}\rangle$	$\lvert\theta_{11}\rangle$	$\lvert\theta_{12}\rangle$	$\lvert\theta_{13}\rangle$	$\lvert\theta_{14}\rangle$	$\lvert\theta_{15}\rangle$	$\lvert\theta_{16}\rangle$	$\lvert\theta_{17}\rangle$	$\lvert\theta_{18}\rangle$	$\lvert\theta_{19}\rangle$	$\lvert\theta_{20}\rangle$
$\lvert L\rangle$	2417	2413	2352	2359	2423	2412	2390	2358	2393	2289	2234
$\lvert R\rangle$	2490	2546	2590	2709	2633	2615	2717	2722	2709	2711	2548
$\lvert H\rangle$	2792	2347	1724	1187	790	432	376	388	666	1056	1534
$\lvert D\rangle$	4157	4323	4332	4098	3743	3164	2441	1797	1278	781	527
$\lvert V\rangle$	1772	2471	3168	3800	4262	4785	4627	4508	4231	3884	3306
$\lvert A\rangle$	338	359	563	816	1447	1932	2548	3107	3610	3940	4192

	$\lvert+\tfrac{1}{2}\rangle$	$\lvert-\tfrac{1}{2}\rangle$	$\lvert\theta_1\rangle$	$\lvert\theta_2\rangle$	$\lvert\theta_3\rangle$	$\lvert\theta_4\rangle$	$\lvert\theta_5\rangle$	$\lvert\theta_6\rangle$	$\lvert\theta_7\rangle$	$\lvert\theta_8\rangle$	$\lvert\theta_9\rangle$
$\lvert L\rangle$	0.6947	0.0341	0.0362	0.0344	0.0346	0.0341	0.0353	0.0333	0.0337	0.0359	0.0364
$\lvert R\rangle$	0.0469	0.7293	0.0405	0.0383	0.0395	0.0370	0.0371	0.0359	0.0355	0.0364	0.0382
$\lvert H\rangle$	0.2804	0.4137	0.0336	0.0427	0.0513	0.0563	0.0615	0.0624	0.0602	0.0592	0.0538
$\lvert D\rangle$	0.3828	0.3811	0.0060	0.0069	0.0100	0.0167	0.0246	0.0357	0.0440	0.0533	0.0637
$\lvert V\rangle$	0.4443	0.3713	0.0416	0.0310	0.0213	0.0129	0.0077	0.0061	0.0067	0.0119	0.0186
$\lvert A\rangle$	0.3547	0.3568	0.0701	0.0623	0.0590	0.0502	0.0411	0.0316	0.0209	0.0139	0.0087

	$\lvert\theta_{10}\rangle$	$\lvert\theta_{11}\rangle$	$\lvert\theta_{12}\rangle$	$\lvert\theta_{13}\rangle$	$\lvert\theta_{14}\rangle$	$\lvert\theta_{15}\rangle$	$\lvert\theta_{16}\rangle$	$\lvert\theta_{17}\rangle$	$\lvert\theta_{18}\rangle$	$\lvert\theta_{19}\rangle$	$\lvert\theta_{20}\rangle$
$\lvert L\rangle$	0.0386	0.0386	0.0376	0.0377	0.0387	0.0386	0.0382	0.0377	0.0383	0.0366	0.0357
$\lvert R\rangle$	0.0398	0.0407	0.0414	0.0433	0.0421	0.0418	0.0434	0.0435	0.0433	0.0433	0.0407
$\lvert H\rangle$	0.0446	0.0375	0.0276	0.0190	0.0126	0.0069	0.0060	0.0062	0.0107	0.0169	0.0245
$\lvert D\rangle$	0.0664	0.0691	0.0692	0.0655	0.0598	0.0506	0.0390	0.0287	0.0204	0.0125	0.0084
$\lvert V\rangle$	0.0283	0.0395	0.0506	0.0607	0.0681	0.0765	0.0740	0.0721	0.0676	0.0621	0.0528
$\lvert A\rangle$	0.0054	0.0058	0.0090	0.0131	0.0231	0.0309	0.0407	0.0497	0.0577	0.0630	0.0670

Real part

Imaginary part

$\langle\cdot|\rho|\cdot\rangle$	$|+\frac{1}{2},\mathrm{L}\rangle$	$|+\frac{1}{2},\mathrm{R}\rangle$	$|-\frac{1}{2},\mathrm{L}\rangle$	$|-\frac{1}{2},\mathrm{R}\rangle$
$\langle+\frac{1}{2},\mathrm{L}|$	0.458	0.054	-0.015	-0.418
$\langle+\frac{1}{2},\mathrm{R}|$	0.054	0.032	0.002	-0.028
$\langle-\frac{1}{2},\mathrm{L}|$	-0.015	0.002	0.023	-0.013
$\langle-\frac{1}{2},\mathrm{R}|$	-0.418	-0.028	-0.013	0.488

$\langle\cdot|\rho|\cdot\rangle$	$|+\frac{1}{2},\mathrm{L}\rangle$	$|+\frac{1}{2},\mathrm{R}\rangle$	$|-\frac{1}{2},\mathrm{L}\rangle$	$|-\frac{1}{2},\mathrm{R}\rangle$
$\langle+\frac{1}{2},\mathrm{L}|$	0.000	0.006	0.004	-0.067
$\langle+\frac{1}{2},\mathrm{R}|$	-0.006	-0.000	-0.014	-0.004
$\langle-\frac{1}{2},\mathrm{L}|$	-0.004	0.014	-0.000	0.006
$\langle-\frac{1}{2},\mathrm{R}|$	0.067	0.004	-0.006	0.000

D.1.2. Unfiltered photons, with background correction

The numeric values shown here are used to reconstruct the density matrix shown in Figure 7.9. The same density matrix is shown below

Sequence repetitions:	960 M	Average repetition rate:	14 kHz
Total photon events:	563062	Estimated background:	21019
Signal events:	**542043**		

	$\lvert+\tfrac{1}{2}\rangle$	$\lvert-\tfrac{1}{2}\rangle$	$\lvert\theta_1\rangle$	$\lvert\theta_2\rangle$	$\lvert\theta_3\rangle$	$\lvert\theta_4\rangle$	$\lvert\theta_5\rangle$	$\lvert\theta_6\rangle$	$\lvert\theta_7\rangle$	$\lvert\theta_8\rangle$	$\lvert\theta_9\rangle$
$\lvert L\rangle$	42678	1337	2182	2073	2086	2049	2127	2004	2024	2167	2198
$\lvert R\rangle$	1814	44497	2399	2262	2334	2179	2185	2113	2087	2144	2256
$\lvert H\rangle$	16798	25035	2028	2598	3136	3443	3769	3826	3691	3629	3287
$\lvert D\rangle$	23201	22983	299	351	547	969	1460	2153	2675	3256	3905
$\lvert V\rangle$	26984	22391	2520	1852	1245	725	397	297	337	659	1080
$\lvert A\rangle$	21365	21528	4307	3819	3613	3059	2488	1899	1226	786	466

	$\lvert\theta_{10}\rangle$	$\lvert\theta_{11}\rangle$	$\lvert\theta_{12}\rangle$	$\lvert\theta_{13}\rangle$	$\lvert\theta_{14}\rangle$	$\lvert\theta_{15}\rangle$	$\lvert\theta_{16}\rangle$	$\lvert\theta_{17}\rangle$	$\lvert\theta_{18}\rangle$	$\lvert\theta_{19}\rangle$	$\lvert\theta_{20}\rangle$
$\lvert L\rangle$	2336	2332	2271	2278	2342	2331	2309	2277	2312	2208	2153
$\lvert R\rangle$	2356	2412	2456	2575	2499	2481	2583	2588	2575	2577	2414
$\lvert H\rangle$	2716	2271	1648	1111	714	356	300	312	590	980	1458
$\lvert D\rangle$	4079	4245	4254	4020	3665	3086	2363	1719	1200	703	449
$\lvert V\rangle$	1688	2387	3084	3716	4178	4701	4543	4424	4147	3800	3222
$\lvert A\rangle$	258	279	483	736	1367	1852	2468	3027	3530	3860	4112

	$\lvert+\tfrac{1}{2}\rangle$	$\lvert-\tfrac{1}{2}\rangle$	$\lvert\theta_1\rangle$	$\lvert\theta_2\rangle$	$\lvert\theta_3\rangle$	$\lvert\theta_4\rangle$	$\lvert\theta_5\rangle$	$\lvert\theta_6\rangle$	$\lvert\theta_7\rangle$	$\lvert\theta_8\rangle$	$\lvert\theta_9\rangle$
$\lvert L\rangle$	0.7085	0.0222	0.0362	0.0344	0.0347	0.0340	0.0353	0.0333	0.0336	0.0360	0.0365
$\lvert R\rangle$	0.0301	0.7387	0.0398	0.0376	0.0388	0.0362	0.0363	0.0351	0.0347	0.0356	0.0375
$\lvert H\rangle$	0.2789	0.4156	0.0337	0.0431	0.0521	0.0572	0.0626	0.0635	0.0613	0.0603	0.0546
$\lvert D\rangle$	0.3852	0.3815	0.0050	0.0058	0.0091	0.0161	0.0242	0.0357	0.0444	0.0541	0.0648
$\lvert V\rangle$	0.4480	0.3717	0.0418	0.0308	0.0207	0.0120	0.0066	0.0049	0.0056	0.0109	0.0179
$\lvert A\rangle$	0.3547	0.3574	0.0715	0.0634	0.0600	0.0508	0.0413	0.0315	0.0204	0.0131	0.0078

	$\lvert\theta_{10}\rangle$	$\lvert\theta_{11}\rangle$	$\lvert\theta_{12}\rangle$	$\lvert\theta_{13}\rangle$	$\lvert\theta_{14}\rangle$	$\lvert\theta_{15}\rangle$	$\lvert\theta_{16}\rangle$	$\lvert\theta_{17}\rangle$	$\lvert\theta_{18}\rangle$	$\lvert\theta_{19}\rangle$	$\lvert\theta_{20}\rangle$
$\lvert L\rangle$	0.0388	0.0387	0.0377	0.0378	0.0389	0.0387	0.0384	0.0378	0.0384	0.0367	0.0358
$\lvert R\rangle$	0.0391	0.0401	0.0408	0.0428	0.0415	0.0412	0.0429	0.0430	0.0428	0.0428	0.0401
$\lvert H\rangle$	0.0451	0.0377	0.0274	0.0185	0.0119	0.0059	0.0050	0.0052	0.0098	0.0163	0.0242
$\lvert D\rangle$	0.0677	0.0705	0.0706	0.0667	0.0608	0.0512	0.0392	0.0285	0.0199	0.0117	0.0075
$\lvert V\rangle$	0.0280	0.0396	0.0512	0.0617	0.0694	0.0780	0.0754	0.0734	0.0689	0.0631	0.0535
$\lvert A\rangle$	0.0043	0.0046	0.0080	0.0122	0.0227	0.0308	0.0410	0.0503	0.0586	0.0641	0.0683

Real part

Imaginary part

$\langle \cdot \lvert \rho \rvert \cdot \rangle$	$\lvert +\frac{1}{2}, \mathrm{L} \rangle$	$\lvert +\frac{1}{2}, \mathrm{R} \rangle$	$\lvert -\frac{1}{2}, \mathrm{L} \rangle$	$\lvert -\frac{1}{2}, \mathrm{R} \rangle$
$\langle +\frac{1}{2}, \mathrm{L} \rvert$	0.458	0.054	-0.015	-0.418
$\langle +\frac{1}{2}, \mathrm{R} \rvert$	0.054	0.032	0.002	-0.028
$\langle -\frac{1}{2}, \mathrm{L} \rvert$	-0.015	0.002	0.023	-0.013
$\langle -\frac{1}{2}, \mathrm{R} \rvert$	-0.418	-0.028	-0.013	0.488

$\langle \cdot \lvert \rho \rvert \cdot \rangle$	$\lvert +\frac{1}{2}, \mathrm{L} \rangle$	$\lvert +\frac{1}{2}, \mathrm{R} \rangle$	$\lvert -\frac{1}{2}, \mathrm{L} \rangle$	$\lvert -\frac{1}{2}, \mathrm{R} \rangle$
$\langle +\frac{1}{2}, \mathrm{L} \rvert$	0.000	0.006	0.004	-0.067
$\langle +\frac{1}{2}, \mathrm{R} \rvert$	-0.006	-0.000	-0.014	-0.004
$\langle -\frac{1}{2}, \mathrm{L} \rvert$	-0.004	0.014	-0.000	0.006
$\langle -\frac{1}{2}, \mathrm{R} \rvert$	0.067	0.004	-0.006	0.000

D.1.3. Filtered photons, without background correction

Sequence repetitions:	960 M		Average repetition rate:	14 kHz
Total photon events:	17956		Estimated background:	3851
Signal events:	**17956**			

	$\left|+\frac{1}{2}\right\rangle$	$\left|-\frac{1}{2}\right\rangle$	$\left|\theta_1\right\rangle$	$\left|\theta_2\right\rangle$	$\left|\theta_3\right\rangle$	$\left|\theta_4\right\rangle$	$\left|\theta_5\right\rangle$	$\left|\theta_6\right\rangle$	$\left|\theta_7\right\rangle$	$\left|\theta_8\right\rangle$	$\left|\theta_9\right\rangle$
$\left|L\right\rangle$	183	169	12	12	19	21	15	14	16	20	21
$\left|R\right\rangle$	197	2536	131	145	136	152	128	139	120	136	145
$\left|H\right\rangle$	193	1373	73	101	86	90	68	77	86	76	71
$\left|D\right\rangle$	188	1293	64	66	58	66	65	53	75	74	89
$\left|V\right\rangle$	186	1257	68	71	81	72	62	72	78	69	68
$\left|A\right\rangle$	227	1142	81	76	72	72	84	74	76	81	65

	$\left|\theta_{10}\right\rangle$	$\left|\theta_{11}\right\rangle$	$\left|\theta_{12}\right\rangle$	$\left|\theta_{13}\right\rangle$	$\left|\theta_{14}\right\rangle$	$\left|\theta_{15}\right\rangle$	$\left|\theta_{16}\right\rangle$	$\left|\theta_{17}\right\rangle$	$\left|\theta_{18}\right\rangle$	$\left|\theta_{19}\right\rangle$	$\left|\theta_{20}\right\rangle$
$\left|L\right\rangle$	10	15	16	15	14	20	17	16	14	18	20
$\left|R\right\rangle$	127	125	122	140	130	152	139	155	148	124	121
$\left|H\right\rangle$	73	76	75	78	78	74	79	86	69	64	83
$\left|D\right\rangle$	87	74	83	77	74	68	87	48	71	74	73
$\left|V\right\rangle$	74	81	82	85	71	71	76	96	79	82	87
$\left|A\right\rangle$	58	79	65	74	68	62	68	68	71	87	77

	$\left|+\frac{1}{2}\right\rangle$	$\left|-\frac{1}{2}\right\rangle$	$\left|\theta_1\right\rangle$	$\left|\theta_2\right\rangle$	$\left|\theta_3\right\rangle$	$\left|\theta_4\right\rangle$	$\left|\theta_5\right\rangle$	$\left|\theta_6\right\rangle$	$\left|\theta_7\right\rangle$	$\left|\theta_8\right\rangle$	$\left|\theta_9\right\rangle$
$\left|L\right\rangle$	0.0916	0.0846	0.0065	0.0065	0.0100	0.0109	0.0080	0.0075	0.0085	0.0104	0.0109
$\left|R\right\rangle$	0.0985	1.2623	0.0657	0.0726	0.0682	0.0761	0.0642	0.0697	0.0602	0.0682	0.0726
$\left|H\right\rangle$	0.0965	0.6837	0.0368	0.0508	0.0433	0.0453	0.0343	0.0388	0.0433	0.0383	0.0358
$\left|D\right\rangle$	0.0940	0.6439	0.0323	0.0333	0.0294	0.0333	0.0328	0.0269	0.0378	0.0373	0.0448
$\left|V\right\rangle$	0.0930	0.6259	0.0343	0.0358	0.0408	0.0363	0.0313	0.0363	0.0393	0.0348	0.0343
$\left|A\right\rangle$	0.1134	0.5687	0.0408	0.0383	0.0363	0.0363	0.0423	0.0373	0.0383	0.0408	0.0328

	$\left|\theta_{10}\right\rangle$	$\left|\theta_{11}\right\rangle$	$\left|\theta_{12}\right\rangle$	$\left|\theta_{13}\right\rangle$	$\left|\theta_{14}\right\rangle$	$\left|\theta_{15}\right\rangle$	$\left|\theta_{16}\right\rangle$	$\left|\theta_{17}\right\rangle$	$\left|\theta_{18}\right\rangle$	$\left|\theta_{19}\right\rangle$	$\left|\theta_{20}\right\rangle$
$\left|L\right\rangle$	0.0055	0.0080	0.0085	0.0080	0.0075	0.0104	0.0090	0.0085	0.0075	0.0095	0.0104
$\left|R\right\rangle$	0.0637	0.0627	0.0612	0.0702	0.0652	0.0761	0.0697	0.0776	0.0741	0.0622	0.0607
$\left|H\right\rangle$	0.0368	0.0383	0.0378	0.0393	0.0393	0.0373	0.0398	0.0433	0.0348	0.0323	0.0418
$\left|D\right\rangle$	0.0438	0.0373	0.0418	0.0388	0.0373	0.0343	0.0438	0.0244	0.0358	0.0373	0.0368
$\left|V\right\rangle$	0.0373	0.0408	0.0413	0.0428	0.0358	0.0358	0.0383	0.0483	0.0398	0.0413	0.0438
$\left|A\right\rangle$	0.0294	0.0398	0.0328	0.0373	0.0343	0.0313	0.0343	0.0343	0.0358	0.0438	0.0388

Real part

Imaginary part
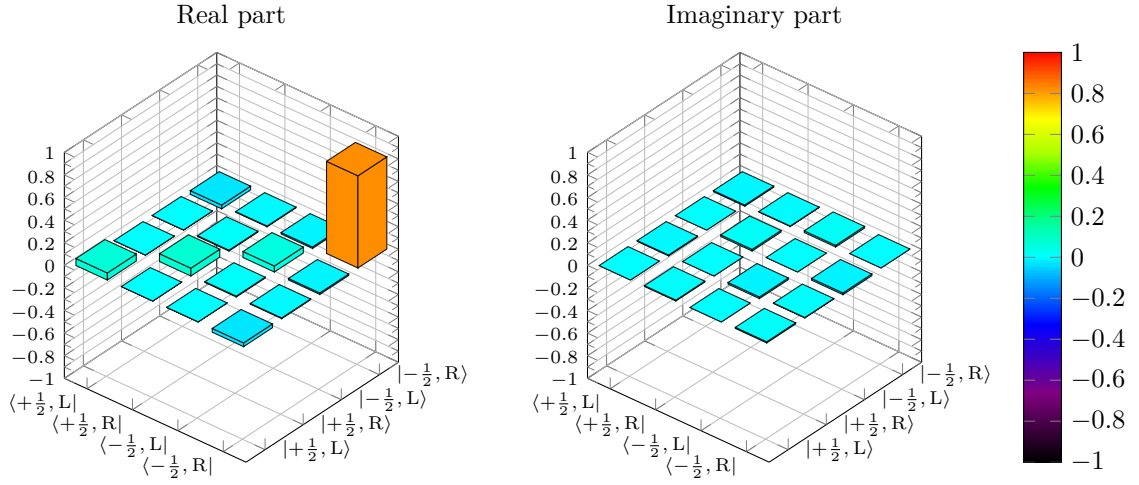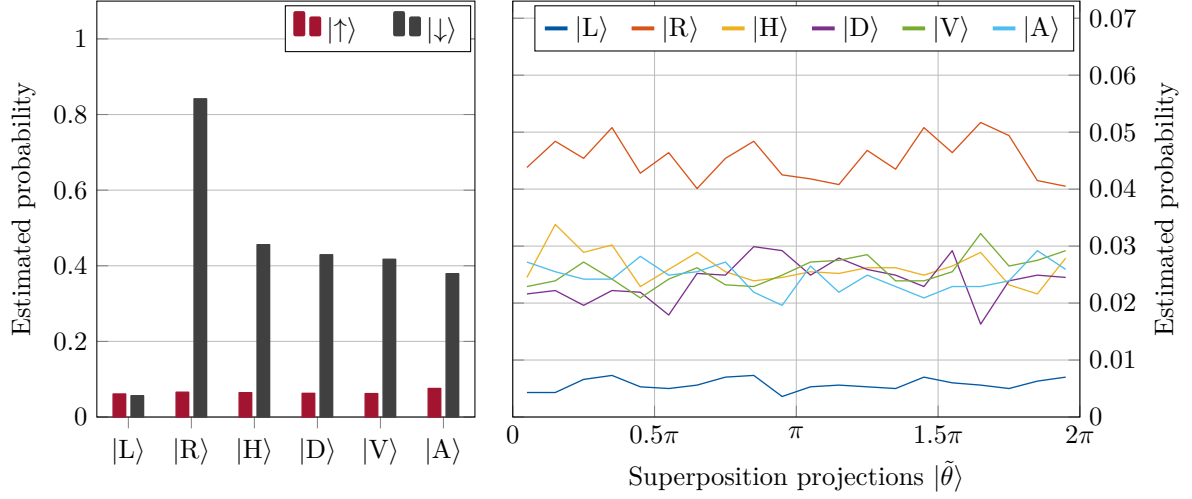
$\langle\cdot|\rho|\cdot\rangle$	$|+\frac{1}{2},\mathrm{L}\rangle$	$|+\frac{1}{2},\mathrm{R}\rangle$	$|-\frac{1}{2},\mathrm{L}\rangle$	$|-\frac{1}{2},\mathrm{R}\rangle$
$\langle+\frac{1}{2},\mathrm{L}|$	0.062	−0.000	0.001	−0.033
$\langle+\frac{1}{2},\mathrm{R}|$	−0.000	0.069	0.007	−0.006
$\langle-\frac{1}{2},\mathrm{L}|$	0.001	0.007	0.053	−0.013
$\langle-\frac{1}{2},\mathrm{R}|$	−0.033	−0.006	−0.013	0.816

$\langle\cdot|\rho|\cdot\rangle$	$|+\frac{1}{2},\mathrm{L}\rangle$	$|+\frac{1}{2},\mathrm{R}\rangle$	$|-\frac{1}{2},\mathrm{L}\rangle$	$|-\frac{1}{2},\mathrm{R}\rangle$
$\langle+\frac{1}{2},\mathrm{L}|$	−0.000	−0.008	0.000	−0.010
$\langle+\frac{1}{2},\mathrm{R}|$	0.008	0.000	0.014	−0.004
$\langle-\frac{1}{2},\mathrm{L}|$	−0.000	−0.014	0.000	0.015
$\langle-\frac{1}{2},\mathrm{R}|$	0.010	0.004	−0.015	−0.000

D.1.4. Filtered photons, with background correction

The numeric values shown here are used to reconstruct the density matrix shown in Figure 7.9. The same density matrix is shown below

Sequence repetitions:	960 M	Average repetition rate:	14 kHz
Total photon events:	17956	Estimated background:	3851
Signal events:	**14383**		

	$\left|+\frac{1}{2}\right\rangle$	$\left|-\frac{1}{2}\right\rangle$	$\left|\theta_1\right\rangle$	$\left|\theta_2\right\rangle$	$\left|\theta_3\right\rangle$	$\left|\theta_4\right\rangle$	$\left|\theta_5\right\rangle$	$\left|\theta_6\right\rangle$	$\left|\theta_7\right\rangle$	$\left|\theta_8\right\rangle$	$\left|\theta_9\right\rangle$
$\left|L\right\rangle$	69	49	2	2	5	8	3	3	3	5	6
$\left|R\right\rangle$	64	2358	116	130	121	137	113	124	105	121	130
$\left|H\right\rangle$	70	1203	58	86	71	75	53	62	71	61	56
$\left|D\right\rangle$	53	1122	47	49	41	49	48	36	58	57	72
$\left|V\right\rangle$	67	1096	52	55	65	56	46	56	62	53	52
$\left|A\right\rangle$	95	992	63	58	54	54	66	56	58	63	47

	$\left|\theta_{10}\right\rangle$	$\left|\theta_{11}\right\rangle$	$\left|\theta_{12}\right\rangle$	$\left|\theta_{13}\right\rangle$	$\left|\theta_{14}\right\rangle$	$\left|\theta_{15}\right\rangle$	$\left|\theta_{16}\right\rangle$	$\left|\theta_{17}\right\rangle$	$\left|\theta_{18}\right\rangle$	$\left|\theta_{19}\right\rangle$	$\left|\theta_{20}\right\rangle$
$\left|L\right\rangle$	2	3	3	3	4	5	4	4	3	4	6
$\left|R\right\rangle$	112	110	107	125	115	137	124	140	133	109	106
$\left|H\right\rangle$	58	61	60	63	63	59	64	71	54	49	68
$\left|D\right\rangle$	70	57	66	60	57	51	70	31	54	57	56
$\left|V\right\rangle$	58	65	66	69	55	55	60	80	63	66	71
$\left|A\right\rangle$	40	61	47	56	50	44	50	50	53	69	59

	$\left|+\frac{1}{2}\right\rangle$	$\left|-\frac{1}{2}\right\rangle$	$\left|\theta_1\right\rangle$	$\left|\theta_2\right\rangle$	$\left|\theta_3\right\rangle$	$\left|\theta_4\right\rangle$	$\left|\theta_5\right\rangle$	$\left|\theta_6\right\rangle$	$\left|\theta_7\right\rangle$	$\left|\theta_8\right\rangle$	$\left|\theta_9\right\rangle$
$\left|L\right\rangle$	0.0434	0.0308	0.0021	0.0021	0.0038	0.0054	0.0026	0.0023	0.0027	0.0040	0.0045
$\left|R\right\rangle$	0.0403	1.4604	0.0727	0.0813	0.0758	0.0857	0.0708	0.0776	0.0659	0.0758	0.0813
$\left|H\right\rangle$	0.0438	0.7454	0.0368	0.0541	0.0449	0.0473	0.0337	0.0393	0.0449	0.0387	0.0356
$\left|D\right\rangle$	0.0337	0.6952	0.0296	0.0308	0.0258	0.0308	0.0302	0.0228	0.0364	0.0358	0.0450
$\left|V\right\rangle$	0.0418	0.6791	0.0329	0.0348	0.0410	0.0354	0.0292	0.0354	0.0391	0.0336	0.0329
$\left|A\right\rangle$	0.0594	0.6147	0.0398	0.0367	0.0342	0.0342	0.0416	0.0354	0.0367	0.0398	0.0299

	$\left|\theta_{10}\right\rangle$	$\left|\theta_{11}\right\rangle$	$\left|\theta_{12}\right\rangle$	$\left|\theta_{13}\right\rangle$	$\left|\theta_{14}\right\rangle$	$\left|\theta_{15}\right\rangle$	$\left|\theta_{16}\right\rangle$	$\left|\theta_{17}\right\rangle$	$\left|\theta_{18}\right\rangle$	$\left|\theta_{19}\right\rangle$	$\left|\theta_{20}\right\rangle$
$\left|L\right\rangle$	0.0016	0.0025	0.0027	0.0025	0.0030	0.0039	0.0034	0.0030	0.0025	0.0033	0.0042
$\left|R\right\rangle$	0.0702	0.0690	0.0671	0.0783	0.0721	0.0857	0.0776	0.0875	0.0832	0.0683	0.0665
$\left|H\right\rangle$	0.0368	0.0387	0.0380	0.0399	0.0399	0.0374	0.0405	0.0449	0.0343	0.0312	0.0430
$\left|D\right\rangle$	0.0438	0.0358	0.0413	0.0376	0.0358	0.0320	0.0438	0.0197	0.0339	0.0358	0.0351
$\left|V\right\rangle$	0.0366	0.0410	0.0416	0.0435	0.0348	0.0348	0.0379	0.0503	0.0397	0.0416	0.0447
$\left|A\right\rangle$	0.0255	0.0385	0.0299	0.0354	0.0317	0.0280	0.0317	0.0317	0.0336	0.0435	0.0373

Real part

Imaginary part
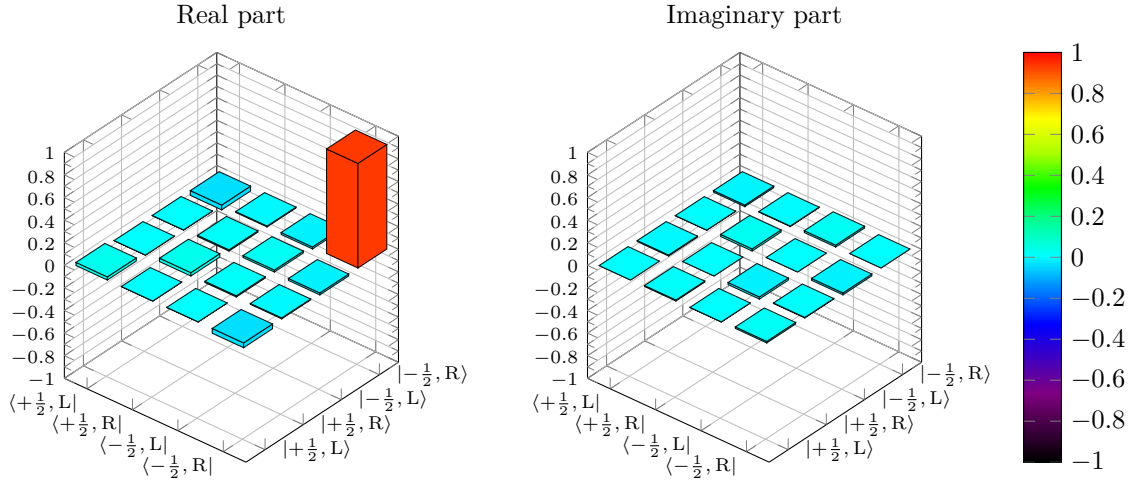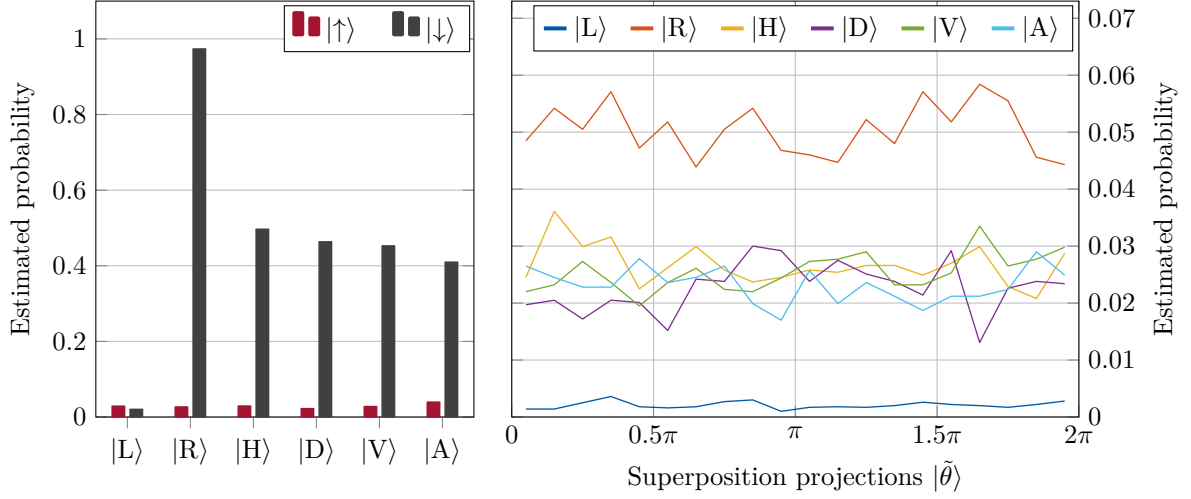
$\langle\cdot|\rho|\cdot\rangle$	$|+\frac{1}{2},\mathrm{L}\rangle$	$|+\frac{1}{2},\mathrm{R}\rangle$	$|-\frac{1}{2},\mathrm{L}\rangle$	$|-\frac{1}{2},\mathrm{R}\rangle$
$\langle+\frac{1}{2},\mathrm{L}|$	0.028	−0.000	0.001	−0.042
$\langle+\frac{1}{2},\mathrm{R}|$	−0.000	0.030	0.011	−0.008
$\langle-\frac{1}{2},\mathrm{L}|$	0.001	0.011	0.017	−0.017
$\langle-\frac{1}{2},\mathrm{R}|$	−0.042	−0.008	−0.017	0.925

$\langle\cdot|\rho|\cdot\rangle$	$|+\frac{1}{2},\mathrm{L}\rangle$	$|+\frac{1}{2},\mathrm{R}\rangle$	$|-\frac{1}{2},\mathrm{L}\rangle$	$|-\frac{1}{2},\mathrm{R}\rangle$
$\langle+\frac{1}{2},\mathrm{L}|$	−0.000	−0.009	−0.001	−0.013
$\langle+\frac{1}{2},\mathrm{R}|$	0.009	0.000	0.019	−0.004
$\langle-\frac{1}{2},\mathrm{L}|$	0.001	−0.019	0.000	0.016
$\langle-\frac{1}{2},\mathrm{R}|$	0.013	0.004	−0.016	−0.000

D.2. 393 nm atom-photon entanglement: bichromatic scheme

D.2.1. Unfiltered photons, without background correction

	$|+\frac{1}{2}\rangle$	$|-\frac{1}{2}\rangle$	$|-\rangle$	$|+\rangle$	$|-i\rangle$	$|+i\rangle$
$|A\rangle$	16669	17460	18600	15761	7939	26350
$|D\rangle$	18339	18360	19187	17656	27570	8758
$|V\rangle$	20565	17048	29569	8809	18283	19880
$|H\rangle$	13808	19241	7841	24365	16891	15965
$|R\rangle$	2399	33860	19213	16965	18571	18290
$|L\rangle$	32411	2142	18009	16085	17328	17530

Sequence repetitions: 1080 M

Average repetition rate: 14 kHz

Total photon events: 637717

Estimated background: 40603

Signal events: **637717**

$|A\rangle$	0.235	0.246	0.262	0.222	0.112	0.372
$|D\rangle$	0.259	0.259	0.271	0.249	0.389	0.124
$|V\rangle$	0.290	0.241	0.417	0.124	0.258	0.281
$|H\rangle$	0.195	0.272	0.111	0.344	0.238	0.225
$|R\rangle$	0.034	0.478	0.271	0.239	0.262	0.258
$|L\rangle$	0.457	0.030	0.254	0.227	0.245	0.247
	$|+\frac{1}{2}\rangle$	$|-\frac{1}{2}\rangle$	$|-\rangle$	$|+\rangle$	$|-i\rangle$	$|+i\rangle$
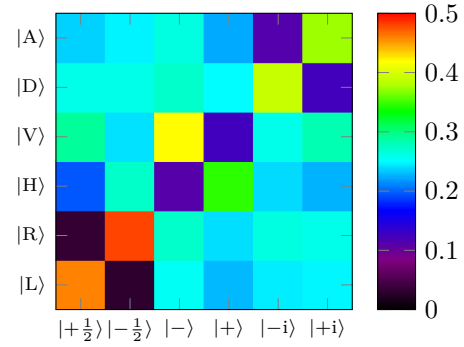
Real part
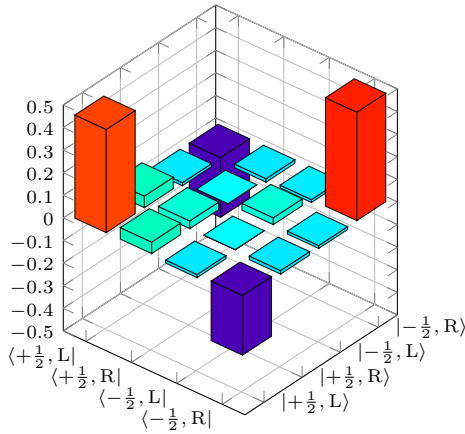
Imaginary part
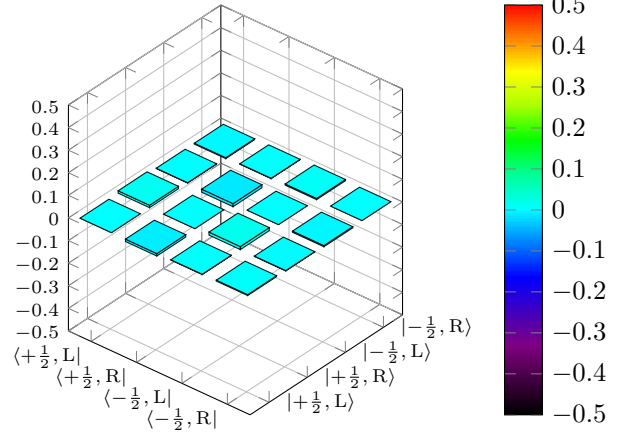
$\langle\cdot|\rho|\cdot\rangle$	$|+\frac{1}{2},L\rangle$	$|+\frac{1}{2},R\rangle$	$|-\frac{1}{2},L\rangle$	$|-\frac{1}{2},R\rangle$
$\langle+\frac{1}{2},L|$	0.456	0.051	−0.013	−0.264
$\langle+\frac{1}{2},R|$	0.051	0.034	−0.000	−0.016
$\langle-\frac{1}{2},L|$	−0.013	−0.000	0.030	−0.013
$\langle-\frac{1}{2},R|$	−0.264	−0.016	−0.013	0.479

$\langle\cdot|\rho|\cdot\rangle$	$|+\frac{1}{2},L\rangle$	$|+\frac{1}{2},R\rangle$	$|-\frac{1}{2},L\rangle$	$|-\frac{1}{2},R\rangle$
$\langle+\frac{1}{2},L|$	−0.000	0.011	−0.002	−0.004
$\langle+\frac{1}{2},R|$	−0.011	0.000	−0.013	0.002
$\langle-\frac{1}{2},L|$	0.002	0.013	−0.000	0.005
$\langle-\frac{1}{2},R|$	0.004	−0.002	−0.005	0.000

D.2.2. Unfiltered photons, with background correction

The numeric values shown here are used to reconstruct the density matrix shown in Figure 7.11. The same density matrix is shown below

	$|+\frac{1}{2}\rangle$	$|-\frac{1}{2}\rangle$	$|-\rangle$	$|+\rangle$	$|-\mathrm{i}\rangle$	$|+\mathrm{i}\rangle$
$|A\rangle$	15671	16240	17503	14711	6845	25341
$|D\rangle$	17275	17246	18082	16496	26309	7725
$|V\rangle$	19374	15902	28401	7655	17263	18737
$|H\rangle$	12692	18177	6681	23167	15709	14751
$|R\rangle$	1382	32651	18151	15805	17414	17213
$|L\rangle$	31268	963	16893	14936	16152	16329

Sequence repetitions: 1080 M

Average repetition rate: 14 kHz

Total photon events: 637717

Estimated background: 40603

Signal events: 597110

$|A\rangle$	0.236	0.245	0.264	0.222	0.103	0.382
$|D\rangle$	0.260	0.260	0.273	0.249	0.397	0.116
$|V\rangle$	0.292	0.240	0.428	0.115	0.260	0.282
$|H\rangle$	0.191	0.274	0.101	0.349	0.237	0.222
$|R\rangle$	0.021	0.492	0.274	0.238	0.262	0.259
$|L\rangle$	0.471	0.015	0.255	0.225	0.243	0.246
	$|+\frac{1}{2}\rangle$	$|-\frac{1}{2}\rangle$	$|-\rangle$	$|+\rangle$	$|-\mathrm{i}\rangle$	$|+\mathrm{i}\rangle$

Real part

Imaginary part
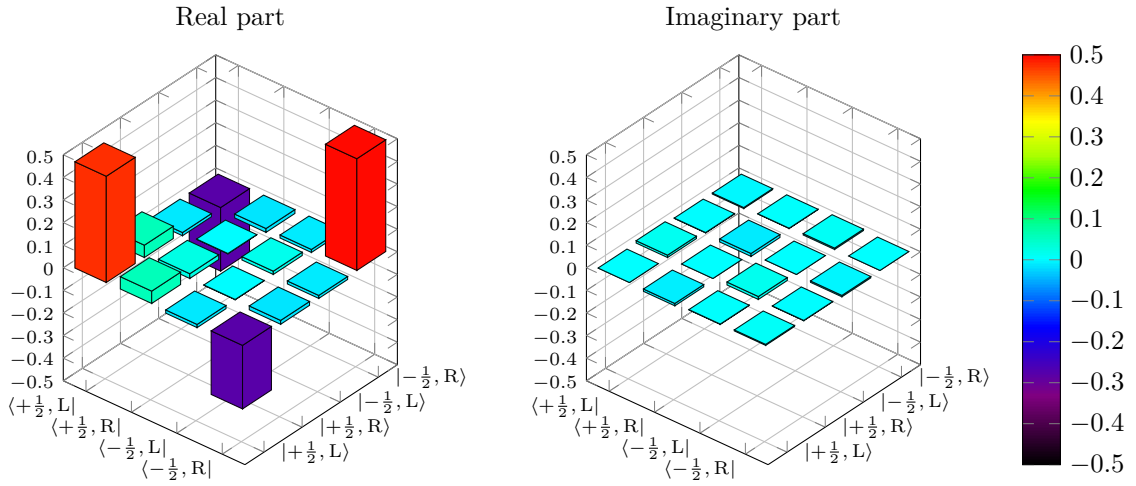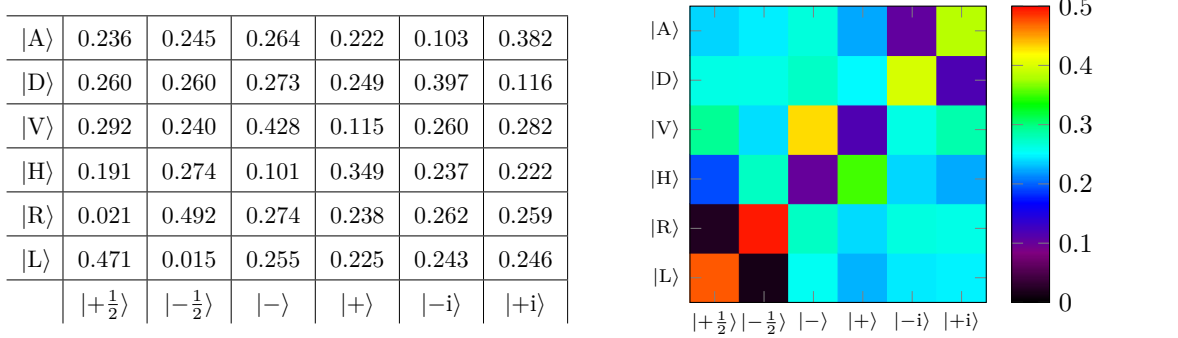
$\langle\cdot|\rho|\cdot\rangle$	$|+\frac{1}{2},L\rangle$	$|+\frac{1}{2},R\rangle$	$|-\frac{1}{2},L\rangle$	$|-\frac{1}{2},R\rangle$
$\langle+\frac{1}{2},L|$	0.470	0.055	−0.014	−0.281
$\langle+\frac{1}{2},R|$	0.055	0.021	−0.001	−0.017
$\langle-\frac{1}{2},L|$	−0.014	−0.001	0.015	−0.013
$\langle-\frac{1}{2},R|$	−0.281	−0.017	−0.013	0.494

$\langle\cdot|\rho|\cdot\rangle$	$|+\frac{1}{2},L\rangle$	$|+\frac{1}{2},R\rangle$	$|-\frac{1}{2},L\rangle$	$|-\frac{1}{2},R\rangle$
$\langle+\frac{1}{2},L|$	−0.000	0.010	−0.002	−0.004
$\langle+\frac{1}{2},R|$	−0.010	0.000	−0.013	0.001
$\langle-\frac{1}{2},L|$	0.002	0.013	−0.000	0.006
$\langle-\frac{1}{2},R|$	0.004	−0.001	−0.006	−0.000

D.2.3. Filtered photons, without background correction

	$|+\frac{1}{2}\rangle$	$|-\frac{1}{2}\rangle$	$|-\rangle$	$|+\rangle$	$|-i\rangle$	$|+i\rangle$
$|A\rangle$	745	813	784	735	171	1307
$|D\rangle$	808	708	808	768	1223	206
$|V\rangle$	783	697	1329	168	718	738
$|H\rangle$	668	733	180	1284	764	750
$|R\rangle$	153	1347	718	702	714	782
$|L\rangle$	1291	176	811	749	733	775

Sequence repetitions: 1080 M

Average repetition rate: 14 kHz

Total photon events: 26839

Estimated background: 4956

Signal events: **26839**

$|A\rangle$	0.250	0.273	0.263	0.246	0.058	0.438
$|D\rangle$	0.271	0.237	0.271	0.258	0.410	0.069
$|V\rangle$	0.263	0.234	0.445	0.057	0.241	0.247
$|H\rangle$	0.224	0.246	0.061	0.430	0.256	0.251
$|R\rangle$	0.052	0.451	0.241	0.235	0.239	0.262
$|L\rangle$	0.433	0.059	0.272	0.251	0.246	0.260
	$|+\frac{1}{2}\rangle$	$|-\frac{1}{2}\rangle$	$|-\rangle$	$|+\rangle$	$|-i\rangle$	$|+i\rangle$

Real part

Imaginary part
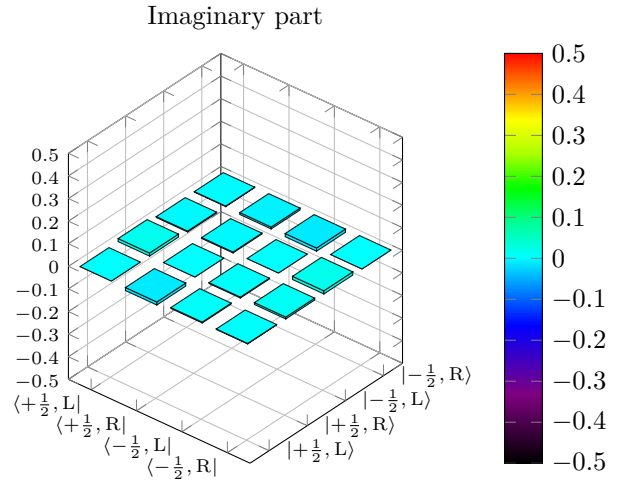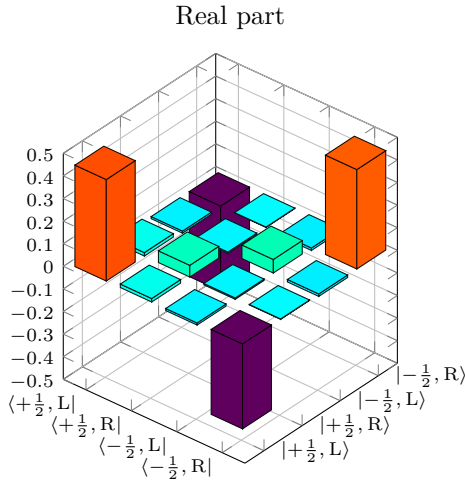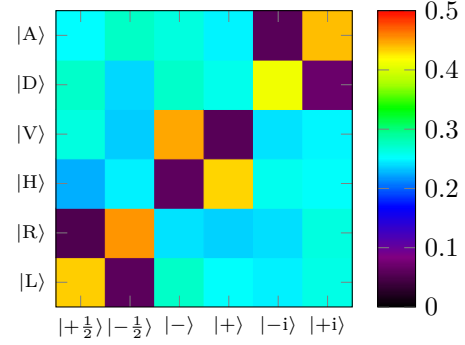
$\langle\cdot|\rho|\cdot\rangle$	$|+\frac{1}{2},L\rangle$	$|+\frac{1}{2},R\rangle$	$|-\frac{1}{2},L\rangle$	$|-\frac{1}{2},R\rangle$
$\langle+\frac{1}{2},L|$	0.449	0.015	−0.009	−0.376
$\langle+\frac{1}{2},R|$	0.015	0.052	−0.006	−0.002
$\langle-\frac{1}{2},L|$	−0.009	−0.006	0.060	−0.011
$\langle-\frac{1}{2},R|$	−0.376	−0.002	−0.011	0.440

$\langle\cdot|\rho|\cdot\rangle$	$|+\frac{1}{2},L\rangle$	$|+\frac{1}{2},R\rangle$	$|-\frac{1}{2},L\rangle$	$|-\frac{1}{2},R\rangle$
$\langle+\frac{1}{2},L|$	0.000	0.013	−0.004	−0.002
$\langle+\frac{1}{2},R|$	−0.013	0.000	−0.004	−0.008
$\langle-\frac{1}{2},L|$	0.004	0.004	0.000	−0.014
$\langle-\frac{1}{2},R|$	0.002	0.008	0.014	−0.000

D.2.4. Filtered photons, with background correction

The numeric values shown here are used to reconstruct the density matrix shown in Figure 7.11. The same density matrix is shown below

Sequence repetitions: 1080 M
Average repetition rate: 14 kHz
Total photon events: 26839
Estimated background: 4956
Signal events: **21891**

	$\lvert+\tfrac{1}{2}\rangle$	$\lvert-\tfrac{1}{2}\rangle$	$\lvert-\rangle$	$\lvert+\rangle$	$\lvert-\mathrm{i}\rangle$	$\lvert+\mathrm{i}\rangle$
$\lvert A\rangle$	632	656	663	601	35	1184
$\lvert D\rangle$	708	595	666	620	1093	39
$\lvert V\rangle$	660	553	1172	8	599	600
$\lvert H\rangle$	558	593	55	1144	628	603
$\lvert R\rangle$	20	1215	578	554	557	626
$\lvert L\rangle$	1143	38	664	597	593	641

$\lvert A\rangle$	0.260	0.270	0.273	0.247	0.015	0.486
$\lvert D\rangle$	0.291	0.245	0.274	0.255	0.449	0.016
$\lvert V\rangle$	0.271	0.227	0.481	0.004	0.246	0.247
$\lvert H\rangle$	0.229	0.244	0.023	0.470	0.258	0.248
$\lvert R\rangle$	0.009	0.499	0.238	0.228	0.229	0.257
$\lvert L\rangle$	0.470	0.016	0.273	0.245	0.244	0.264
	$\lvert+\tfrac{1}{2}\rangle$	$\lvert-\tfrac{1}{2}\rangle$	$\lvert-\rangle$	$\lvert+\rangle$	$\lvert-\mathrm{i}\rangle$	$\lvert+\mathrm{i}\rangle$

Real part

Imaginary part

$\langle\cdot\lvert\rho\rvert\cdot\rangle$	$\lvert+\tfrac{1}{2},L\rangle$	$\lvert+\tfrac{1}{2},R\rangle$	$\lvert-\tfrac{1}{2},L\rangle$	$\lvert-\tfrac{1}{2},R\rangle$
$\langle+\tfrac{1}{2},L\rvert$	0.498	0.011	−0.011	−0.470
$\langle+\tfrac{1}{2},R\rvert$	0.011	0.009	−0.003	−0.009
$\langle-\tfrac{1}{2},L\rvert$	−0.011	−0.003	0.016	−0.011
$\langle-\tfrac{1}{2},R\rvert$	−0.470	−0.009	−0.011	0.477

$\langle\cdot\lvert\rho\rvert\cdot\rangle$	$\lvert+\tfrac{1}{2},L\rangle$	$\lvert+\tfrac{1}{2},R\rangle$	$\lvert-\tfrac{1}{2},L\rangle$	$\lvert-\tfrac{1}{2},R\rangle$
$\langle+\tfrac{1}{2},L\rvert$	−0.000	0.007	−0.006	−0.001
$\langle+\tfrac{1}{2},R\rvert$	−0.007	−0.000	0.002	−0.001
$\langle-\tfrac{1}{2},L\rvert$	0.006	−0.002	0.000	−0.011
$\langle-\tfrac{1}{2},R\rvert$	0.001	0.001	0.011	0.000

D.3. 854 nm atom-photon entanglement: bichromatic scheme

D.3.1. Unfiltered photons, Wollaston prism output 1

	Sequence repetitions APE:	297 M
Sequence repetitions BELL:	132 M
Average repetition rate:	57 kHz
Total photon events:	225809
Signal events APE:	**158410**
Signal events BELL:	**67399**

	$|+\tfrac{3}{2}\rangle$	$|-\tfrac{1}{2}\rangle$	$|-\rangle$	$|+\rangle$	$|-\mathrm{i}\rangle$	$|+\mathrm{i}\rangle$
$|A\rangle$	6798	2367	4542	4450	6219	2924
$|D\rangle$	6801	2549	4137	4908	2687	6231
$|V\rangle$	6645	2542	2667	6175	4432	4227
$|H\rangle$	6943	2359	6143	2695	4281	4685
$|R\rangle$	93	5390	2325	2971	2743	2589
$|L\rangle$	11577	109	5719	5328	5512	5647

$|A\rangle$	0.386	0.135	0.258	0.253	0.353	0.166
$|D\rangle$	0.386	0.145	0.235	0.279	0.153	0.354
$|V\rangle$	0.378	0.144	0.152	0.351	0.252	0.240
$|H\rangle$	0.394	0.134	0.349	0.153	0.243	0.266
$|R\rangle$	0.005	0.306	0.132	0.169	0.156	0.147
$|L\rangle$	0.658	0.006	0.325	0.303	0.313	0.321
	$|+\tfrac{3}{2}\rangle$	$|-\tfrac{1}{2}\rangle$	$|-\rangle$	$|+\rangle$	$|-\mathrm{i}\rangle$	$|+\mathrm{i}\rangle$
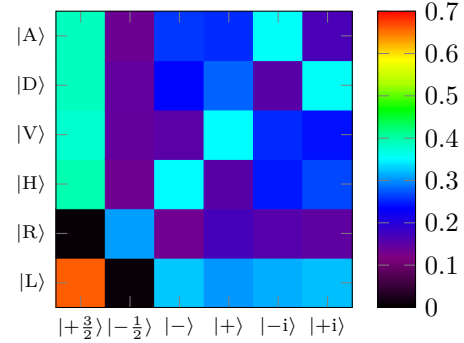
Real part
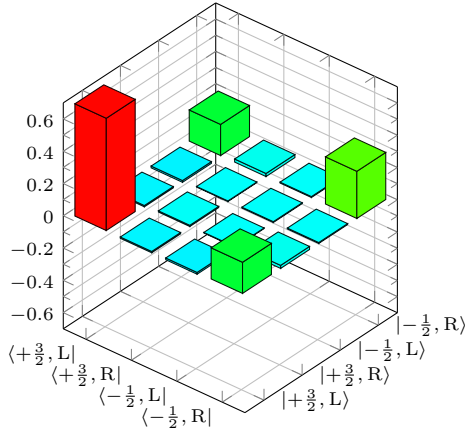
Imaginary part
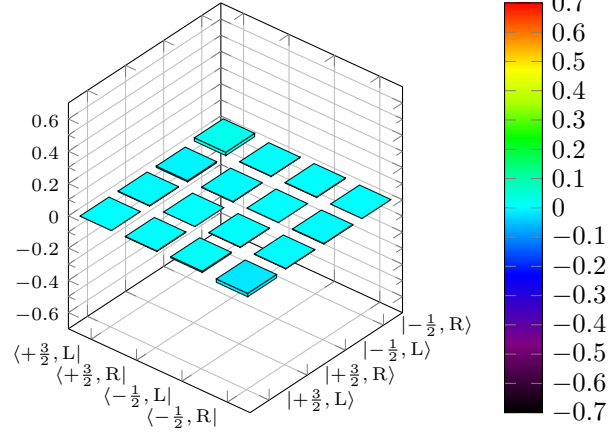
$\langle\cdot|\rho|\cdot\rangle$	$|+\tfrac{3}{2},\mathrm{L}\rangle$	$|+\tfrac{3}{2},\mathrm{R}\rangle$	$|-\tfrac{1}{2},\mathrm{L}\rangle$	$|-\tfrac{1}{2},\mathrm{R}\rangle$
$\langle+\tfrac{3}{2},\mathrm{L}|$	0.696	−0.008	−0.011	0.193
$\langle+\tfrac{3}{2},\mathrm{R}|$	−0.008	0.007	0.004	0.019
$\langle-\tfrac{1}{2},\mathrm{L}|$	−0.011	0.004	0.005	0.005
$\langle-\tfrac{1}{2},\mathrm{R}|$	0.193	0.019	0.005	0.292

$\langle\cdot|\rho|\cdot\rangle$	$|+\tfrac{3}{2},\mathrm{L}\rangle$	$|+\tfrac{3}{2},\mathrm{R}\rangle$	$|-\tfrac{1}{2},\mathrm{L}\rangle$	$|-\tfrac{1}{2},\mathrm{R}\rangle$
$\langle+\tfrac{3}{2},\mathrm{L}|$	0.000	−0.004	−0.008	0.021
$\langle+\tfrac{3}{2},\mathrm{R}|$	0.004	0.000	−0.003	0.003
$\langle-\tfrac{1}{2},\mathrm{L}|$	0.008	0.003	0.000	0.004
$\langle-\tfrac{1}{2},\mathrm{R}|$	−0.021	−0.003	−0.004	0.000

D.3.2. Unfiltered photons, Wollaston prism output 2

	$\vert+\frac{3}{2}\rangle$	$\vert-\frac{1}{2}\rangle$	$\vert-\rangle$	$\vert+\rangle$	$\vert-i\rangle$	$\vert+i\rangle$
$\vert A\rangle$	4185	2888	3553	3254	4691	2000
$\vert D\rangle$	3847	3017	3209	3424	1774	4897
$\vert V\rangle$	4007	2914	1863	4933	3442	3265
$\vert H\rangle$	4164	2782	4975	1899	3356	3486
$\vert R\rangle$	42	4978	2225	2765	2374	2485
$\vert L\rangle$	9015	56	4333	4061	4278	4358

Sequence repetitions APE: 297 M

Sequence repetitions BELL: 132 M

Average repetition rate: 57 kHz

Total photon events: 174541

Signal events APE: 122795

Signal events BELL: 51746

$\vert A\rangle$	0.307	0.212	0.260	0.238	0.344	0.147
$\vert D\rangle$	0.282	0.221	0.235	0.251	0.130	0.359
$\vert V\rangle$	0.294	0.214	0.137	0.362	0.252	0.239
$\vert H\rangle$	0.305	0.204	0.365	0.139	0.246	0.255
$\vert R\rangle$	0.003	0.365	0.163	0.203	0.174	0.182
$\vert L\rangle$	0.661	0.004	0.318	0.298	0.314	0.319
	$\vert+\frac{3}{2}\rangle$	$\vert-\frac{1}{2}\rangle$	$\vert-\rangle$	$\vert+\rangle$	$\vert-i\rangle$	$\vert+i\rangle$

Real part

Imaginary part
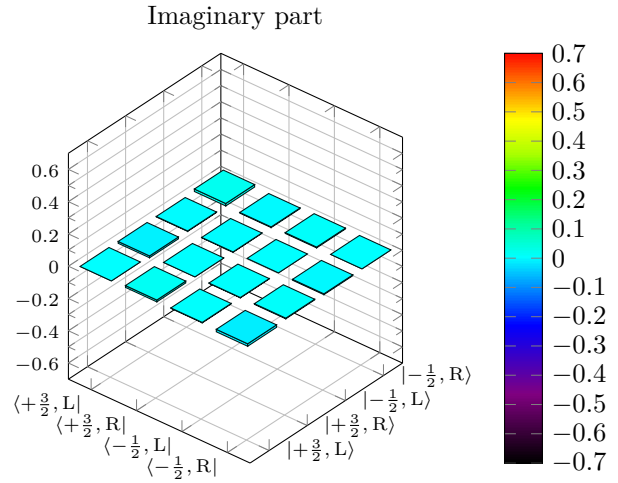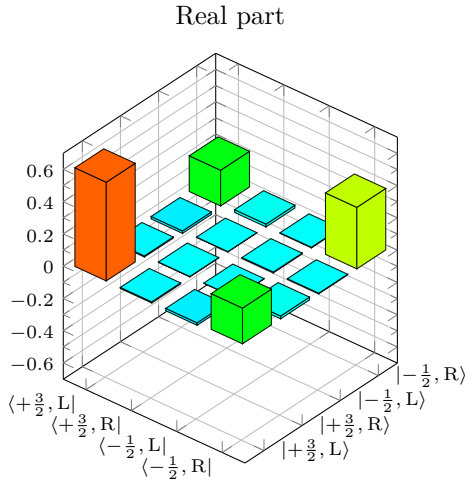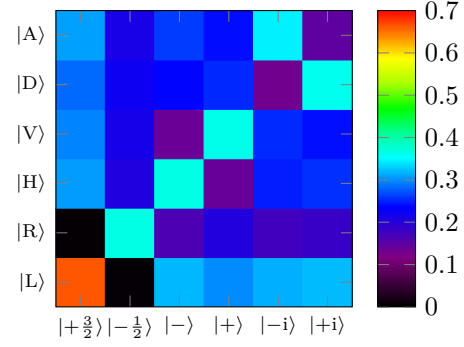
$\langle\cdot\vert\rho\vert\cdot\rangle$	$\vert+\frac{3}{2},L\rangle$	$\vert+\frac{3}{2},R\rangle$	$\vert-\frac{1}{2},L\rangle$	$\vert-\frac{1}{2},R\rangle$
$\langle+\frac{3}{2},L\vert$	0.611	−0.007	−0.015	0.221
$\langle+\frac{3}{2},R\vert$	−0.007	0.003	0.002	0.017
$\langle-\frac{1}{2},L\vert$	−0.015	0.002	0.005	0.004
$\langle-\frac{1}{2},R\vert$	0.221	0.017	0.004	0.381

$\langle\cdot\vert\rho\vert\cdot\rangle$	$\vert+\frac{3}{2},L\rangle$	$\vert+\frac{3}{2},R\rangle$	$\vert-\frac{1}{2},L\rangle$	$\vert-\frac{1}{2},R\rangle$
$\langle+\frac{3}{2},L\vert$	0.000	−0.011	−0.003	0.015
$\langle+\frac{3}{2},R\vert$	0.011	0.000	−0.002	−0.004
$\langle-\frac{1}{2},L\vert$	0.003	0.002	0.000	0.005
$\langle-\frac{1}{2},R\vert$	−0.015	0.004	−0.005	0.000

D.3.3. Unfiltered photons, Wollaston prism both outputs

The numeric values shown here are used to reconstruct the density matrix shown in Figure 7.16. The same density matrix is shown below

Sequence repetitions APE:	297 M
Sequence repetitions BELL:	132 M
Average repetition rate:	57 kHz
Total photon events:	400350
Signal events APE:	**281205**
Signal events BELL:	**119145**

	$\lvert+\frac{3}{2}\rangle$	$\lvert-\frac{1}{2}\rangle$	$\lvert-\rangle$	$\lvert+\rangle$	$\lvert-i\rangle$	$\lvert+i\rangle$
$\lvert A\rangle$	10983	5255	8095	7704	10910	4924
$\lvert D\rangle$	10648	5566	7346	8332	4461	11128
$\lvert V\rangle$	10652	5456	4530	11108	7874	7492
$\lvert H\rangle$	11107	5141	11118	4594	7637	8171
$\lvert R\rangle$	135	10368	4550	5736	5117	5074
$\lvert L\rangle$	20592	165	10052	9389	9790	10005

$\lvert A\rangle$	0.351	0.168	0.259	0.247	0.349	0.158
$\lvert D\rangle$	0.341	0.178	0.235	0.267	0.143	0.356
$\lvert V\rangle$	0.341	0.175	0.145	0.355	0.252	0.240
$\lvert H\rangle$	0.355	0.165	0.356	0.147	0.244	0.262
$\lvert R\rangle$	0.004	0.332	0.146	0.184	0.164	0.162
$\lvert L\rangle$	0.659	0.005	0.322	0.300	0.313	0.320
	$\lvert+\frac{3}{2}\rangle$	$\lvert-\frac{1}{2}\rangle$	$\lvert-\rangle$	$\lvert+\rangle$	$\lvert-i\rangle$	$\lvert+i\rangle$

Real part

Imaginary part
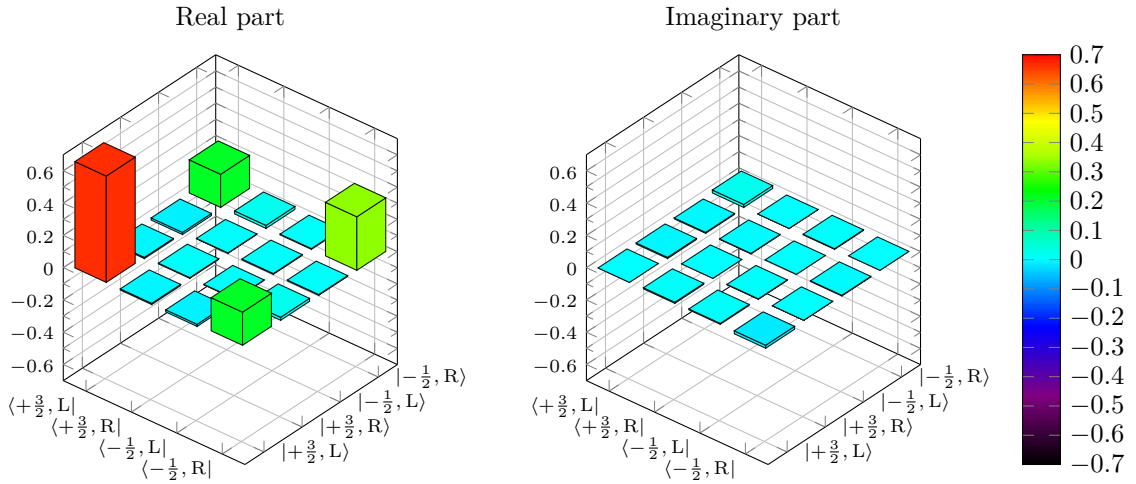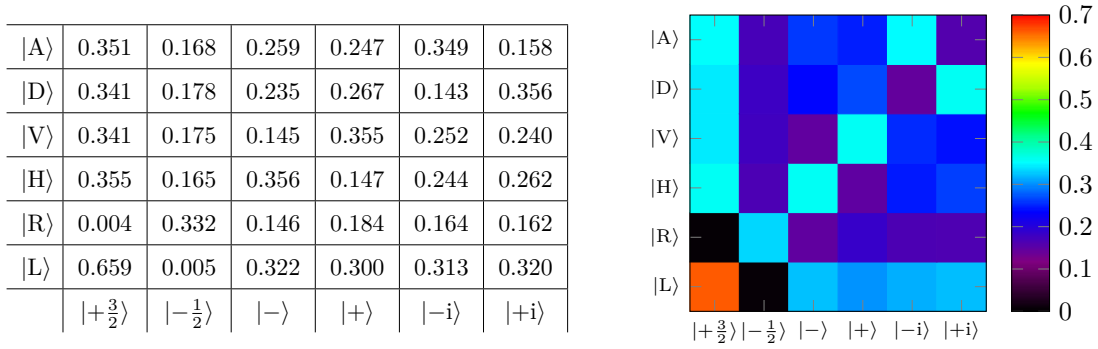
$\langle\cdot\lvert\rho\rvert\cdot\rangle$	$\lvert+\frac{3}{2},L\rangle$	$\lvert+\frac{3}{2},R\rangle$	$\lvert-\frac{1}{2},L\rangle$	$\lvert-\frac{1}{2},R\rangle$
$\langle+\frac{3}{2},L\rvert$	0.659	−0.007	−0.013	0.205
$\langle+\frac{3}{2},R\rvert$	−0.007	0.005	0.003	0.019
$\langle-\frac{1}{2},L\rvert$	−0.013	0.003	0.005	0.005
$\langle-\frac{1}{2},R\rvert$	0.205	0.019	0.005	0.332

$\langle\cdot\lvert\rho\rvert\cdot\rangle$	$\lvert+\frac{3}{2},L\rangle$	$\lvert+\frac{3}{2},R\rangle$	$\lvert-\frac{1}{2},L\rangle$	$\lvert-\frac{1}{2},R\rangle$
$\langle+\frac{3}{2},L\rvert$	0.000	−0.007	−0.006	0.018
$\langle+\frac{3}{2},R\rvert$	0.007	0.000	−0.003	−0.000
$\langle-\frac{1}{2},L\rvert$	0.006	0.003	0.000	0.004
$\langle-\frac{1}{2},R\rvert$	−0.018	0.000	−0.004	0.000

D.3.4. Filtered photons, Wollaston prism output 1

	$\left|+\frac{3}{2}\right\rangle$	$\left|-\frac{1}{2}\right\rangle$	$\left|-\right\rangle$	$\left|+\right\rangle$	$\left|-\mathrm{i}\right\rangle$	$\left|+\mathrm{i}\right\rangle$
Sequence repetitions APE:	216 M					

	$\left|+\frac{3}{2}\right\rangle$	$\left|-\frac{1}{2}\right\rangle$	$\left|-\right\rangle$	$\left|+\right\rangle$	$\left|-\mathrm{i}\right\rangle$	$\left|+\mathrm{i}\right\rangle$
$\left|\mathrm{A}\right\rangle$	391	313	345	390	688	31
$\left|\mathrm{D}\right\rangle$	434	286	357	321	31	692
$\left|\mathrm{V}\right\rangle$	396	295	33	696	330	387
$\left|\mathrm{H}\right\rangle$	471	310	643	27	429	299
$\left|\mathrm{R}\right\rangle$	9	722	295	398	326	416
$\left|\mathrm{L}\right\rangle$	740	18	392	334	343	316

Sequence repetitions APE: 216 M

Sequence repetitions BELL: 96 M

Average repetition rate: 41 kHz

Total photon events: 18638

Signal events APE: 12904

Signal events BELL: 5734

	$\left|+\frac{3}{2}\right\rangle$	$\left|-\frac{1}{2}\right\rangle$	$\left|-\right\rangle$	$\left|+\right\rangle$	$\left|-\mathrm{i}\right\rangle$	$\left|+\mathrm{i}\right\rangle$
$\left|\mathrm{A}\right\rangle$	0.273	0.218	0.241	0.272	0.479	0.022
$\left|\mathrm{D}\right\rangle$	0.303	0.200	0.249	0.224	0.022	0.482
$\left|\mathrm{V}\right\rangle$	0.276	0.206	0.024	0.485	0.230	0.270
$\left|\mathrm{H}\right\rangle$	0.328	0.216	0.448	0.019	0.299	0.209
$\left|\mathrm{R}\right\rangle$	0.007	0.503	0.206	0.278	0.227	0.290
$\left|\mathrm{L}\right\rangle$	0.515	0.013	0.273	0.233	0.239	0.220
	$\left|+\frac{3}{2}\right\rangle$	$\left|-\frac{1}{2}\right\rangle$	$\left|-\right\rangle$	$\left|+\right\rangle$	$\left|-\mathrm{i}\right\rangle$	$\left|+\mathrm{i}\right\rangle$

Real part

Imaginary part
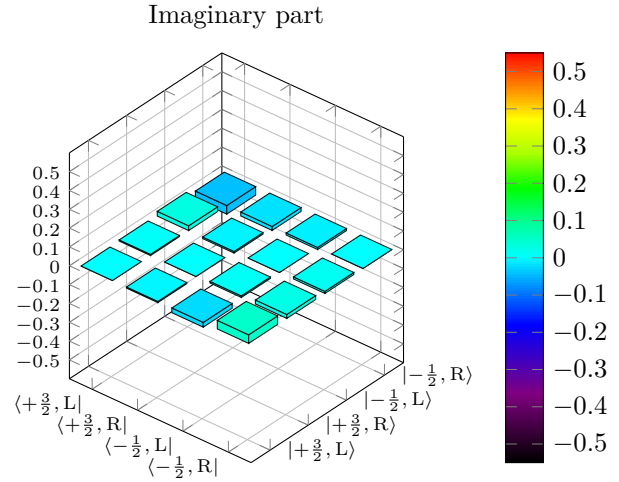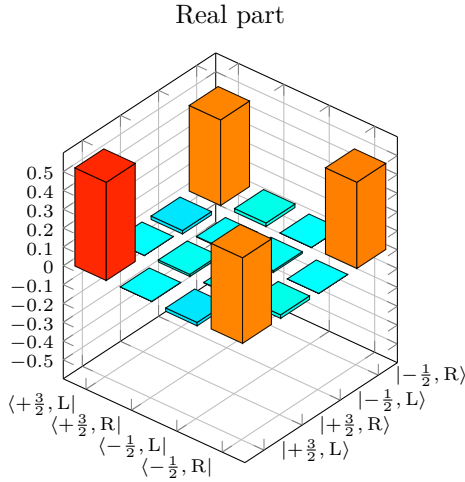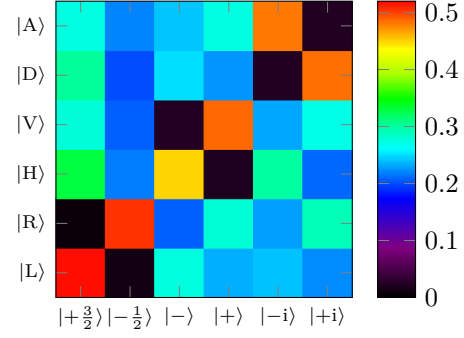
$\langle\cdot|\rho|\cdot\rangle$	$\left|+\frac{3}{2},\mathrm{L}\right\rangle$	$\left|+\frac{3}{2},\mathrm{R}\right\rangle$	$\left|-\frac{1}{2},\mathrm{L}\right\rangle$	$\left|-\frac{1}{2},\mathrm{R}\right\rangle$
$\left\langle+\frac{3}{2},\mathrm{L}\right|$	0.521	0.001	−0.018	0.455
$\left\langle+\frac{3}{2},\mathrm{R}\right|$	0.001	0.011	0.003	0.019
$\left\langle-\frac{1}{2},\mathrm{L}\right|$	−0.018	0.003	0.010	0.000
$\left\langle-\frac{1}{2},\mathrm{R}\right|$	0.455	0.019	0.000	0.458

$\langle\cdot|\rho|\cdot\rangle$	$\left|+\frac{3}{2},\mathrm{L}\right\rangle$	$\left|+\frac{3}{2},\mathrm{R}\right\rangle$	$\left|-\frac{1}{2},\mathrm{L}\right\rangle$	$\left|-\frac{1}{2},\mathrm{R}\right\rangle$
$\left\langle+\frac{3}{2},\mathrm{L}\right|$	0.000	0.006	0.025	−0.045
$\left\langle+\frac{3}{2},\mathrm{R}\right|$	−0.006	0.000	−0.008	−0.021
$\left\langle-\frac{1}{2},\mathrm{L}\right|$	−0.025	0.008	0.000	−0.011
$\left\langle-\frac{1}{2},\mathrm{R}\right|$	0.045	0.021	0.011	0.000

D.3.5. Filtered photons, Wollaston prism output 2

Sequence repetitions APE:	216 M	
Sequence repetitions BELL:	96 M	
Average repetition rate:	41 kHz	
Total photon events:	16879	
Signal events APE:	**11565**	
Signal events BELL:	**5314**	

	$\lvert+\tfrac{3}{2}\rangle$	$\lvert-\tfrac{1}{2}\rangle$	$\lvert-\rangle$	$\lvert+\rangle$	$\lvert-i\rangle$	$\lvert+i\rangle$
$\lvert A\rangle$	239	413	316	347	626	22
$\lvert D\rangle$	261	408	342	255	29	644
$\lvert V\rangle$	248	375	33	666	296	326
$\lvert H\rangle$	296	358	602	17	367	319
$\lvert R\rangle$	10	615	265	333	309	335
$\lvert L\rangle$	645	10	347	279	320	292

$\lvert A\rangle$	0.186	0.321	0.246	0.270	0.486	0.018
$\lvert D\rangle$	0.203	0.317	0.266	0.199	0.023	0.500
$\lvert V\rangle$	0.193	0.292	0.026	0.517	0.230	0.254
$\lvert H\rangle$	0.230	0.279	0.468	0.014	0.285	0.248
$\lvert R\rangle$	0.009	0.478	0.206	0.259	0.240	0.261
$\lvert L\rangle$	0.501	0.009	0.270	0.217	0.249	0.227
	$\lvert+\tfrac{3}{2}\rangle$	$\lvert-\tfrac{1}{2}\rangle$	$\lvert-\rangle$	$\lvert+\rangle$	$\lvert-i\rangle$	$\lvert+i\rangle$

Real part

Imaginary part
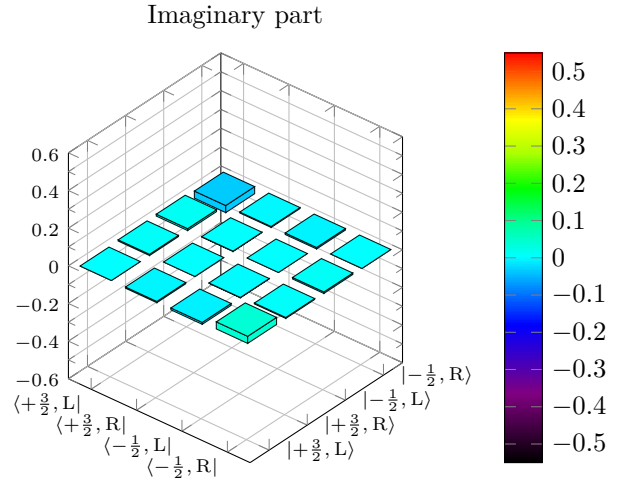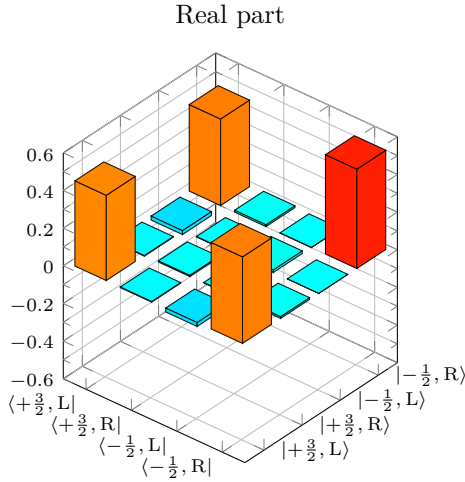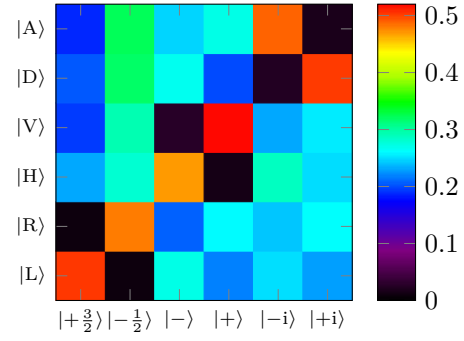
$\langle\cdot\lvert\rho\rvert\cdot\rangle$	$\lvert+\tfrac{3}{2},\mathrm{L}\rangle$	$\lvert+\tfrac{3}{2},\mathrm{R}\rangle$	$\lvert-\tfrac{1}{2},\mathrm{L}\rangle$	$\lvert-\tfrac{1}{2},\mathrm{R}\rangle$
$\langle+\tfrac{3}{2},\mathrm{L}\rvert$	0.452	−0.003	−0.021	0.459
$\langle+\tfrac{3}{2},\mathrm{R}\rvert$	−0.003	0.006	0.003	0.010
$\langle-\tfrac{1}{2},\mathrm{L}\rvert$	−0.021	0.003	0.014	0.001
$\langle-\tfrac{1}{2},\mathrm{R}\rvert$	0.459	0.010	0.001	0.527

$\langle\cdot\lvert\rho\rvert\cdot\rangle$	$\lvert+\tfrac{3}{2},\mathrm{L}\rangle$	$\lvert+\tfrac{3}{2},\mathrm{R}\rangle$	$\lvert-\tfrac{1}{2},\mathrm{L}\rangle$	$\lvert-\tfrac{1}{2},\mathrm{R}\rangle$
$\langle+\tfrac{3}{2},\mathrm{L}\rvert$	0.000	0.006	0.010	−0.037
$\langle+\tfrac{3}{2},\mathrm{R}\rvert$	−0.006	0.000	0.002	−0.005
$\langle-\tfrac{1}{2},\mathrm{L}\rvert$	−0.010	−0.002	0.000	−0.008
$\langle-\tfrac{1}{2},\mathrm{R}\rvert$	0.037	0.005	0.008	0.000

D.3.6. Filtered photons, Wollaston prism both outputs

The numeric values shown here are used to reconstruct the density matrix shown in Figure 7.16. The same density matrix is shown below

	$|+\frac{3}{2}\rangle$	$|-\frac{1}{2}\rangle$	$|-\rangle$	$|+\rangle$	$|-i\rangle$	$|+i\rangle$
$|A\rangle$	630	726	661	737	1314	53
$|D\rangle$	695	694	699	576	60	1336
$|V\rangle$	644	670	66	1362	626	713
$|H\rangle$	767	668	1245	44	796	618
$|R\rangle$	19	1337	560	731	635	751
$|L\rangle$	1385	28	739	613	663	608

Sequence repetitions APE: 216 M
Sequence repetitions BELL: 96 M
Average repetition rate: 41 kHz
Total photon events: 35517
Signal events APE: **24469**
Signal events BELL: **11048**

$|A\rangle$	0.232	0.267	0.243	0.271	0.483	0.020
$|D\rangle$	0.256	0.255	0.257	0.212	0.022	0.491
$|V\rangle$	0.237	0.246	0.025	0.501	0.230	0.262
$|H\rangle$	0.282	0.246	0.458	0.017	0.293	0.227
$|R\rangle$	0.007	0.491	0.206	0.269	0.234	0.276
$|L\rangle$	0.509	0.011	0.272	0.226	0.244	0.224
	$|+\frac{3}{2}\rangle$	$|-\frac{1}{2}\rangle$	$|-\rangle$	$|+\rangle$	$|-i\rangle$	$|+i\rangle$

Real part

Imaginary part
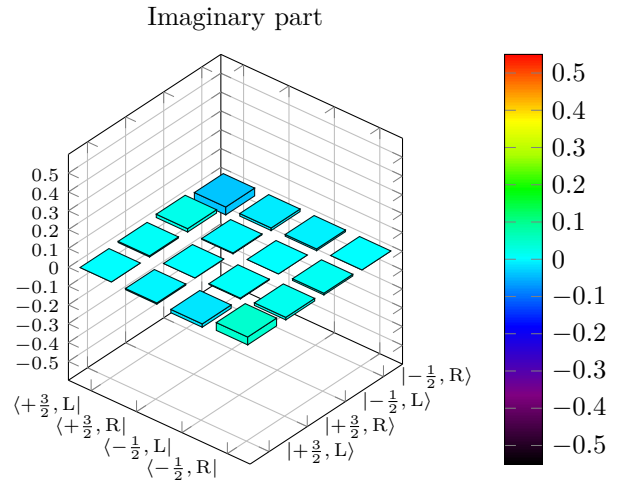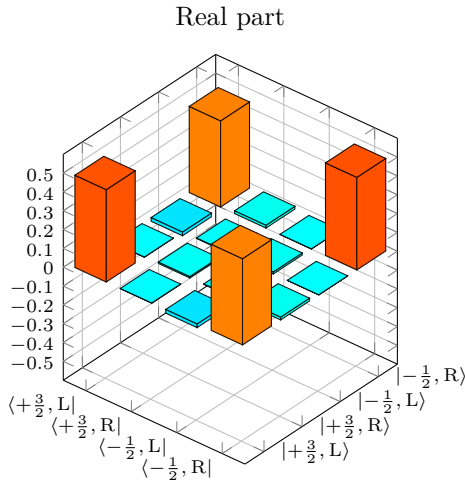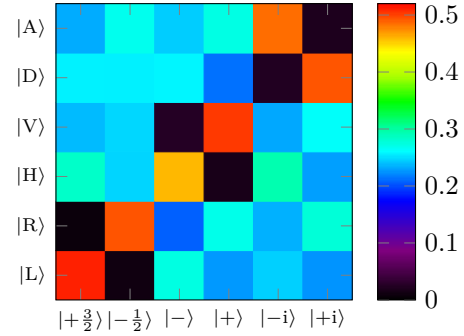
$\langle\cdot|\rho|\cdot\rangle$	$|+\frac{3}{2},L\rangle$	$|+\frac{3}{2},R\rangle$	$|-\frac{1}{2},L\rangle$	$|-\frac{1}{2},R\rangle$
$\langle+\frac{3}{2},L|$	0.490	−0.001	−0.020	0.458
$\langle+\frac{3}{2},R|$	−0.001	0.008	0.003	0.015
$\langle-\frac{1}{2},L|$	−0.020	0.003	0.011	0.001
$\langle-\frac{1}{2},R|$	0.458	0.015	0.001	0.491

$\langle\cdot|\rho|\cdot\rangle$	$|+\frac{3}{2},L\rangle$	$|+\frac{3}{2},R\rangle$	$|-\frac{1}{2},L\rangle$	$|-\frac{1}{2},R\rangle$
$\langle+\frac{3}{2},L|$	0.000	0.006	0.018	−0.042
$\langle+\frac{3}{2},R|$	−0.006	0.000	−0.004	−0.014
$\langle-\frac{1}{2},L|$	−0.018	0.004	0.000	−0.009
$\langle-\frac{1}{2},R|$	0.042	0.014	0.009	0.000

E. My Reserach: Milestones and Experiments. And more Experiments.

In February 2015, I started my PhD at the $^{40}\text{Ca}^+$ ion experiment in Saarbrücken. I spent the first time to develop the MATLAB scripts that controls the new HYDRA-II and to program many different pulse sequences required for the different experiments that were performed at this time. The experience I gathered with the ion experiment and the experimental control as well as the automation of the measurement process that followed from the new experimental control made the long measurement sessions possible during which I gathered the data presented in this work. Main part of the work during this time was the implementation of the Mølmer-Sørensen gate for the entanglement of two ions together with Pascal.

In 2016, I started to work on the new cavity locker what became the focus of my work in the next years. The new cavity locker was needed for the stabilization of the 393 nm laser but also to stabilize the analysis cavity for the spectrum measurements. In that sense, the work on the cavity locker and the Bachelor projects from Christian, Jurek, and Max, who worked on the setup of the 393 nm analysis cavity paved the way to the topic of this thesis. Together with Jurek, I measured the first single photon spectra with the analysis cavity setup. In this case the 393 nm resonance fluorescence. After these measurements, I decided to measure spectra of single Raman-scattered photons, which I was able to do for the first time in late 2018.

However, instead of being able to continue the work on Raman-scattered photons, a shortcut in the brigth trap rendered it not usable anymore with the old settings. We had to reduce the radio frequency power that drives the quadrupole electrodes to temporally solve the problem. At the same time we decided to rebuild the dark trap. This was done in late 2019. With the temporally solution I could continue my spectrum measurements that showed the need of evacuated tubes for the transfer lock scheme to become independent of air pressure drifts. With these tubes I could measure the first spectrum with the final setup in august 2019.

From this point, I measured the spectra and the atom-photon entanglement that are presented in this work. Furthermore, I started working on the extension of the three level model to support in the analysis of my spectra. Additionally, in the first half of 2021, I supervised the Bachelor thesis of Jelena which was devoted to setup the 854 nm cavity. The measurements of 854 nm photon spectra and the atom-photon entanglement done with this cavity complement

the work done with 393 nm photons.

As the first years of my research were devoted to the projects that paved the way to the measurement of the Raman-photon spectra almost all results were obtained after august 2019. The presented measurements sum up to a total non-stop measurement time of 43 full days during which a measuring sequence was running. From these 43 days, I spend almost 40 days with the measurement of 393 nm spectra. The remaining time was spend to measure 854 nm spectra and the 393 nm respective 854 nm atom-photon entanglement. In total, I performed during these 43 "measurement days":

- $62 \cdot 10^3$ sequences for 393 nm photon generation with a total number of $2.3 \cdot 10^{11}$ repetitions,

- 1100 sequences for 854 nm photon generation with a total number of $3.5 \cdot 10^9$ repetitions,

- 14000 spectroscopies of the $S_{1/2}$ ground state to control the magnetic field,

- 2600 spectroscopies of 729 nm transitions,

- 1800 854 nm dark resonance spectroscopies to calibrate 393 nm and 854 nm detunings,

- 1500 pulse amplitude scans on 729 nm transitions to calibrate (mainly) π-pulses,

- 950 spectroscopies of the 854 nm transition,

- and 60 pulse amplitude scans on the $S_{1/2}$ ground state transitions to calibrate a $\frac{\pi}{2}$-pulse.

With the executed sequences I detected a total number of $4.1 \cdot 10^7$ 393 nm photons and $1.1 \cdot 10^6$ 854 nm photons.

F. The Cavity Locker

This appendix was added on a voluntary basis after the evaluation of the thesis.
It supplements the short description of the cavity locker in Chapter 3 by a more detailed
description of the functionality and the hardware.

The development of the new cavity locker[1] was motivated by the need of a cavity locker for
the analysis cavity and more cavity lockers for the transfer lock scheme that is used to stabilize
most of the lasers. The requirements for the new cavity locker can be derived from these two
applications. To stabilize the analysis cavity a high output resolution and the possibility to
hold and continue the feedback loop is required. The last requirement is because the chopper
switches the feedback beam periodically on and off (see Section 3.3). To stabilize the transfer
cavities the cavity locker has to cover a large range to compensate drifts over several days (from
pressure changes e.g.). In the old version the large output range was achieved by combining two
feedback loops [54, 67]. A fast feedback loop with high resolution compensates high frequency
noise by addressing a piezo that shifts a mirror, while a slow feedback loop with large range
keeps the voltage applied to the piezo around $0\,V$ by changing the temperature of the cavity.
This design has two advantages compared to a single output. First, one can use "normal"
electronics as the typical range of $\pm 10\,V$ is sufficient to scan the cavity over multiple cavity
modes [2]. Furthermore, the resolution is improved compared to a single output that covers
the whole required range because the fast output covers only a small range. As this approach
was well established for many years the new cavity locker was designed in the same way. The
development of this new version was started by my coworkers Stephan Kucera and Konstantin
Klein. I continued and finished the development beginning from a rudimentary version up to
the version that is currently used in the laboratory. This version is described in the following
sections, starting with the user interface and the modes of operation of the cavity locker.
Afterwards I discuss the hardware and a part of the software that is required for the operation.
Because some of the software was only slightly changed from the first version I also refer to the
work of Konstantin Klein [70], where the first steps of the development are described.

---

[1]With cavity locker I refer to the whole "box" with the hardware and software that is used to stabilize the
cavity to the reference laser. The hardware contains a module (called *MK-cavity-locker*) that generates the
output voltage. Both parts are not to be mixed up.

[2]Together with the response of the piezo(s) that shift(s) the mirror.

F.1. The user interface and cavity locker states

In contrast to the old cavity locker which is controlled by knobs and switches, the user interface of the new cavity locker (see Figure F.1) is implemented on a Raspberry Pi. The user interface contains displays for cavity scans, the state of the cavity locker, parameters of the feedback loops as well as debug information. Several buttons allow to control the state of the cavity locker and finally, one can set all necessary parameters that are needed for the operation, as for example the scan range. Because the Raspberry Pi can be accessed remotely, also the cavity locker can be controlled remotely, which is one main difference compared to the old cavity locker. [3] The disadvantage of the Raspberry Pi is that it is not suitable for implementing a real-time control loop. For this purpose a microcontroller is used, which is controlled by the Raspberry Pi.
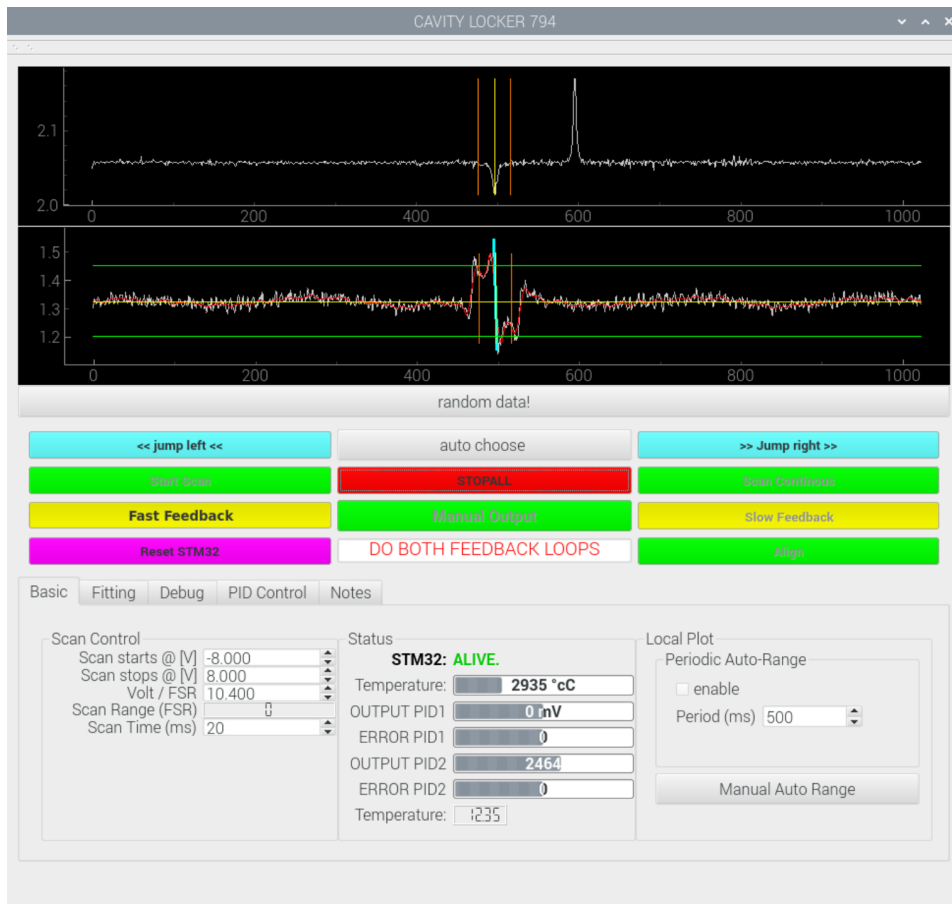
Figure F.1.: User interface of the cavity locker for the 794 nm transfer cavity. The color of the control buttons and the state display window indicate that both feedback loops are executed. More details are given in the text.

---

[3]A server structure, which would allow to control the cavity locker from different computers at the same time, is prepared rudimentary but not finished. A consequence of this preparation is that the values in the user interface are updated about once every second from a parameter storage.

The user inter face

Two graphs are placed at the top of the user interface to display the last measured cavity scan (top: cavity reflection; below: **P**ound-**D**rever-**H**all (PDH) error signal). The displayed graphs show the measured data (white), the smoothed data that is used to find the PDH slope (red), the found PDH slope (cyan), the set point and position of the slope (yellow), the maximal and minimal PDH error value that are used in the search-slope algorithm when the feedback loop is initialized (green) and some auxiliary lines (orange).

Below the graphs ten colored buttons allow to control the state of the cavity locker (details see below). The **STOPALL** button acts as a panic button that is used to return to the idle state if something goes wrong. Similarly, the **Reset STM32** button reboots the microcontroller. The current state of the cavity locker is shown in the window below the **Manual Output** button and by coloring the respective state button in yellow. At the same time a gray font indicate buttons that can not be pressed. In the shown example both feedback loops are running, thus the **Fast Feedback** button and the **Slow Feedback** button are yellow. Because the fast feedback loop has to be excited first, the font of the **Slow Feedback** button is gray.

On the bottom of the user interface there are five tabs that are used to control parameters and to display values from the feedback loops, debug information and information for the daily use. The *Basic* tab contains the scan parameters (start voltage, stop voltage, Volt/FSR [4] and scan time), displays for the error signal, the output value of the fast (PID1) and slow (PID2) feedback loop as well as the current temperature of the cavity. The box on the right side is an artifact from an earlier version that has currently no functionality. In the *Fitting* tab one sets parameters for the data analysis algorithms that are used to find and fit the PDH error slope [5]. On can set values for the filters that smooth the measurement data, the relative depth of a dip to be considered as a possible cavity resonance, and the minimal absolute gradient that is required to recognize a PDH error slope. By changing the relative depth of a dip and the minimal absolute gradient of the PDH error slope one can sort out unwanted slopes (from higher order modes e.g.). The *Debug* tab contains different sub tabs to display debug information from the SPI communication between the Raspberry Pi and the microcontroller or information from the fitting process. As an example the fitted PDH error slopes of reflection dips are listed. For both feedback loops the proportional, integral, differential as well as a global gain are set in the tab *PID Control*. There, one can also define a manual set point for the feedback loops. Usually the set point of the slow feedback loop is set manually, while the set point of the fast feedback loop is determined from the measured PDH signal. Finally the tab *Notes* contains information for the daily use as for example how much the wave length of the laser that is stabilized to the cavity changes, if the cavity is stabilized to the next cavity mode.

---

[4]The value "Volt/FSR" does not influence the cavity scan but is used in the slope-search algorithm.

[5]This find-fit-slope algorithm is not to mix up with the slope-search algorithm that moves the cavity to resonance when initializing the fast feedback.

The cavity locker states

After an initialization routine the cavity locker enters the **Idle** state, where only the temperature of the cavity is measured frequently, while the outputs are set to a predefined value. By pressing the buttons **Start Scan**, **Scan Continous**, **Fast Feedback**, **Manual Output**, **Slow Feedback**, or **Align** in the user inter face the following states of the cavity locker are accessed. [6]

Single scan: A single cavity scan is measured and displayed in the user interface. There are always 1024 voltage points measured evenly distributed over the whole scan range. The find-fit-slope algorithm searches and fits the Pound-Drever-Hall error signal slope. Additionally the set point for the stabilization and voltage levels (maximal and minimal) that are required for the slope-search-algorithm to find the PDH slope when initializing the fast feedback loop are determined.

Continuous Scan: The cavity is scanned continuously. The measured cavity reflection and PDH error signal are displayed in the cavity locker GUI. Because the transfer of the measured data from the microcontroller to the Raspberry Pi is slow, the repetition rate of the continuous scan is small and not suited for alignment purposes.

Slow Feedback: The slow feedback loop controls the temperature of the cavity. In this state the slow feedback loop uses the measured temperature to generate the error signal.

Fast Feedback: The fast feedback loop controls the cavity length by moving one of the mirrors. The fast feedback loop can only be turned on, if a single scan has be performed and a PDH slope was found. If the fast feedback is running, the buttons **jump left** or **jump right** can be used to stabilize the cavity to the next resonant mode that is separated from the current mode by the free spectral range (or half the free spectral range for a confocal cavity). [7] To find the resonance if the fast feedback loop is started or the jump buttons are pressed the slope-search-algorithm is performed (see below).

Both Feedbacks: Both feedback loops are turned on the stabilize the cavity to the reference laser. The fast feedback loop holds the cavity on resonance while the slow feedback loop keeps the output voltage of the fast feedback loop around zero. To achieve this, the slow feedback loop uses the output voltage of the fast feedback loop as error signal. Although the temperature of the cavity is not needed for this control loop, it is still measured to have the current value available for the case that the stabilization has to be reinitialized. To run both feedback loops the slow feedback loop has to be turned on first. Analog to the **Fast Feedback** state, the **Jump left** or **Jump right** buttons can be used to go to the next cavity mode.

Continuous Scan with Slow Feedback: Same mode as "Continuous Scan" but with the slow feedback loop turned on.

---

[6]Not all states can be accessed directly from the idle state.
[7]This functionality was called "The magic button" in the old cavity locker.

Align Scan: For alignment purposes the cavity is scanned continuously but without transferring data from the microcontroller to the Raspberry Pi. In this case each cavity scan is started directly after the previous one finished. Consequently, the repetition rate of the cavity scans is given by the sum of the scan time (as set in the user interface) and the time it takes to step from the last voltage point of the previous scan to the first voltage point of the next scan.

Align Scan with Slow Feedback: Same mode as "Align Scan" but with the slow feedback loop turned on.

Manual Output: The output of both feedback loops are set to a fixed value.

Manual Output with Slow Feedback: The output of the fast feedback loop is set to a fixed value, while the slow feedback loop controls the temperature of the cavity.

Each of these states contains several sub states, where the needed parameters as for example the scan range and the scan time are send from the Raspberry Pi to the microcontroller. Afterwards the desired operation is done before an exit sub state ensures that all output values that were changed are set back to the values that are used during idle times (or during the slow feedback loop).

F.2. Basic algorithms

To enable the cavity locker states described in the previous section several basic algorithms and functions are needed. These algorithms and functions are executed on the Raspberry Pi (the find-fit-slope algorithm), on the microcontroller (the search-slope algorithm) or on both platforms at the same time (the communication protocol). In this section I describe some of these algorithms or functions. Addition to these algorithms and functions there are functions implemented on the microcontroller that enable external hardware components as for example the high resolution DAC AD5791 that provides the output voltage of the fast feedback loop.

Communication from Raspberry Pi to STM32F4

To send commands from the Raspberry Pi to the microcontroller or to send data in the other direction a SPI protocol is implemented with the Raspberry Pi as the master and the microcontroller as the slave. Each command is defined as 10-bit integer on both sides together with the information whether an answer is expected (for example the command `CTRLCMD_get_temperature`) or not (example: `CTRLCMD_set_pid1_setpoint`). The SPI command send by the Raspberry Pi triggers an interrupt routine at the microcontroller during which the command is executed. If an answer is expected this answer is prepared and read while sending the dummy command `CTRLCMD_reading_slave_answer`. As the SPI controller of the Raspberry Pi can handle multiple chip selects the implemented protocol allows to control up to three microcontroller with the same Raspberry Pi.

As major change in this protocol, I lowered the interrupt priority of the SPI communication below the priority of the interrupts of the feedback loops. This lower priority is required to avoid the risk of failure of the feedback loops every time a SPI command is send and processed by the microcontroller. As a consequence of the lower priority of the SPI interrupt, the SPI communication does not work reliable if the fast feedback loop is executed. To reduce this problem a few work arounds had to be implemented [8]. In hindsight, it would have been probability better to implement a new communication protocol using the USB controller available on the evaluation board. However in the first versions of the microcontroller program, the internal clocks were set wrong with the consequence that the USB controller did not work. At the time I found this "bug" the cavity locker was already very advanced and I decided to keep the SPI communication implemented by Konstantin.

The find-fit-slope algorithm

The find-fit-slope algorithm detects the PDH error slope in the data measured with a single cavity scan. As first step all dips in the measured cavity reflection are put in a list (vertical yellow line in Figure F.1). In the second step for each of these dips it is tested whether there is an PDH error slope or not. The algorithm checks for the maximal and minimal value of the measured PDH error signal in a window around the dip (orange lines in Figure F.1). Then the slope is fitted for a smaller window between the maximal and minimal PDH error signal. If the absolute value of the fitted slope is larger than a given threshold the corresponding dip is added to a list with identified PDH error slopes. As last step, from all found PDH error slopes the last one is selected and displayed in the user interface (cyan line in Figure F.1 [9]). The measured data is also used to determine the set point of the feedback loop (horizontal yellow line) and two threshold values (horizontal green lines). The threshold values are needed for the slope-search algorithm that finds the cavity resonance for example when the fast feedback is started.

The slope-search algorithm

The slope-search algorithm is executed to find the cavity resonance when the fast feedback is started or one of the jump buttons was pressed. In both cases the output voltage of the fast feedback loop is moved to a point left (or right) of the cavity resonance outside of the PDH shape (e.g. to the voltage at the scan point 200 for a resonance at the point 500, see Figure F.1) [10]. The exact distance is determined using the value of the "Volt/FSR" parameter. From the start point of the algorithm the cavity is shifted towards the resonance while tracking the PDH error signal. If the error signal crosses the upper threshold (green horizontal line) a flag is set in the algorithm. The next time a value below the set point (horizontal yellow line) is

---

[8]As an example, I check if the microcontroller state machine changed after I send the respective command.

[9]If there are multiple reflection dips only the lines from the selected dip are displayed.

[10]The exact execution depends on the sign of the slop or which button was pressed. Here I describe the exemplary situation for the displayed scan with an start from the left side.

measured, the cavity is at resonance and the feedback loop is started to hold the cavity on resonance.

Chopper state detection

At the analysis cavity setups, the chopper switches periodically between the feedback beam and the photon beam (see Section 3.3). The chopper wheel is build from a computer hard disk and contains three types of sectors (drawing see [71]). For the first 30° the feedback beam is open. Afterwards there are 10° where both beams are blocked followed by a 130° sector where the photon beam is open and an other 10° sector where both beams are closed. This sequence is repeated for the second half of the chopper.

The first purpose of the algorithm to detect the chopper state is to continuously measure the rotation speed of the chopper. A photo diode measures whether the feedback beam (or a second beam) goes through the chopper or not (the 30° sector). The signal is digitized with a comparator setup (see hardware section) and detected by the microcontroller, where the period of a half rotation is measured continuously with an interrupt timer. Continuously measuring this chopper period brings robustness against fluctuations of the rotation speed of the chopper and the advantage that different rotation speeds can be used.

The second part of the algorithm detects the actual chopper state. A few interrupt cycles after the photo diode detected that the feedback beam is opened the chopper state is set to *lock_open*. In this state all algorithms and functions that require the feedback beam, as for example the fast feedback loop, are executed. After a fixed time (14 % of the measured period) the chopper state is set to *both_closed* where all algorithms that require the feedback beam are paused. After a defined waiting time (about 6 % of the measured period) the chopper state is set to *photon_open* as it is expected that the photon beam is now opened. By switching a digital line to high this state is heralded for other parts of the experiment as for example the pulse sequence that generates Raman photons. Again, after a defined time (70 % of the measured period) the chopper state is changed to *lock_wait* and the digital line indicating the *photon_open* state is switched back to low. The state machine remains in this waiting state until the photo diode detects that the feedback beam has opened again. The puffer times in the state detection of the chopper compared to the physical setup are introduced to avoid artifacts that may occur when a beam is opened only partially.

F.3. Hardware

The new cavity locker hardware is build in a modular design what allows to exchange individual modules if they are broken or need to be modified for a special purpose. Furthermore it is possible to combine several cavity locker units in the same case because some modules can "supply" several cavity locker units. In total, a single cavity locker requires a module that holds the *Raspberry Pi*, an *Analog Supply* and a *Voltage Reference* module. Additionally to these "supply" modules the cavity locker contains a *Pound-Drever-Hall* module and a *Feedback*

control module. Up to three of these last modules can be put into the same rack so that a single cavity locker box can feedback control three transfer cavities. In case of the cavity locker for the analysis cavity an additional *comparator* module digitizes a photo diode signal to detect the chopper state.

In the following sections I will discuss the function, setup and purpose of each of these modules. Some of the modules were designed by myself from scratch, while others were adapted and further developed from existing designs (often from Stephan Kucera). If possible, they are designed with integrated circuits that turned out to be "useful" or "easy to handle" and performed well in many previous electronic projects realized in our research group by myself and others.

MK-raspberry-supply

The *MK-raspberry-supply* module (schematic see Figure F.2) contains a mounting for the Raspberry Pi that runs the user interface of the cavity locker as well as sockets to connect the digital power supply ($+5\,\mathrm{V}$) and a second independent power supply that drives the heating wire ($+12\,\mathrm{V}$) of the slow feedback loop.
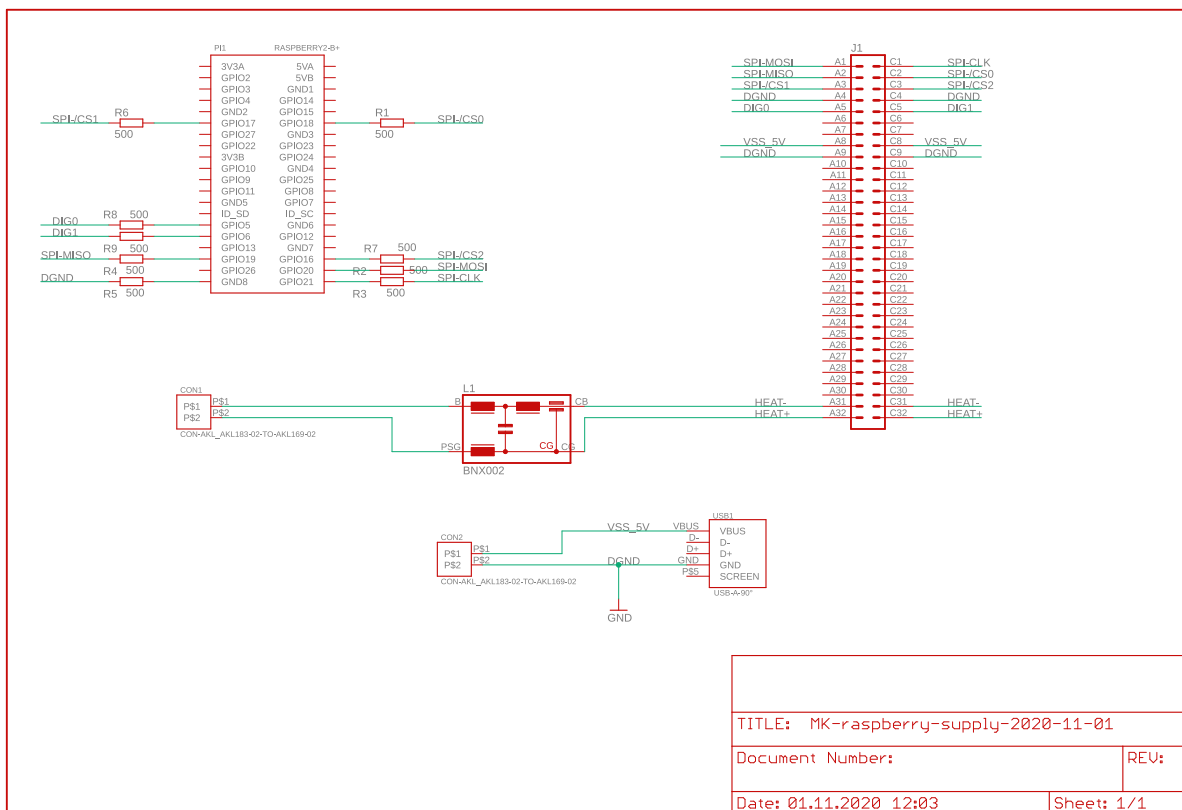
Figure F.2.: Schematic of the *MK-raspberry-supply* module that is used to mount the Raspberry Pi.

Figure F.3.: Schematic of the *MK-analog-supply-fixed* module that generates the supply voltages for the analog circuits from the power grid. The connector *J1* shows all signals that are exchanged between individual modules over the back plane installed in the rack.

MK-analog-supply-fixed

To avoid high frequency noise coming from a switched-mode power supply the analog parts of the circuit are driven by a self build linear power supply. The *MK-analog-supply-fixed* module (schematic see Figure F.3) provides a $\pm15\,\text{V}$ and a $+12\,\text{V}$ supply voltage and the analog ground (AGND). To avoid negative influence of the transformer onto other parts of the cavity locker unit, the module is shielded with a thin μ-metal foil. Without this shielding one could observe $50\,\text{Hz}$ noise on signals generated by the other modules.

Figure F.4.: Schematic of the *MK-voltage-reference* module that generates several reference voltages from a $+5\,\text{V}$ voltage reference chip LT1027.

MK-voltage-reference

To supply the digital-to-analog converter (DAC) as well as for the operation of the Pound-Drever-Hall (PDH) module good reference voltages are needed. They have to be long time stable to reduce drifts of the PDH error signal (offset and phase) and require a low noise for the DAC that sets the voltage for the piezo that shifts one of the cavity mirrors. These reference voltages are supplied by the *MK-voltage-reference* module (schematic see Figure F.4) that contains the $+5\,\text{V}$ voltage reference chip LT1027 from Linear technology (now Analog Devices) as central element. The LT1027 provides a very low temperature drift, a good long term stability, and a low noise. The voltage supplied by the voltage reference is amplified with the precision operational amplifier LT1097 to generate reference voltages at $\pm 5\,\text{V}$, $\pm 10\,\text{V}$ and $+12\,\text{V}$. To transfer the good parameters of the original reference voltage to the generated reference voltages, only resistors with low temperature coefficients are used. For the reference voltages a root-mean-square broadband noise of about $20\,\text{µV}$ was reached. Additionally to the reference voltages, the voltage reference module supplies a $0\,\text{V}$ reference voltage, as it turned out that the periodic conversion process of the analog-to-digital converter on the *MK-cavity-locker* module (see below) lead to a small shift of the analog ground. As reason, I identified the increased power consumption of the analog-to-digital converter during the conversion process, which lead to a small voltage along the analog ground circuit due to the small resistance [11].

---

[11]The small shift could be observed, If the reference voltages or the DAC output were measured against the analog ground. The voltage difference between two reference voltages ($+5\,\text{V}$ and $-5\,\text{V}$ e.g.) was not affected.
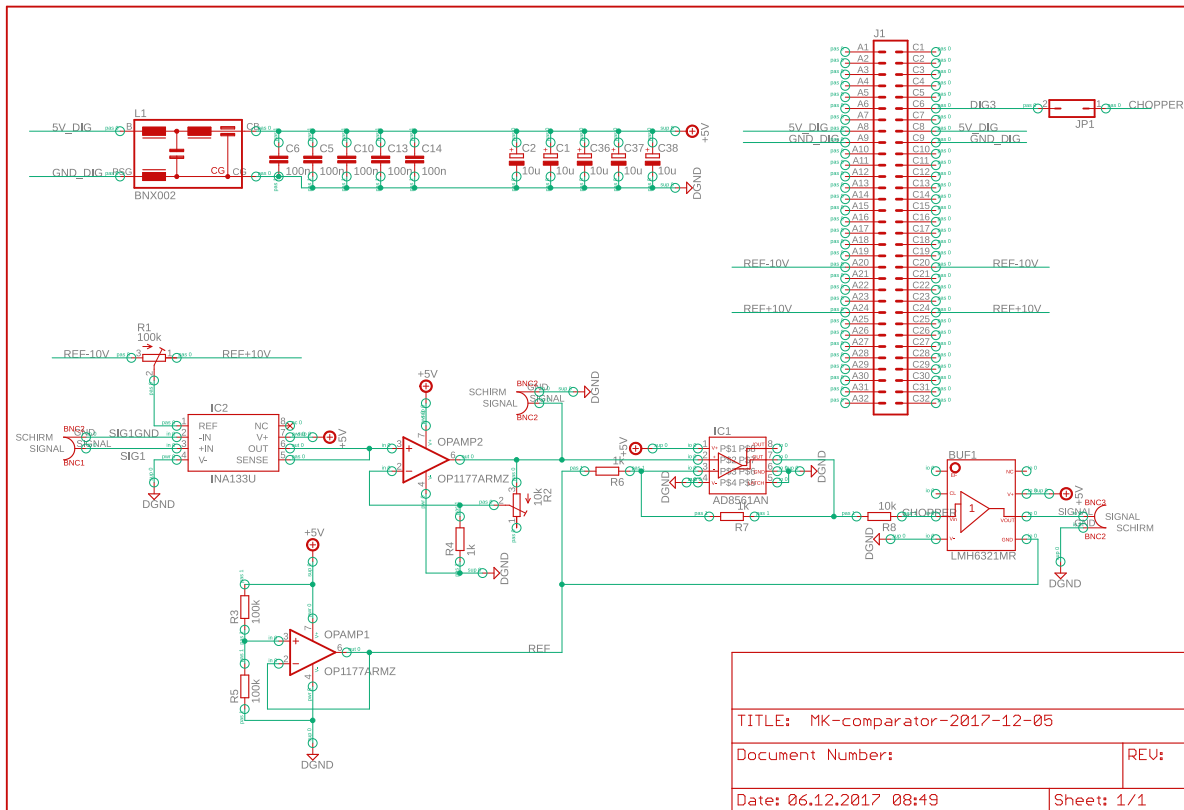
Figure F.5.: Schematic of the *MK-comparator* module that is used to digitize the photo diode signal, which indicates the chopper position.

MK-comparator

At the analysis cavity setup the reference beam is coupled onto a photo diode to detect whether the reference beam or the photon beam is shone onto the analysis cavity. [12] For this purpose, the voltage is digitized by the *MK-comparator* module (Schematic see Figure F.5) in order to be able to read it at a digital input of the microcontroller. First an offset voltage is subtracted before the signal is amplified and fed into a fast comparator (AD8561). To avoid oscillation around the switching point of the comparator, the comparator is set up with a hysteresis between both output states. The generated digital signal is send to the microcontroller over the back plane and buffered for a monitor output.

---

[12]In case of the 854 nm analysis cavity a second green laser beam is send through the same chopper window as the reference beam.

MK-PDH

The module *MK-PDH* (Schematic see Figure F.6) generates the Pound-Drever-Hall error signal from the measured cavity reflection and the reference oscillator. The generated error signal is is feed into the control loop that controls the cavity length. A fast photo diode, with a bandwidth larger than the modulation frequency of the reference laser, measures the cavity reflection. The measured reflection is feed into the *MK-PDH* module together with the reference oscillator that modulates the reference laser. The input voltage is filtered with a band pass filter (PIF 21.4+ from Mini Circuits, typically the phase modulation is done with about 20 MHz) to remove unwanted frequency components (for example the 26 MHz from the ion trap) and amplified (MAN 1LN from Mini Circuits) before the signal is feed into a phase detector (RPD-1+). As second signal, the phase shifted reference oscillator (JSPHS-26 from Mini Circuits) is feed into the phase detector. The generated output of the phase detector is amplified and sent through a low pass filter to generate the PDH error signal. This error signal is send to the cavity locker module and to a monitor output. The photo diode signal is also amplified, low pass filtered and sent to the cavity locker module and a monitor output. While the photo diode signal is not required for the feedback loop itself it is used for alignment purposes and the algorithm that finds the slope of the PDH error signal. External potentiometers allow to control the amplification and offset of the PDH error signal and the measured cavity reflection as well as the phase shift of the reference oscillator.
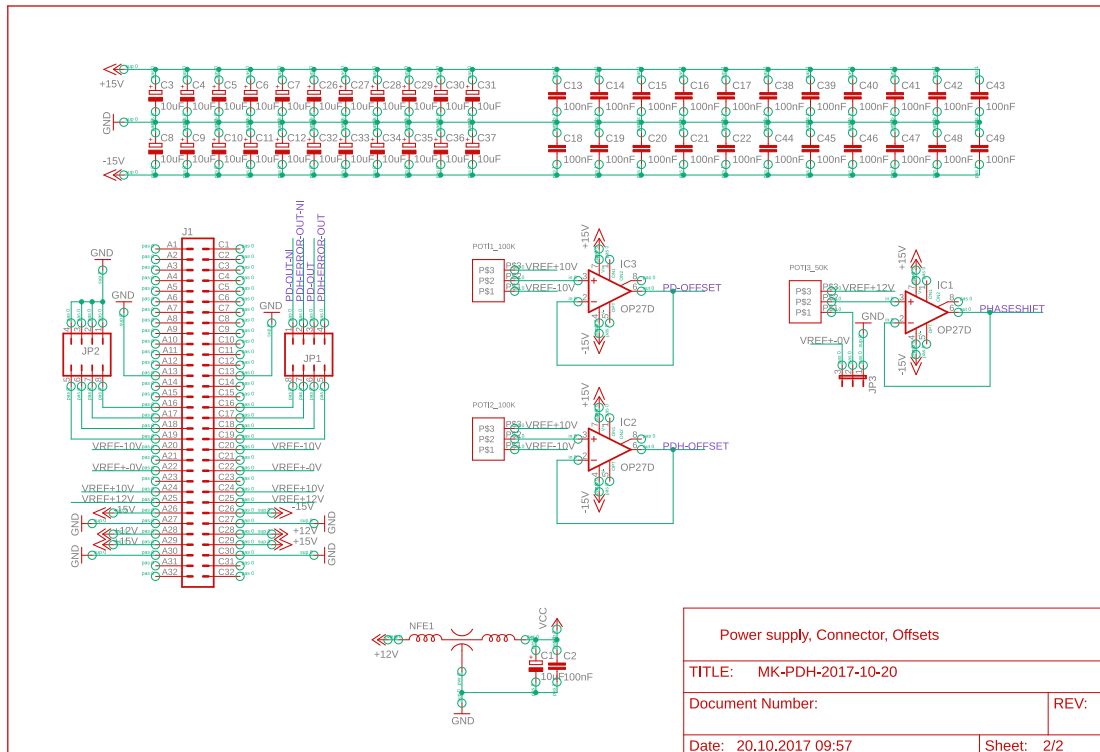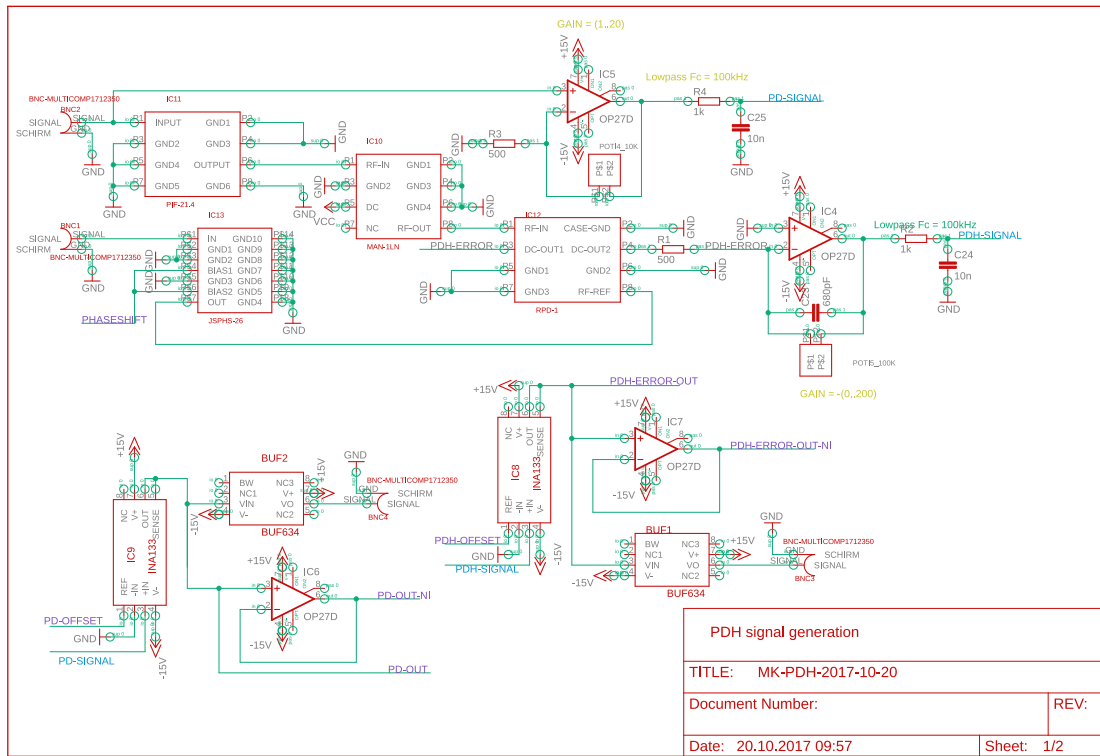
Figure F.6.: Schematic of the *MK-PDH* module. (top) Generation of the Pound-Drever-Hall signal and amplification of the measured cavity reflection. The chips IC10 to IC13 are optimized for a modulation frequency of about 20 MHz. (bottom) Supply circuits and generation of the offset voltages.

MK-cavity-locker

The *MK-cavity-locker* module (Schematic see Figures F.7 and F.8) contains the electronic to read and process the PDH error signal and to generate the feedback controlled output signals that set the length of the transfer cavity.

The module contains the STM32F407G microcontroller on an evaluation board (STM32F407G-DISC1) that enables easy programming and use of the components (ADC, DAC, SPI) of the microcontroller. With the internal ADCs the PDH error signal and the cavity reflection are measured during cavity scans and for the feedback loop. An internal DAC controls the output of the "slow" feedback loop [13]. The SPI controllers are used to set the output of an external high resolution DAC (AD5791/AD5781, from Analog Devices), to read the temperature of the cavity with an external ADC (LTC2442, from Linear Technology, now Analog Devices) as well as for the communication with the Raspberry Pi. Finally, four buffered digital outputs are used for trigger and monitor signals during the operation.

The output of the fast feedback loop is set by an external 20-bit (AD5791, for the analyse cavity) or 18-bit (AD5781, for the transfer cavity) DAC, which offers a low noise ($7.5\,\mathrm{nV}/\sqrt{\mathrm{Hz}}$), a low drift ($< 0.05\,\mathrm{ppm/°C}$), high accuracy ($1\,\mathrm{ppm}$), a fast settling time ($1\,\mathrm{\mu s}$) and a high resolution (20-bit corresponds to $\approx 20\,\mathrm{\mu V}$ for a $\pm 10\,\mathrm{V}$ input). Both versions use the same SPI commands with the only difference that the last data bits have no effect in the 18-bit version. The 20-bit resolution translates to approximately $1.8\,\mathrm{kHz}$ for the $393\,\mathrm{nm}$ analysis cavity respective $830\,\mathrm{Hz}$ for the $854\,\mathrm{nm}$ analysis cavity, what is small compared to the line width of the respective cavities ($\Delta\nu_{393} = 622(4)\,\mathrm{kHz}$ respective $\Delta\nu_{854} = 1.689(7)\,\mathrm{MHz}$, see Section 3.3) and is thus sufficient to control the analysis cavities. Additionally, this DAC was easier to handle compared to the DAC used in the first version (DAC8871 from Texas Instruments) where I was not able to eliminate voltage overshoots (also called output voltage glitch) at major carrier transitions. With additional circuit elements, the voltage output is referenced against the $0\,\mathrm{V}$ or $-10\,\mathrm{V}$ reference to get either a bipolar $\pm 10\,\mathrm{V}$ output or an unipolar $0...20\,\mathrm{V}$ output range.

The output of the slow feedback loop is set by an internal DAC of the microcontroller because the 12-bit resolution is sufficient there. The output sets the current through a heating wire by controlling the gate voltage of a MOSFET.

The photo diode reflection and PDH error signal from the *MK-PDH* module are read with internal ADCs of the microcontroller. The temperature of the cavity is measured with a temperature dependent resistor (PT1000 or NTC resistor) using a Wheatstone bridge and an external ADC (LTC2442). To avoid negative influence on the other reference voltages the LTC2442 uses an independent voltage reference (LT1027). Unfortunately, I was not able to reach the design resolution of the ADC due to large noise. I could not conclusively determine if the noise was caused by the measurement setup or the readout process of the ADC [14]. However, with digital oversampling in the microcontroller I reached a sufficient resolution for the temperature control of the cavity.

---

[13]The prepared option to add the output of a second DAC to the output of the fast feedback loop is not used.

[14]A different ADC (LTC2440) brought the additional, new problem that the input signal had to be buffered.
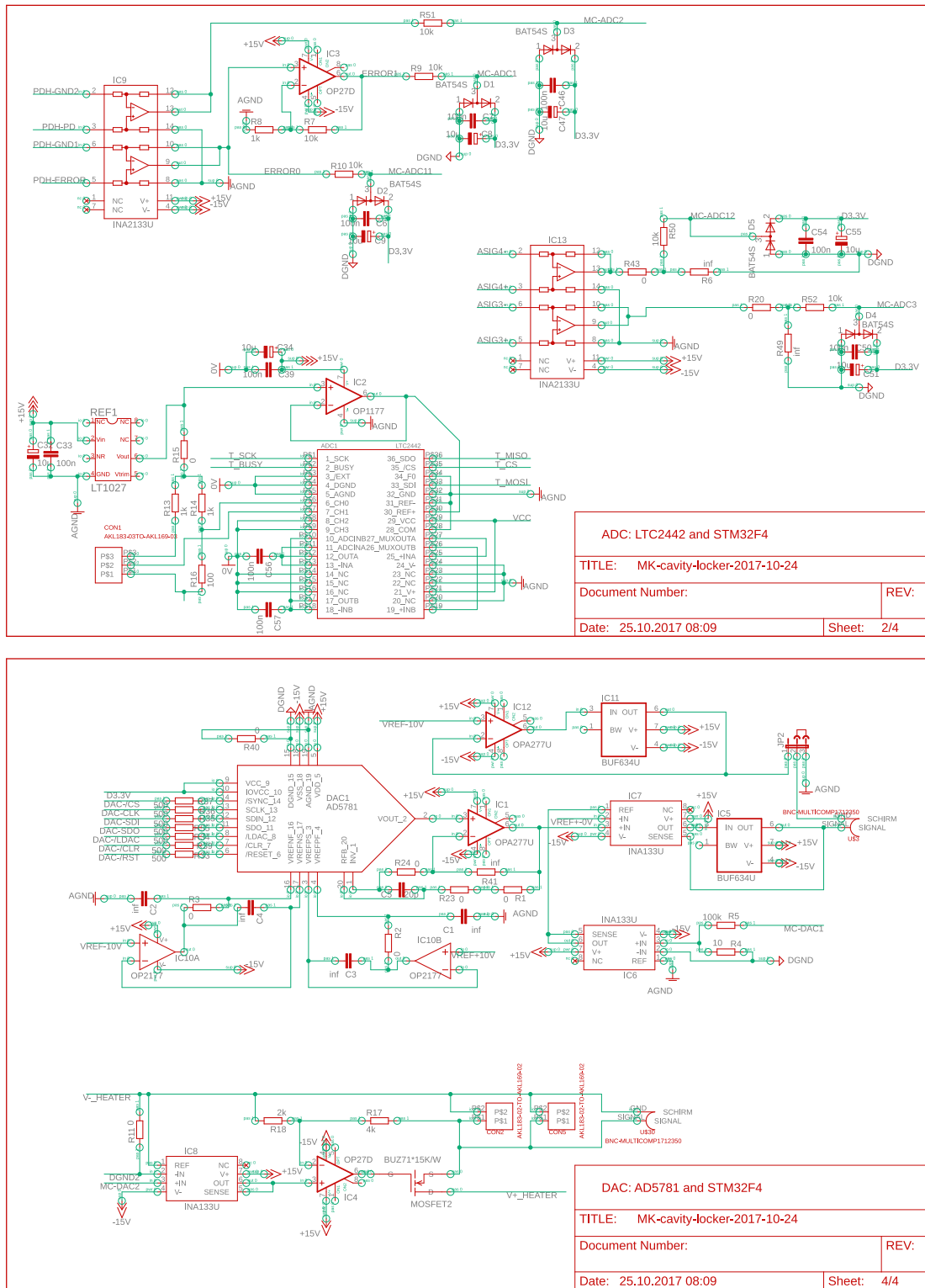
Figure F.7.: First part of the schematic of the *MK-cavity-locker* module. (top) Circuits to read signals from the *MK-PDH* module and the cavity temperature. (bottom) Circuits to create the output voltage with the high resolution DAC and the output of the slow feedback loop.
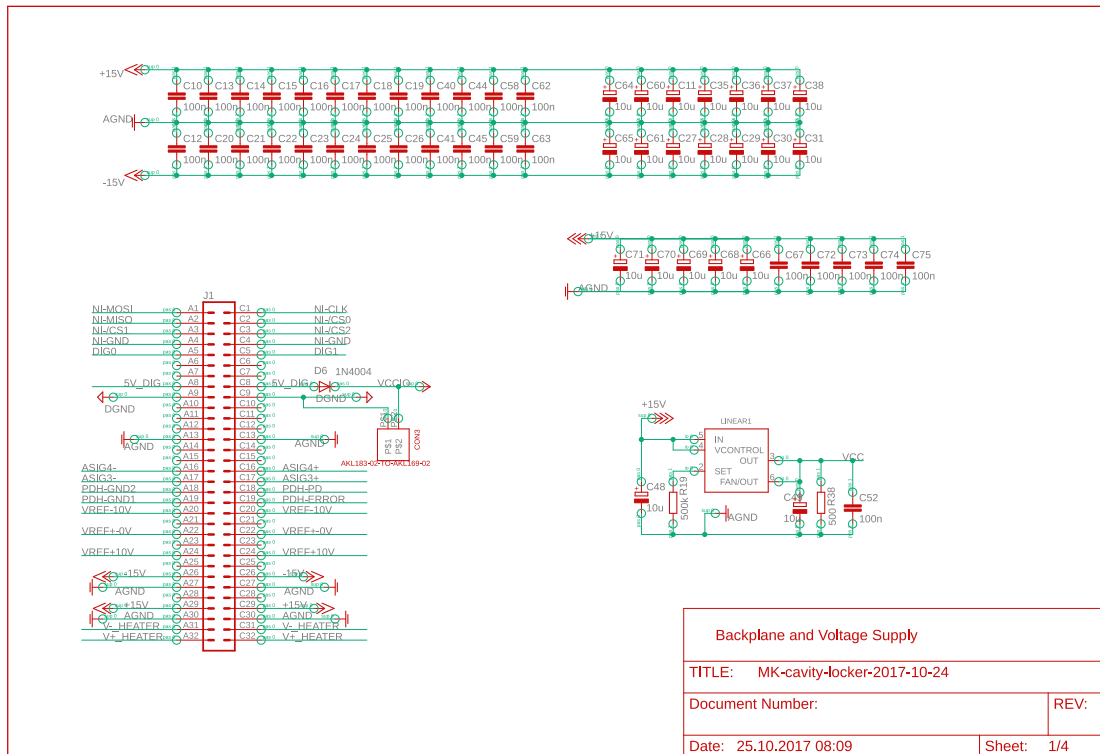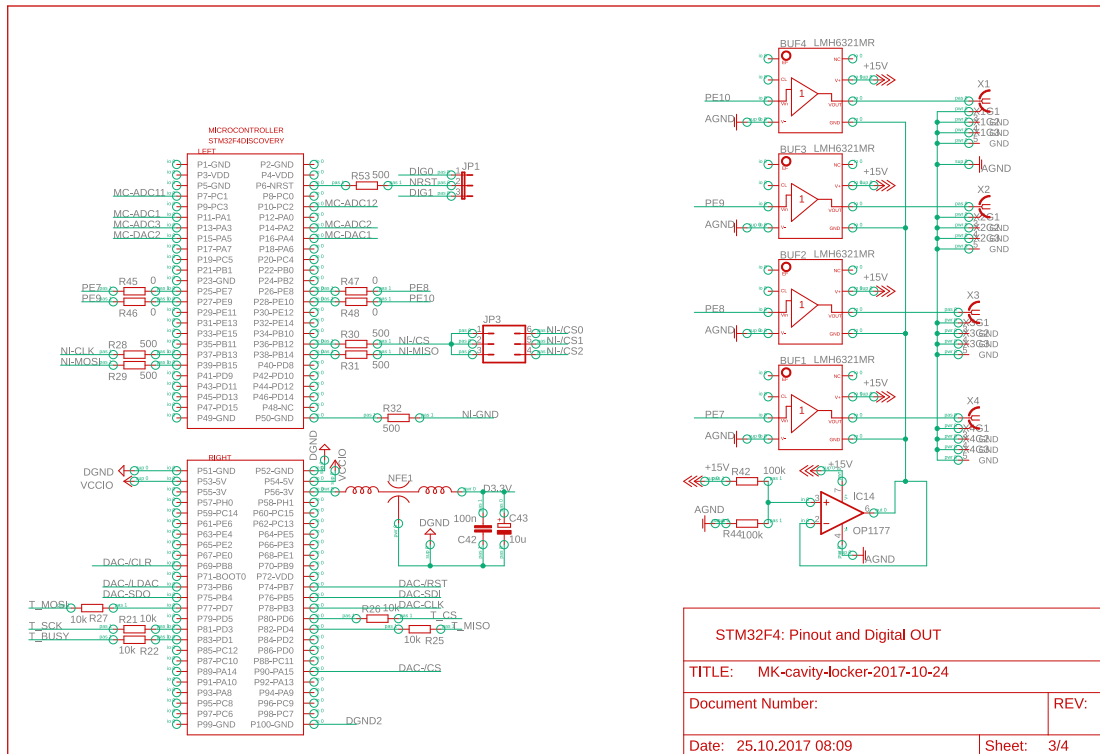
Figure F.8.: Second part of the schematic of the *MK-cavity-locker* module. (top) Supply voltages and pin-out of the backplane connector. (bottom) Pin-out of the microcontroller evaluation board and the buffered digital outputs.

G. Pictures of the analyse cavity setups

This appendix was added on a voluntary basis after the evaluation of the thesis.
It shows pictures of the analyse cavity setups that are drawn schematically in Figure 3.4 and
Figure 3.6.

In the three pictures, the short gray tube contains the 854 nm analysis cavity, while the long
tube contains the 393 nm cavity. The pink fiber collimator holder at the 393 nm setup corre-
spond to the feedback beam (blue fiber), the photon beam (no fiber connected) and the output
beam. In case of the 854 nm setup only the feedback beam (right most collimator) and the
photon beam input (middle collimator) are visible. The output collimator is located at the left
side that is cut out in the first picture.
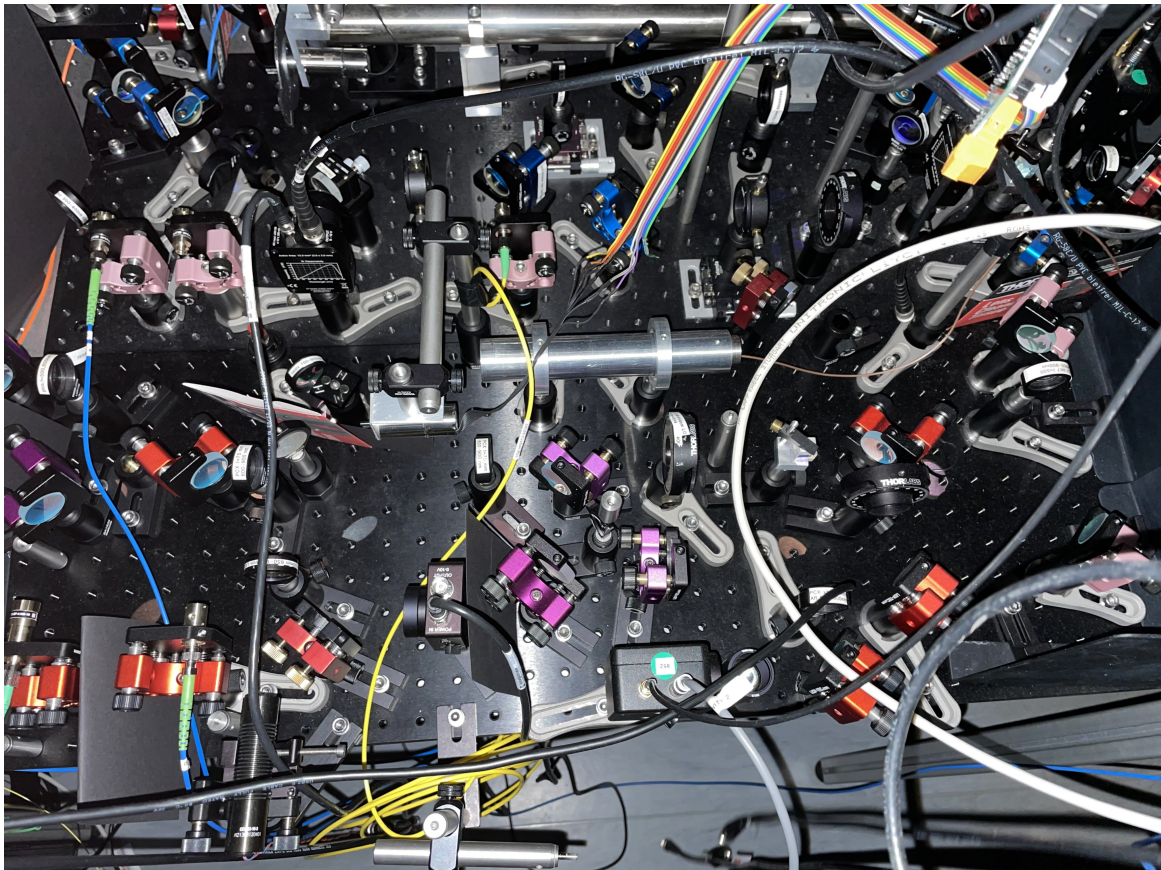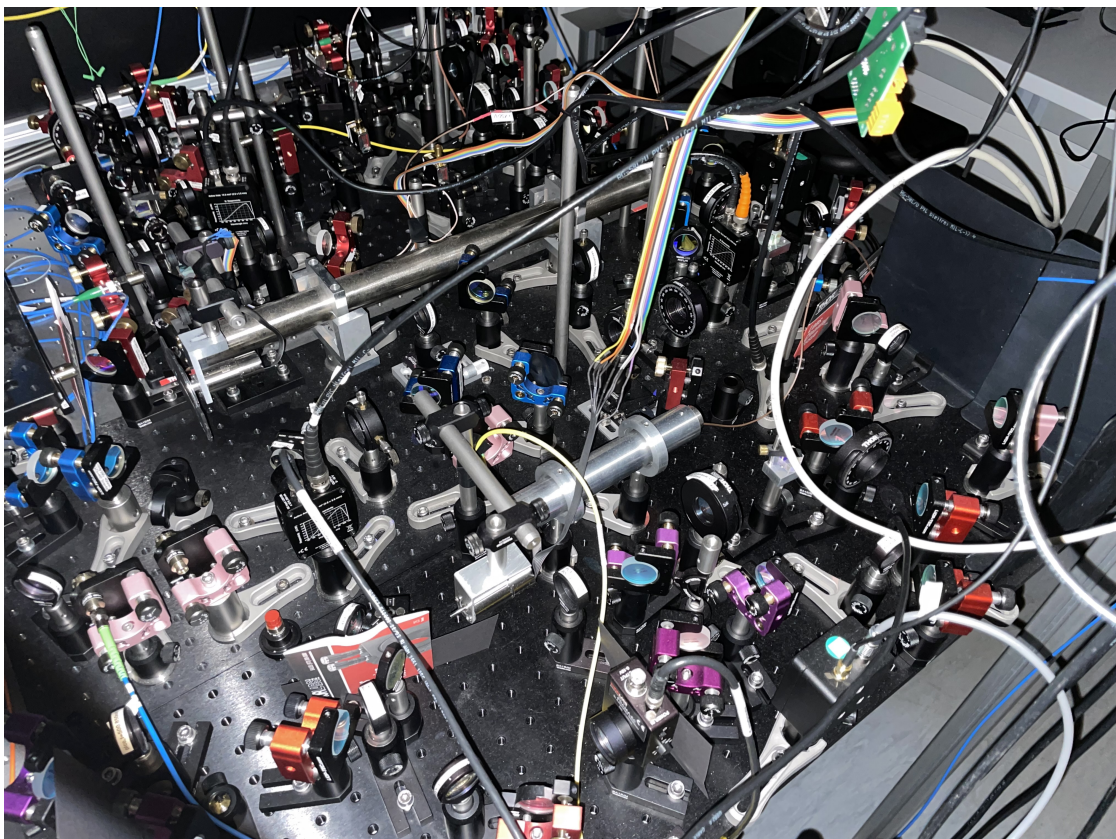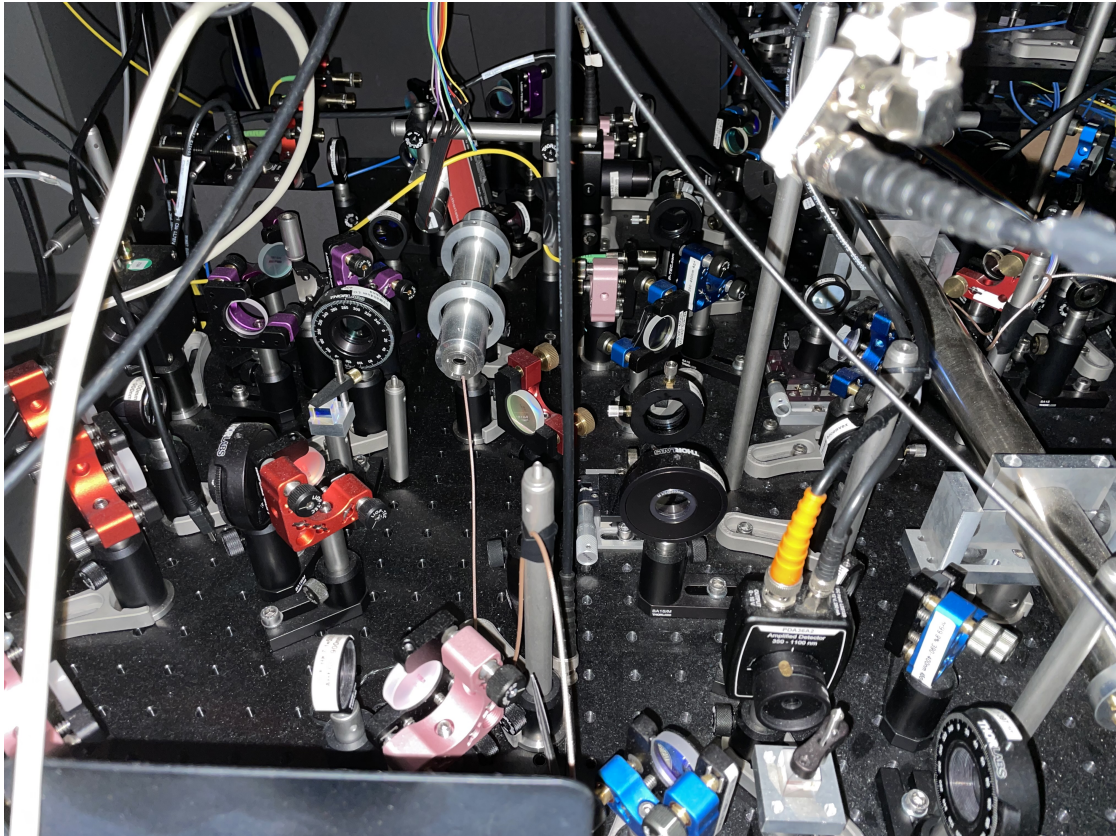
Bibliography

[1] H. J. Kimble. The quantum internet. *Nature* **453** 1023–1030 (2008).

[2] D. P. DiVincenzo. The Physical Implementation of Quantum Computation. *Fortschr. Phys.* **48** 771–783 (2000).

[3] J. Yin, J.-G. Ren, H. Lu, Y. Cao, H.-L. Yong, Y.-P. Wu, C. Liu, S.-K. Liao, F. Zhou, Y. Jiang, X.-D. Cai, P. Xu, G.-S. Pan, J.-J. Jia, Y.-M. Huang, H. Yin, J.-Y. Wang, Y.-A. Chen, C.-Z. Peng and J.-W. Pan. Quantum teleportation and entanglement distribution over 100-kilometre free-space channels. *Nature* **488** 185–188 (2012).

[4] X.-S. Ma, T. Herbst, T. Scheidl, D. Wang, S. Kropatschek, W. Naylor, B. Wittmann, A. Mech, J. Kofler, E. Anisimova, V. Makarov, T. Jennewein, R. Ursin and A. Zeilinger. Quantum teleportation over 143 kilometres using active feed-forward. *Nature* **489** 269–273 (2012).

[5] J.-G. Ren, P. Xu, H.-L. Yong, L. Zhang, S.-K. Liao, J. Yin, W.-Y. Liu, W.-Q. Cai, M. Yang, L. Li, K.-X. Yang, X. Han, Y.-Q. Yao, J. Li, H.-Y. Wu, S. Wan, L. Liu, D.-Q. Liu, Y.-W. Kuang, Z.-P. He, P. Shang, C. Guo, R.-H. Zheng, K. Tian, Z.-C. Zhu, N.-L. Liu, C.-Y. Lu, R. Shu, Y.-A. Chen, C.-Z. Peng, J.-Y. Wang and J.-W. Pan. Ground-to-satellite quantum teleportation. *Nature* **549** 70–73 (2017).

[6] M. Bock, P. Eich, S. Kucera, M. Kreis, A. Lenhard, C. Becher and J. Eschner. High-fidelity entanglement between a trapped ion and a telecom photon via quantum frequency conversion. *Nat. Commun.* **9** 1998 (2018).

[7] V. Krutyanskiy, M. Meraner, J. Schupp, V. Krcmarsky, H. Hainzer and B. P. Lanyon. Light-matter entanglement over 50 km of optical fibre. *npj Quantum Inf.* **5** 72 (2019).

[8] W. K. Wootters and W. H. Zurek. A single quantum cannot be cloned. *Nature* **299** 802–803 (1982).

[9] H.-J. Briegel, W. Dür, J. I. Cirac and P. Zoller. Quantum Repeaters: The Role of Imperfect Local Operations in Quantum Communication. *Phys. Rev. Lett.* **81** 5932–5935 (1998).

[10] S. Abruzzo, S. Bratzik, N. K. Bernardes, H. Kampermann, P. van Loock and D. Bruß. Quantum repeaters and quantum key distribution: Analysis of secret-key rates. *Phys. Rev. A* **87** 052315 (2013).

[11] P. Müller and J. Eschner. Single calcium-40 ion as quantum memory for photon polarization: a case study. *Appl. Phys. B* **114** 303–306 (2013).

[12] C. Kurz, M. Schug, P. Eich, J. Huwer, P. Müller and J. Eschner. Experimental protocol for high-fidelity heralded photon-to-atom quantum state transfer. *Nat. Commun.* **5** 5527 (2014).

[13] A. Lenhard, M. Bock, C. Becher, S. Kucera, J. Brito, P. Eich, P. Müller and J. Eschner. Telecom-heralded single-photon absorption by a single atom. *Phys. Rev. A* **92** 063827 (2015).

[14] C. Kurz, P. Eich, M. Schug, P. Müller and J. Eschner. Programmable atom-photon quantum interface. *Phys. Rev. A* **93** 062348 (2016).

[15] J. Brito, S. Kucera, P. Eich, P. Müller and J. Eschner. Doubly heralded single-photon absorption by a single atom. *Appl. Phys. B* **122** 36 (2016).

[16] M. Almendros, J. Huwer, N. Piro, F. Rohde, C. Schuck, M. Hennrich, F. Dubin and J. Eschner. Bandwidth-Tunable Single-Photon Source in an Ion-Trap Quantum Network. *Phys. Rev. Lett.* **103** 213601 (2009).

[17] C. Kurz, J. Huwer, M. Schug, P. Müller and J. Eschner. A high-rate source for single photons in a pure quantum state. *New J. Phys.* **15** 055005 (2013).

[18] M. Keller, B. Lange, K. Hayasaka, W. Lange and H. Walther. Continuous generation of single photons with controlled waveform in an ion-trap cavity system. *Nature* **431** 1075–1078 (2004).

[19] M. Schug, C. Kurz, P. Eich, J. Huwer, P. Müller and J. Eschner. Quantum interference in the absorption and emission of single photons by a single ion. *Phys. Rev. A* **90** 023829 (2014).

[20] P. Müller, T. Tentrup, M. Bienert, G. Morigi and J. Eschner. Spectral properties of single photons from quantum emitters. *Phys. Rev. A* **96** 023861 (2017).

[21] J. Höffges. Untersuchung der Resonanzfluoreszenz eines einzelnen gespeicherten Ions. Ph.D. thesis, Ludwig-Maximilian-Universität München (1997).

[22] Y. Stalgis. Laser–Fluoreszenz– und Absorptionsspektroskopie an einem einzelnen Ion. Ph.D. thesis, Universität Hamburg (1998).

[23] L. Béguin, J.-P. Jahn, J. Wolters, M. Reindl, Y. Huo, R. Trotta, A. Rastelli, F. Ding, O. G. Schmidt, P. Treutlein and R. J. Warburton. On-demand semiconductor source of 780-nm single photons with controlled temporal wave packets. *Phys. Rev. B* **97** 205304 (2018).

[24] T. M. Sweeney, S. G. Carter, A. S. Bracker, M. Kim, C. S. Kim, L. Yang, P. M. Vora, P. G. Brereton, E. R. Cleveland and D. Gammon. Cavity-stimulated Raman emission from a single quantum dot spin. *Nat. Photonics* **8** 442–447 (2014).

[25] P. C. Müller. A quantum networkof single ions and single photons: «on the way» and «off the trail». Ph.D. thesis, Universität des Saarlandes (2021).

[26] J. Jin and D. A. Church. Precision lifetimes for the Ca$^+$ 4p^2 P levels: Experiment challenges theory at the 1% level. *Phys. Rev. Lett.* **70** 3213 (1993).

[27] A. Kreuter, C. Becher, G. P. T. Lancaster, A. B. Mundt, C. Russo, H. Häffner, C. Roos, W. Hänsel, F. Schmidt-Kaler, R. Blatt and M. S. Safronova. Experimental and theoretical study of the 3d ^2D–level lifetimes of ^{40}Ca$^+$. *Phys. Rev. A* **71** 032504 (2005).

[28] R. Gerritsma, G. Kirchmair, F. Zähringer, J. Benhelm, R. Blatt and C. F. Roos. Precision measurement of the branching fractions of the 4p ^{2}P$_{3/2}$ decay of Ca II. *Eur. Phys. J. D* **50** 13–19 (2008).

[29] M. Ramm, T. Pruttivarasin, M. Kokish, I. Talukdar and H. Häffner. Precision Measurement Method for Branching Fractions of Excited $P_{1/2}$ States Applied to ^{40}Ca$^+$. *Phys. Rev. Lett.* **111** 023004 (2013).

[30] P. Baumgart. D$_{5/2}$ Zeeman Substates Dressed by a Radio Frequency Magnetic Field: Spectroscopy and Theory. Bachelor's thesis (2021).

[31] W. Paul and H. Steinwedel. Ein neues Massenspektrometer Ohne Magnetfeld. *Zeitschrift Naturforschung Teil A* **8** 448 (1953).

[32] E. Fischer. Die dreidimensionale Stabilisierung von Ladungsträgern in einem Vierpolfeld. *Z. Für Phys.* **156** 1–26 (1959).

[33] W. Neuhauser, M. Hohenstatt, P. E. Toschek and H. Dehmelt. Localized visible Ba$^+$ mono-ion oscillator. *Phys. Rev. A* **22** 1137–1140 (1980).

[34] J. Chiaverini, R. Blakestad, J. Britton, J. Jost, C. Langer, D. Leibfried, R. Ozeri and D. Wineland. Surface-electrode architecture for ion-trap quantum information processing. *Quantum Information and Computation* **5** 419–439 (2005).

[35] C. E. Pearson, D. R. Leibrandt, W. S. Bakr, W. J. Mallard, K. R. Brown and I. L. Chuang. Experimental investigation of planar ion traps. *Phys. Rev. A* **73** 032307 (2006).

[36] D. Stick, W. K. Hensinger, S. Olmschenk, M. J. Madsen, K. Schwab and C. Monroe. Ion trap in a semiconductor chip. *Nat. Phys.* **2** 36–39 (2005).

[37] W. K. Hensinger, S. Olmschenk, D. Stick, D. Hucul, M. Yeo, M. Acton, L. Deslauriers, C. Monroe and J. Rabchuk. T-junction ion trap array for two-dimensional ion shuttling, storage, and manipulation. *Appl. Phys. Lett.* **88** 034101 (2006).

[38] H. Kaufmann, T. Ruster, C. T. Schmiegelow, M. A. Luda, V. Kaushal, J. Schulz, D. von Lindenfels, F. Schmidt-Kaler and U. G. Poschinger. Fast ion swapping for quantum-information processing. *Phys. Rev. A* **95** 052319 (2017).

[39] W. Paul. Electromagnetic traps for charged and neutral particles. *Reviews of Modern Physics* **62** 531–540 (1990).

[40] D. Leibfried, R. Blatt, C. Monroe and D. Wineland. Quantum dynamics of single trapped ions. *Rev. Mod. Phys.* **75** 281–324 (2003).

[41] S. T. Gulde. Experimental Realization of Quantum Gates and the Deutsch-Jozsa Algorithm with Trapped ^{40}Ca$^+$ Ions. Ph.D. thesis, Leopold-Franzens-Universität Innsbruck (2003).

[42] M. A. Nielsen and I. L. Chuang. Quantum Computation and Quantum Information. Cambridge University Press (2009).

[43] D. A. Steck. Quantum and Atom Optics. Available online at http://steck.us/teaching (revision 0.11.6, 24 February 2017).

[44] M. B. Plenio and S. Virmani. An introduction to entanglement measures. *Quantum Information and Computation* **7** 1–51 (2007).

[45] D. F. V. James, P. G. Kwiat, W. J. Munro and A. G. White. Measurement of qubits. *Phys. Rev. A* **64** 052312 (2001).

[46] J. F. Clauser, M. A. Horne, A. Shimony and R. A. Holt. Proposed Experiment to Test Local Hidden-Variable Theories. *Phys. Rev. Lett.* **23** 880–884 (1969).

[47] I. V. Hertel and C.-P. Schulz. Atome, Moleküle und optische Physik 1. Springer, Berlin Heidelberg (2017).

[48] D. Meschede. Optik, Licht und Laser. Vieweg+Teubner, Wiesbaden (2008).

[49] N. Ismail, C. C. Kores, D. Geskus and M. Pollnau. Fabry-Pérot resonator: spectral line shapes, generic and related Airy distributions, linewidths, finesses, and performance at low or frequency-dependent reflectivity. *Opt. Express* **24** 16366 (2016).

[50] G. Süssmann. Uncertainty Relation: From Inequality to Equality. *Zeitschrift für Naturforschung A* **52** 49–52 (1997).

[51] W. P. Schleich. Quantum Optics in Phase Space. Wiley, Berlin (2001).

[52] F. Rohde. Remote ion traps for quantum networking: Two-photon interference and correlations. Ph.D. thesis, Institute of Photonic Sciences (2009).

[53] C. Schuck. Interfacing single ions and single photonsfor quantum networks. Ph.D. thesis, Institute of Photonic Sciences (2009).

[54] M. Almendros. Towards Long-Distance Quantum Communication. Ph.D. thesis, Institute of Photonic Sciences (2010).

[55] J. Huwer. Experimental tools for quantum networking operations with single photonsand single ions. Ph.D. thesis, Universität des Saarlandes (2013).

[56] M. Schug. Single photons from single ions: quantum interference and distant ion interaction. Ph.D. thesis, Universität des Saarlandes (2015).

[57] C. Kurz. Quantum networking with single ions and single photons interfaced in free space. Ph.D. thesis, Universität des Saarlandes (2015).

[58] S. Kucera. Experimental distribution of entanglement in ion-photon quantum networks: Photon-pairs as resource. Ph.D. thesis, Universität des Saarlandes (2019).

[59] R. P. Eich. Single-ion based quantum interface for quantum-network applications. Ph.D. thesis, Universität des Saarlandes (2019).

[60] M. Bock. Polarization-Preserving Quantum Frequency Conversion for Trapped-Atom based Quantum Networks. Ph.D. thesis, Universität des Saarlandes (2021).

[61] M. Schug, J. Huwer, C. Kurz, P. Müller and J. Eschner. Heralded Photonic Interaction between Distant Single Ions. *Phys. Rev. Lett.* **110** 213603 (2013).

[62] F. Laurent. Design, Simulation, and Construction of a Novel Ion Trap for Quantum Networking. Master's thesis, Universität des Saarlandes (2022).

[63] R. B. Blakestad, C. Ospelkaus, A. P. VanDevender, J. H. Wesenberg, M. J. Biercuk, D. Leibfried and D. J. Wineland. Near-ground-state transport of trapped-ion qubits through a multidimensional array. *Phys. Rev. A* **84** 032314 (2011).

[64] T. Ruster, C. T. Schmiegelow, H. Kaufmann, C. Warschburger, F. Schmidt-Kaler and U. G. Poschinger. A long-lived Zeeman trapped-ion qubit. *Appl. Phys. B* **122** (2016).

[65] O. Elshehy. Permanent-magnet-based Zeeman field generation in an ion trap. Master's thesis, Universität des Saarlandes (2018).

[66] H. Lahm. Supression of magnetic-noise-induced decoherence in Zeeman trapped-ion qubits. Master's thesis, Universität des Saarlandes (2021).

[67] F. Rohde, M. Almendros, C. Schuck, J. Huwer, M. Hennrich and J. Eschner. A diode laser stabilization scheme for $^{40}Ca^+$ single-ion spectroscopy. *J. Phys. B: At. Mol. Opt. Phys.* **43** 115401 (2010).

[68] B. Edlén. The Refractive Index of Air. *Metrologia* **2** 71–80 (1966).

[69] E. Riedle, S. H. Ashworth, J. T. Farrell and D. J. Nesbitt. Stabilization and precise calibration of a continuous-wave difference frequency spectrometer by use of a simple transfer cavity. *Rev. Sci. Instrum.* **65** 42–48 (1994).

[70] K. Klein. Optische Resonatoren für die Laser-Stabilisierung und für die Spektralanalyse einzelner Photonen. Master's thesis, Universität des Saarlandes (2016).

[71] C. Haen. Spektralanalyse von Einzelphotonen. Bachelor's thesis (2017).

[72] J. Frey. Spektrale Messungen an der Resonanzfluoreszenz einzelner Atome. Bachelor's thesis (2018).

[73] M. L. Bergerhoff. Spektren der Resonanzfluoreszenz eines einzelnen Calciumions. Bachelor's thesis (2019).

[74] J. M. C. M. Ritter. Anregung eines ^{40}Ca$^+$-Ions zur Erzeugung von Atom-Photon-Verschränkung. Master's thesis, Universität des Saarlandes (2021).

[75] S. Kucera. Digitale LASER-Leistungsstabilisierung für Einzelatomspektroskopie. Master's thesis, Universität des Saarlandes (2013).

[76] M. Kreis. Magnetfeldstabilisierung für Hochpräzise Einzelatom Spektroskopie. Master's thesis, Universität des Saarlandes (2014).

[77] J. Eschner, G. Morigi, F. Schmidt-Kaler and R. Blatt. Laser cooling of trapped ions. *Journal of the Optical Society of America B* **20** 1003 (2003).

[78] S. Stenholm. The semiclassical theory of laser cooling. *Rev. Mod. Phys.* **58** 699–739 (1986).

[79] F. Diedrich, J. C. Bergquist, W. M. Itano and D. J. Wineland. Laser Cooling to the Zero-Point Energy of Motion. *Phys. Rev. Lett.* **62** 403–406 (1989).

[80] G. Morigi, J. Eschner and C. H. Keitel. Ground State Laser Cooling Using Electromagnetically Induced Transparency. *Phys. Rev. Lett.* **85** 4458–4461 (2000).

[81] C. F. Roos, D. Leibfried, A. Mundt, F. Schmidt-Kaler, J. Eschner and R. Blatt. Experimental Demonstration of Ground State Laser Cooling with Electromagnetically Induced Transparency. *Phys. Rev. Lett.* **85** 5547–5550 (2000).

[82] J. Roßnagel, K. N. Tolazzi, F. Schmidt-Kaler and K. Singer. Fast thermometry for trapped ions using dark resonances. *New J. Phys.* **17** 045004 (2015).

[83] C. Lisowski, M. Knoop, C. Champenois, G. Hagel, M. Vedel and F. Vedel. Dark resonances as a probe for the motional state of a single ion. *Appl. Phys. B* **81** 5–12 (2005).

[84] K. Toyoda, H. Shiibara, S. Haze, R. Yamazaki and S. Urabe. Experimental study of the coherence of a terahertz-separated metastable-state qubit in ^{40}Ca$^+$. *Phys. Rev. A* **79** 023419 (2009).

[85] M. Ježek, J. Fiurášek and Z. Hradil. Quantum inference of states and processes. *Phys. Rev. A* **68** 012305 (2003).

[86] S. T. Flammia, A. Silberfarb and C. M. Caves. Minimal Informationally Complete Measurements for Pure States. *Foundations of Physics* **35** 1985–2006 (2005).

[87] S.-Y. Zhu, L. M. Narducci and M. O. Scully. Quantum-mechanical interference effects in the spontaneous-emission spectrum of a driven atom. *Phys. Rev. A* **52** 4791–4802 (1995).

[88] S. Yuan and J.-Y. Gao. Effects of quantum interference on the spontaneous emission in a coherently driven three-level atom. *Eur. Phys. J. D* **11** 267–272 (2000).

[89] C. Cohen-Tannoudji, J. Dupont-Roc and G. Grynberg. Atom-Photon Interactions. Wiley (2004).

[90] V. Weisskopf and E. Wigner. Berechnung der natürlichen Linienbreite auf Grund der Diracschen Lichttheorie. *Zeitschrift für Physik* **63** 54–73 (1930).

[91] S. H. Autler and C. H. Townes. Stark Effect in Rapidly Varying Fields. *Phys. Rev.* **100** 703–722 (1955).

[92] K. Mølmer, Y. Castin and J. Dalibard. Monte Carlo wave-function method in quantum optics. *Journal of the Optical Society of America B* **10** 524 (1993).

[93] S.-Y. Zhu and M. O. Scully. Quantum interference effects in the Autler-Townes spontaneous spectrum. *Phys. Lett. A* **201** 85–90 (1995).

[94] M. O. Scully and K. Drühl. Quantum eraser: A proposed photon correlation experiment concerning observation and "delayed choice" in quantum mechanics. *Phys. Rev. A* **25** 2208–2213 (1982).

[95] A. Lenhard. Quantum Photonic Interfaces between Atomic and Telecommunication Wavelengths. Ph.D. thesis, Universität des Saarlandes (2015).

[96] A. Stute, B. Casabone, P. Schindler, T. Monz, P. O. Schmidt, B. Brandstätter, T. E. Northup and R. Blatt. Tunable ion–photon entanglement in an optical cavity. *Nature* **485** 482–485 (2012).

[97] A. Stute. A light-matter quantum interface:ion-photon entanglementand state mapping. Ph.D. thesis, Leopold-Franzens-Universitat Innsbruck (2012).

[98] J. Arenskötter. Photonenpaarquelle für Einzelatom-Einzelphoton Wechselwirkung. Master's thesis, Universität des Saarlandes (2016).

[99] K. Mølmer and A. Sørensen. Multiparticle Entanglement of Hot Trapped Ions. *Phys. Rev. Lett.* **82** 1835–1838 (1999).

[100] A. Sørensen and K. Mølmer. Quantum Computation with Ions in Thermal Motion. *Phys. Rev. Lett.* **82** 1971–1974 (1999).

[101] J. B. Wübbena, S. Amairi, O. Mandel and P. O. Schmidt. Sympathetic cooling of mixed-species two-ion crystals for precision spectroscopy. *Phys. Rev. A* **85** 043412 (2012).

Danksagung